University of Windsor

Scholarship at UWindsor

Electronic Theses and Dissertations | Theses, Dissertations, and Major Papers

10-8-2019

On the Modeling, Analysis and Development of PMSM: For Traction and Charging Application

Shruthi Mukundan
University of Windsor

Follow this and additional works at: https://scholar.uwindsor.ca/etd

Recommended Citation

Mukundan, Shruthi, "On the Modeling, Analysis and Development of PMSM: For Traction and Charging Application" (2019). *Electronic Theses and Dissertations*. 7824.
https://scholar.uwindsor.ca/etd/7824

This online database contains the full-text of PhD dissertations and Masters' theses of University of Windsor students from 1954 forward. These documents are made available for personal study and research purposes only, in accordance with the Canadian Copyright Act and the Creative Commons license—CC BY-NC-ND (Attribution, Non-Commercial, No Derivative Works). Under this license, works must always be attributed to the copyright holder (original author), cannot be used for any commercial purposes, and may not be altered. Any other use would require the permission of the copyright holder. Students may inquire about withdrawing their dissertation and/or thesis from this database. For additional inquiries, please contact the repository administrator via email (scholarship@uwindsor.ca) or by telephone at 519-253-3000ext. 3208.

On the Modeling, Analysis and Development of PMSM: For Traction and Charging Application

By

Shruthi Mukundan

A Dissertation
Submitted to the Faculty of Graduate Studies
through the Department of Electrical & Computer Engineering
in Partial Fulfillment of the Requirements for
the Degree of Doctor of Philosophy
at the University of Windsor

Windsor, Ontario, Canada

© 2019 Shruthi Mukundan

ON THE MODELING, ANALYSIS AND DEVELOPMENT OF PMSM: FOR TRACTION AND CHARGING APPLICATION

By

Shruthi Mukundan

APPROVED BY:

____
X. Liang, External Examiner
University of Saskatchewan

____
A. Edrisy
Department of Mechanical, Automotive and Materials Engineering

____
A. Emadi
Department of Electrical and Computer Engineering

____
M. Azzouz
Department of Electrical and Computer Engineering

____
J. Tjong, Co–Advisor
Department of Mechanical, Automotive and Materials Engineering

____
N. C. Kar, Advisor
Department of Electrical and Computer Engineering

October 8, 2019

DECLARATION OF CO–AUTHORSHIP / PREVIOUS PUBLICATIONS

I hereby declare that this thesis incorporates material that is result of joint research, as follows:

This dissertation includes the outcome of publications which also have co–authors who are/were graduate students or post–doctoral fellows supervised by Dr. Narayan Kar. In all cases, only primary contributions of the author towards these publications are included in this dissertation. The contribution of co–authors was primarily through the provision of assistance in experimentation and analysis.

I am aware of the University of Windsor Senate Policy on Authorship and I certify that I have properly acknowledged the contribution of other researchers to my thesis, and have obtained written permission from each of the co–authors to include the above materials in my thesis.

I certify that, with the above qualification, this thesis, and the research to which it refers, is the product of my own work. This thesis includes nine original papers that have been previously published/submitted for publication in peer reviewed IEEE Transactions and IEEE International conferences, as follows:

Thesis Chapter	**Publication Title/Full Citation**	**Publication Status**
Chapters 2 & 7	**S. Mukundan**, H. Dhulipati, K. L. V. Iyer, C. Lai, K. Mukherjee and N. C. Kar, “Comparative Performance Analysis of 3–Phase IPMSM Rotor Configurations with Dampers for Integrated Charging Application in EVs,” in proc. of *IEEE* 43*rd* *Annual Conf. of the Ind. Electronics Society* (IECON), Beijing, China, 2017, pp. 1856–1861.	*Published*
Chapter 3	**S. Mukundan**, H. Dhulipati, E. Ghosh, G Feng, and N. C. Kar, “Non–Dominated Sorting Genetic Algorithm Based Investigation of Optimal Odd Slot Numbers for Stator Shifted Fractional–Slot Wound PMSMs,” Accepted for presentation at *IEEE Energy Conv. Congress and Exposition* (ECCE), Baltimore, USA, September 2019.	*Accepted for publication*

Chapter 4	**S. Mukundan**, H. Dhulipati, G. Feng, J. Tjong and N. C. Kar, "Modeling and Analysis of Novel Star–Delta Winding Configuration with Odd Slot Numbers for Reduced Space Harmonics Using Winding Function," in proc. of *IEEE International Electric Machines & Drives Conference* (IEMDC), San Diego, CA, USA, 2019, pp. 1910–1916.	*Published*
Chapter 5	**S. Mukundan**, H. Dhulipati, J. Tjong, and N. C. Kar, "Parameter Determination of PMSM using Coupled Electromagnetic and Thermal Model Incorporating Current Harmonics," *IEEE Transactions on Magnetics*, vol. 54, no. 11, pp. 1–5, Nov. 2018.	*Published*
Chapter 6	**S. Mukundan**, E. Ghosh, H. Dhulipati, J. Tjong, and N.C. Kar, "Pareto ACO Algorithm Based Optimal Design of IPM Rotor Utilizing Star–Delta Winding Harmonics towards Maximum Torque Density and Extended Operating Range," submitted to *IEEE Transactions on Energy Conversion*, 2019.	*Submitted*
Chapter 6	**S. Mukundan**, K. L. V. Iyer, H. Dhulipati, K. Mukherjee, Jimi Tjong and N. C. Kar, "Response Surface Methodology based Optimization of Surface PM Machine Incorporating Stator Slotting and PM Sizing Effects to Extend the Operating Limits for Direct–Drive EV Application," in proc. of *IEEE International Conference on Electric Machines* (ICEM), Switzerland, 2016, pp. 2045–2051.	*Published*
Chapter 7	**S. Mukundan**, H. Dhulipati, C. Lai, K. Mukherjee, J. Tjong and N. C. Kar, "Design and Optimization of Traction IPMSM with Asymmetrical Damper Bars for Integrated Charging Capability using Evolutionary Algorithm", in *IEEE Transactions on Energy Conversion*, vol. 33, no. 4, pp. 2060–2069, Dec. 2018.	*Published*
Chapter 8	**S. Mukundan**, H. Dhulipati, L. Chauvin, A. Edrisy, J. Tjong, and N. C. Kar, "Comparative Performance Analysis of Copper and Aluminum Wound Fractional–Slot PMSMs for High–Speed Traction Application," Accepted for presentation at the *IEEE 22nd International Conference on Electrical Machines and Systems* (ICEMS), China, August 2019.	*Accepted for publication*

Chapter 8	**S. Mukundan**, H. Dhulipati, K. L. V. Iyer, N. C. Kar and K. Mukherjee, "Comparison of inductance determination methods of PMSMs for EV application," in proc. of *IEEE* 30th *Canadian Conference on Electrical and Computer Engineering* (CCECE), Windsor, ON, 2017, pp. 1–4.	*Published*

I certify that I have obtained a written permission from the copyright owners to include the above published materials in my dissertation. I certify that the above material describes work completed during my registration as a graduate student at the University of Windsor.

I declare that, to the best of my knowledge, my thesis does not infringe upon anyone's copyright nor violate any proprietary rights and that any ideas, techniques, quotations, or any other material from the work of other people included in my thesis, published or otherwise, are fully acknowledged in accordance with the standard referencing practices. Furthermore, to the extent that I have included copyrighted material that surpasses the bounds of fair dealing within the meaning of the Canada Copyright Act, I certify that I have obtained a written permission from the copyright owners to include such materials in my thesis.

I declare that this is a true copy of my thesis, including any final revisions, as approved by my thesis committee and the Graduate Studies office, and that this thesis has not been submitted for a higher degree to any other University or Institution.

ABSTRACT

Permanent magnet synchronous machines (PMSMs) are widely implemented commercially available traction motors owing to their high torque production capability and wide operating speed range. However, to achieve significant electric vehicle (EV) global market infiltration in the coming years, the technological gaps in the technical targets of the traction motor must be addressed towards further improvement of driving range per charge of the vehicle and reduced motor weight and cost. Thus, this thesis focuses on the design and development of a novel high speed traction PMSM with improved torque density, maximized efficiency, reduced torque ripple and increased driving range suitable for both traction and integrated charging applications.

First, the required performance targets are determined using a drive cycle based vehicle dynamic model, existing literature and roadmaps for future EVs. An unconventional fractional–slot distributed winding configuration with a coil pitch of 2 is selected for analysis due to their short end–winding length, reduced winding losses and improved torque density. For the chosen baseline topology, a non–dominated sorting genetic algorithm based selection of optimal odd slot numbers is performed for higher torque production and reduced torque ripple. Further, for the selected odd slot–pole combination, a novel star–delta winding configuration is modeled and analyzed using winding function theory for higher torque density, reduced spatial harmonics, reduced torque ripple and machine losses.

Thereafter, to analyze the motor performance with control and making critical decisions on inter–dependent design parameter variations for machine optimization, a parametric design approach using a novel coupled magnetic equivalent circuit model and thermal model incorporating current harmonics for fractional–slot wound PMSMs was developed and verified. The developed magnetic circuit model incorporates all machine non–linearities including effects

of temperature and induced inverter harmonics as well as the space harmonics in the winding inductances of a fractional–slot winding configuration. Using the proposed model with a pareto ant colony optimization algorithm, an optimal rotor design is obtained to reduce the magnet utilization and obtain maximized torque density and extended operating range.

Further, the developed machine structure is also analyzed and verified for integrated charging operation where the machine's winding inductances are used as line inductors for charging the battery thereby eliminating the requirement of an on–board charger in the powertrain and hence resulting in reduced weight, cost and extended driving range. Finally, a scaled–down prototype of the proposed PMSM is developed and validated with experimental results in terms of machine inductances, torque ripple, torque–power–speed curves and efficiency maps over the operating speed range. Subsequently, understanding the capabilities and challenges of the developed scaled–down prototype, a full–scale design with commercial traction level ratings, will be developed and analyzed using finite element analysis. Further recommendations for design improvement, future work and analysis will also be summarized towards the end of the dissertation.

This is for you Amma, Ani, Ammamma and Thatha…

For being my source of inspiration, strength, love and support throughout…

I love you all…

ACKNOWLEDGEMENTS

Firstly, I would like to thank the Almighty for giving me such an amazing opportunity and instilling the courage and will to see through this entire journey. I would like to express my profound gratitude to my pillar of strength and a super woman, my mother, for single handedly providing me all the love, support, motivation and encouragement, without which I would not be who I am today. This is for you, amma, for all your hard work, prayers and belief in me. To my angel of a brother, Ani, for always standing by my side through all ups and downs, his relentless love and support, without which I would not have been able to do this. To my ammamma and late thatha, for being my biggest role models, constant source of motivation and unconditional love for which I am eternally grateful. I know he is constantly watching over and protecting me from above.

Dr. Narayan C. Kar, my supervisor at CHARGE Labs, for all his kindness, positivity, encouragement, determination and always believing in me from the first day at University of Windsor. I could not have asked for a better role model to look up to and learn so much. He has provided me with wonderful opportunities, outstanding resources, facilities and valuable life lessons. I can proudly say that I am a lot wiser now in many aspects because of him. He has constantly motivated all of us in the lab to be a team player and has molded me into the researcher, leader and person that I am today, for which no amount of thanks would be enough. Also, to Eunha Chu, for her unconditional love, kindness, support and for making the lab feel like home.

I would like to thank my co–supervisor, Dr. Jimi Tjong for his constant support with respect to all research needs and providing access to the facilities at Ford for prototype development. His key insights from the industrial side has been immensely useful and has opened up to new ideas and thoughts.

I would like to express my gratitude to my committee members Dr. Arezoo Emadi, Dr. Maher Azzouz and Dr. Afsaneh Edrisy for their constant support, kind words and investing their time to evaluate my research and providing me with their valuable suggestions. A special thanks to Dr. Xiaodong Liang, for agreeing to serve as my external examiner of this dissertation and providing me with insightful suggestions to further improve the research conducted in this thesis.

I would also like to thank Dr. Kaushik Mukherjee for his technical assistance and for reminding me and everyone in the lab the importance of fundamentals.

My sincere and deepest gratitude to Dr. Lakshmi Varaha Iyer, for being the best mentor, guide, companion and support system from my day one in Windsor. His positive attitude, determination, hard work and out–of–the–box thinking has been very addictive and educational. I have immensely enjoyed all the technical and non–technical discussions I have had with him throughout.

I would like to thank my best friend, partner–in–crime and support system, Ms. Himavarsha Dhulipati for all the laughter, love and for tolerating and encouraging me since day one. I could not have done this without her technical assistance and constant nagging of keeping up with deadlines. I would also like to thank my friend, Dr. Eshaan Ghosh, for his support, worldly wisdom, technical assistance and for bringing out the extra level of patience in me.

My sincere thanks to Ze Li for being there in spite of many hurdles and helping me with all the experiments in the lab. I would also like to thank Dr. Xiaomin Lu, Dr. Chunyan Lai and Dr. Guodong Feng for their technical help and thoughtful ideas. I would also like to thank Dr. Seog Kim, Dr. Wenlong Li and Alex Bourgalt for all the technical support throughout the prototype development process.

I would also like to thank all the members of CHARGE Labs who have been my family and friends throughout. A special thanks to Dr. Aiswarya Balamurali, "soon–to–be" Dr. Aida Mollaeian, Animesh Anik and Philip Korta for all the fun, laughter and enduring tester woes together. I have learnt a lot from each and every one from the lab both technically and otherwise.

My sincere thanks to Andrew Jenner, Denis Beaulieu, Bruce Durfy and all the members of the mechanical workshop at UWindsor for tolerating our constant nagging and all their continuous support to build several test setups and solve mechanical issues. A special thanks to Andria Ballo and Connie Iaquinta for their support and smiles.

A special thanks to Dr. Sheng Tiantian for building the prototype so quickly and efficiently and for his support all the way from across the world.

My heartfelt thanks and appreciation to my best friend, Mr. R. S. Praveen, for supporting and tolerating me throughout this journey and showing me nothing but love and happiness.

TABLE OF CONTENTS

LIST OF TABLES

LIST OF FIGURES

LIST OF ABBREVIATIONS

Abbreviation		Explanation
ACO	:	Ant Colony Optimization
AWG	:	American Wire Gauge
BEV	:	Battery Electric Vehicle
CPSR	:	Constant Power Speed Range
DOE	:	Department of Energy
EMF	:	Electromagnetic Force
EV	:	Electric Vehicle
FEA	:	Finite Element Analysis
FFT	:	Fast Fourier Transformation
FSCW	:	Fractional–Slot Concentrated Winding
FSDW	:	Fractional–Slot Distributed Winding
ICE	:	Internal Combustion Engine
IGBT	:	Insulated–Gate Bipolar Transistor
IPM	:	Interior Permanent Magnet
IPMSM	:	Interior Permanent Magnet Synchronous Machine
LCM	:	Least Common Multiple
LPTN	:	Lumped Parameter Thermal Network
MEC	:	Magnetic Equivalent Circuit
MMF	:	Magneto Motive Force
MTPA	:	Maximum Torque Per Ampere
NSGA	:	Non–Dominated Sorting Genetic Algorithm
PM	:	Permanent Magnet
PMSM	:	Permanent Magnet Synchronous Machine
RMS	:	Root Mean Square
RT	:	Real Time
THD	:	Total Harmonic Distortion
US	:	United States
WLTC	:	Worldwide Lightweight Test Cycle

Chapter 1
Introduction

This chapter presents an overview of the current electric vehicle (EV) market including a background literature compilation on the state–of–the–art technology at the component level such as traction motors, drives and battery charging infrastructure which are the major areas of foci in this dissertation. Based on the study conducted, the opportunities and challenges associated with electrified transportation are identified and the global requirements of the traction motor were established towards addressing these key issues. Further, from the literature survey conducted on commercially available high–speed traction motors, the technical targets for the advancement of motor technology in terms of weight, cost, efficiency and driving range are defined. Section 1.4 summarizes the objectives of the research and development conducted in this thesis towards mitigating the challenges associated with existing EV drivetrain components. Section 1.5 highlights all the research contributions of this thesis towards achieving the set technical targets. Subsequently, Section 1.6 presents the dissertation layout encapsulating the research conducted. Further background literature corresponding to specific research topics presented in this dissertation is provided in the respective chapters.

1.1. Electric Vehicle Market: Opportunities and Challenges

With growing environmental awareness and depleting natural resources caused by internal combustion engines (ICEs), the global market for electric vehicles (EVs) has been rapidly increasing [1]. Over the last decade, substantial interest towards electrification has urged automotive manufactures around the world towards EV production contributing towards sales growth by almost 54% between 2016 and 2017 [2]. The global EV stock is growing exponentially and the projected market is over $270 billion by 2019 with almost 72% growth in 2020 as seen in Fig. 1.1 [3]. With promising future, automakers and researchers are constantly attempting to enhance the vehicle drivetrain at both system and component levels to accelerate the adoption of EVs. Various design solutions incorporating new structures and materials based on available technology have been developed to match the performance of a typical combustion engine vehicle. However, from comparisons across leading EV models, the cost difference between EV and ICE vehicles to this day is over $13,000 [4]. Furthermore, unlike gasoline vehicles, the expansion of the EV market is restricted due to the limited driving range per single charge of the battery. For instance, as of 2018, only the Tesla Model S offers a range over 300 miles per single charge of the battery. While this could be addressed by improving the energy storage system density in the vehicle by using innovative materials, unlike gas stations, the number of charging stations available are very limited. Although the global number of charging stations is expected to reach 26.38 million units by 2024, charging stations must be installed by public authorities, commercial

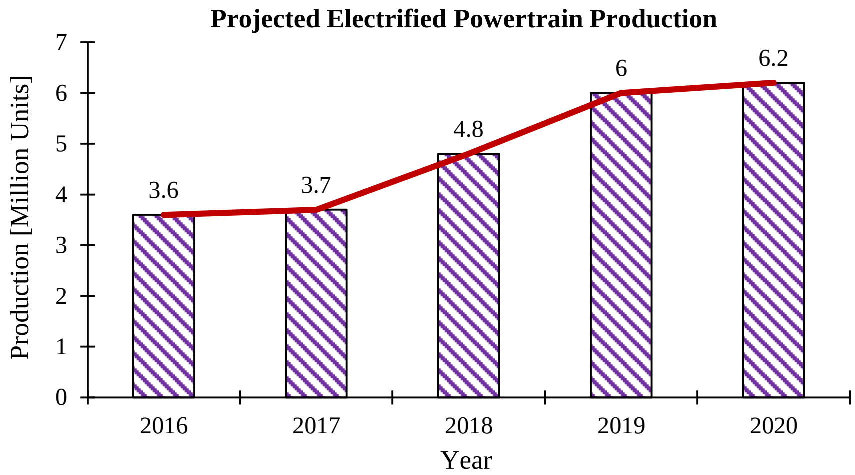

Fig. 1.1. Projected market for electrified powertrain production.

TABLE 1.1
COMPARISON OF COMMERCIALLY AVAILABLE EVS IN TERMS OF COST AND DRIVING RANGE

Vehicle	**Range [km]**	**Cost [$]**
Tesla Model S	555	99,315
Chevy Bolt EV	383	33,745
Tesla Model X	381	104,315
Jaguar I–Pace	377	63,025
Tesla Model 3	354	54,315
Audi e–Tron	328	68,295
Nissan Leaf	243	23,375
Volkswagen e–Golf	201	25,290
Hyundai Ioniq Electric	200	23,735
Ford Focus Electric	185	29,120
BMW i3	184	37,945
Kia Soul EV	179	33,950
Honda Clarity Electric	143	37,510
Mercedes B–Class Electric Drive	143	50,650
Fiat 500e	140	26,790

enterprises and some major employers in order to stimulate the market for electric vehicles. Table 1.1 summarizes the details of commercially available EVs in terms of cost and drive range [5], [6].

Thus, it can be seen that to capture share in this rapidly growing market, automotive industries and researchers across the world must address the following challenges:

- Reducing the price and total cost of the vehicle: This can be addressed by reducing the material usage of the individual drivetrain components including the traction motor, inverter and battery storage.
- Delivering increased performance and driving range: This can be perceived as a by–product of the aforementioned challenge as well. Reducing the overall drivetrain weight could increase the driving range. Also, innovative technologies or materials to improve the energy storage density could be a plausible solution.
- Providing convenient and rapid charging infrastructure: With increasing consumer demand and shifting government policies, more charging infrastructures could be developed.

In order to mitigate the aforementioned challenges, two main research targets are identified namely: to develop drivetrain components, specifically, a traction motor with reduced weight and cost and hence improve the charging capability and driving range of the EV. Thus, in the subsequent sections, comprehensive study on existing commercial traction motors and charging infrastructure will be presented and final research objectives will be highlighted.

1.2. Review of Commercially Available High–Speed Traction Motors

In a typical electric vehicle powertrain, the traction motor is the main component which decides the functionality and capability of the entire vehicle. The inverter ratings, battery utilization and the vehicle’s driving range are all determined based on the motor’s performance. Therefore, automakers and researchers are constantly working towards developing new and promising high–performance traction motors. However, the search for the best or optimized traction motor with economical, light–weight and highly efficient characteristics is still on–going. Further, with improved power electronics technology and high–end switching devices, the operating frequencies and hence the expected operating speed range of the traction motors are constantly increasing. On the other hand, with rocketing prices of rare–earth magnets, the research for cost–effective solutions and alternate rare–earth free designs is on–going. Therefore, in this section, based on existing commercial traction motors, the technical targets of the high–speed traction motor to be developed in this thesis will be established.

Commercially available EVs are dominantly driven by permanent magnet synchronous machines due to their high torque capability, increased speed range and better efficiency compared to their induction machine counterparts. Similar to ICE based vehicles, the traction motor must be capable of delivering high torques at low speeds during starting and up–hill drives, quick acceleration from stop to start, high power at high speeds during cruising and highway driving conditions. Further, the key performance factors of the motor include high efficiency, high temperature tolerant capacity, fault tolerance, high power and torque densities with compact size and weight, reliability, robustness and affordability. The desired traction motor characteristics over the entire speed range in order to satisfy all the vehicle driving conditions is illustrated in Fig. 1.2. In case of battery EVs, the typical DC bus voltage range varies from 100 – 800 V. In this thesis, similar to predominant North American automakers, a 400 V DC bus system is chosen for the traction motor.

Table 1.2 compares various features of commercially used high–speed traction motors in terms of peak power and torque capabilities, maximum speed, motor weight and power and torque densities [7], [8]. All the traction motors indicated in the table are predominantly permanent magnet synchronous motors only. The motor weight includes the motor casing as well and it can be observed that a typical traction motor's torque density lies between the 5 – 8 Nm/kg and the power density lies between 1 – 3 kW/kg. The maximum speed varies up to almost 15,000 rpm highlighting the wide drive range. Moreover, it is important to note that, with at least 10% weight reduction of the electric vehicle powertrain, a 5% increase in driving range is obtained which is a phenomenal advantage. On the other hand, developing such high volume motors to achieve the

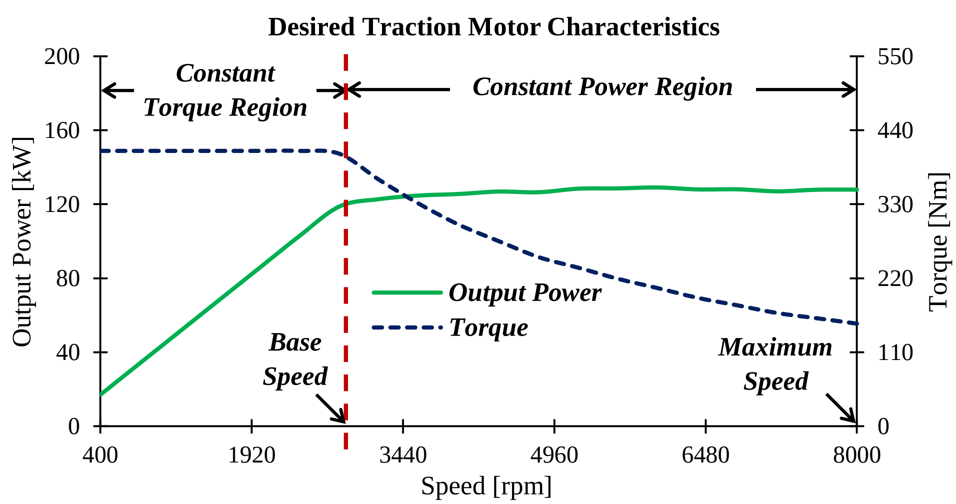

Fig. 1.2. Desired traction motor performance characteristics.

TABLE 1.2
FEATURES OF COMMERCIALLY AVAILABLE HIGH–SPEED TRACTION MOTORS

Vehicle Model	Peak Power	Peak Torque	Maximum Speed	Motor Weight [kg]	Specific Power Density [kW/kg]	Torque Density [Nm/kg]
2012 Leaf	80	280	10,400	56	1.4	5
2011 Sonata	30	205	6,000	33	1.1	6.2
2010 Prius	60	207	13,500	96	1.6	2.2
2008 LS600h Lexus	110	300	10,230	275	2.5	1.1
2007 Camry	79	270	14,000	134	1.7	2
2004 Prius	50	400	6,000	55	1.1	7.3
2016 BMW i3	125	250	11,400	42	3	6
2012 Ford Focus EV	100	282	8,800	37	2.7	7.6
Volvo C30 Electric	89	250	9,500	50	1.78	5
Fiat 500e	83	202	12,800	32	2.59	6.3
Mercedes SLS AMG	138	252	13,000	45	3.07	5.6
Renault Fluence	70	227	11,000	36	1.94	6.3

high speed and high power targets is not a very cost effective solution. Although the traction motor designs and performance characteristics have improved significantly with time, to achieve wider market outreach of 35% BEVs in 2040, the US Department of Energy (DOE) have set technical targets for 2020 traction motors as $8/kW with a power density of 1.6 kW/kg [9].

Thus, from the above study, the following macro level goals for the traction motor to be developed can be established:

1. Reduced weight and cost of the traction motor
2. Increased torque and power densities
3. Extended driving range

However, in order to set motor characteristic targets, a general understanding of high–speed motor operation is required. Figs. 1.3(a) and (b) illustrate two high–speed motors namely the Ford Focus EV and TM4 motors which were comprehensively tested and analyzed in the laboratory. The motors were both rated for a peak power of about 110 kW and a peak torque above 250 Nm. The maximum operating speeds of the Ford Focus motor and TM4 motor are 8,800 rpm and 10,250 rpm respectively. It was observed that while the motors have reasonably high power densities, they suffer from high core and eddy current losses as expected in any high–speed motor. Due to the high operating frequencies, it is of significance to maintain the core losses within acceptable range

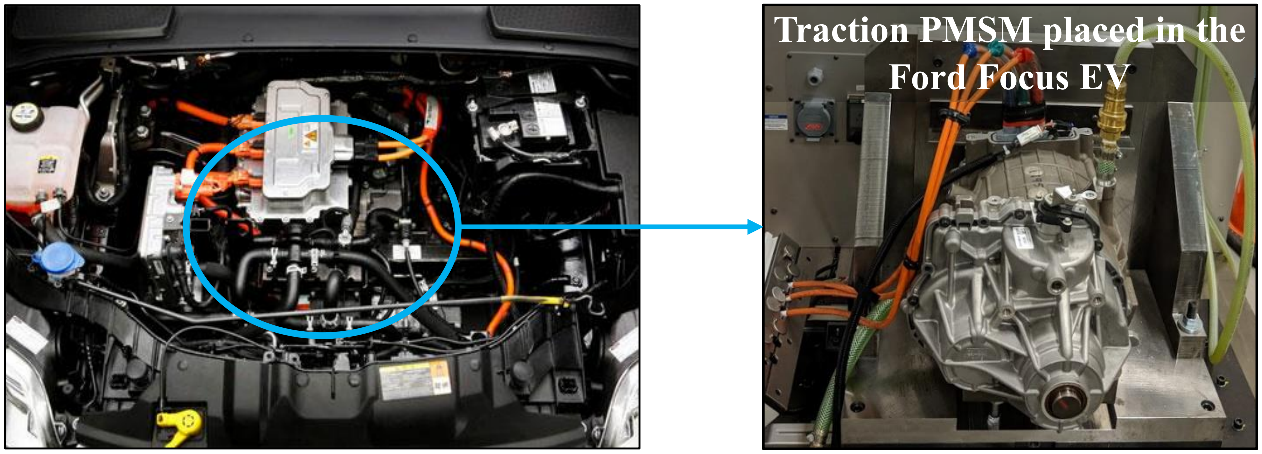

(a)

(b)

Fig. 1.3. Commercially available high–speed traction motors tested in the laboratory. (a) Ford Focus EV traction motor. (b) TM4 motor.

to achieve high efficiencies. Also, because of the high–speed operation, the motors have high centrifugal forces, noise and vibration which translates to torque ripple. Another major challenge associated with such motors is the thermal management. The motors require a good cooling system to accommodate the temperature rise without any irreversible damages. Thus, apart from the macro level goals, it is important to develop a traction motor with: improved machine efficiency, reduced torque ripple and a good cooling system.

1.3. Review of Available Charging Schemes and Infrastructures

While reducing the motor size and weight also translates to better battery utilization, in order to address the driving range per single charge challenge associated with BEVs, it is important to work on the charging infrastructure as well. Electric vehicle battery charging schemes are mainly classified into 3 types depending on the power level, type of charging and the charging time. The

TABLE 1.3
AVAILABLE CHARGING INFRASTRUCTURE AND POWER CONDITIONS [14]

Charging Level	Power Conditions	Charger Location	Power Flow	Charging Time	Infrastructure Cost
Level 1	120 V, 20 A, Up to 1.9 kW AC	On–board Single Phase	Unidirectional	4 – 11 hours	\$500 – \$880
Level 2	240 V, 80 A, Up to 19.2 kW AC	On–board Single/3–Phase	Unidirectional/ Bidirectional	2 – 6 hours	\$1,000 – \$3,000
Level 3	DC Fast Charging Up to 62.5 kW	Off–board 3–Phase	Unidirectional	0.2 – 1 hour	\$30,000 – \$160,000

TABLE 1.4
CHARGING LEVELS AVAILABLE FOR COMMERCIAL EVS [15]

Vehicle Model	Battery Type and Energy	All–Electric Range [km]	Level 1		Level 2		Level 3	
			Power [kW]	Time [Hours]	Power [kW]	Time [Hours]	Power [kW]	Time [Minutes]
Toyota Prius	Li–Ion 4.4 kWh	23	1.4	3	3.8	2.5	NA	NA
Chevrolet Volt	Li–Ion 16 kWh	64	0.96 – 1.4	5 – 8	3.8	2 – 3	NA	NA
Mitsubishi i–MiEV	Li–Ion 16 kWh	154	1.5	7	3	14	50	30
Nissan Leaf	Li–Ion 24 kWh	161	1.8	12 – 16	3.3	6 – 8	> 50	15 – 30
Tesla Roadster	Li–Ion 53 kWh	394	1.8	> 30	9.6 – 16.8	4 – 12	NA	NA

chargers can either be on–board or off–board capable of unidirectional and/or bidirectional power flow [10], [11]. While unidirectional chargers are simple, cost–effective, and require minimum hardware without the harmful effects of harmonic injection back to the grid, they require active control of the charging current and are restricted by power limits [12]. On the other hand, bidirectional chargers support both charge from the grid and battery energy injection back to the grid with relatively higher power density and faster control [13]. However, such chargers suffer from large component cost and harmful impact of uncontrolled power back to the grid. Battery chargers are classified as level 1, 2 and 3 based on the charging power type and level. Table 1.3 summarizes the available charging conditions and compares the different charging infrastructures [14]. Table 1.4 presents the charging levels available for some commercial EVs [15].

Existing EVs are typically equipped with unidirectional on–board chargers that uses a rectifier to convert the grid supply to power the battery. However, commercial on–board chargers occupy space in the EV under the hood and also are restricted to only level 1 charging. Furthermore, such low cost chargers induce 2nd order harmonics to the battery thereby degrading the battery lifetime and also result in low power factors causing poor charging power quality characteristics which further affects the driving range [16], [17]. Therefore, in order to overcome these challenges with existing charging infrastructure and to allow for fast charging and extended driving range, the charging function is integrated into the existing electric drive system through integrated charging

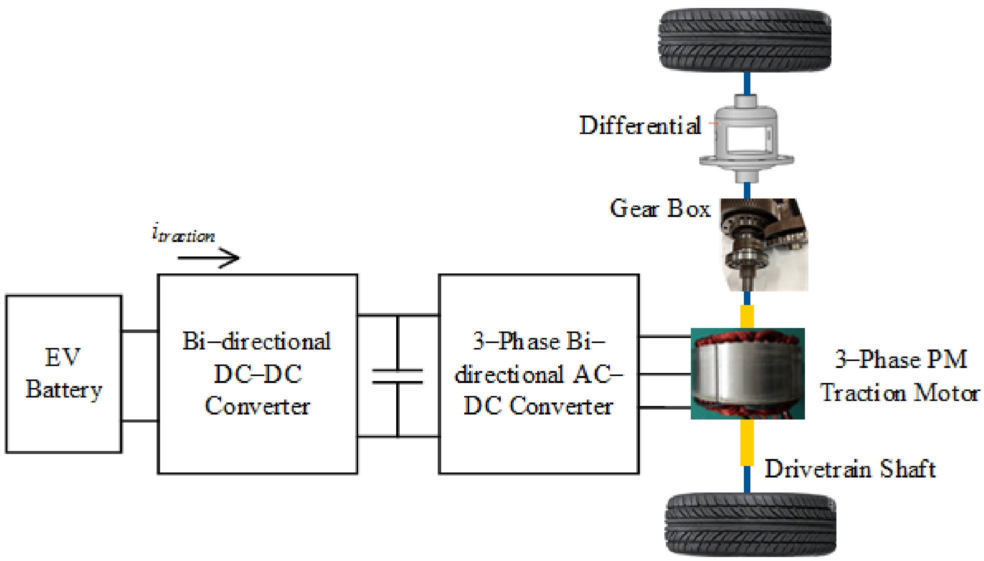

(a)

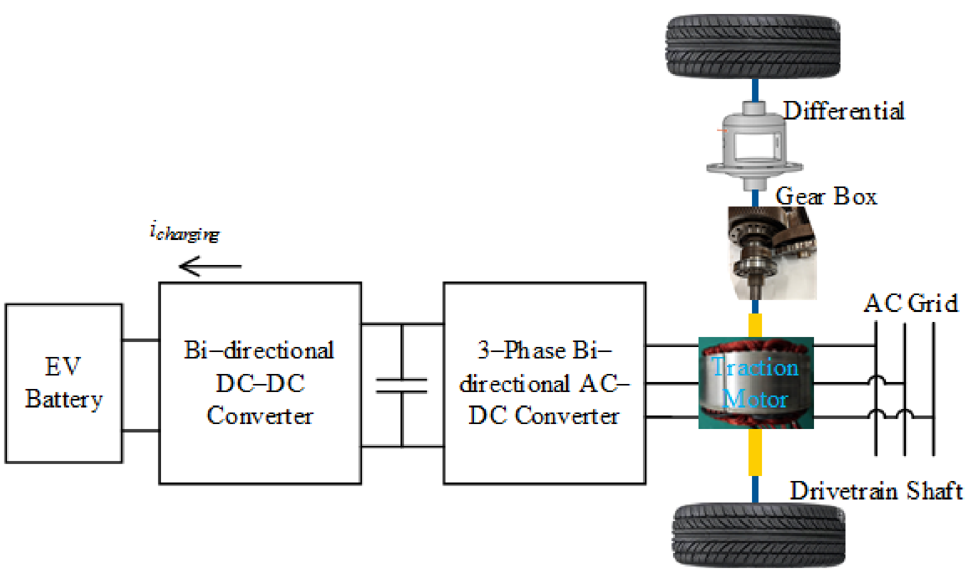

(b)

Fig. 1.4. Schematic of EV powertrain during different operating conditions. (a) During traction operation. (b) During integrated charging operation.

technology [18], [19]. The possibility to utilize existing traction motor drive components towards providing additional level–3 fast charging capacity results in elimination of the on–board charger leading to reduction in overall weight and cost of the vehicle and hence extended drive range.

Since the charging and traction operations do not occur simultaneously, the motor stator windings can be utilized as line filter inductors for charging when the vehicle is in stand–still conditions as shown in Fig. 1.4. Such integrated chargers not only facilitate low–cost, high–power, fast charging solutions but also significantly improves the power quality with near unity power factor and reduced harmonics to the battery/grid [20]. Various integrated charging solutions have been proposed in literature with both induction machines and permanent magnet machines [21] [22]. Authors in [23] have analyzed the ideal inductance value for a 3–phase surface PMSM when used for integrated charging. [24] compares the performance of a 3–phase surface PMSM and an interior PMSM for integrated charging operation. It was observed that while surface PMSMs are ideal choices for integrated charging with respect to balanced voltages and currents, they suffer from high risk of PM demagnetization and increased frequency based losses during charging. On the other hand, even though interior PMSMs can overcome these challenges, due to their salient nature, asymmetrical voltages and currents are induced across the machine windings during charging which could result in DC harmonic injection thereby deteriorating the battery life [25] [26]. Various solutions have been proposed in literature to overcome these shortcomings including implementing damper bars [27], using split windings [28], multiphase machines [29], etc. However, all these methods require complicated hardware reconfiguration, advanced control methodologies and complex power electronic systems which might affect the traction operation or lead to significant increase in overall system losses, weight and cost of the vehicle. Thus, further research is required to identify the ideal topology or design solution to implement a 3–phase permanent magnet traction motor for integrated charging application. The author does understand that while novel design solutions can be identified for integrated charging application, advancements in battery technology, charging technology, installation of more charging structures must harmonize as well to achieve the projected EV market growth. However, the scope of this thesis is restricted to developing and analyzing a traction motor capable of being utilized for integrated charging as well.

1.4. Thesis Research Objectives

The overall objective of this thesis is to model, analyze and develop a novel high–speed traction permanent magnet synchronous motor which is suitable for both traction and integrated charging applications. While this dissertation only considers a battery electric vehicle, the underlying concepts and proposed motor design can be extrapolated and applied accordingly to any application.

In an effort to overcome the major bottlenecks of high vehicle drivetrain component cost and limited driving range per single charge of EVs, this thesis proposes a novel permanent magnet synchronous machine for both traction and integrated charging applications. Further, based on the comprehensive literature study, the proposed innovative high–speed traction motor must have reduced weight and cost, improved torque density, maximized efficiency, reduced torque ripple and extended speed range. In order to design and analyze the traction motor for the desired performance characteristics under various operating conditions, an accurate and new comprehensive closed form analytical model is required. The associated background literature specific to analytical modeling will be presented in the subsequent chapters. Thus, considering the challenges and opportunities associated with high–speed traction motors for EVs, the following research objectives are formulated for this dissertation:

1. To develop a novel analytical model for accurate performance evaluation of a PMSM for traction and charging applications
2. Using the proposed analytical model, develop and experimentally validate a futuristic high–speed traction PMSM with
    1. Maximized torque density
    2. Improved efficiency
    3. Reduced torque ripple

The following steps or sub–tasks are implemented in this dissertation in order to meet the aforementioned research objectives:

I. <u>Preliminary Definitions:</u> Using a vehicle dynamics model, the quantitative property of all the technical targets will be calculated; a baseline topology suitable for the desired objectives will be chosen; and the preliminary structural aspects of the motor will be estimated using simple closed form equations

II. <u>Slot–Pole Analysis</u>: For the chosen baseline topology, an optimal slot–pole combination is selected to obtain higher torque and reduced torque ripple

III. <u>Improved Winding Configuration</u>: For the selected slot–pole combination, an improved winding configuration for higher torque density, reduced losses and torque ripple will be developed

IV. Proposed Analytical Model for Performance Evaluation: A novel analytical model considering all machine non–linearities, inverter harmonics and temperature effects for performance evaluation of the inverter–fed PMSM will be developed

V. Optimal Rotor Structure using Novel Analytical Method: Using the proposed model, an optimal rotor structure is developed for the winding configuration for improved torque density, extended operating range and improved efficiency

VI. Performance Analysis of Proposed PMSM: A drive cycle analysis of the final proposed PMSM will be performed; and the machine will be analyzed for integrated charging operation, continuous and peak traction operating conditions using FEA

VII. Prototype Development and Experimental Validation: Based on the performance analysis, the scaled–down proposed PMSM will be prototyped and validated experimentally at various operating conditions

VIII. Full–Scale Motor Development: Understanding the merits and demerits of the proposed scaled–down PMSM, a full–scale design will be proposed and analyzed using FEA for peak and continuous traction operation

1.5. Thesis Research Contributions

This thesis proposes novel and innovative motor modeling methods to develop a new high–speed traction PMSM with high torque density, maximized efficiency and reduced torque ripple suitable for traction and integrated charging application. The major contributions of this thesis to meet the established research objectives are listed as follows:

1. To develop a novel analytical model for accurate performance evaluation of a high–speed PMSM for traction and charging applications
   - **Contribution I**: Novel coupled magnetic circuit model considering all machine non–linearities including space harmonics, magnetic saturation, stator slotting, flux leakage, current harmonics and temperature effects for accurate motor performance evaluation
   - **Contribution II**: *dq*–axis based modeling of novel asymmetrical damper bars for interior PMSMs for integrated charging application
2. Using the proposed analytical model, develop and experimentally validate a futuristic

high–speed traction PMSM with maximized torque density, improved efficiency and minimum torque ripple

- **Contribution III**: Non–dominated sorting genetic algorithm based optimal slot–pole selection for innovative fractional–slot distributed windings with coil pitch of 2 for reduced end–winding length, high torque and reduced torque ripple
- **Contribution IV**: Winding function based analysis of coil distribution of unconventional star–delta windings with odd slots for reduced space harmonics, minimum torque ripple and reduced winding losses
- **Contribution V**: Pareto Ant–Colony optimization based design of novel IPM rotor structure for star–delta windings for improved torque density, extended operating range and improved machine efficiency
- **Contribution VI**: Implementing proposed star–delta wound high–speed traction IPMSM for integrated charging application

1.6. Organization of the Dissertation

This dissertation has 9 chapters including this introductory chapter, presenting the research work and novel research contributions conducted towards the overall research objectives. The dissertation layout is as follows:

Chapter 2 presents a vehicle dynamic model based procedure to fix the output performance targets of the full–scale and scaled–down motors including the rated and maximum speeds, peak and continuous powers and torques for a typical Ford Focus 2018 EV. The rated and maximum currents, DC voltage limits, motor efficiency, torque ripple and active motor weight targets are set based on FreedomCar 2020 EV targets. Further, preliminary structural dimensions of the machine are calculated using conventional D^2L approach and other structural restrictions including copper fill factor, slot pitch and pole pitch are set based on practical limitations. Based on the target performances and traction motor requirements, a baseline machine topology, in this thesis, a fractional–slot wound interior permanent magnet motor is taken up for analysis.

Chapter 3 presents a non–dominated sorting genetic algorithm (NSGA) based optimal slot–pole selection for slot–shifted fractional slot wound PMSMs with coil pitch of 2 for reduced space harmonics, high torque and reduced torque ripple. Unlike conventional stator slot shifting approach of simply using twice the stator slot numbers of the baseline machine, this chapter aims to expand the design solution for slot shifted fractional–slot wound machines by analyzing all feasible slot–pole combinations.

Chapter 4 explores the possibility of implementing novel odd slot numbers with star–delta winding configuration towards reduced spatial harmonic content, torque ripple minimization and improved torque density. In an effort to reduce the spatial harmonic contents in fractional–slot windings, appropriate coil and turns distribution among the two winding sets of star–delta winding topology will be analyzed using winding function theory.

Chapter 5 demonstrates a novel magnetic equivalent circuit (MEC) model incorporating effects of machine nonlinearities such as magnetic saturation, temperature rise, and introduction of spatial and time harmonic contents for parameter determination of PMSMs. With advent in permanent magnet synchronous machine (PMSM) structure and inverter topologies, accurate parameter determination is of significance for high–performance control, analysis and making critical decisions on inter–dependent design parameter variations for machine optimization. The proposed coupled electromagnetic and thermal model will be validated for various operating conditions of a fractional–slot distributed wound (FSDW) laboratory PMSM with finite element analysis (FEA) and experimental investigations.

In *Chapter 6*, a Pareto Ant Colony optimization (ACO) is implemented to obtain the optimal rotor structure for the proposed star–delta winding configuration to maximize the torque density, improve machine efficiency and extend the operating speed range. While existing literature is limited to topologies with near sinusoidal rotor magneto motive force (MMF) distribution, in this chapter, an IPMSM rotor design with non–sinusoidal rotor MMF will be developed for star–delta winding configuration.

Chapter 7 presents a computationally efficient magnetic equivalent circuit model based differential evolutionary algorithm to optimally design and analyze a traction IPMSM with novel asymmetrical damper bars for integrated charging capability. The major objectives of optimization are to obtain minimum torque during charging and high electromagnetic torque per unit machine losses during traction condition thereby ensuring maximized operating efficiency. Based on the analysis and understanding the practical challenges associated with using asymmetrical dampers in the machine, a simplistic approach of using combined star–delta wound PMSMs for integrated charging application is proposed. A comprehensive analysis of the proposed star–delta wound

PMSM topology from the previous chapters, for integrated charging application is presented in this chapter.

In *Chapter 8*, in order to assess the proposed machine's traction capability, a drive–cycle based analysis is conducted for common drive cycles including urban, highway and worldwide lightweight test cycle (WLTC) for a commercially available Ford Focus vehicle. Further, considering the comprehensive performance analysis conducted in the previous chapters, a prototype of the scaled–down 3–phase fractional–slot star–delta wound interior permanent magnet motor will be developed and validated experimentally. Subsequently, understanding the capabilities and challenges in the developed scaled–down prototype, a full–scale design with traction level ratings highlighted in Chapter 2, will be developed and analyzed using finite element analysis. Further recommendations for design improvement, future work and analysis will also be summarized towards the end of the chapter.

Chapter 9 is the conclusions chapter summarizing all the research work and contributions made towards achieving the research objectives and developing the proposed high–speed motor for traction and charging applications in this dissertation. Future work to be conducted to continue the research work in this dissertation will be presented.

1.7. References

[1] Worldwide number of battery electric vehicles in use from 2012 to 2018, [online], Available: https://www.statista.com/statistics/270603/worldwide–number–of–hybrid–and–electric–vehicles–since–2009/, [Accessed on January, 2018].

[2] Electric vehicles and electric utilities, [online], Available: https://www.adlittle.com/en/insights/viewpoints/electric–vehicles–and–electric–utilities, [Accessed on January, 2018].

[3] Global EV Outlook 2019, IEA, Paris, [online], Available: www.iea.org/publications/reports/globalevoutlook2019/, [Accessed on January, 2018].

[4] Costs and benefits of electric cars vs. conventional vehicles, [online], Available: https://www.energysage.com/electric–vehicles/costs–and–benefits–evs/evs–vs–fossil–fuel–vehicles/, [Accessed on January, 2018].

[5] Available: https://insideevs.com/reviews/344001/compare–evs/, [Accessed on January, 2018].

[6] E. A. Grunditz and T. Thiringer, "Performance Analysis of Current BEVs Based on a Comprehensive Review of Specifications," *IEEE Transactions on Transportation Electrification*, vol. 2, no. 3, pp. 270–289, Sept. 2016.

[7] T. Burress and S. Campbell, "Benchmarking EV and HEV power electronics and electric machines," in proc. of *IEEE Transportation Electrification Conference and Expo (ITEC)*, Detroit, MI, 2013, pp. 1–6.

[8] A. M. El–Refaie, "Motors/generators for traction/propulsion applications: A review," *IEEE Vehicular Technology Magazine*, vol. 8, no. 1, pp. 90–99, March 2013.
[9] Vehicle Technologies Program, U.S. Department of Energy, "FY2015 Electric Drive Technologies Annual Progress Report," 2016. [online], Available: http://www1.eere.energy.gov/library/asset_handler.aspx?src=https://energy.gov/sites/prod/files/2016/03/f30/FY%202015%20Electric%20Drive%20Technologies%20Annual%20Report.pdf&id=7375, [Accessed on July, 2017].
[10] M. A. Fasugba and P. T. Krein, "Gaining vehicle–to–grid benefits with unidirectional electric and plug–in hybrid vehicle chargers," in proc. of *IEEE Veh. Power and Propulsion Conf.*, Sep. 2011, pp. 1–6.
[11] Y. Lee, A. Khaligh, and A. Emadi, "Advanced integrated bi–directional AC/DC and DC/DC converter for plug–in hybrid electric vehicles," *IEEE Trans. on Vehicular Technology*, vol. 58, no. 3, pp. 3970–3980, Oct. 2009.
[12] M. A. Fasugba and P. T. Krein, "Cost benefits and vehicle–to–grid regulation services of unidirectional charging of electric vehicles," in proc. of *IEEE Energy Convers. Congr. Expo.* (*ECCE*), Sep. 2011, pp. 827–834.
[13] Y. Du, S. Lukic, B. Jacobson, and A. Huang, "Review of high power isolated bi–directional DC–DC converters for PHEV/EV DC charging infrastructure," in proc. of *IEEE Energy Conversion Congr. Expo.* (*ECCE*), Sep. 2011, pp. 553–560.
[14] S. Haghbin *et al.*, "Integrated chargers for EV's and PHEV's: examples and new solutions," in proc. of *The XIX International Conference on Electrical Machines* (*ICEM*), Rome, 2010, pp. 1–6.
[15] M. Yilmaz and P. T. Krein, "Review of Battery Charger Topologies, Charging Power Levels, and Infrastructure for Plug–In Electric and Hybrid Vehicles," *IEEE Transactions on Power Electronics*, vol. 28, no. 5, pp. 2151–2169, May 2013.
[16] M. Grenier, M. H. Aghdam, and T. Thiringer, "Design of on–board charger for plug–in hybrid electric vehicle," in proc. of *Power Elect., Machine and Drives* (*PEMD*), 2010, pp. 1–6.
[17] J. S. Kim *et. al.*, "Design and implementation of a high–efficiency on–board battery charger for electric vehicles with frequency control strategy," in proc of *IEEE Veh. Power Propulsion Conf.*, Sep. 2010, pp. 1–6.
[18] W. E. Rippel, "Integrated traction inverter and battery charger apparatus," U.S. Patent 4 920 475, Apr. 1990.
[19] W. E. Rippel and A. G. Cocconi, "Integrated motor drive and recharge system," U.S. Patent 5099186, Mar. 1992.
[20] A. G. Cocconi, "Combined motor drive and battery charger system," U.S. Patent 5 341 075, Aug. 1994.
[21] S. K. Sul and S. J. Lee, "An integral battery charger for four–wheel drive electric vehicle," *IEEE Trans. Ind. Appl.*, vol. 31, no. 5, pp. 1096–1099, Sep./Oct. 1995.
[22] S. Haghbin, S. Lundmark, M. Alakula, and O. Carlson, "An isolated high–power integrated charger in electrified vehicle applications," *IEEE Trans. Veh. Technol.*, vol. 60, no. 9, pp. 4115–4126, Nov. 2011.
[23] C. Lai, K. L. V. Iyer, K. Mukherjee, and N. C. Kar, "Analysis of electromagnetic torque and effective winding inductance in a surface mounted PMSM during integrated battery charging operation," *IEEE Transactions on Magnetics*, vol. 51, no. 11, 2015.
[24] K. L. V. Iyer, C. Lai, S. Mukundan, H. Dhulipati, K. Mukherjee and N. C. Kar, "Investigation of Challenges in Interior and Surface Permanent Magnet Synchronous Machines during

Integrated Charging Operation in Electric Vehicles," *International Journal of Powertrains*, vol. 7, no. 4, 2018.

[25] X. Lu, K. L. V. Iyer, K. Mukherjee, and N. C. Kar, "Investigation of integrated charging and discharging incorporating interior permanent magnet machine with damper bars for electric vehicles," *IEEE Transactions on Energy Conversion*, vol. 31, pp. 260–269, March 2016.

[26] K. L. V. Iyer, C. Lai, S. Mukundan, H. Dhulipati, K. Mukherjee and N. C. Kar, "Investigation of Interior Permanent Magnet Motor with Dampers for Electric Vehicle Propulsion and Mitigation of Saliency Effect during Integrated Charging Operation," *IEEE Transactions on Vehicular Technology*, 2018 [Early Access].

[27] S. Haghbin, K. Khan, S. Zhao, M. Alakula, S. Lundmark, and O. Carlson, "An integrated 20–kW motor drive and isolated battery charger for plug–in vehicles," *IEEE Transactions on Power Electronics*, vol. 28, no. 8, pp. 4013–4029, Aug. 2013.

[28] E. Levi, R. Bojoi, F. Profumo, H. A. Toliyat, and S. Williamson, "Multiphase induction motor drives – A technology status review," *IET Electric Power Applications*, vol. 1, no. 4, pp. 489–516, 2007.

Chapter 2

Performance Target Definition of the Traction Motor for a Typical Compact Electric Vehicle

2.1. Introduction

This chapter presents the traction motor's output performance target definitions for a typical compact electric vehicle (EV). These targets are calculated using vehicle dynamics based analytical equations, details of a commercially available EV, existing traction motors, drives and transmission systems and comprehensive literature study. The proposed motor specifications or design targets are determined for a typical North American compact vehicle and in this thesis, a Ford Focus 2018 vehicle from the automotive market is chosen [1]. First, the vehicle dynamics based analytical equations are used to calculate the continuous and peak torque and power target ratings as well as the desired base and maximum speeds of the motor. According to the research objectives highlighted in Chapter 1, the target traction motor should also be capable of assisting in charging operation. Thus, based on the existing charging power levels and required current and voltage ratings, the motor's charging targets are determined. In this thesis, the motor windings will be targeted to be utilized as inductive filters for a typical level 3 DC fast charging system [2]. Therefore, considering both the traction and charging requirements, and based on available laboratory traction motor drives and test systems, other performance targets including operating speed range, rated current, maximum current and DC bus voltage limit are fixed. Further, other performance targets such as active motor weight, torque density, torque ripple and rated efficiency are determined from commercially available traction motors and FreedomCar 2020 EV targets [3].

The preliminary structural dimensions such as the machine diameter and effective stack length are determined using conventional D^2L formulation approach [4]. Also, certain structural restrictions including copper fill factor, slot pitch and pole pitch are set based on practical limitations, previous design experiences and motor design conventions.

Thereafter, based on the target performances and traction motor requirements, along with the understanding of the merits and demerits of existing machine configurations, a baseline machine topology is selected for further analysis and improvement. In this thesis, a fractional–slot wound interior permanent magnet motor is taken up for analysis.

2.2. Performance Target Definition for Traction and Charging Operation Using Vehicle Dynamics Model

In order to design a traction motor for a typical compact vehicle, the initial step is to determine the continuous and peak torque and speed ratings of the electric motor using a base vehicle specification. In this thesis, the traction motor will be designed for a typical Ford Focus 2018 electric vehicle. Thus, knowing the maximum torque requirement at the vehicle wheels, T_w, the variable gear ratio at the first gear, i_g, the fixed gear ratio, i_o, and the efficiency of the transmission system, η, the maximum or peak torque capability of the traction motor, T_p can be calculated using (2.1). By convention, the continuous torque of the motor is considered to be half of the peak torque value [5].

$$T_w = i_g i_o \eta T_p \tag{2.1}$$

Similarly, the maximum speed capability of the motor in rpm, N_p, can be calculated using the maximum speed of the vehicle at the wheels in km/h, v, and the vehicle tire radius, r_d as in (2.2) and (2.3).

$$N_w = \frac{N_p}{i_g i_o} \tag{2.2}$$

$$v = \frac{3.6\pi N_w r_d}{30} \tag{2.3}$$

Table 2.1 summarizes the base vehicle specifications of the Ford Focus vehicle under consideration. While the individual gear ratios could not be obtained, the final gear ratio, which is the product of i_g and i_o was found to be 7.8 [6]. Thus, for a wheel radius of 17" and a transmission efficiency of 98%, the peak torque and the maximum speed of the motor was calculated to be about 287 Nm and 9,970 rpm respectively. Generally, the operating speed range from the base speed to the maximum speed of a typical traction motor ranges from 3 to 7 [7]. Taking the lowest value of close to 3, the base speed can be estimated to be about 3,000 rpm. Therefore, from the computed base speed and peak torque, the motor peak power was found to be 90.2 kW. Similarly, for the same base speed and continuous torque considered, the continuous power can be calculated to be 45 kW. Table 2.2 summarizes the calculated traction motor performance targets and compares with the Ford Focus Electric's traction motor ratings obtained from [6] indicating very close agreement. Thus, with the base vehicle requirements and specifications, the traction motor ratings can be easily estimated. The Ford Focus Electric 2018 vehicle and the existing traction motor are

TABLE 2.1
BASE VEHICLE SPECIFICATION OF EXISTING FORD FOCUS ELECTRIC VEHICLE

Parameter	Value
Gear ratio	7.82
Torque at shaft	2,200 Nm
Vehicle speed	1,275 rpm

TABLE 2.2
FORD FOCUS ELECTRIC'S TRACTION MOTOR RATINGS

Performance Characteristics		Ford Focus 2018 Motor Ratings[1]	Calculated Motor Ratings
Power	Continuous	45 kW	45 kW
	Peak	107 kW	90.2 kW
Torque	Continuous	150 Nm	143.5 Nm
	Peak	184 lbs–ft or 245 Nm	287 Nm
Base Speed	Wheel	60 km/hr	60 km/hr
	Motor	< 3,000 rpm	3,000 rpm
Maximum Speed	Wheel	> 135 km/hr	185 km/hr
	Motor	> 8,800 rpm	9,970 rpm

(a) (b)

Fig. 2.1. Ford Focus 2018 compact electric vehicle under consideration. (a) Ford Focus 2018 EV. (b) Traction motor used in the vehicle for propulsion.

illustrated in Fig. 2.1.

The Ford Focus 2018 vehicle is equipped with a 33.5 kWh liquid cooled lithium ion battery which is charged using a 6.6 kW on–board charger operated at 240 V and 30 A. However, the on–board charger takes about 5.5 hours to charger the battery from zero to full. Also, the vehicle has a DC charging capability of 50 kW [6]. Typical level 3 fast charging DC voltages and currents range between 300 – 500 V and 100 – 350 A respectively [8]. Thus, if the motor windings are designed to accommodate the required charging power level within the feasible current and voltage ranges, it can be considered for integrated charging operation. The peak power of the Ford Focus

TABLE 2.3
FREEDOMCAR 2020 PERFORMANCE TARGETS

Parameter	Target
Rated Efficiency	> 95 %
Torque Ripple	< 5 %
DC Operating Voltage	200 – 450 V
Maximum Phase Current	400 A_{rms}
Characteristic Current	< 400 A_{rms}
Line–to–line Back EMF	< 600 V_{peak}
Mass	≤ 35 kg
Volume	≤ 9.7 *l*

traction motor is about 45 kW with an input voltage range from 250 to 420 V DC and a peak current of 400 A rms and hence can be utilized for integrated charging. While the vehicle dynamics based analytical equations and existing traction motor ratings provide a foundation to fix the traction motor's fundamental performance targets, other operating characteristics including efficiency, torque ripple and DC bus limits, etc. are set based on the FreedomCar 2020 specifications [9] which are summarized in Table 2.3.

Further, the dynamic performance characteristics of the motor can be predicted through a drive cycle analysis using a detailed vehicle dynamics model. Drive cycles are a data series of speed variations as a function of time which are used as input to a particular vehicle dynamic model and translated to the required motor torque and speed points [10]. Also, this helps in fine–tuning or confirming the motor ratings determined above. The desired wheel torque is initially calculated from the tractive forces acting on the vehicle which include the aerodynamic drag, rolling resistance, friction and force due to gravity [11]. Further, using the gear ratio of the vehicle under consideration, the desired motor torque is calculated from the wheel torque using (2.1). The vehicle dynamics model parameters of the 2018 Ford Focus are implemented for analysis and summarized in Table 2.4 [6].

Transient performance of the EV against an EPA federal test procedure drive cycle was analyzed through simulation studies [12]. Figs. 2.2(a), (b) and (c) show the motor speed, torque and power requirements as a function of time. Further, the corresponding calculated torque speed envelope points expected from the motor is shown in Fig. 2.2(d). It can be seen from the figure that a 43 kW motor with a maximum torque and speed of 132 Nm and 5,716 rpm respectively will be capable of satisfying the urban drive cycle under analysis thereby confirming the motor ratings calculated previously using analytical equations. Also, the motor must be designed to obtain

TABLE 2.4
FORD FOCUS 2018 ELECTRIC VEHICLE PARAMETERS

Symbol	Description	Value	Symbol	Description	Value
M_v	Vehicle mass	1700	ρ	Density of air	1.202
A_v	Frontal vehicle surface area	2.77	C_d	Drag coefficient	0.33
r	Wheel radius	0.3284 m	g	Gravitational acceleration	9.81
i_g	Gear ratio	7.8	f_{rr}	Rolling resistance coefficient	0.013
n	Transmission efficiency	98%	α	Road grade	0° to 3°
v	Vehicle speed	Varying (m/s)	v_w	Wind speed	0 m/s

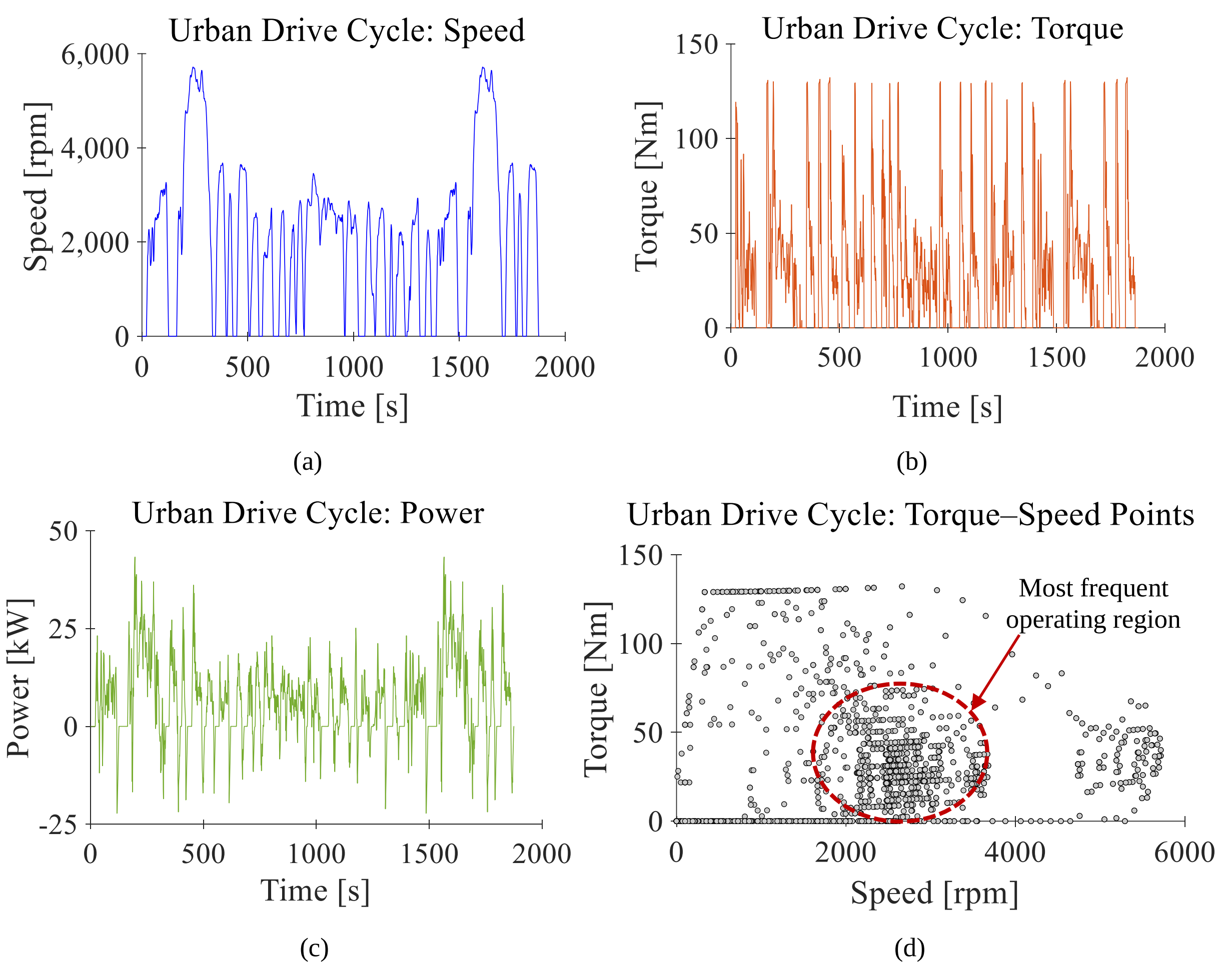

Fig. 2.2. Transient performance analysis requirements of the EV against the urban drive cycle obtained from vehicle dynamic model simultation. (a) Motor speed. (b) Torque. (c) Power. (d) Required motor torque–speed envelope.

high efficiency at the operating points corresponding to the most frequent operating region within the base speed as indicated in Fig. 2.2(d).

Thus, from the analysis conducted in this section, the target motor performance definition can be summarized as in Table 2.5. However, for proof–of–concept development and laboratory testing purposes, the motor performance targets are scaled down. The scaling factor can be

TABLE 2.5
MOTOR TARGET PERFORMANCE DEFINITION

Ratings		Ford Focus 2018/ Full Scale Targets[6]	Scaled Down Prototype
Power	Continuous	45 kW	22 kW
	Peak	107 kW	45 kW
Torque	Continuous	150 Nm	70 Nm
	Peak	184 lbs–ft or 245 Nm	150 Nm
Base Speed	Wheel	60 km/hr	60 km/hr
	Motor	< 3,000 rpm	3,000 rpm
Maximum Speed	Wheel	> 135 km/hr	185 km/hr
	Motor	> 8,800 rpm	> 9,000 rpm
Active Weight		< 37 kg	< 15 kg
Specific Power		> 2.9 kW/kg	> 2.25 kW/kg
Torque Density		> 6.76 Nm/kg	> 7.5 Nm/kg
Torque Ripple		< 10 %	< 5%
Rated Efficiency		> 95 %	> 95%

arbitrarily chosen depending upon the desire objectives, testing facilities, prototyping capabilities, etc. However, in this thesis, the scaling factor is decided keeping in mind that the peak operation of the scaled down motor should at least meet the continuous performance targets of the full–scale machine. Accordingly, the performance targets of the scaled down motor prototype to be analyzed, modeled, developed and tested are summarized in Table 2.5.

2.3. Preliminary Structural Parameter Calculation for Scaled–down Motor Prototype

This section details the calculation of certain preliminary structural parameters of the scaled down motor prototype using a conventional machine design procedure commonly referred as the D^2L approach. Also, certain structural and performance limits are highlighted in this section. The D^2L design procedure is a top–bottom approach where the machine's structural aspects are designed for a particular rated efficiency, torque and speed assuming a simple output coefficient, C_o as defined in (2.4) [13].

$$Q = C_o D^2 L n_s \tag{2.3}$$

$$C_o = \frac{11 k_w B_{av} ac}{1000} \tag{2.4}$$

Where D and L are the active machine dimensions indicating the stator outer diameter and the stack length respectively, k_w is the fundamental winding factor of the machine based on the slot–pole combination chosen [14], B_{av} and ac are the specific magnetic and electric loadings of the machine respectively, n_s is the rated speed in rps, and Q is the apparent input power for a known motor output power, rated efficiency and power factor. Typical values of B_{av} for a traction permanent magnet synchronous machine (PMSM) range between 0.7 and 0.9 T and ac varies between 30,000 and 50,000 AT/m [13]. Once the D^2L product is obtained, D and L are separated using an aspect ratio factor, k, which ranges between 0.5 to 1 for typical traction motors [15].

$$k = \frac{L}{D} \tag{2.5}$$

On the other hand, if the total number of stator slots, S, and rotor poles, p, are known, the magnetic and electric loadings can be calculated using (2.6) and (2.7) where ϕ is the flux per pole and I_{ph} is the rated phase current and Z is the total number of conductors in the stator.

$$B_{av} = \frac{\phi p}{\pi D L} \tag{2.6}$$

$$ac = \frac{I_{ph} Z}{\pi D} \tag{2.7}$$

Thus, using the above details, the machine's active dimensions can be easily calculated. However, for the scaled down prototype, the machine dimensions were fixed based on the existing fixtures available in the laboratory. The selected dimensions of D = 134 mm and L = 75 mm were verified for the output power using (2.3) and (2.4). Thus, for an assumed k_w of 0.95, B_{av} of 0.85 T, ac of 45,000 AT/m, target rated efficiency of 95% and power factor of about 0.85, the apparent power was calculated to be about 27 kW for a base speed of 3,000 rpm. This apparent power corresponds to an output power of 22 kW thereby meeting the required performance targets indicated in Table 2.5 as well satisfying the design equations (2.3) and (2.4).

Other structural details will be estimated in the subsequent chapters once the slot–pole combination of the machine is fixed. These dimensions including the stator tooth width (w_t), rotor pole pitch (τ), stator core thickness (d_{core}) and rotor yoke depth (d_{yoke}) are restricted mainly by saturation limits of the electric steel material at each part of the machine [16]. Equations (2.8) – (2.11) illustrate the procedure to calculate the indicated dimensions based on the corresponding flux density (B) limits [16]. φ in (2.8) is the pole arc value which is the equivalent arc of the rotor occupied by one pole in the machine. Similarly, the magnet flux density, B_m, which depends on the magnet width, b_{mag}, must be designed almost equal to the magnet materials remnant flux density [16].

$$B_{t/3} = \frac{p\phi\tau}{\varphi S L w_{t/3}} \tag{2.8}$$

$$B_{core} = \frac{\phi}{2Ld_{core}} \tag{2.9}$$

$$B_{yoke} = \frac{\phi}{2Ld_{yoke}} \tag{2.10}$$

$$B_m = \frac{\phi}{L_{mag} b_{mag}} \tag{2.11}$$

On the other hand, the copper weight or the number of conductors per slot is limited by the slot fill factor which is the ratio of the copper area in one stator slot to the total slot area [13]. From practical knowledge, the slot fill factor is limited to 60% only. Also, the conductors per slot and hence the turns per phase, T_{ph}, is limited by the DC voltage limit. For a 400 V DC bus voltage, the maximum induced line voltage, V_L, must ideally be within 50% of the DC voltage. From (2.12), it can be seen that, for a rated operating frequency, f, and phase voltage, E_{ph}, the T_{ph} can be calculated. Furthermore, the current ratings of the motor under peak and continuous motor operation are dictated by the current density, δ_s, which is calculated using (2.13). With a cooling system, the continuous and peak current densities values are 14 A/mm^2 and 25 A/mm^2 respectively. Therefore, for the conductor wire diameter, d_s, satisfying these current densities, the slot fill factor limit and producing an electric loading within the specified range, the peak and continuous rated currents can be calculated.

$$T_{ph} = \frac{E_{ph}}{4.44 f k_w \phi} \tag{2.12}$$

$$\delta_s = \frac{I_{ph}}{a_s} \tag{2.13}$$

$$d_s = \sqrt{\frac{4a_s}{\pi}} \tag{2.14}$$

Thus, the selected machine dimensions from this section for the motor to be analyzed are summarized in Table 2.6. So, it can be seen that, using (2.3) – (2.14), the base structural parameters of the machine for a specific output power and target rated efficiency within saturation limits can be obtained. However, for other operating characteristics including the operating speed range, the

TABLE 2.6
PRELIMINARY STRUCTURAL MOTOR PARAMETERS

Parameter	Value
Stator Inner Diameter (*D*)	134 mm
Stack Length (*L*)	75 mm
Slot Fill Factor	60%
Continuous Current Density	14 A/mm^2
Peak Current Density	25 A/mm^2

reluctance torque component and permanent magnet flux linkage value, comprehensive design methodologies such as magnetic circuit model and *dq*–axis theory based equations must be used as indicated in the subsequent chapters.

2.4. Baseline Topology Selection for Scaled–down Motor Prototype

While the sections above set the performance targets and preliminary structural parameters of the scaled down motor prototype to be developed, it is of importance to fix a machine topology before further analysis. According to the research objectives highlighted in Chapter 1 and the performance targets thus obtained, a high–speed traction PMSM with high torque density, maximized efficiency and minimum torque ripple must be developed which is capable of integrated charging operation as well. It is well–established in literature that for high–speed operation, interior PMSMs are more suitable than the surface mount PMSMs due to their lower risk of demagnetization and high mechanical stability [17] – [19]. Further, due to their high reluctance component, the amount of expensive rare–earth magnets required to produce the rated torque is lesser than surface mount PMSMs thereby resulting in increased torque density and reduced cost. Also, due to increased torque production from the reluctance component, the rated current is lesser than the surface mount PMSMs resulting in reduced copper losses and hence improved rated efficiency. On the other hand, authors in [20], compare the performance of a surface and interior PMSM with same ratings and conclude that the surface PMSMs result in balanced sinusoidal voltages with reduced oscillating torque making them well–suited for charging operation. However, compared to interior PMSMs, the surface PMSMs suffer from higher magnet losses and are prone to demagnetization even during charging. Therefore, considering all the merits and demerits during both traction and charging application, an interior PMSM is chosen for further analysis in this thesis.

Among the existing rotor topologies of interior PMSMs, the v–shaped magnets have the highest torque capability due to their high flux focusing effect [21]. On the other hand, the spoke magnet configuration requires higher magnet volume to produce the rated torque. Authors in [22] compared all the interior PMSMs rotor topologies with damper bars for integrated charging application. While it was observed that the straight magnets result in near symmetrical voltage waveforms, spoke type magnets resulted in reduced oscillating torque and the v–shaped magnets result in reduced saliency effects during charging. Thus, considering the high speed, high torque density and integrated charging requirements, a v–shaped interior PMSM rotor topology is considered as baseline.

Similarly, extensive literature exists on comparison of distributed and concentrated winding configurations summarizing that while distributed windings have high fundamental winding factors and reduced space harmonics, concentrated windings result in short end winding lengths and high torque densities [23] – [25]. Thus, considering both the winding configurations, in this thesis, a fractional–slot distributed winding configuration is taken up for analysis. While limited literature exists on this configuration, it is known that they are suitable for high–speed, high–power applications [26], [27] and are implemented in commercial vehicles such as Ford Focus, Sonata Hybrid, etc. [28]. This configuration results in relatively lower space harmonics, increased torque production and extended operating range. Generally, the coil span for fractional–slot distributed windings are higher than 3, resulting in fairly higher end winding material wastage [27], [29].

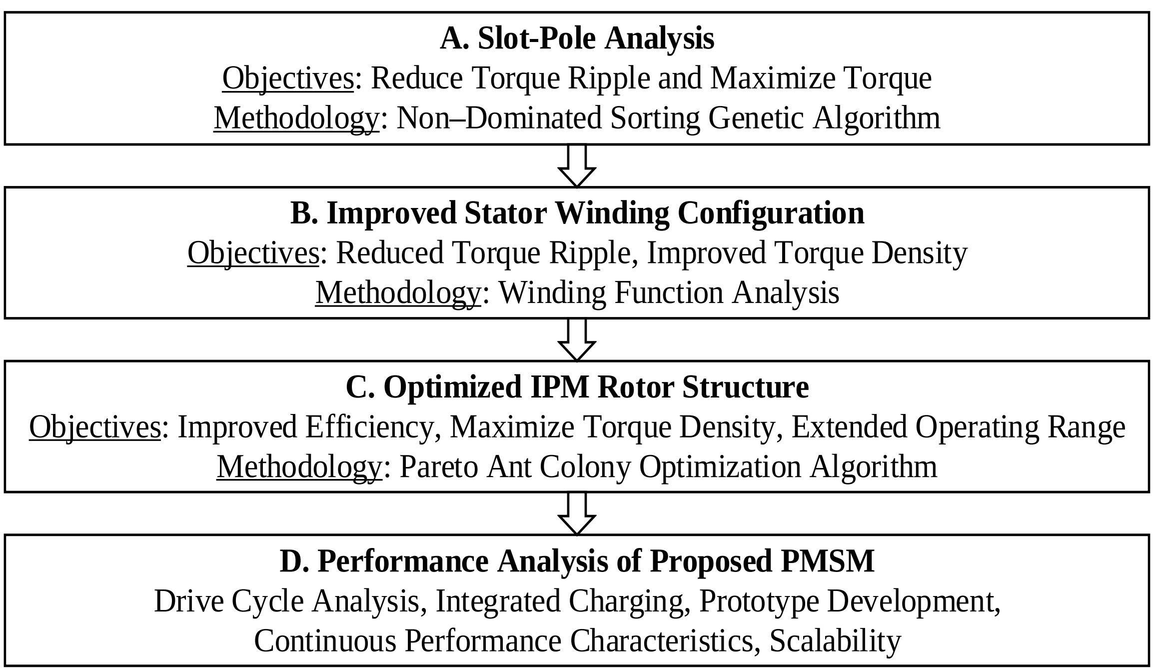

Fig. 2.3. Flowchart highlighting the work flow conducted in subsequent chapters.

Therefore, in an effort to overcome this challenge, this thesis proposes a fractional–slot distributed winding configuration with a coil pitch of 2, which is very similar to the slot–shifted winding topology for fractional–slot concentrated windings for space harmonic reduction [30]. In conclusion, in this thesis, a fractional–slot distributed wound interior PMSM is chosen as the baseline topology for further analysis in the subsequent chapters as indicated in the flowchart shown in Fig. 2.3.

2.5. Conclusions

In this chapter, the traction motor's output performance target definitions including the continuous and peak torque and power target ratings as well as the desired base and maximum speeds of the motor for a typical compact electric vehicle (EV) were calculated using vehicle dynamics based analytical equations, details of a commercially available Ford Focus EV, existing traction motors, drives and transmission systems and comprehensive literature study. Further, based on the existing charging power levels and required current and voltage ratings, the motor's charging targets were determined. Other performance targets such as active motor weight, torque density, torque ripple and rated efficiency were fixed based on commercially available traction motors and FreedomCar 2020 EV targets. The preliminary structural dimensions and certain structural restrictions were calculated using conventional D^2L formulation approach, practical limitations, previous design experiences and motor design conventions. Thereafter, based on the target performances and traction motor requirements, along with the understanding of the merits and demerits of existing machine configurations, a baseline machine topology was selected for further analysis and improvement. In this thesis, a fractional–slot distributed wound interior permanent magnet motor is taken up for analysis.

2.6. References

[1] 2014 Ford Focus Electric Brochure, [online], Available: https://www.ford.com/services/assets/Brochure?make=Ford&model=FocusElectric&year=2014, [Accessed on August 9, 2018].

[2] X. Lu, K. L. V. Iyer, K. Mukherjee, and N. C. Kar, "Investigation of integrated charging and discharging incorporating interior permanent magnet machine with damper bars for electric vehicles," *IEEE Transactions on Energy Conversion*, vol. 31, pp. 260–269, March 2016.

[3] E. Carraro and N. Bianchi, "Design and comparison of interior permanent magnet synchronous motors with non–uniform airgap and conventional rotor for electric vehicle applications," *IET Electric Power Applications.*, vol. 8, pp. 240–249, 2014.

[4] T. A. Lipo, *Introduction to AC Machine Design*, 3rd ed. Madison, WI, USA: Univ. Wisconsin–Madison, pp. 65, 70,79–80, 2009.

[5] M. Ehsani, Y. Gao, and A. Emadi, Modern Electric, Hybrid Electric, and Fuel Cell Vehicles, CRC Press, USA, 2010, pp. 30–51, 105–108.
[6] 2018 Ford Focus Electric Specifications, [online], Available: https://www.ford.ca/cars/focus/models/focus–electric/, [Accessed on April 9, 2018].
[7] D. M. Ionel, J. F. Eastham, T. J. E. Miller, and E. Demeter, “Design considerations for permanent magnet synchronous motors for flux weakening applications,” *IEE Proceedings–Electric Power Applications*, vol. 145, no. 5, pp. 435–440, 1998.
[8] I. Subotic, N. Bodo, E. Levi, B. Dumnic, D. Milicevic and V. Katic, "Overview of fast on–board integrated battery chargers for electric vehicles based on multiphase machines and power electronics," *IET Electric Power Applications*, vol. 10, no. 3, pp. 217–229, 3 2016.
[9] U. S. Department of Energy, "FY 2011 Vehicle Technologies Program Wide Funding Opportunity Announcement Funding Opportunity Number: DE–FOA–0000239," 2011, pp. 17–18.
[10] P. Korta, K. L. V. Iyer, C. Lai, K. Mukherjee, J. Tjong and N. C. Kar, "A novel hybrid approach towards drive–cycle based design and optimization of a fractional slot concentrated winding SPMSM for BEVs," *in proc. of IEEE Energy Conversion Congress and Exposition* (*ECCE*), Cincinnati, OH, 2017, pp. 2086–2092.
[11] J. M. Miller, Propulsion Systems for Hybrid Vehicles. Stevenage: IET, 2010.
[12] EPA Urban Dynamometer Driving Schedule (UDDS), Available online at: https://www3.epa.gov/otaq/standards/light–duty/udds.htm. Accessed on March 20, 2016.
[13] A. K. Sawhney, A Course on Electrical Machine Design, New Delhi, India: Dhanpat Rai & Co, 2011, pp. 11.41–11.42.
[14] S. Mukundan H. Dhulipati, E. Ghosh, G. Feng, and N. C. Kar, “Non Dominated Sorting Genetic Algorithm Based Investigation of Optimal Odd Slot Numbers for Stator Shifted Fractional Slot Wound PMSMs,” accepted for publication in *IEEE Energy Conversion Congress and Exposition* (*ECCE*), Baltimore, USA, September 2019.
[15] J. R. Hendershot Jr. and T. J. E. Miller, Design of Brushless Permanent–Magnet Motors, Magna Physics Publishing and Clarendon Press, Ox–ford, 1994, pp. 3.12–3.15.
[16] R. Krishnan, Permanent Magnet Synchronous and Brushless DC Motor Drives, CRC Press, 2010, pp. 72–73.
[17] K. L. V. Iyer *et. al*., "Design considerations for permanent magnet machine drives for direct–drive electric vehicles," in proc. of *IEEE Int. Elec. Machines & Drives Conf. (IEMDC)*, Idaho, 2015, pp. 1170–1176.
[18] T. Kenjo and S. Nagamori, *Permanent–magnet and brushless DC motors*, Oxford University Press, 1985.
[19] P. B. Reddy, A. M. El–Refaie, K. K. Huh, J. K. Tangudu, and T. M Jahns, “Comparison of Interior and Surface PM Machines Equipped with Fractional–Slot Concentrated Windings for Hybrid Traction Appli–cations,” *IEEE Trans. on Ener. Conv.*, vol. 27, 2012.
[20] K. L. V. Iyer, C. Lai, S. Mukundan , H. Dhulipati , K. Mukherjee and N. C. Kar, “Investigation of Challenges in Interior and Surface Permanent Magnet Synchronous Machines during Integrated Charging Operation in Electric Vehicles ,” *International Journal of Powertrains*, vol. 7, no. 4, 2018.
[21] F. Charih, F. Dubas, C. Espanet and D. Chamagne, "Performances comparison of PM machines with different rotor topologies and similar slot and pole numbers," in proc. of *International Symposium on Power Electronics Power Electronics, Electrical Drives, Automation and Motion*, Sorrento, 2012, pp. 56–59.

[22] S. Mukundan H. Dhulipati, K. L. V. Iyer, C. Lai, K. Mukherjee and N. C. Kar, “Comparative Performance Analysis of 3 Phase IPMSM Rotor Configurations with Dampers for Integrated Charging Application in EVs,” in proc of *IEEE* 43*rd* *Annual Conf of the Ind Electronics Society* (*IECON*), Beijing, China, 2017.
[23] A. M. EL–Refaie, "Fractional–Slot Concentrated–Windings Synchronous Permanent Magnet Machines: Opportunities and Challenges," in *IEEE Trans. on Industrial Electronics*, vol. 57, no. 1, pp. 107–121, Jan. 2010.
[24] F. Magnussen, P. Thelin and C. Sadarangani, "Performance evaluation of permanent magnet synchronous machines with concentrated and distributed windings including the effect of field–weakening," in proc. of 2*nd* *International Conference on Power Electronics, Machines and Drives* (*PEMD*), Edinburgh, UK, 2004, pp. 679–685 Vol.2.
[25] J. K. Tangudu and T. M. Jahns, "Comparison of interior PM machines with concentrated and distributed stator windings for traction applications," in proc. of *IEEE Vehicle Power and Propulsion Conference*, Chicago, IL, 2011, pp. 1–8.
[26] L. Hao, "Design and analysis of IPM machine with bar wound fractional slot distributed winding for automotive traction application," in proc. of *IEEE Energy Conv. Congress and Exposition*, Denver, CO, 2013, pp. 598–605.
[27] S. Bandyopadhyay, M. van der Geest and H. Polinder, "Design optimisation of high performance fractional–slot distributed winding PM Synchronous machines for In–wheel application in Electric Vehicles," in proc. of 8*th* *IET International Conference on Power Electronics, Machines and Drives* (*PEMD*), Glasgow, 2016, pp. 1–7.
[28] T. Burress and S. Campbell, "Benchmarking EV and HEV power electronics and electric machines," in proc. of *IEEE Transportation Electrification Conference and Expo* (*ITEC*), Detroit, MI, 2013, pp. 1–6.
[29] J. Choi, Y. Park and S. Jang, "Experimental Verification and Electromagnetic Analysis for Performance of Interior PM Motor According to Slot/Pole Number Combination," *IEEE Transactions on Magnetics*, vol. 48, no. 2, pp. 987–990, Feb. 2012.
[30] P. B. Reddy *et*. *al*., "Generalized Approach of Stator Shifting in Interior Permanent–Magnet Machines Equipped with Fractional–Slot Concentrated Windings," *IEEE Transactions on Industrial Electronics*, vol. 61, no. 9, pp. 5035–5046, Sept. 2014.

Chapter 3

Optimal Slot–Pole Selection for Fractional–Slot PMSMs using Non–Dominated Sorting Genetic Algorithm

3.1. Introduction

Electric vehicles (EVs) equipped with permanent magnet synchronous machines (PMSMs) having fractional–slot windings are extensively used owing to their high torque density, lower material consumption and minimum torque ripple. However, such machines have high characteristic spatial harmonic contents resulting in increased rotor losses, magnet eddy current losses and noise and vibrations deteriorating the machine's performance. Many methods to reduce these space harmonics have been analyzed in literature including multi–phase topology [1], multi–layer windings [2], stator and rotor skewing [3], [4], magnet segmentation and employing different turns per coil [5]. However, all the aforementioned methods suffer from manufacturing complexities, increased copper consumption and reduction in the machine's torque production. On the other hand, stator slot shifting is a commonly used method resulting in improved machine efficiency and flux–weakening performance with ease of manufacture [6]–[8]. Existing literature on slot shifting methods use twice the number of slots already present in the concentrated wound machine resulting in a fractional–slot topology with coil pitch of 2 which provides a good compromise between conventional concentrated and distributed winding configurations. Such configurations improve the magneto motive force (MMF) distribution, lowering the effective rotor losses, torque ripple and also increase the torque production capability by increasing the reluctance torque component of the machine. However, by simply using twice the stator slot number of the baseline machine, certain slot–pole combinations, especially odd slot numbers are not taken into account for investigation. Moreover, implementing odd slot numbers with fractional–slot topology is expected to significantly reduce the cogging torque and torque ripple in the machine [9]. Thus, this chapter aims to expand the design solution for slot shifted fractional–slot wound machines by analyzing all feasible slot–pole combinations. A non–dominated sorting genetic algorithm (NSGA) based optimal slot–pole selection is implemented considering various machine performance characteristics and verified using finite element analysis (FEA).

3.2. Stator Slot Shifting in Fractional–slot PMSMs

A. Concept of Conventional Slot Shifted PMSMs

To reduce the harmonic content of a baseline fractional slot concentrated wound (FSCW) machine, the general concept of stator slot shifting is to integrate two such FSCW stators with the same slot–pole combination, resulting in a slot shifted machine configuration with a coil span of 2. The two FSCW stators are shifted by an electrical angle to reduce the harmonic content and still maintain relatively the same torque capability. The coils per phase of both the FSCW stators are connected in series and hence results in a slot number exactly twice as that of the baseline FSCW machine [10]. Thus, for the same rotor structure, the baseline FSCW machine with S stator slots with high harmonic contents is modified to a slot shifted machine with $2S$ slots and a coil span of 2 with relatively lower spatial harmonics [11]. This concept of conventional stator slot shifting is illustrated in Fig. 3.1.

The 12–slot, 10–pole FSCW configuration is most commonly selected for stator slot shifting [12], [13]. The resultant 24–slot, 10–pole slot shifted machine exhibits reduced space harmonic contents as expected. Further, such slot shifted topologies have reduced torque ripple and cogging torque in the machine. However, by adapting this procedure, all feasible slot–pole combinations, especially with odd slots are eliminated, limiting the design solution space. Also, implementing odd slots with fractional slot configuration is expected to further reduce the harmonics and machine losses and hence improve the overall torque production and machine efficiency [14]. Thus, this chapter attempts to study the feasibility of slot shifted machine configurations with odd slot numbers.

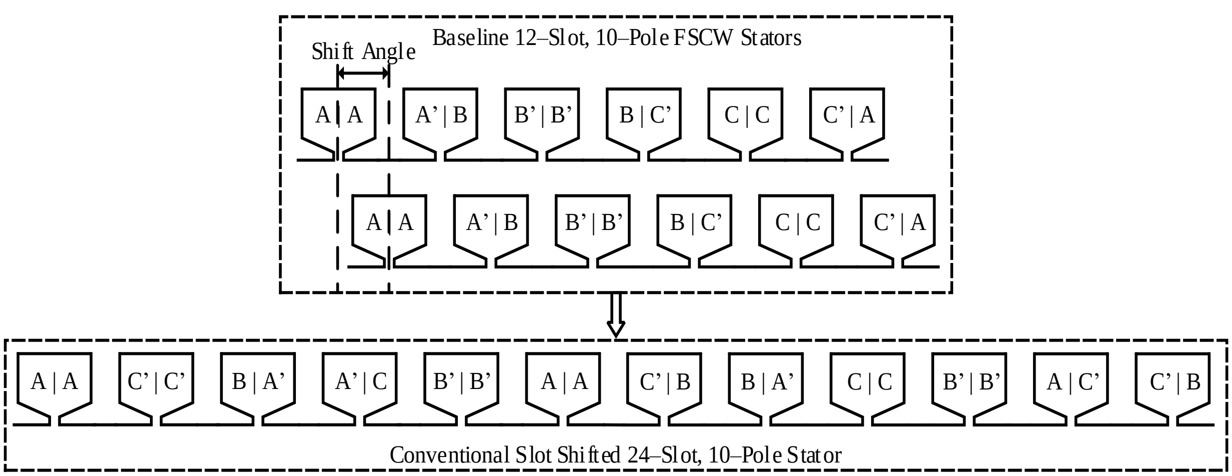

Fig. 3.1. Concept of conventional stator slot shifting of fractional slot wound PMSMs.

B. Slot–Pole Combination Based Performance Analysis

The choice of slot–pole combination significantly affects the machine's material consumption, rated parameters and performance characteristics [15]. Consider a fractional–slot concentrated wound PMSM with S stator slots and p pole numbers and n–phases. In conventional methods as explained above, to obtain slot shifted configuration, for the same p poles, the stator slots are simply changed from S to $2S$, eliminating other feasible slot numbers between this range and above. Thus, to obtain a slot shifted fractional–slot wound configuration with coil pitch of 2, the general requirements are: 1) the slot number should be a multiple of the phase number; and 2) the slot per pole must be between $1.5/n$ and $2.5/n$ as represented by (3.1).

$$\left.\begin{aligned} &S \in ni; \quad i = 1,2,\ldots\infty \\ &1.5/n < S/p < 2.5/n \end{aligned}\right\} \tag{3.1}$$

In general, if the coil pitch is 2, the slot per pole per phase, q can be represented as a simple fraction with denominator, d which represents the number of units the machine can be symmetrically divided into and the numerator, M indicates the number of stator slots per phase in a unit.

Based on the slot–pole combination, the star of slots method gives a direct relation between the machine's space harmonics and the slot and pole numbers. Thus, for a n–phase machine, the total number of phasors in a slot star will be nM contributing towards 180º of an electrical cycle. The electrical slot angle, α_s which is the angle contributed by each phasor and the mechanical slot angle, α_m are given by [16]

$$\left.\begin{aligned} q &= M/d \\ \alpha_s &= 180p/S \\ \alpha_m &= 180/nM = \alpha_s/d \end{aligned}\right\} \tag{3.2}$$

While most of the slot–pole combinations satisfy all the above mentioned conditions, in order to obtain equally balanced n–phase voltages, the windings must be symmetrically distributed in each unit across the entire machine. This condition is given by (3.3), where D is a whole number for any integral value of C. Only when D is a whole number, symmetrically balanced voltages are obtained.

$$D = \frac{1 + nMC}{d}; \; C \in 1,2,\ldots\infty \tag{3.3}$$

Thus, for any slot–pole combination, if conditions represented by (3.1) – (3.3) are satisfied, a slot shifted fractional–slot wound configuration with coil pitch of 2 can be obtained. Further, the above conditions can be universally applied for a n–phase machine even with conditions where the slot number is lesser than the pole number [17].

In this section, various performance characteristics for slot–pole combinations of 3–, 5–, 6– and 9–phase machines are analyzed. The stator slot numbers are restricted up to i = 15 from (3.1), considering practical scenarios since slot numbers higher than that will result in increase in the machine's volume and cannot be placed in an EV. Similarly, pole numbers up to 40 are analyzed keeping in mind the restrictions of the switching frequency in case of high–speed traction machines. Therefore, for the large dataset obtained by varying S, p and n, the three main factors namely – fundamental winding factor (k_{w1}), harmonic winding factors (k_{wh}) and THD are calculated analytically using (3.4) – (3.6) [18]. Harmonic winding factors up to 20$^{\text{th}}$ order are considered since higher order harmonics have significantly low magnitudes and can be neglected.

$$k_{w1} = \frac{\sin\left(\frac{\pi}{2n}\right)}{M\sin\left(\frac{\pi}{2nM}\right)}\cos\left(\frac{\pi}{nM}\right) \tag{3.4}$$

$$k_{wh} = \frac{\sin\left(\frac{h\pi}{2n}\right)}{M\sin\left(\frac{h\pi}{2nM}\right)}\cos\left(\frac{h\pi}{nM}\right) \tag{3.5}$$

$$THD = \frac{\sqrt{\sum_{h=1,3,..}^{\infty} k_{wh}^2 / h}}{k_{w1}} \tag{3.6}$$

Further, the net cogging torque, T_{cog} as expressed in (3.7) [18] must be minimized. Higher the LCM of slot and pole numbers, the cogging frequency also increases with reduced magnitudes, thereby reducing the net cogging torque.

$$\left.\begin{aligned} T_{cog} &= \sum_{h=1}^{\infty} T_h \sin\left(hN_{cog}\theta + \varphi_h\right) \\ N_{cog} &= LCM(S, p) \end{aligned}\right\} \tag{3.7}$$

Where T_h is the per unitized peak value of cogging torque for the h^{th} harmonic order, θ is the rotor mechanical position and φ_h is the phase angle of the corresponding cogging torque. For a fixed DC bus voltage and machine volume, the motor performance can be analyzed for a target torque production by defining the permanent magnet (PM) flux linkage and the *dq*–axis inductances in terms of the slot–pole numbers [18]. The PM flux linkage, λ_{pm} can be obtained as

$$\lambda_{pm} = \sum_{h=1,3,5,\ldots} \frac{E_h M \sin\left(h\pi/2nM\right)}{\omega_h \sin\left(h\pi/2n\right)} \tag{3.8}$$

Where E_h is the per unitized peak value of induced voltage for the h^{th} harmonic order and ω_h is the corresponding speed of rotation. Furthermore, the phase inductances, L_{ph} can also be expressed in terms of the machine's physical structure and can be transformed to corresponding *dq*–axis values using conventional transformational equations [18].

$$L_{ph} = \frac{\mu_0 \pi D L T_{ph}^2 k_{w1}^2}{l_g p^2} \tag{3.9}$$

Where μ_0 is the absolute permeability, D and L are the machine's outer diameter and stack length respectively, T_{ph} is the number of turns per phase and l_g is the air–gap length.

Also, if the machine's material properties are known, the machine losses can also be expressed in terms of S and p as in (3.10), where χ_{cu} is the copper loss coefficient, depending upon the operating current density, slot fill factor, and wire material properties; χ_{tooth} and χ_{core} are the core loss coefficients at the stator tooth and machine core. The core loss coefficients depend mainly on the steel core material property, operating frequency and rated current and voltage. For ease of computation, most of the above mentioned properties are kept constant for all machines. The operating frequency is directly dependent on the pole number while the rated currents can be expressed in terms of the slot and pole numbers as well.

$$P_{losses} = \chi_{cu} S_s mp + \left[\chi_{tooth}\left(S_s^2/p\right)\right] + \left(\chi_{core}/p\right) \tag{3.10}$$

Furthermore, for a total number of coils per phase given by dM, an effective coil resistance, R_c, and per unit current I_m, the current angle γ to obtain the maximum torque per unit winding losses can be obtained as

$$\frac{T_e}{P_{copper}} = \frac{\frac{3p}{4}\left[\lambda_{pm}/I_m \sin\gamma + \left(L_d - L_q\right)\sin 2\gamma\right]}{ndMI_m^2 R_c} \tag{3.11}$$

Thus, for any slot–pole combination satisfying (3.1) – (3.3), including odd slot numbers, the slot–shifted motor performance attributes can be estimated using (3.4) – (3.11).

C. Comparative Performance Analysis of Slot Shifted PMSMs with Odd and Even Slots

For the feasible slot–pole combinations satisfying conditions (3.1) – (3.3), a comparison of the parameters obtained using (3.4) – (3.11) is performed for conventional and proposed slot shifted machines. The comparative study is extended towards conventional FSCW machines with coil pitch of 1 to highlight its demerits over stator slot shifted configurations. Thus, the values of THD and k_{w1} obtained from various feasible slot–pole combinations for 3–, 5–, 6– and 9–phase numbers are illustrated in Figs. 3.2 – 3.5 respectively. From the figures, it is obvious that for a particular pole number, the choice of feasible slot number after slot shifting is not only restricted to 2*S*. For instance, a 3–phase FSCW machine with 12–slots and 10–poles can be slot shifted to either 18–slots, 10–poles; or 21–slots, 10–poles; and the most commonly obtained 24–slots, 10–poles configuration. Most importantly, the choice of odd slot numbers opens a wide range of possible designs that need to be investigated. Also, it can be observed that for certain phase numbers, the possibility of implementing a slot shifted winding configuration with coil pitch 2, cannot be obtained for a few pole numbers. For instance, in case of 3–phase machines, although concentrated wound configurations with 6– and 18–pole machines are possible, stator shifted configurations cannot be obtained. This is because, for such slot–pole combinations, as mentioned in the previous section, although conditions (3.1) and (3.2) are satisfied, there is no integral value of *P* which satisfies condition (3.3). Hence, the phase voltages may not be completely balanced and symmetrical leading to further torque ripple in the machine.

Another observation is that, as the phase number increases, the advantage of reduction in THD from slot shifted machines when compared to FSCW machines reduces. These discrepancies can be attributed to the fact that the high spatial subharmonic contents in concentrated wound machines tend to decrease with higher phase number [19]. However, the fundamental winding factor obtained for slot shifted machines are always higher than that of FSCW machines for any phase number which directly translates to improved torque production. As the number of slots increases and the winding configuration moves towards slot–shifted winding configuration, the MMF distribution tends to become more sinusoidal, increasing the winding factor value. Further, it can be seen that for 3–, 5– and 9–phase machines, for certain pole numbers, the feasible slot shifted machines are equipped with only odd slot numbers. This feature highlights the contribution of the study conducted in this chapter. While conventional slot shifting methods would have completely eliminated the possibility of such a slot–pole combination, this study expands the design solution space. Contrarily, for 6–phase machines, it is impossible to have an odd slot number irrespective of the winding configuration [20]. Further, it can be seen that odd slot numbers always have lower THD than even slot numbers. Although the difference is not too significant in terms of k_{w1}, the merits of odd slots can be observed from cogging torque. Due to minimized interaction of each pole with the slots, the cogging frequency increases with reduced magnitudes leading to minimal net radial forces in case of odd slot numbers. To illustrate the benefits of slot shifted machines especially with odd slot numbers in terms of THD, k_{w1} and cogging torque, a sample set of slot–pole combinations are summarized in Table 3.1.

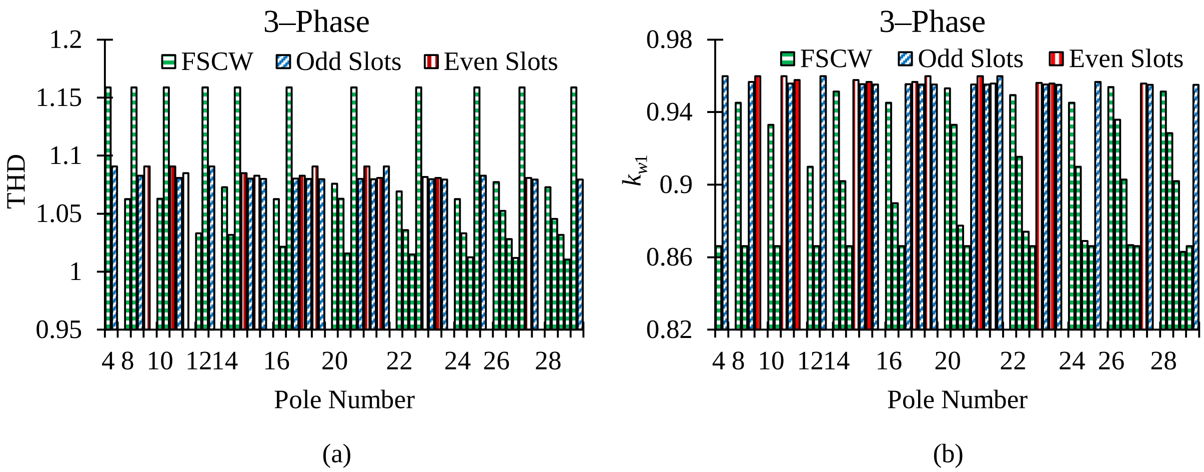

Fig. 3.2. Comparative performance analysis of concentrated wound and stator slot shifted 3–phase PMSMs with even and odd slot numbers. (a) THD. (b) k_{w1}.

TABLE 3.1
SAMPLE SLOT–POLE COMBINATION ANALYSIS

n	p	S	Coil Pitch	q	LCM	k_{w1}	THD	T_{cog}
3	10	12	1	0.4	60	0.93	1.06	0.39
		15	1	0.5	30	0.87	1.16	0.98
		18	2	0.6	90	0.96	1.09	0.83
		21	2	0.7	210	0.96	1.08	0.18
		24	2	0.8	120	0.96	1.08	0.71
5	14	15	1	0.21	210	0.98	1.15	0.18
		20	1	0.29	140	0.88	1.05	0.80
		25	2	0.36	350	0.98	1.17	0.68
		30	2	0.43	210	0.99	1.17	0.18
6	20	24	1	0.2	120	0.97	1.12	0.71
		30	1	0.25	60	0.87	1.16	0.39
		48	2	0.4	240	0.99	1.22	1.00
9	16	18	1	0.13	144	0.98	1.17	0.80
		27	2	0.19	432	0.99	1.27	0.34
		36	2	0.25	144	0.99	1.34	0.80

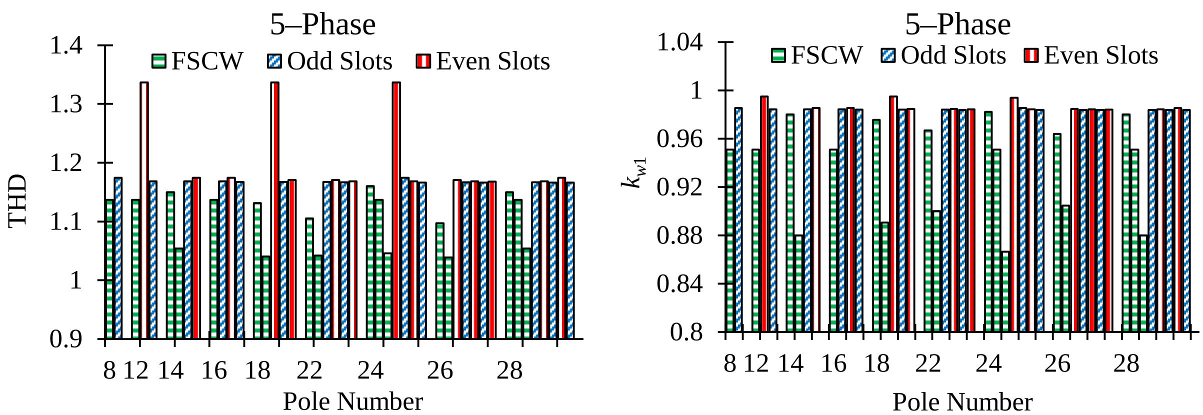

(a) (b)

Fig. 3.3. Comparative performance analysis of concentrated wound and stator slot shifted 5–phase PMSMs with even and odd slot numbers. (a) THD. (b) k_{w1}.

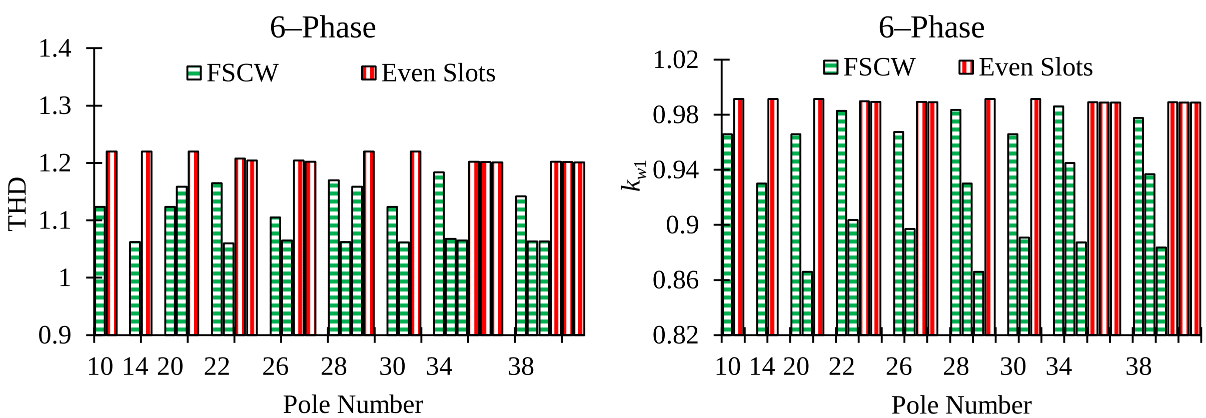

(a) (b)

Fig. 3.4. Comparative performance analysis of concentrated wound and stator slot shifted 6–phase PMSMs with even and odd slot numbers. (a) THD. (b) k_{w1}.

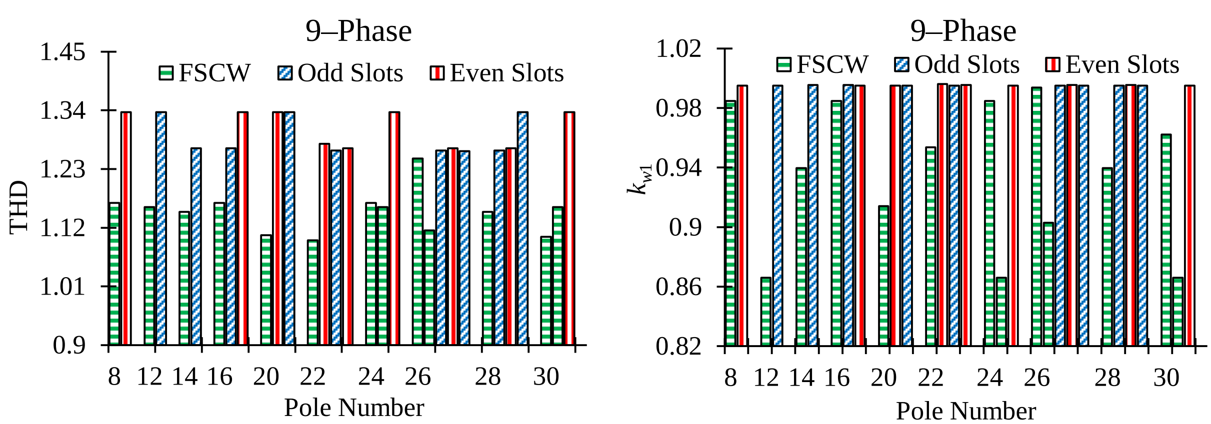

(a) (b)

Fig. 3.5. Comparative performance analysis of concentrated wound and stator slot shifted 9–phase PMSMs with even and odd slot numbers. (a) THD. (b) k_{w1}.

3.3. Optimal Slot–Pole Selection for Stator Slot Shifted PMSMs

A. Optimal Slot–Pole Selection Problem Statement

The fundamental objective of slot shifting is to minimize the spatial harmonic contents and obtain better sinusoidal voltages and reduced machine losses. While high slot numbers result in lower slot leakage reactances and high cogging torque frequencies, in order to obtain sinusoidal voltages, it is important to have high fundamental winding factor and almost negligible harmonic winding factors leading to minimum THD. The cogging frequency increases with reduced magnitudes by using higher LCM of slot and pole numbers. Further, with odd slot numbers, an additional reduction of cogging torque magnitude is achieved. On the other hand, while high slot and pole numbers improve the torque production of the machine, the winding losses correspondingly increase, resulting in reduced efficiency. Furthermore, while odd slot numbers result in reduced torque ripple, even slot numbers provide machine symmetry and low net radial forces. Similarly, while higher pole numbers result in low flux leakage and hence higher magnet utilization it can result in reduced constant power speed range [21].

Thus, it is observed that depending upon the primary required performance objective, the choice of optimal slot–pole combination varies. In other words, there exists multiple pareto fronts among the set of feasible solutions. In case of conventional multi–objective optimization problems, a prior weight for each objective is set to estimate the optimal solution. However, in this case, assigning weights to different performance characteristics will result in a biased or local optimal solution and would be very application specific. Therefore, a multi objective optimization algorithm capable of identifying a global optimal point is required. Hence, in this chapter, non–dominated sorting genetic algorithm (NSGA) is implemented to estimate an optimal slot–pole combination for slot shifted machines. NSGA based optimization improves the adaptive fit of the solution space to a pareto front for the objective function. Thus, the parameter set, Ω_j as in (3.12), for the j^{th} iteration can be obtained by varying S, p and n for various integral values satisfying conditions (3.1) – (3.3). The objective function, $J(\Omega_j)$ can be defined as in (3.13) using all the performance characteristics as defined in (3.4) – (3.11).

$$\Omega_j \subseteq \lfloor S_j, p_j, n_j \rfloor \tag{3.12}$$

$$J(\Omega) = f\left\{-k_{w1}, THD, T_{cog}, P_{losses}, -{T_e}/{P_{copper}}\right\} \tag{3.13}$$

The negative sign before the k_{w1} and electromagnetic torque per unit winding losses indicate maximizing function while the remaining characteristics are minimized.

To estimate the machine performance characteristics under consideration, certain assumptions and constraints are required. Therefore, to provide a generalized analysis, the overall machine dimensions, air gap length, rated power and speed ratings, core and magnet material properties used are kept constant for all feasible slot–pole combinations. The wire diameter and turns per phase are estimated for a specific slot fill factor and a continuous current density of 14 A/mm^2 for the copper conductors. Using the estimated turns per phase and a per unitized E_h for a 400 V DC bus system, (3.8) and (3.9) can be calculated. The loss coefficients used in (3.10) are predominantly material dependent and are kept constant. Further, for a fixed rated current value, the maximum torque capability can be easily obtained. However, the optimum current angle γ, is maintained as 0^o for preliminary analysis. It is vital to avoid magnetic saturation of the stator teeth and demagnetization of the magnet material at rated current conditions. So, the maximum flux density at the stator tooth and rotor PM are kept as constraints. Thus, from the optimization algorithm, best design candidates for slot shifting of fractional–slot wound PMSMs for 3–, 5–, 6– and 9–phases PMSMs are obtained.

B. NSGA Based Optimization Approach

NSGA is a widely implemented elitism based non–dominated sorting method used to rank and sort each feasible individual based on a simple crowding distance estimator [22]. Unlike priori weight based multi objective optimization methods, NSGA provides a faster non–dominated sorting approach with better estimation of pareto fronts [23]. It was observed in [24], that NSGA resulted in better optimum values of the objective function when compared to other multi objective optimization methods. Further, it was seen that NSGA results in better convergence and distribution of solutions, efficient constraint–handling method and relatively faster approach in [25]. Thus, NSGA method was chosen in this chapter to select an optimal slot–pole combination for slot shifted PMSMs.

The overall process of the optimization algorithm is detailed as follows and summarized in a flowchart shown in Fig. 3.6. For the limits indicated in (3.1), an initial population of various slot–pole combinations for different phase numbers are created. Then, each individual is ranked and sorted based on non–dominated criteria as in (3.14). For instance, a particular individual with parameter set, Ω_j, will dominate another individual Ω_i only if all the objectives for Ω_j is not worse than that of Ω_i and at least one objective should be better than that of Ω_i. Further, after the sorting is completed, a simple crowding distance estimator as in (3.15) is used for the objective function to determine if a particular individual of a pareto front will be passed over to the successive offspring generation. The distance of each individual from every other individual in the population is estimated based on the maximum and minimum limits of the objective function, J_{max} and J_{min}. Thus, the most crowded individual is passed to the next generation. This helps to avoid the local maxima and hence allows for better distribution of the solution. Subsequently, conventional genetic algorithm procedure takes over, where the individuals for the next generation are selected and binary crossover and polynomial mutation of the population occurs. Finally, recombination of the offspring population and the parent generation results in the next generation. The overall procedure is repeated till the population size exceeds the current population size.

$$J(\Omega_i) \preceq J(\Omega_j) \tag{3.14}$$

$$J(\Omega_i)_{distance} = J(\Omega_i)_{distance} + \frac{[J(\Omega_{i+1}) - J(\Omega_{i-1})]}{J_{\max} - J_{\min}} \tag{3.15}$$

The machine structural and performance parameter limits maintained in this analysis are summarized in Table 3.2. The optimal slot–pole combinations obtained for slot shifted fractional–slot wound PMSMs for 3–, 5–, 6– and 9–phases PMSMs obtained from the NSGA algorithm are summarized in Table 3.3. It is important to note that other optimal pareto fronts could exist as well for the defined dataset. Furthermore, if a specific parameter is targeted for optimization, for example high winding factor or minimized losses, a totally different pareto front and hence a different set of optimal slot–pole combination could exist. However, the scope of the chapter is to prove that it is possible to expand the design solution for slot–shifted PMSMs by implementing unconventional slot numbers as well. Furthermore, this study provides a guideline for machine designers to obtain an optimal slot–pole combination for a specific application or a specific target performance.

TABLE 3.2
MACHINE STRUCTURAL AND PERFORMANCE PARAMETER LIMITS

Rated Torque	70 Nm	Core Material	M1929G
Rated Power	22 kW	PM Material	NdFeB 35
Base Speed	3,000 rpm	Slot Fill Factor	65%
Maximum Speed	10,000 rpm	Rated Current	78 A
DC Bus Voltage	400 V	Air Gap Length	0.5 mm
Stator Tooth Saturation Limit	1.7 T	PM Demagnetization Limit	0.6 T

TABLE 3.3

PERFORMANCE CHARACTERISTICS OF OPTIMAL SLOT–POLE COMBINATIONS

S	p	n	k_{w1}	THD	T_{cog}	P_{losses}	T_e/P_{copper}
39	16	3	0.96	1.08	0.78	751	111.4
15	8	5	0.99	1.17	0.71	722	114.9
24	14	6	0.99	1.22	0.47	807	115.3
27	14	9	0.99	1.27	0.3	962	112.3

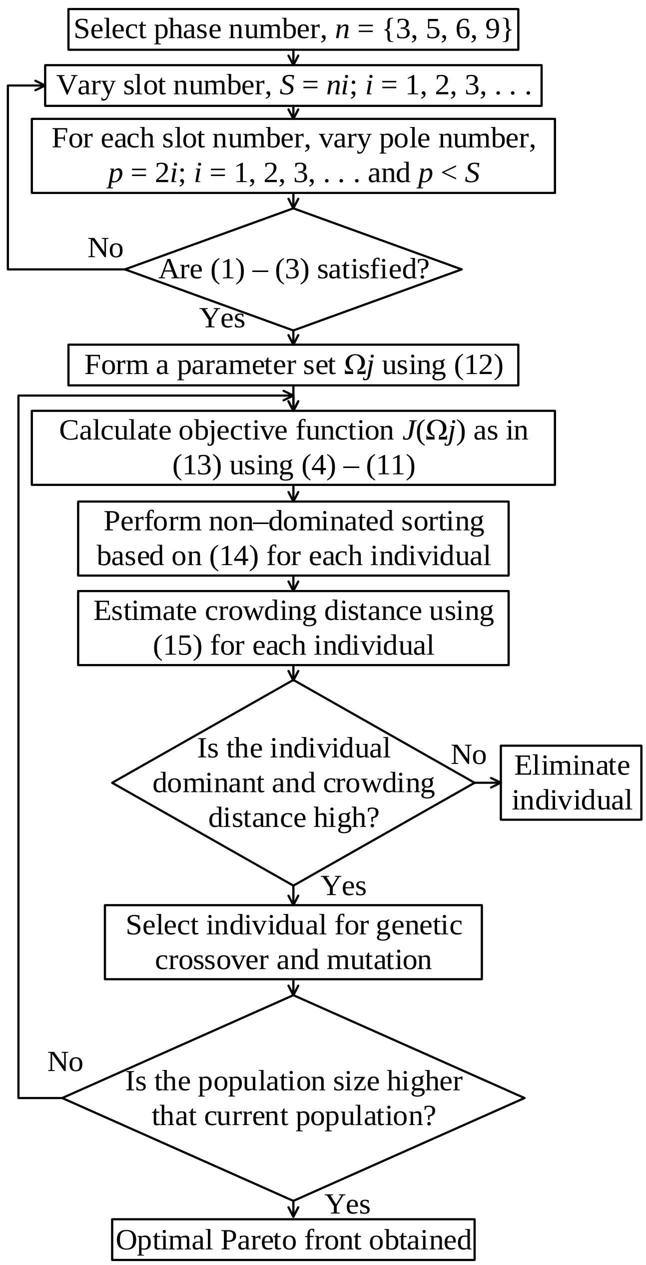

Fig. 3.6. Flowchart illustrating the NSGA based optimization approach.

C. Validation of Optimal Slot–Pole Combination for 3–Phase Slot Shifted PMSM

In this section, the proposed optimal slot–pole combination for the 3–phase slot shifted PMSM is validated using finite element analysis (FEA) and experimental data. To highlight the objective of the study, electromagnetic models of a conventional FSCW machine, conventional slot shifted PMSM with even slot number and the proposed slot shifted PMSM are developed as shown in Fig. 3.7 with the winding layout of Phase A highlighted in red. The 16–pole rotor, machine dimensions, PM volume and slot fill factor are all kept constant. A conventional interior permanent magnet rotor with v–shaped magnets was used for analysis. Table 3.4 summarizes the preliminary comparison of the fundamental winding factor, THD and cogging torque. The concentrated wound machine with 18 slots and the conventional slot shifted machine with 36 slots have the same LCM and hence the same cogging torque. However, the fundamental winding factor of the slot shifted machine has improved slightly resulting in reduced THD. On the other hand, the proposed slot shifted machine with 39 slots has significantly higher LCM resulting in 3.2% reduction in cogging torque while still maintaining the fundamental winding factor similar to the 36 slot machine. Thus, it is expected that with improved torque production, the proposed machine should also be capable of producing better efficiency and minimized torque ripple and improved operating range.

Further, to analyze the spatial harmonic contents of the three machines under consideration, the no–load induced voltages at rated speed of 3,000 rpm were obtained as shown in Fig. 3.8(a). The harmonic spectrum in Fig 3.8(b) is obtained from Fourier transformation of the induced voltages. The fundamental component of the 18–slot FSCW machine is slightly higher than the slot shifted machines due to increased turns per phase in the machine. However, the trend observed in the harmonic spectrum remains the same. It can be seen that the higher order harmonic contents of the slot shifted 36–slot and 39–slot machines are always lower than that of the FSCW machine indicating better waveform quality. Furthermore, between

TABLE 3.4
PERFORMANCE VALIDATION OF OPTIMAL SLOT–POLE COMBINATION FOR 3–PHASE SLOT SHIFTED MACHINE

Configuration	S	p	n	k_{w1}	THD	T_{cog}
Concentrated Winding	18	16	3	0.95	1.09	0.8
Conventional Slot–Shifted Machine	36			0.96	1.1	0.8
Proposed Slot–Shifted Machine	39			0.96	1.06	0.77

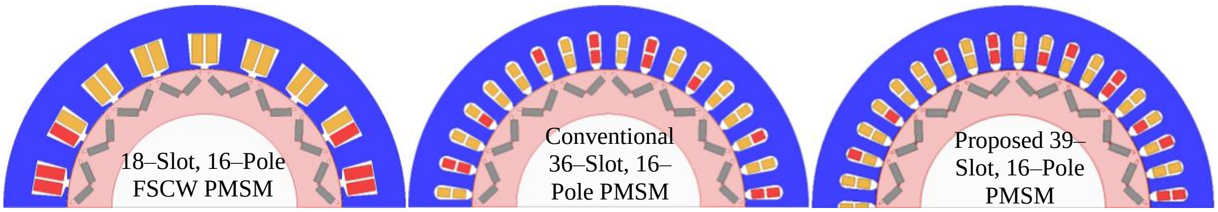

(a) (b) (c)

Fig. 3.7. Electromagnetic models developed for the machines analyzed with the Phase A winding layout highlighted in red. (a) Conventional 18–slot, 16–pole FSCW PMSM. (b) Conventional slot shifted 36–slot, 16–pole PMSM. (c) Proposed slot shifted 39–slot, 16–pole PMSM.

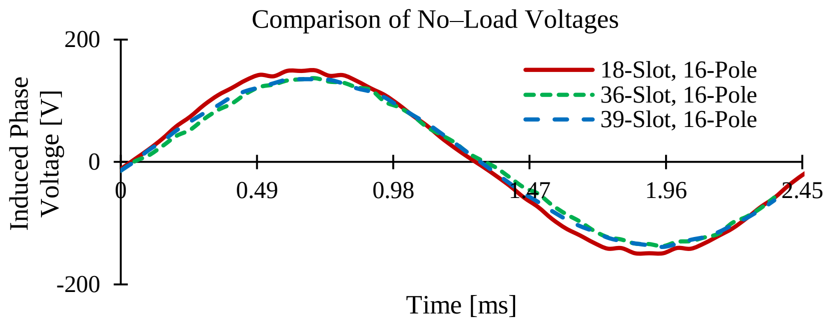

(a)

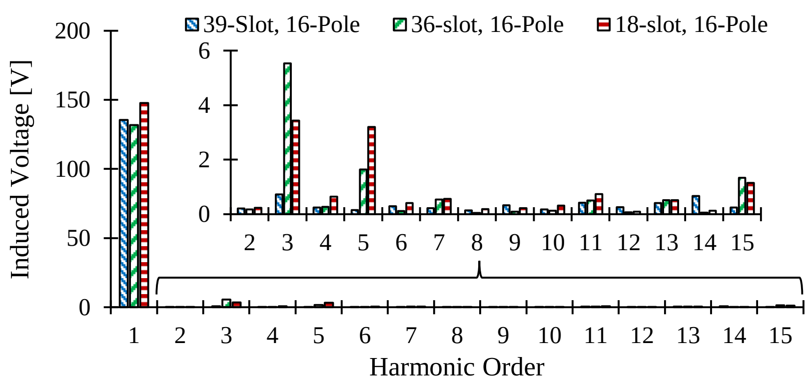

(b)

Fig. 3.8. Comparison of spatial harmonic contents of the concentrated wound 18–slot machine, conventional slot shifted 36–slot machine and proposed slot shifted 39–slot machine topologies. (a) No–load induced phase A voltage at rated speed of 3,000 rpm. (b) Harmonic spectrum.

the slot shifted machines, the 5th and 7th order torque ripple producing harmonics of the 39–slot machine is significantly lower than that of the 36–slot machine as expected. Although certain 3rd order harmonics of the 39–slot machine is higher, these harmonics are eliminated in the line voltages like any traction machine.

The electromagnetic torque capability and the torque ripple contents of the aforementioned 3 machine configurations were compared as shown in Fig. 3.9. It is important to note that all the 3 machines were designed for the structural, material and performance details as give in Table 3.2.

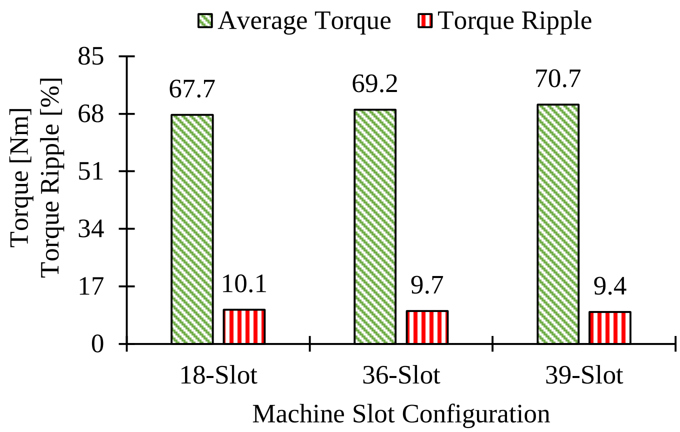

Fig. 3.9. Comparison of average electromagnetic torque and torque ripple content of the concentrated wound 18–slot machine, conventional slot shifted 36–slot machine and proposed slot shifted 39–slot machine topologies.

Thus, for the same machine volume, rated voltage and currents, the proposed 39–slot, 16–pole machine produces the highest rated torque of 70.7 Nm which is 4% and 2.3% higher than that produced by the 18–slot and 36–slot machine respectively. Further, the 18–slot, 36–slot and proposed 39–slot machines have a torque ripple content of 10.1%, 9.7% and 9.4% respectively, clearly indicating the inherent advantage obtained from the odd slot configuration. Thus, considering the advantages obtained from the proposed slot shifted machine configuration in terms of various performance characteristics, the 39–slot, 16–pole motor was chosen as the optimal slot–pole combination for prototyping.

3.4. Conclusions

In this chapter, to expand the feasible design solutions for stator slot shifted fractional–slot wound PMSMs, investigation of odd slot numbers for *n*–phase machines was performed. Further, a non–dominated sorting genetic algorithm, is implemented for optimal slot–pole selection for each phase number. Thus, depending on the target performance requirement, the algorithm is implemented to select the optimal slot–pole combination. The following observations were made:

1. The fundamental winding factor of stator shifted machines is always greater than that of concentrated wound machines.
2. Unlike conventional stator shifting methods with even slot numbers, odd slot numbers result in reduced space harmonics, minimum THD and cogging torque.
3. Odd slot numbers with fractional–slot windings result in higher torque production, reduced torque ripple and increased machine efficiency and operating range due to reduced spatial harmonic contents.

Hence, this chapter provides a convenient guideline for designers to select optimal slot–pole combinations for a *n*–phase stator shifted fractional–slot wound PMSM.

3.5. References

[1] H. Dhulipati *et. al*., "Investigation of 6–phase surface PM machines with concentrated windings for reduction in space harmonics, leakage inductance and magnet loss in direct–drive EV," in proc. of *XXII Int. Conference on Electrical Machines (ICEM)*, 2016, pp. 811–817.

[2] V. Rallabandi, N. Taran and D. M. Ionel, "Multilayer concentrated windings for axial flux PM machines," in proc. of *IEEE Conference on Electromagnetic Field Computation (CEFC)*, Miami, 2016, pp. 1–1.

[3] H. Dhulipati, S. Mukundan, K. L. V. Iyer and N. C. Kar, "Skewing of stator windings for reduction of spatial harmonics in concentrated wound PMSM," in proc. of *IEEE 30th Canadian Conference on Electrical and Computer Engineering (CCECE)*, Windsor, 2017, pp. 1–4.

[4] R. Islam and A. P. Ortega, "Practical aspects of implementing skew angle to reduce cogging torque for the mass–production of permanent magnet synchronous motors," in proc. of *20th International Conference on Electrical Machines and Systems (ICEMS)*, Sydney, 2017, pp. 1–5.

[5] A. S. Abdel–Khalik *et. al*., "Effect of Multilayer Windings With Different Stator Winding Connections on Interior PM Machines for EV Applications," *IEEE Trans. on Mag.*, vol. 52, no. 2, pp. 1–7, Feb. 2016.

[6] V. I. Patel *et. al*., "Six–Phase Fractional–Slot–per–Pole–per–Phase Permanent–Magnet Machines With Low Space Harmonics for Electric Vehicle Application," *IEEE Transactions on Industry Applications*, vol. 50, no. 4, pp. 2554–2563, July–Aug. 2014.

[7] P. B. Reddy *et. al*., "Generalized Approach of Stator Shifting in Interior Permanent–Magnet Machines Equipped With Fractional–Slot Concentrated Windings," *IEEE Transactions on Industrial Electronics*, vol. 61, no. 9, pp. 5035–5046, Sept. 2014.

[8] X. Chen and J. Wang, "Magnetomotive force harmonic reduction techniques for fractional–slot non–overlapping winding configurations in permanent–magnet synchronous machines," in *Chinese Journal of Electrical Engineering*, vol. 3, no. 2, pp. 102–113, September 2017.

[9] J. R. Hendershot Jr. and T. J. E. Miller, *Design of Brushless Permanent magnet Motors*, Magna Physics Publishing and Clarendon Press, Oxford,1994, pp. 3.12–3.15.

[10] A. S. Abdel–Khalik *et. al*., "A Six–Phase 24–Slot/10–Pole Permanent–Magnet Machine With Low Space Harmonics for Electric Vehicle Applications," *IEEE Trans. on Mag.*, vol. 52, no. 6, pp. 1–10, 2016.

[11] G. Dajaku *et. al*., "Reduction of Low Space Harmonics for the Fractional Slot Concentrated Windings Using a Novel Stator Design," *IEEE Transactions on Magnetics*, vol. 50, no. 5, pp. 1–12, May 2014.

[12] G. Dajaku and D. Gerling, "A Novel 24–Slots/10–Poles Winding Topology for Electric Machines," in proc. of *IEEE International Electric Machines & Drives Conference (IEMDC)*, Canada, 2011, pp. 65–70.

[13] G. Dajaku and D. Gerling, "New methods for reducing the cogging torque and torque ripples of PMSM," in proc. of *4th International Electric Drives Production Conference (EDPC)*, Nuremberg, 2014, pp. 1–7.

[14] R. Krishnan, *Permanent Magnet Synchronous and Brushless DC Motor Drives*, CRC Press, 2010, pp. 3–34.
[15] K. L. V. Iyer *et. al*., "Design considerations for permanent magnet machine drives for direct–drive electric vehicles," in proc. of *IEEE Int. Elec. Machines & Drives Conf. (IEMDC)*, Idaho, 2015, pp. 1170–1176.
[16] A. K. Sawhney, *A Course on Electrical Machine Design*, New Delhi, India: Dhanpat Rai & Co, 2011, pp. 11.41–11.42.
[17] V. I. Patel and J. Wang, "Assessment of 12–slot, 14–pole permanent magnet flux switching machine with hybrid excitation for electric vehicle application," in proc. of *IEEE Energy Conversion Congress and Exposition*, Denver, 2013, pp. 5092–5099.
[18] T. A. Lipo, *Introduction to AC Machine Design*, 3rd ed. Madison, WI, USA: Univ. Wisconsin–Madison, pp. 65, 70,79–80, 2009.
[19] E. Levi, “Multi–phase electric machines for variable–speed applications,” *IEEE Trans. on Ind. Elec.*, vol. 55, no. 5, pp. 1893–1909, 2008.
[20] T. Kenjo and S. Nagamori, *Permanent–magnet and brushless DC motors*, Oxford University Press, 1985.
[21] Z. Q. Zhu and D. Howe, "Influence of design parameters on cogging torque in permanent magnet machines," *IEEE Transactions on Energy Conversion*, vol. 15, no. 4, pp. 407–412, Dec, 2000.
[22] K. Deb, A. Pratap, S. Agarwal and T. Meyarivan, "A fast and elitist multiobjective genetic algorithm: NSGA–II," *IEEE Transactions on Evolutionary Computation*, vol. 6, no. 2, pp. 182–197, April 2002.
[23] K. Deb and H. Jain, "An Evolutionary Many–Objective Optimization Algorithm Using Reference–Point–Based Nondominated Sorting Approach, Part I: Solving Problems With Box Constraints," *IEEE Trans. on Evol. Computation*, vol. 18, no. 4, pp. 577–601, Aug. 2014.
[24] H. Jain *et. al*., "An Evolutionary Many–Objective Optimization Algorithm Using Reference–Point Based Nondominated Sorting Approach, Part II: Handling Constraints and Extending to an Adaptive Approach," *IEEE Trans. on Evol. Comp.*, vol. 18, no. 4, pp. 602–622, 2014.
[25] G. Bhargav *et. al*., “Multi–objective optimization of vehicle passive suspension system using NSGA–II, SPEA2 and PESA–II,” *Procedia Technol.*, vol. 23, pp. 361–368, Apr. 2016.

Chapter 4

Novel Star–Delta Winding Configuration with Odd Slots for Reduced Space Harmonics Using Winding Function

4.1. Introduction

Understanding the necessity to reduce the spatial harmonic contents in fractional–slot wound machines, the previous chapter proposed an optimal slot–pole combination for slot–shifted winding configurations with reduced end winding material wastage. However, to further minimize the torque ripple content in the machine, additional reduction of space harmonics is necessary. Compared to existing space harmonic reduction methods, implementing combined star–delta windings in fractional–slot wound PMSMs is a viable and effective solution due to their practicality, high winding factor, reduced winding losses and no requirement of additional inverter for operation [1], [2]. Comprehensive literature exists on the theory and analysis of star–delta winding topology in terms of winding connection [3], winding factor calculation [4] and reduction of magneto motive force (MMF) spatial harmonics [5], [6]. However, conventional slot–pole combinations implemented for star–delta windings are restricted to multiples of 6 only [7], [8], since they emulate a conventional 6–phase configuration with 30° displacement between the star and delta connected winding sets. Furthermore, due to the inherent turns ratio of √3 between the two winding sets, unlike actual 6–phase configurations, certain harmonic orders of $6k$±1 are not completely eliminated resulting in torque ripple in the machine [9]. Also, implementing such topologies in high–speed machines with lower turns per phase can be challenging with such restricted applicable slot–pole combinations [10]. Hence, with further investigation on appropriate coil and turns distribution among the two winding sets, unconventional design solutions for star–delta winding topology could be feasible. Thus, in order to utilize the proposed slot–pole combination in Chapter 3, this chapter explores the possibility of implementing novel odd slot numbers with star–delta winding configuration towards reduced spatial harmonic content, torque ripple minimization and improved torque density.

4.2. Winding Function Based Modeling of Star–delta Winding Configuration

In case of a 3–phase combined star–delta winding configuration, the total number of coils, q within the 60° phase spread are distributed among the star and delta winding sets to obtain the required turns ratio of √3. While the two winding sets can be connected in parallel or series, this

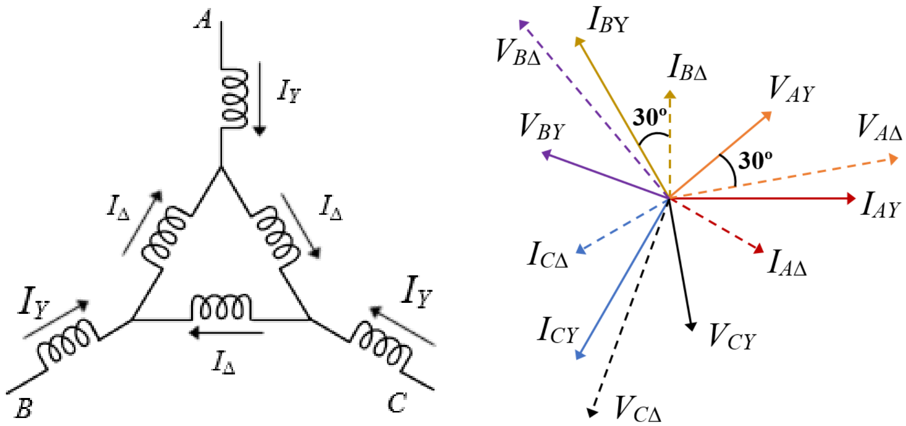

Fig. 4.1. Combined star–delta winding configuration. (a) Star–delta winding sets. (b) Phasor diagram emulating a multiphase topology.

chapter considers only the series connection as shown in Fig. 4.1 as it is more suitable for high–speed applications and also does not produce any harmful circulating currents as observed in the parallel connected topologies [11]. The coil distribution among the two winding sets directly affects the spatial harmonic contents in the machine. Winding function provides a graphical representation of the phase winding distribution along the stator circumference, θ, indicated by (4.1) [12]

$$T_c(\theta) = t_c(\theta) - \{t_c(\theta)\} \tag{4.1}$$

where $t_c(\theta)$ is the turn's function which defines the turns enclosed by a flux path within a coil span and $\{t_c(\theta)\}$ is the average value of the turns function. The winding function is usually represented for the base unit of the machine. For both distributed and concentrated windings, with S stator slots and p poles, the slot per pole per phase, Q can be represented as a simple fraction with denominator, d which represents the number of units the machine can be symmetrically divided into and the numerator, M indicates the number of stator slots per phase in a unit.

$$Q = S/mp = M/d \tag{4.2}$$

In order to obtain equally balanced m–phase voltages, the windings must be symmetrically distributed in each unit across the entire machine. This condition is given by (4.3), where for any integral value of C, only when D is a positive integer, symmetrically balanced voltages are obtained.

$$D = \frac{1 + mMC}{d};\ C \in 1,2,\ldots\infty \tag{4.3}$$

For a balanced m–phase system, the current excitation with k^{th} time harmonic content is given by

$$I(t)=\sum_{i=1}^{m}\sum_{k=2}^{\infty} I_k \sin k\left(\omega t-(i-1)\frac{2\pi}{m}\right) \tag{4.4}$$

where I_k is the peak phase supply current, ω is the electrical supply angular frequency and t is the time period. Thus, from the winding function and the input current excitation with k^{th} time harmonic order, the i^{th} phase effective MMF distribution, $\Im_{i,k,n,Y\Delta}$ along the stator circumference with n^{th} spatial harmonic order is given by

$$\Im_{i,k,n,Y\Delta}(\theta,t)=\Im_{i,k,n,Y}(\theta,t)+\Im_{i,k,n,\Delta}(\theta,t) \tag{4.5}$$

$$\left.\begin{aligned}\Im_{i,k,n,Y}(\theta,t)=\frac{\Im_{k,n,Y}}{2}&\cos\left\{k\omega t-n\frac{d}{2}\theta-(i-1)\frac{k-n}{m}2\pi\right\}\\ -\frac{\Im_{k,n,Y}}{2}&\cos\left\{k\omega t+n\frac{d}{2}\theta-(i-1)\frac{k+n}{m}2\pi\right\}\end{aligned}\right\} \tag{4.6}$$

$$\left.\begin{aligned}\Im_{i,k,n,\Delta}(\theta,t)=\frac{\Im_{k,n,\Delta}}{2}&\cos\left\{k\omega t-n\frac{d}{2}\theta-(k-n)\left[\frac{(i-1)}{m}2\pi+\phi_\Delta\right]\right\}\\ -\frac{\Im_{k,n,\Delta}}{2}&\cos\left\{k\omega t+n\frac{d}{2}\theta-(k+n)\left[\frac{(i-1)}{m}2\pi-\phi_\Delta\right]\right\}\end{aligned}\right\} \tag{4.7}$$

$$\left.\begin{aligned}\Im_{k,n,Y}&=\frac{4}{\pi}\frac{q_Y T_{cY} I_k}{nd}k_{wnY}\sin\left(\frac{n\pi}{M}\right)\\ \Im_{k,n,\Delta}&=\frac{4}{\pi}\frac{q_\Delta T_{c\Delta} I_k}{\sqrt{3}nd}k_{wn\Delta}\sin\left(\frac{n\pi}{M}\right)\end{aligned}\right\} \tag{4.8}$$

where, the winding factor for the star (Y) and delta (Δ) winding sets can be written as in (4.9) and (4.10) respectively where q_Y and q_Δ are the coils per phase, T_{cY} and $T_{c\Delta}$ are the turns per coil, a_Y and a_Δ is the number of parallel paths of the star and delta winding sets respectively and χ is the slot opening angle [13].

$$k_{wnY}=\frac{\frac{T_{cY}}{a_Y}\sin\left(\frac{n\pi q_Y}{2mM}\right)}{\frac{q_Y T_{cY}}{a_Y}\sin\left(\frac{n\pi}{2mM}\right)}\cos\left(\frac{n\pi N_Y}{mM}\right)\frac{\sin(n\chi_Y/2)}{n\chi_Y/2} \tag{4.9}$$

$$k_{wn\Delta}=\frac{\frac{T_{c\Delta}}{a_\Delta}\sin\left(\frac{n\pi q_\Delta}{2mM}\right)}{\frac{q_\Delta T_{c\Delta}}{a_\Delta}\sin\left(\frac{n\pi}{2mM}\right)}\cos\left(\frac{n\pi N_\Delta}{mM}\right)\frac{\sin(n\chi_\Delta/2)}{n\chi_\Delta/2} \tag{4.10}$$

It is known that the ratio of magnitudes of currents in the delta and the star winding set is √3.

Thus, it is imperative that to get a balanced system, the MMF produced by both the winding sets must be equal.

$$\left.\begin{aligned} \frac{q_Y T_{cY}}{a_Y} I_{kY} \sin(k\omega t) &= \frac{q_\Delta T_{c\Delta}}{a_\Delta} I_{k\Delta} \sin(k\omega t - \phi_\Delta) \\ \phi_\Delta &= \sin^{-1}\left(\frac{\sqrt{3} q_Y T_{cY} a_\Delta}{q_\Delta T_{c\Delta} a_Y}\right) \cong \frac{\pi}{6} \end{aligned}\right\} \tag{4.11}$$

Therefore, the exact coil distribution for the winding sets can be modeled from (4.11) for a balanced system. The above equation allows the possibility of unconventional slot–pole combinations capable of satisfying the required turns ratio. It is of significance to note that although the star–delta windings emulate a 6–phase topology, the resultant configuration is still a 3–phase winding which allows exploration of slot–pole combinations which are non–multiples of 6. Thus, with the elimination of n^{th} spatial harmonic order given by (4.12), the harmonic winding factor reduces and the fundamental component increases, resulting in a direct increment in torque production.

$$n = \begin{cases} \dfrac{j\pi}{\Phi_\Delta} \mp 1, & j = 1,3,5\cdots\infty \\ \dfrac{2j\pi}{\Phi_\Delta} \mp 1, & j = 1,2,3\cdots\infty \end{cases} \tag{4.12}$$

Further, it can be observed from (4.11) that, three possible cases of coil distribution arise which can satisfy the condition provided the parallel paths in both the winding sets are equal.

Case 1: The product of q and T_c of the star and delta winding sets must satisfy (4.11)

TABLE 4.1
SLOT–POLE ANALYSIS FOR STAR–DELTA WINDINGS

Stator Slot (S)	Pole Pair ($p/2$)	d	M
$3v$, $v = 2z\pm1$, $z\epsilon Z$	All	Even	Odd
$6v$, $v = 2z\pm1$, $z\epsilon Z$	Odd	Odd	Odd
	Even	Even	Odd
$12v$, $v = 2z\pm1$, $z\epsilon Z$	Odd	Odd	Even
	Even	Even	Odd
		Odd	Odd
$12v$, $v = 2z$, $z\epsilon Z$	Odd	Odd	Even
	Even	Even	Odd
		Odd	Even

Case 2: If the coils are equally split among the two sets, turns ratio, $T_{c\Delta}/T_{cY}$ is maintained at √3

Case 3: The turns of both the winding sets are maintained the same as a conventional 3–phase wound machine and hence the coil distribution must maintain a ratio of √3

While case 1 facilitates relatively more design solutions, case 2 might not result in the exact turns ratio required and case 3 allows ease of manufacture with no additional copper losses by using the same conductors as a conventional 3–phase winding. Thus, further analysis is required to understand which possible winding connection results in the least harmonic content and high torque density. Depending upon the slot–pole number, the total coils per phase, q, can be even or odd thereby affecting the spatial harmonic content. Therefore, Table 4.1 summarizes a slot–pole analysis guideline for star–delta windings for all slot numbers including non–multiples of 6.

4.3. Comparative Performance Investigation of Slot–Pole Combinations for Star–Delta Wound PMSMs

For the purpose of comparative analysis, two PMSMs with the same power ratings, rotor structure and similar turns per phase were designed. The structural and performance details of the fractional–slot interior PMSMs designed with star–delta windings are shown in Table 4.2. The electromagnetic models of the machines as shown in Fig. 4.2, were developed and analyzed at no–load and rated conditions using finite element analysis. The winding distribution for each case study can be modified in the model for both the machines. The first machine is a conventional 36–slot, 16–pole machine and the second one is the proposed 39–slot, 16–pole machine. The winding distribution for both the machines with possible coil and turns distribution satisfying cases 1 – 3 were developed using the winding function theory and are summarized in Table 4.3. The total harmonic distortion factor (THD) is estimated using (4.13) with the fundamental and harmonic winding factors obtained from (4.11).

TABLE 4.2
MACHINE STRUCTURAL AND PERFORMANCE DETAILS

Torque	70 Nm	Speed	3,000 rpm
Stack Length	75 mm	Maximum Speed	10,000 rpm
Stator Diameter	195 mm	Rotor Diameter	133 mm
DC Bus Voltage	400 V	Rated Current	78 A
Magnet	NdFeB35	Electric Steel	M1929G

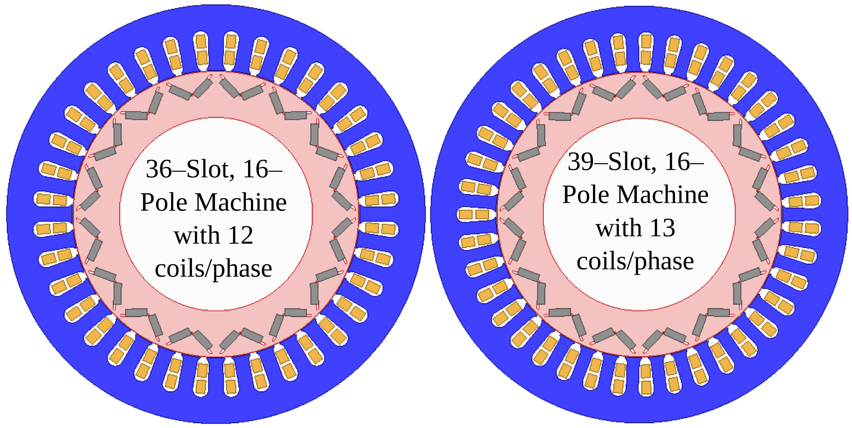

(a) (b)

Fig. 4.2. Electromagnetic models developed for the fractional–slot wound IPMSMs. (a) Conventional 36–slot, 16–pole machine. (b) Novel 39–slot, 16–pole machine.

TABLE 4.3
COIL DISTRIBUTION AND WINDING FACTORS OF ANALYZED STAR–DELTA WOUND PMSMS

Parameter		39–Slot, 16–Pole				36–Slot, 16–Pole			
		3–Phase	Case 1	Case 2	Case3	3–Phase	Case 1	Case 2	Case3
q	q_Y	13	7	6	5	12	8	4	4
	q_Δ		6	7	8		4	8	8
T_c	T_{cY}	4	4	4	5	4	3	6	6
	$T_{c\Delta}$		8	6	5		10	5	6
Fundamental MMF Component		1.24	1.82	1.15	1.3	1.24	1.22	1.22	1.34
THD		1.03	0.74	1.12	1.01	1.01	1.06	1.07	0.96

$$THD = \frac{\sqrt{\sum_{n=1,3,..}^{\infty} k_{wn}^2 / n}}{k_{w1}} \tag{4.13}$$

Figs. 4.3 and 4.4 present the winding function and MMF spectrum analysis in the mechanical domain of the 3–phase and star–delta wound configurations for both the slot–pole combinations respectively. Since both the machines have 16–poles, the 8th harmonic is the fundamental component contributing to the torque production. It can be observed from Fig. 4.4 that, for the 36–slot machine, only even order harmonics are present while the 39–slot machine has both odd and even order harmonics. This is because, the 36–slot machine can be divided into 4 symmetrical units while the 39–slot machine is asymmetrical and can be analyzed as one unit only. However, the effective THD obtained from the 39–slot machine configuration is lower indicating better waveform quality and the 5th and 7th order components contributing to torque ripple are less than that of the 36–slot machine. It can be observed from Table 4.3 that while for the proposed 39–slot machine, lowest THD of 0.74 is obtained in Case 1, for the conventional 36–slot machine, a THD of 0.94 is observed in case 3. Similarly, the maximum fundamental torque producing MMF

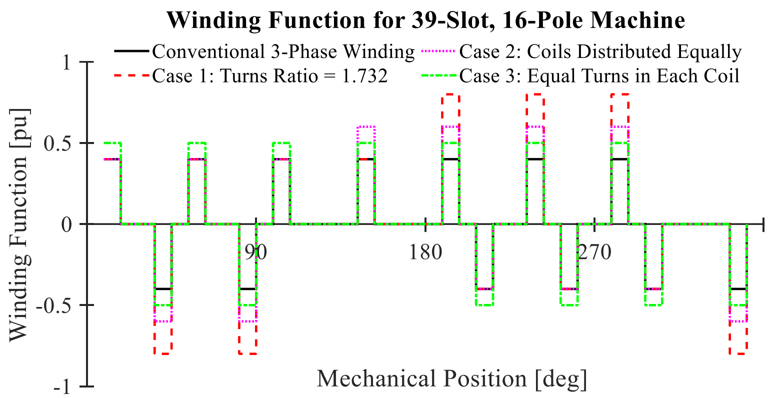

(a)

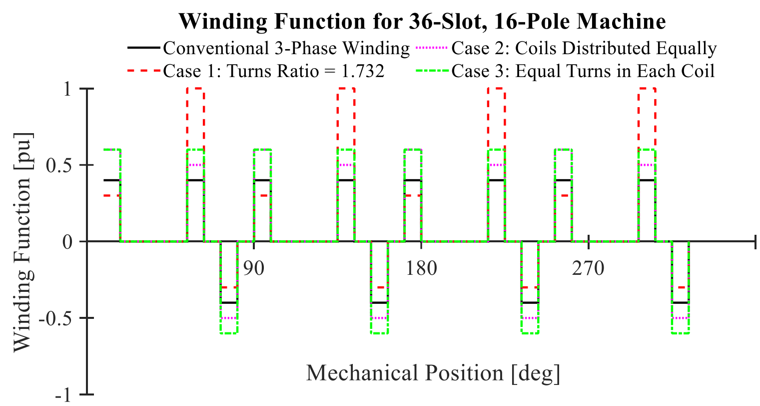

(b)

Fig. 4.3. Comparison of winding functions obtained for conventional 3–phase winding and possible star–delta winding configurations. (a) Conventional 36–slot, 16–pole machine. (b) Novel 39–slot, 16–pole machine.

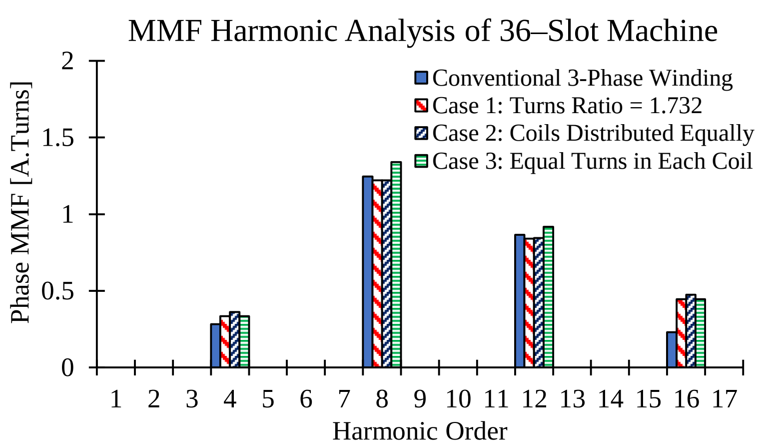

(a)

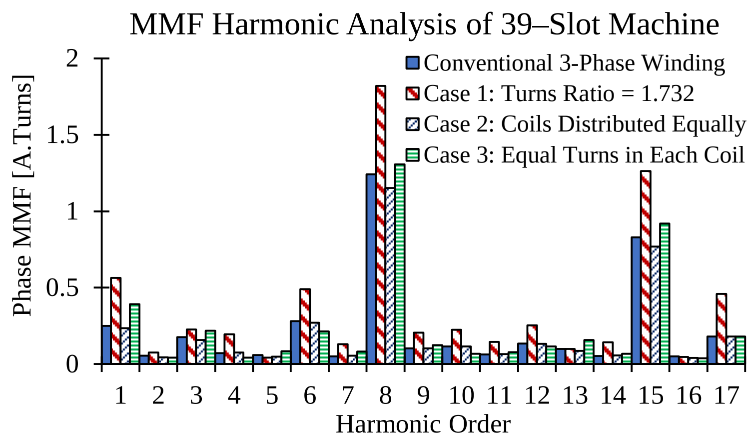

(b)

Fig. 4.4. MMF spectrum analysis obtained for conventional 3–phase winding and possible star–delta winding configurations. (a) Conventional 36–slot, 16–pole machine. (b) Novel 39–slot, 16–pole machine.

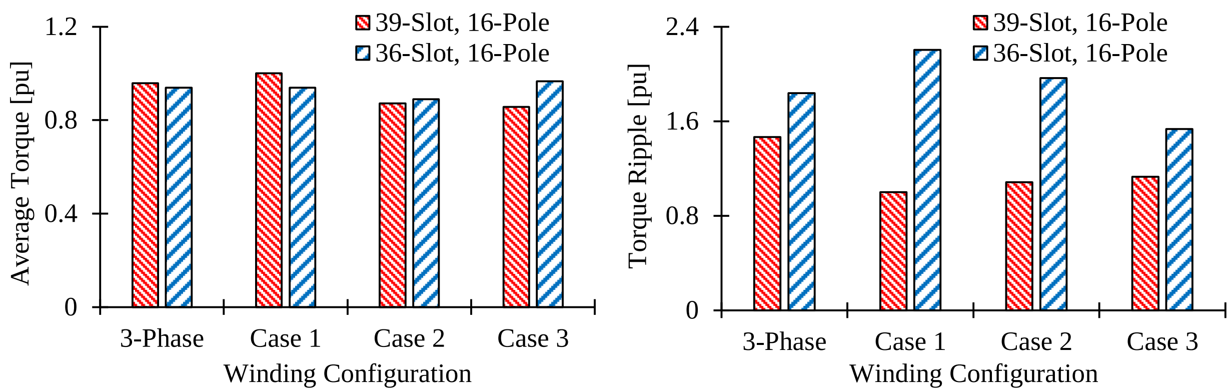

(a) (b)

Fig. 4.5. Comparison of torque and torque ripple obtained for the conventional 36–slot, 16–pole machine and the proposed 39–slot, 16–pole machine. (a) Average torque. (b) Torque ripple.

component for the 39–slot machine is 0.48 more than that of the 36–slot machine. Thus, it can be clearly indicated that odd slot numbers equipped with star–delta windings result in lower spatial harmonic content and higher torque density than the even slot counterparts.

Further, Figs. 4.5(a) and (b) illustrate the average torque and torque ripple components respectively obtained from the machine configurations. The 39–slot machine produces 2.04% more torque in the 3–phase configuration itself and a 6.5% increase in the star–delta configuration for a coil distribution corresponding to Case 1 than the 36–slot machine. The maximum torque densities obtained from the 39–slot and 36–slot machines were 6.2 Nm/kg and 5.9 Nm/kg respectively for relatively same active machine weight. On the other hand, although not significant increase in torque is observed from Cases 2 and 3 for the proposed topology, the torque ripple contents are still lower than that of the conventional 36–slot machine making them suitable design

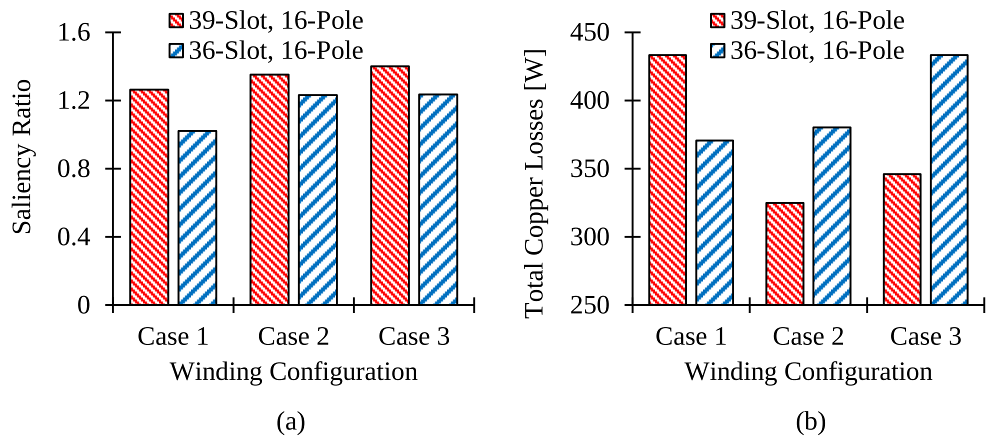

Fig. 4.6. Comparison of saliency ratio and total winding copper losses for the conventional 36–slot, 16–pole machine and the proposed 39–slot, 16–pole machine. (a) Saliency ratio. (b) Total copper losses.

solutions. Therefore, it can be concluded that it is feasible to design a star–delta wound machine with unconventional odd slot numbers with inherent merits including improved torque density and low torque ripple.

Additionally, Fig. 4.6(a) compares the saliency ratio of the two machines for all the winding configurations which is calculated from the ratio of *q*–axis inductance to *d*–axis inductance. It can be seen that maximum saliency ratio is obtained from Case 3 winding configuration for the 39–slot machine although highest torque is obtained from Case 1 winding configuration. From Figs. 4.5(a) and 4.6(a), it can be seen that, only when the turns ratio is close to √3 between the star and delta winding sets, high torque is produced due to the mutual inductances. However, when the required turns ratio is not obtained, major torque production is obtained from the high saliency ratio of the machine. Similarly, for the 36–slot machine, maximum saliency is obtained from Case 3, which is also the winding configuration that produces highest torque. Thus, by modeling the coil distribution and saliency ratio, the effective torque production can be improved significantly. On the other hand, the odd slot number still produces 13.4% higher saliency ratio when compared to the even slot number.

In order to compare the machine efficiency for all the configurations, only copper losses were taken up for analysis, since the machines have the same structure, magnet volume and power ratings. Fig. 4.6(b) illustrated the total copper losses for both the slot–pole combinations at a rated current of 78 Arms/phase. It can be observed that a maximum copper losses of 0.43 kW was obtained from Case 1 for the 39–slot machine and in Case 3 for the 36–slot machine. In both the winding configurations, the delta winding set is equipped with more number of effective turns per phase resulting in higher resistance when compared to the other configurations. Thus, due to the relatively higher copper losses, the machine efficiency for these winding configurations might be slightly lower but compensates with higher torque production. In conclusion, considering various performance characteristics, a 39–slot, 16–pole machine with Case 1 winding configuration resulting in a turns ratio of √3 produces high torque density, lower space harmonics, reduced torque ripple, relatively high saliency ratio and target rated efficiency making it highly suitable for traction application.

4.4. Performance Validation of Proposed 39–Slot, 16–Pole Star–Delta Wound PMSM

The electromagnetic model developed for the proposed 39–slot, 16–pole machine with a coil distribution resulting in a turns ratio of √3 as in case 1 is shown in Fig. 4.7(a) and the internal winding distribution is shown in Fig. 4.7(b). A conventional v–shaped interior PM rotor was chosen for analysis. A coil pitch of 2 was obtained for the chosen slot–pole combination resulting in short end windings and minimal material wastage. The machine was connected in a 3–phase configuration with 7 coils per phase in the star winding set and 6 coils per phase in the delta winding set. In order to verify the waveform quality, Fourier transformation was applied on the no–load induced voltages obtained at low operating speeds to identify any inherent harmonic contents in the machine. Fig. 4.8(a) illustrates the 3–phase near sinusoidal no–load voltage waveforms at low speed and the spatial harmonic spectrum of the phase induced voltages is indicated in Fig. 4.8(b). It can be observed that while the fundamental torque producing component is high, the higher harmonic orders have very low magnitudes indicating good waveform quality.

Further, at full load conditions with an input current of 78 Arms/phase, the machine provides

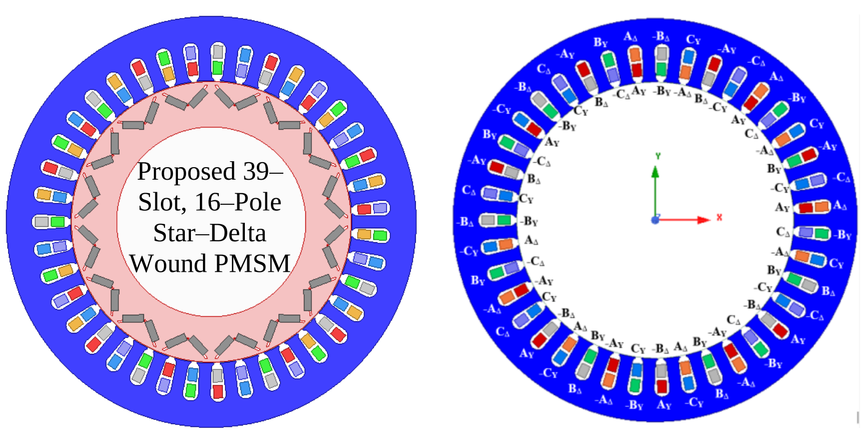

(a) (b)

Fig 4.7. Developed prototype of the proposed 39–slot, 16–pole star–delta wound interior PMSM. (a) Overall structure. (b) Chosen winding configuration.

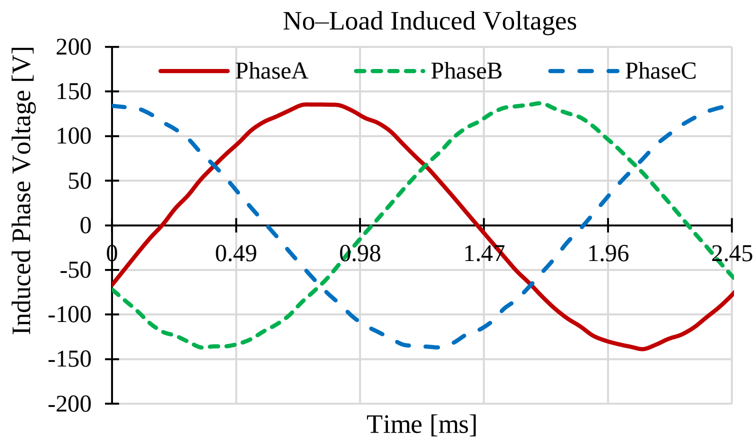

(a)

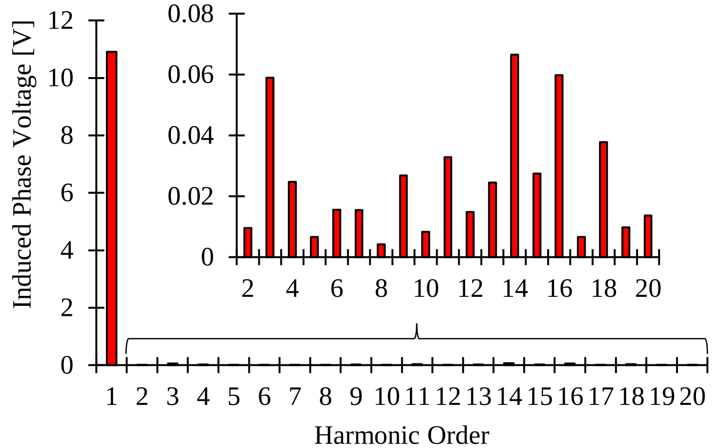

(b)

Fig. 4.8. 3–phase no–load voltages obtained from the developed 39–slot, 16–pole machine at low operating speed to identify spatial harmonic contents. (a) Induced phase voltage waveforms. (b) Spatial harmonic spectrum contents.

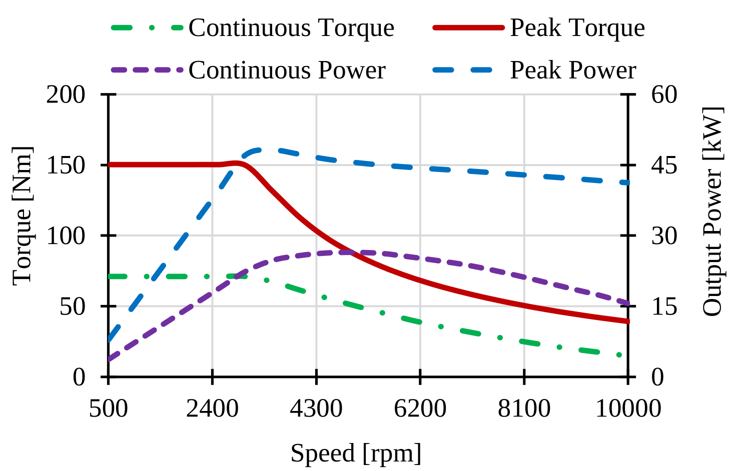

Fig. 4.9. Continuous and peak torque and power–speed characteristics obtained for the novel 39–slot, 16–pole machine at 78 A and 200 A rms/phase currents respectively.

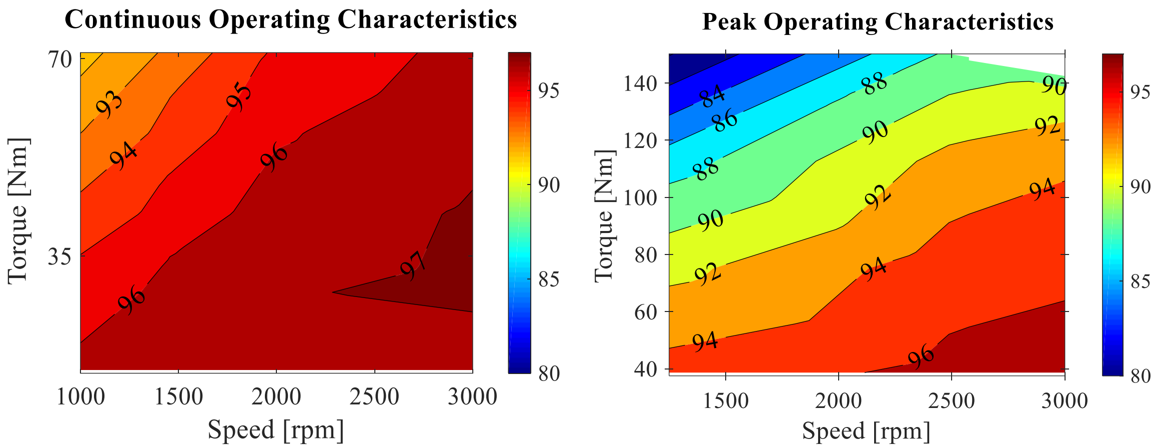

(a) (b)

Fig. 4.10. Efficiency maps obtained for the developed 39–slot, 16–pole machine. (a) Under continuous operating characteristics with input current of 78 A rms/phase. (b) Under peak operating characteristics with input current of 200 A rms/phase.

an average torque of 70.2 Nm with 9.4% torque ripple validating the analysis observed in section 4.3. Fig. 4.9 shows the motor torque and power speed characteristics obtained for a continuous current of 78 A and a peak current of 200 A. The machine is capable of operating up to a maximum speed of 10,000 rpm with a constant power speed range of 3.25. Further, Figs. 4.10(a) and (b) illustrate the efficiency maps of the machine under continuous and peak operating characteristics respectively. A rated efficiency of 97.2% was observed under continuous operating characteristics while a rated efficiency of 96.3% was observed at peak operating characteristics. Therefore, the proposed winding topology satisfy all the required performance characteristics and has significant advantages over the conventional winding topology.

4.5. Conclusions

While existing literature on star–delta windings is restricted to even slot numbers which are multiples of 6, this chapter analyzes unconventional odd slot numbers towards improved torque density, low spatial harmonics and reduced torque ripple. Winding function for fractional–slot windings was implemented to obtain various possible coil distributions between the star and delta connected winding sets for any slot–pole combination for reduced space harmonics. It was observed that odd slot numbers with a coil distribution resulting in a turns ratio of √3 produces improved torque density when compared to the conventional slot numbers due to increased mutual inductances between the two winding sets. Although the saliency ratio obtained for such winding distribution is relatively low, the 5th and 7th harmonic orders in the machine are significantly reduced resulting in low torque ripple. A permanent magnet synchronous machine with the proposed star–

delta winding configuration was developed and its performance characteristics were validated. Furthermore, the feasibility of other possible coil distributions for unconventional slot–pole combinations for star–delta windings leads to more design solutions with low torque ripple and improved machine efficiency. Thus, this chapter provides a guideline for selection and analysis of suitable slot–pole combinations and coil distribution for star–delta winding topologies for various performance targets.

4.6. References

[1] X. Chen and J. Wang, "Magneto motive Force Harmonic Reduction Techniques for Fractional–Slot Non–Overlapping Winding Configurations in Permanent–Magnet Synchronous Machines," *Chinese Journal of Elec. Eng.*, vol. 3, no. 2, pp. 102–113, 2017.

[2] O. Misir, S. M. Raziee, N. Hammouche, C. Klaus, R. Kluge, and B. Ponick, "Prediction of Losses and Efficiency for Three–Phase Induction Machines Equipped with Combined Star–Delta Windings," *IEEE Trans. on Industry Applications*, vol. 53, pp. 3579–3587, Aug. 2017.

[3] W. Zhao, J. Zheng, J. Ji, S. Zhu, and M. Kang, "Star and Delta Hybrid Connection of a FSCW PM Machine for Low Space Harmonics," *IEEE Trans. on Ind. Electronics*, vol. 65, no. 12, pp. 9266–9279, Dec. 2018.

[4] S. M. Raziee *et. al*., "Combined Star–Delta Winding Analysis," *IEEE Trans. on Energy Conversion*, vol. 33, no. 1, pp. 383–394, March 2018.

[5] M. V. Cistelecan *et. al*., "Adjustable Flux Three–Phase AC Machines with Combined Multiple–Step Star–Delta Winding Connections," *IEEE Trans. on Energy Conversion*, vol. 25, no. 2, pp. 348–355, June 2010.

[6] H. Vansompel, P. Sergeant, L. Dupre, and A. Van den Bossche, "A Combined Wye–Delta Connection to Increase the Performance of Axial– Flux PM Machines with Concentrated Windings," *IEEE Trans. Energy Convers*., vol. 27, no. 2, pp. 403–410, Jun. 2012.

[7] M. V. Cistelecan, F. J. T. E. Ferreira, and H. B. Cosan, "Generalized MMF Space Harmonics and Performance Analysis of Combined Multiple–Step, Star–Delta, Three–Phase Windings Applied on Induction Motors," in proc. of *18th Int. Conf. on Elec. Machines*, Vilamoura, 2008.

[8] O. Moros and D. Gerling, "Geometrical and Electrical Optimization of Stator Slots in Electrical Machines with Combined Wye–Delta Winding," in proc. of *Int. Conf. on Elec. Machines*, pp. 2026–2030, 2014.

[9] Y. Lei *et. al*., "Design and Analysis of Star–Delta Hybrid Windings for High–Voltage Induction Motors," *IEEE Transactions on Industrial Electronics*, vol. 58, no. 9, pp. 3758–3767, Sept. 2011.

[10] A. S. Abdel–Khalik, S. Ahmed, and A. Massoud, "Application of Stator Shifting to Five–Phase Fractional–Slot Concentrated Winding Interior Permanent Magnet Synchronous Machine," *IET Electric Power Applications*, vol. 10, no. 7, pp. 681–690, Aug. 2016.

[11] J. R. Hendershot Jr. and T. J. E. Miller, *Design of Brushless Permanent Magnet Motors*, Magna Physics Publishing and Clarendon Press, Oxford, pp. 3.12–3.15, 1994.

[12] C. Jedryczka *et. al*., "Multiphase Permanent Magnet Synchronous Motors with Fractional Slot Windings: The Future of Low Speed Drives?," *Int. Journal of Computation and Mathematics in Electrical and Electronic Engineering*, vol. 35, no. 6, pp. 1937 – 1948, 2016.

[13] S. Bandyopadhyay *et. al*., "Design Optimization of High Performance Fractional–Slot Distributed Winding PM Synchronous Machines for In–Wheel Application in Electric

Vehicles," in proc. of *8th IET International Conference on Power Electronics, Machines and Drives*, Glasgow, 2016.

[14] H. Dhulipati, K. L. V. Iyer, S. Mukundan, K. Mukherjee, J. Tjong, and N. C. Kar, "Investigation of 6–Phase Surface PM Machines with Concentrated Windings for Reduction in Space Harmonics, Leakage Inductance and Magnet Loss in Direct–Drive EV," in proc. of *XXIIth Int. Conf. on Elec. Machines*, pp. 811–817, 2016.

[15] P. C. Krause, O. Wasynczuk, and S. Sudhoff, *Analysis of Electric Machinery and Drive Systems*, Wiley–IEEE Press, 2002.

[16] R. Krishnan, Permanent Magnet Synchronous and Brushless DC Motor Drives, CRC Press, 2010, pp. 3–34.

[17] T. A. Lipo, *Introduction to AC Machine Design*, 3rd ed. Madison, WI, USA: Univ. Wisconsin–Madison, pp. 65, 70,79–80, 2009.

Chapter 5

Novel Coupled Electromagnetic and Thermal Model Incorporating Current Harmonics for PMSMs

5.1. Introduction

With advent in permanent magnet synchronous machine (PMSM) structure and inverter topologies, accurate parameter determination is of significance for high–performance control, analysis and making critical decisions on inter–dependent design parameter variations for machine optimization. However, the machine parameters including permanent magnet (PM) flux linkage and *dq*–axis inductances vary during operation with machine nonlinearities such as magnetic saturation, temperature rise, and introduction of spatial and time harmonic contents contributing towards inaccuracies during machine parameter determination resulting in inefficient motor operation [1] – [3]. Therefore, an accurate motor model which is computationally inexpensive and easier to implement is of prime importance. While classical *dq*–axis modeling fails to accommodate non–sinusoidal winding distributions [4] and effects of temperature rise [5], [6], finite element analysis is computationally expensive and coupling of electromagnetic and thermal analysis including current harmonics becomes complex [7]. Therefore, in this paper, a novel magnetic equivalent circuit (MEC) model incorporating effects of temperature rise and current harmonics has been developed for parameter determination of PMSMs. A lumped thermal model is implemented to determine the temperatures at each point of the machine. The proposed coupled electromagnetic and thermal model has been validated for various operating conditions of a high–speed, fractional–slot distributed wound (FSDW) traction PMSM available in the laboratory with finite element analysis (FEA) and experimental investigations.

5.2. Coupled Electromagnetic and Thermal Analysis of Fractional–Slot Wound PMSMs using Magnetic Equivalent Circuit

In order to study parameter variations due to electromagnetic nonlinearities such as magnetic saturation, flux leakage and slotting effects, a comprehensive magnetic equivalent circuit (MEC) model as illustrated in Fig. 5.1(a) is developed and implemented. In case of motor laminations including the stator core ($1/R_{sy}$), stator tooth ($1/R_{st}$) and rotor yoke ($1/R_{ry}$), the permeances estimated at every operating point are inherently non–linear and is a function of flux flowing through the element respectively. Thus, magnetic saturation in such regions can be represented in terms of the applied magnetic field intensity (H) as in [8]

$$\left.\begin{aligned} B_i &= f_{T_0}(H_i) \\ B_i &= \mu_0\left\{H_i + \left[M_s\left(\coth\left(\frac{H_i+\alpha M}{a}\right) - \left(\frac{a}{H_i - \alpha M}\right)\right)\right]\right\} \end{aligned}\right\} \tag{5.1}$$

where M_s is the saturation magnetization, α represents the intensity of inter–domain coupling and a is a material parameter controlling the shape of the magnetization curve. To solve such non–linear permeances, numerical methods are employed to estimate the flux at each node of MEC for every operating point.

Additionally, air–gap permeance modeling takes into account the stator slotting effect by only considering the overlapping region of the stator and rotor teeth along the entire circumferential position as in (5.4). Where w_{st} and w_{rt} are the stator and rotor tooth widths respectively, w_{so} is the stator slot opening, D_{si} is the stator inner diameter, D_{ro} is the rotor outer diameter, L_{st} is the stack length and δ is the effective air–gap length of the machine.

$$G_{ag} = \begin{cases} G_{\max}, & 0 \le \delta \le \delta_t' \ \mathit{and}\ 2\pi - \delta_t' \le \delta \le 2\pi \\ G_{\max}\dfrac{1+\cos\pi\dfrac{\delta-\delta_t'}{\delta_t-\delta_t'}}{2}, & \delta_t' \le \delta \le \delta_t \\ G_{\max}\dfrac{1+\cos\pi\dfrac{\delta-2\pi+\delta_t'}{\delta_t-\delta_t'}}{2}, & 2\pi-\delta_t \le \delta \le 2\pi-\delta_t' \\ 0, & \delta_t \le \delta \le 2\pi - \delta_t \end{cases} \tag{5.2}$$

$$G_{\max} = \mu_0 L_{st} w_{st}/\delta \tag{5.3}$$

$$\delta_t' = \frac{\left|w_{st}-w_{rt}\right|}{\left(D_{si}+D_{ro}\big/2\right)} \tag{5.4}$$

$$\delta_t = \frac{w_{st}+w_{rt}+w_{so}}{\left(D_{si}+D_{ro}\big/2\right)} \tag{5.5}$$

Further, the stator slot leakage ($R_{s\sigma}$) and rotor inter–pole leakage reluctances ($R_{r\sigma}$) are estimated and incorporated in the model based on the structural data of the PMSM. Moreover, the increase in air–gap permeance due to fringing flux is also determined using the coefficient of fringing flux (c_f) as [9]

$$
\left.\begin{aligned}
c_f &= G_f / G_{ag} \\
G_f &= \mu_0 \frac{L_{st} w_{so}}{\delta \ln\left(\dfrac{w_{st} + w_{so}}{w_{st}}\right)}
\end{aligned}\right\} \tag{5.6}
$$

Thus, all the machine electromagnetic nonlinearities are integrated within reluctance modeling of MEC itself. The effective magneto motive force (mmf) in the air–gap relates both the spatial harmonic contents of order n, resulting from winding distribution and the time harmonics of order k, produced by current excitations. Therefore, parameter variations due to the presence of harmonics can be modeled by using winding mmf as shown in (5.7) as the input to the developed MEC, where ω is the angular speed, m is the number of phases of the machine, τ_p is the pole pitch, T_p is the turns per pole, I_k is the peak current amplitude of k^{th} order in each phase and c_p is

$$
\begin{aligned}
F_{i,k,n}(\theta,t) = {} & \frac{F_{k,n}}{2}\cos\left(k\left[\omega t - (i-1)\frac{2\pi}{m}\right] - n\left[\frac{\pi}{\tau_p}\theta - (i-1)\frac{2\pi}{m}\right]\right) \\
& - \frac{F_{k,n}}{2}\cos\left(k\left[\omega t - (i-1)\frac{2\pi}{m}\right] + n\left[\frac{\pi}{\tau_p}\theta - (i-1)\frac{2\pi}{m}\right]\right)
\end{aligned} \tag{5.7}
$$

$$
F_{k,n} = \frac{4}{\pi}\frac{T_p I_k}{n}\sin\left(\frac{\pi n}{2}\right)\sin\left(\frac{\pi n c_p}{2\tau_p}\right) \tag{5.8}
$$

the coil pitch of the machine. Thus, the model can be implemented for non–sinusoidal winding distributions such as fractional slot winding configurations as well.

Consequently, after all the machine permeances (G), input winding mmf and PM fluxes are estimated, the effective air gap flux (ϕ) can be estimated as (5.9). Further, using node potential method, the magnetic potential (u) at each node and hence the fluxes flowing through each element can be calculated as

$$
\left.\begin{aligned}
\phi &= G_f \int_0^{\tau_p} F_{k,n}\, d\theta \\
[G][u] &= [\phi]
\end{aligned}\right\} \tag{5.9}
$$

Thus, using the estimated fluxes and magnetic potentials, the machine parameters can be calculated. The phase inductances (L_{ph}) can be calculated using the winding distribution as

$$\left.\begin{aligned} L_{ph} &= \frac{2L_{st}\mu_0}{\delta}\int\left(\frac{F_w}{I_k}\right)^2 d\theta \\ F_w &= \sum_{n=1}^{\infty} F_{k,n}\sin\left[\left(\frac{\pi n}{\tau_p}\theta\right)-\left(\frac{n\theta_e}{2}(q-1)\right)\right] \end{aligned}\right\} \tag{5.10}$$

where θ_e is the electrical angle occupied by each slot and q is the coils per phase. In order to obtain the dq–axis inductances, conventional transformation equations can be implemented [10]. The phase flux linkage (λ), the flux matrix obtained from (5.9) can be related to the turns per phase matrix (M_{tp}) as (5.11). The back–emf of the machine at a particular operating frequency (f), can be obtained using the flux linkage matrix.

$$\lambda = M_{tp}\phi \tag{5.11}$$

The machine parameters estimated using (5.10) and (5.11) includes all electromagnetic nonlinearities and effects of space and time harmonics. However, in order to include effects of temperature, it is of importance to detect the operating temperature at each load point and account for parameter variations thus incurred. Hence, a lumped parameter thermal network as illustrated in Fig. 5.1(b) is implemented. Using the machine fluxes and magnetic potentials obtained from (5.9), the machine losses at each node (Q) can be obtained, which are used as input to the thermal model. Depending upon the mode of heat transfer at each node of the machine, the thermal resistances (R_h) are estimated for conduction or convection. Heat transfer due to radiation is ignored for ease of computation. Thus, similar to the MEC, the temperature at each node, T, can be calculated using nodal analysis as

$$\left.\begin{aligned} [G_h][T] &= [Q] \\ G_h &= 1/R_h \end{aligned}\right\} \tag{5.12}$$

Further, to integrate increase in temperature, T, with the magnetic properties of the material, the magnetic permeability (μ) of the material and hence the magnetic reluctance of each part of the machine is updated using (5.13) – (5.15) [11]

$$\left.\begin{aligned} B_r(T) &= B_r(T_0)\chi_B(T) \\ H_c(T) &= H_c(T_0)\chi_H(T) \end{aligned}\right\} \tag{5.13}$$

$$\left.\begin{aligned} \chi_B(T) &= 1 + T(\alpha_1 + \alpha_2 T) - T_0(\alpha_1 + \alpha_2 T_0) - 2T\alpha_2 T_0 \\ \chi_H(T) &= 1 + T(\beta_1 + \beta_2 T) - T_0(\beta_1 + \beta_2 T_0) - 2T\beta_2 T_0 \end{aligned}\right\} \tag{5.14}$$

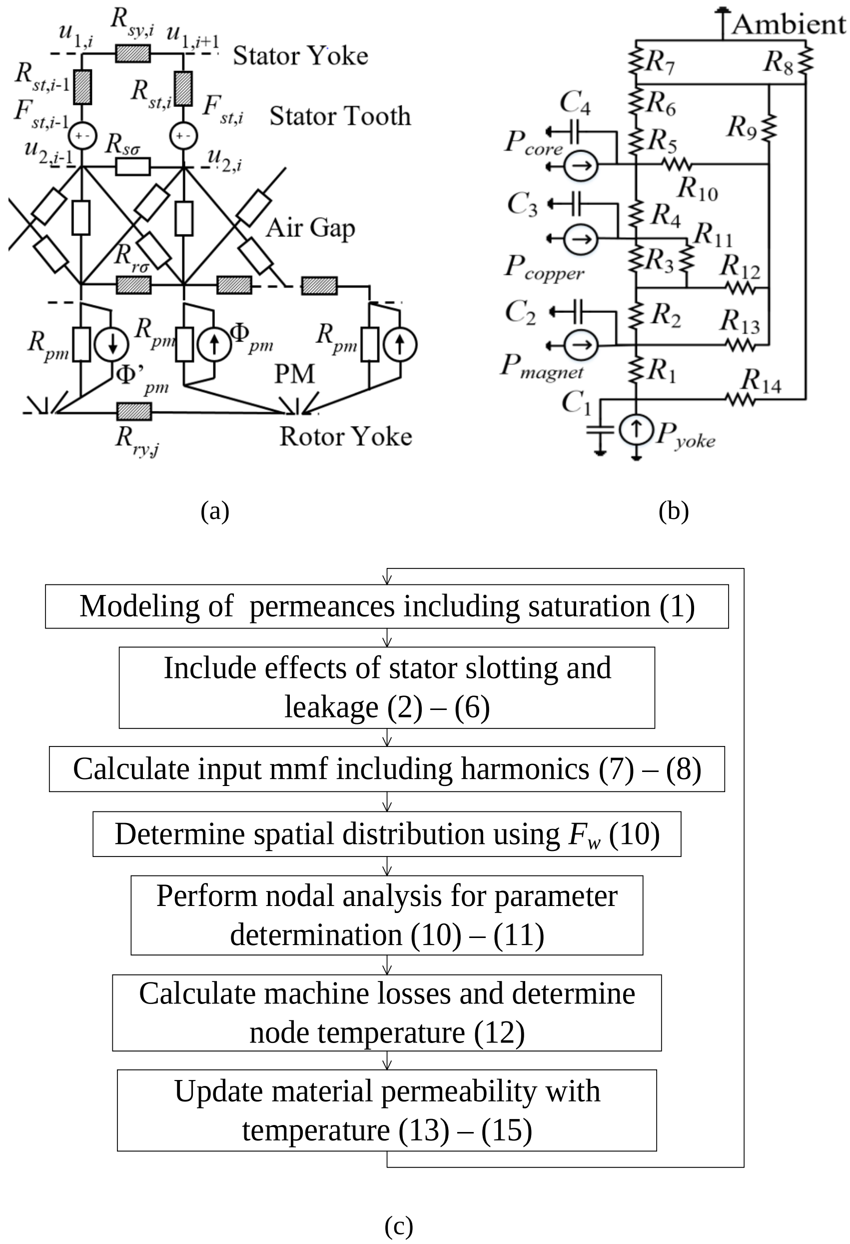

Fig. 5.1. Developed model for coupled electromagnetic and thermal analysis of PMSM. (a) Magnetic equivalent circuit. (b) Lumped thermal model. (c) Flowchart representing the overall procedure for parameter determination including all machine nonlinearities.

$$\left.\begin{aligned} B_i(H_i,T) &= f_{T_0}\left(H_i \Big/ \chi_H(T) \right)\chi_B(T) \\ \mu_r(T_0) &= \frac{1}{\mu_0} B_r(T_0) + 1 \\ \mu_r(T) &= \left(\frac{\chi_B(T)}{\chi_H(T)} \left[\mu_r(T_0) - 1 \right] \right) + 1 \end{aligned}\right\} \tag{5.15}$$

where B_r is the remnant flux density of the material, T_0 is the ambient temperature, α_1, α_2, β_1 and β_2 are material property dependent coefficients, B_i and H_i are the intrinsic operating point on the BH–curve and μ_r is the relative permeability of the material. Hence, for every operating temperature obtained from the thermal model, a complete electromagnetic analysis using MEC as shown from (5.1) – (5.11) must be performed iteratively to obtain a coupled thermal and electromagnetic analysis of the machine under investigation. The developed iterative procedure using the model is illustrated in Fig. 5.1(c) and the parameters thus obtained will include effects of all machine nonlinearities. Using the machine parameters estimated from the model, the electromagnetic torque (T_e) can be calculated from [12]

$$T_{e,\max} = \frac{3p}{4}\left[\lambda_m i_q + \left(L_d - L_q\right) i_d i_q\right] \tag{5.16}$$

5.3. Validation of Proposed Magnetic Equivalent Circuit Model Using FEA and Experimental Investigations

In order to verify the proposed model, a 27–slot, 6–pole, 45 kW fractional–slot distributed wound traction IPMSM existing in the laboratory is taken up for investigation. A laboratory electric powertrain tester with a 130 kW dynamometer was used to run the motor. RT–lab controller along with an IGBT inverter were implemented to perform a field–oriented current control of the traction motor. The complete experimental setup used for experimental investigations is shown in Fig. 5.2. Further, to validate the proposed analytical model, an electromagnetic model of the traction IPMSM was developed and analyzed using FEA. It can be observed from Fig. 5.3 that the no–load induced voltage at the machine's rated speed of 3,000 rpm

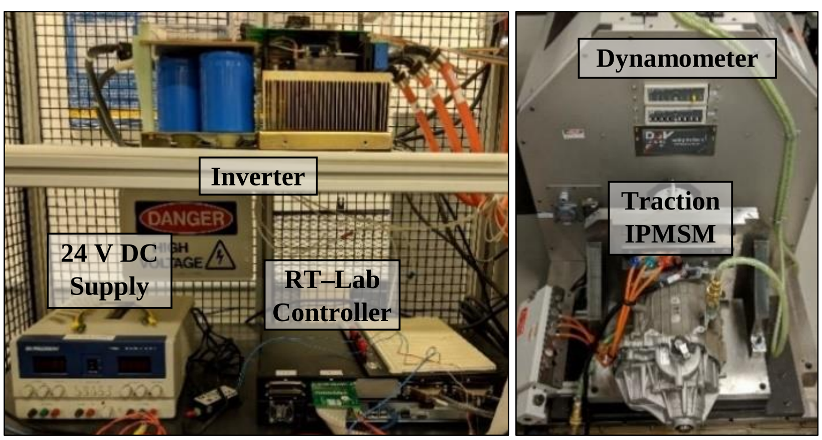

(a) (b)

Fig. 5.2. Laboratory traction IPMSM used for experimental investigation. (a) Field–oriented current control using RT–lab and IGBT inverter. (b) Traction IPMSM coupled to laboratory electric powertrain tester dynamometer.

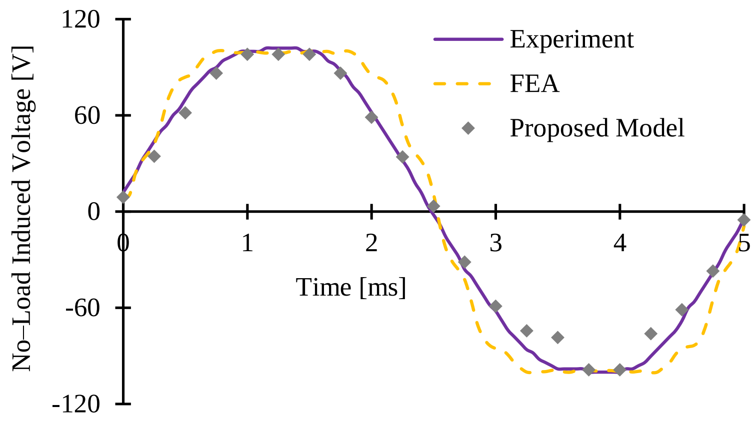

(a)

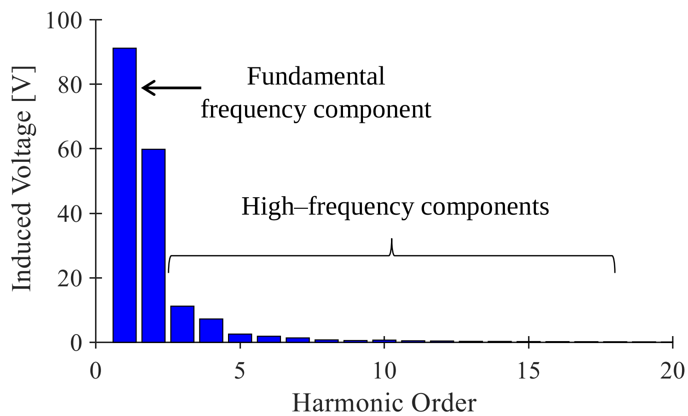

(b)

Fig. 5.3. Comparative analysis of no–load induced voltage of laboratory IPMSM at rated speed of 3,000 rpm and room temperature. (a) Voltage waveform. (b) Harmonic spectrum based on winding distribution.

obtained from back–emf test, FEA and the proposed analytical model are in close agreement. The corresponding harmonic spectrum denotes the spatial harmonic distribution due to the winding configuration of the machine. As seen from Fig. 5.3(b), due to odd slot number and fractional–slot winding, all high frequency components are cancelled and only fifth order component is present. The fundamental component is close to the peak voltage value observed in Fig. 5.3(a). In the proposed model, these harmonics will be modeled using the winding function as denoted in (5.10).

In order to understand the variation of machine parameters namely PM flux linkage (λ_{pm}), d– and q–axis inductances (L_d, L_q), analysis was done at varying load conditions and increasing operating temperatures. Initially, λ_{pm} was analyzed and since, under loading conditions, the flux linkage is the effective air–gap flux linkage, only 3 points were observed and indicated in Fig. 5.4. Clearly, with increasing load, the effective flux linkage will increase to produce useful torque. In order to observe λ_{pm} variation with winding temperature, the machine was loaded at a particular

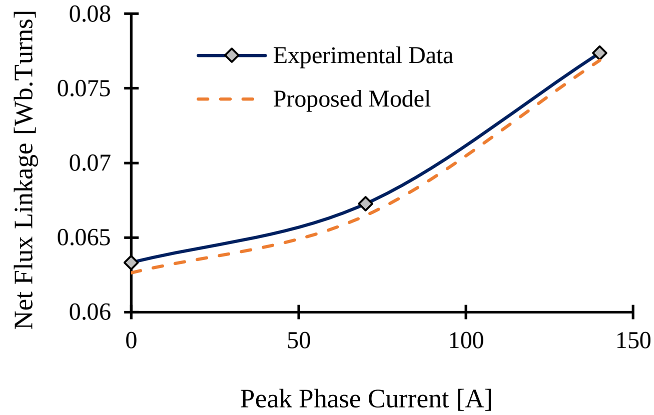

(a)

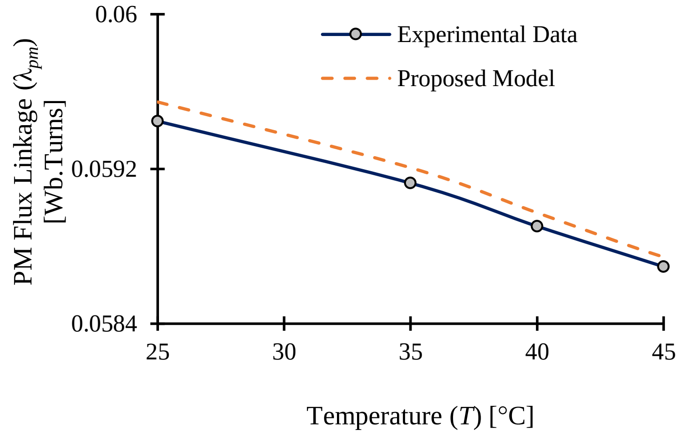

(b)

Fig. 5.4. Variation of PM flux linkage at 3,000 rpm. (a) With increasing load. (b) With increasing temperature.

condition, in this case, 40 Nm at 3,000 rpm and the temperature was deliberately allowed to increase by switching off the coolant supply. Once, the desired temperature at the stator windings was observed, the load to the system was shut off and the back emf waveforms were noted. Figs. 5.4(a) and (b) illustrate close agreement in data obtained from experimental analysis and the analytical model highlighting the accuracy of the estimated parameters. A deterioration of phase flux linkage with increase in temperature can be observed due to demagnetization of PM flux. In case of λ_{pm}, the accuracy observed is more obvious because MEC directly takes into account the material properties for calculation of flux and hence any minor change in operating condition is directly reflected. Since, the induced emf can be obtained as a derivative of the flux linkage, the profile will be the same.

Similarly, the variation of inductances at various loading conditions at the rated speed was observed. The peak currents were increased up to 140 A peak and the phase inductances were calculated using (5.10). The input current harmonics of order 6*k* observed in the experiment were incorporated in the model using (5.7). Knowing the current control angle, the phase inductances were transformed to L_d and L_q in the proposed model. As the current increases, the inductances tend to reduce and saturate. The comparative analysis of results obtained from experiments and the proposed model are shown in Figs. 5.5(a) and (b). The average difference between experimental and calculated data are 0.22 μH and 0.33 μH respectively for L_d and L_q. The slightly higher variation in L_q can be attributed to the current angle since *q*–axis current is the torque–producing component, in practical conditions, it is more prone to current harmonic variation. On the other hand, variation of inductances with temperature is shown in Fig. 5.6. Since L_d lies along the flux path of the magnet, the inductance values tend to remain constant till relatively higher temperatures and then tends to deteriorate as observed in Fig. 5.6. A deviation of 0.38 μH and 0.25 μH from experimental data was observed in L_q and L_d respectively. Although higher deviations

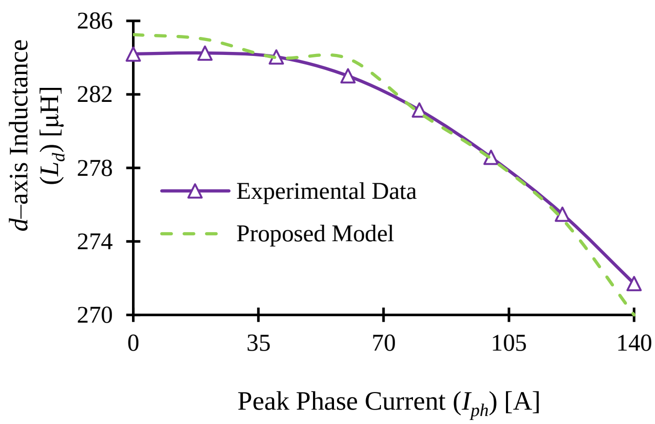

(a)

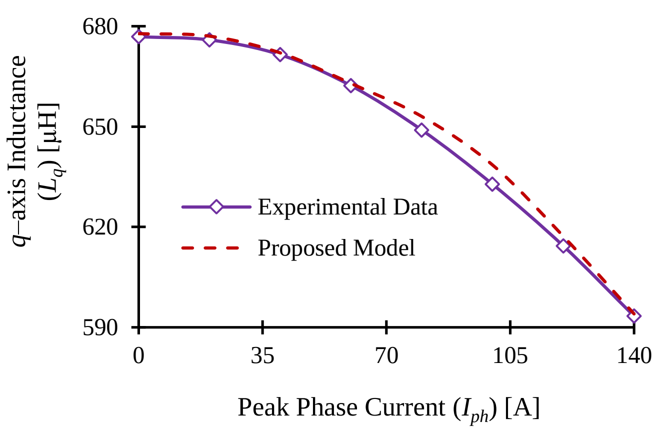

(b)

Fig. 5.5. Variation of inductances with current. (a) L_d. (b) L_q.

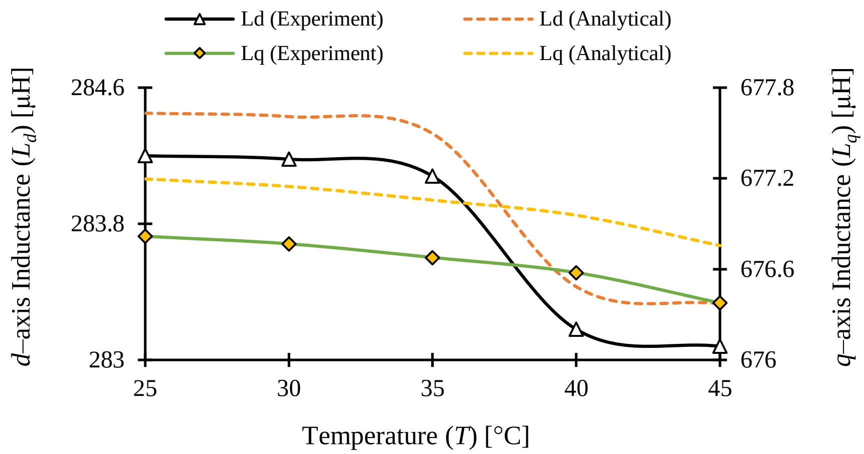

Fig. 5.6. Variation of inductances with temperature.

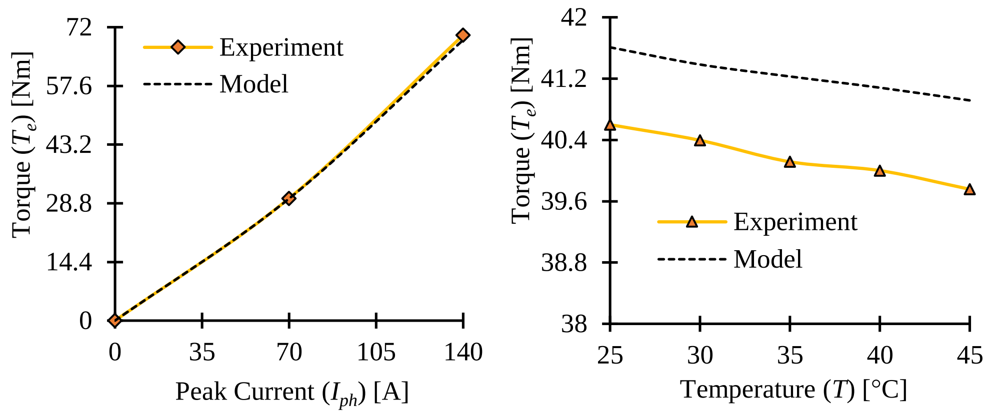

(a) (b)

Fig. 5.7. Variation of electromagnetic torque at 3,000 rpm. (a) With increasing load. (b) With increasing temperature for an input current of 95 A.

from experimental and calculated data are observed at higher temperatures, the model is still within the acceptable range. Further, using the parameters obtained, T_e was estimated and compared with experimental data as shown in Fig. 5.7. It can be seen that although the torque obtained from the analytical model at varying loads is close to the experimental data, under varying temperature conditions there are some discrepancies. An average percentage error of 2.6% was observed. Although the percentage error is minimum, it can be avoided if detailed and accurate information about the material properties were obtained. Thus, the proposed model can be applied for both machine development as well as performance evaluation of a PMSM.

5.4. Conclusions

In this chapter, a coupled electromagnetic and thermal model employing magnetic equivalent circuit (MEC) model capable of incorporating parameter variations due to all machine nonlinearities, temperature effects and harmonic contents was developed and validated for a laboratory traction IPMSM. The model can be applied to PMSMs with non–sinusoidal winding also. The major advantage of the proposed model is that, it can be universally applied to design and analyze even multiphase machines, low speed and high speed motors incorporating innovative materials for the required performance objective. Thus, using the proposed model, accurate modeling and control of motor drive system can be implemented. Further, using the proposed model, critical decisions on inter–dependent design parameter variations for machine optimization can be made. Thus, in the subsequent chapters, using the proposed analytical model, an optimal rotor structure for the selected stator winding configuration will be developed for improved torque density, reduced magnet volume, improved rated efficiency and extended operating range.

5.5. References

[1] K. L. V. Iyer, S. Mukundan, H. Dhulipati, K. Mukherjee, B. Minaker and N. C. Kar, "Design Considerations for Permanent Magnet Machine Drives for Direct–Drive Electric Vehicles," in proc. of *IEEE International Electric Machines & Drives Conference (IEMDC)*, Coeur d'Alene, ID, pp. 1170–1176, 2015.

[2] Q. Wang, S. Niu, and X. Luo, "A novel hybrid dual–PM machine excited by AC with DC bias for electric vehicle propulsion," *IEEE Trans. Ind. Electron.*, vol. 64, pp. 6908–6919, 2017.

[3] Q. Wang, S. Niu, and S. Yang, "Design optimization and comparative study of novel magnetic–geared permanent magnet machines," *IEEE Trans. Magn.*, vol. 53, pp. 1–4, 2017.

[4] C. Lai, G. Feng, K. Mukherjee and N. C. Kar, "Investigations of the Influence of PMSM Parameter Variations in Optimal Stator Current Design for Torque Ripple Minimization," *IEEE Transactions on Energy Conversion*, vol. 32, no. 3, pp. 1052–1062, Sept. 2017.

[5] P. Kakosimos, M. Beniakar, Y. Liu and H. Abu–Rub, "Model Predictive Control for Permanent Magnet Synchronous Motor Drives Considering Cross–Saturation Effects," in proc. of *IEEE Applied Power Electronics Conference and Exposition (APEC)*, Tampa, FL, pp. 1880–1885, 2017.

[6] X. Chen, J. Hu, K. Chen, and Z. Peng, "Modeling of electromagnetic torque considering saturation and magnetic field harmonics in permanent magnet synchronous motor for HEV," *Simul. Model. Pract. Theory*, vol. 66, pp. 212–225, Aug. 2016.

[7] G. Feng, C. Lai and N. C. Kar, "A Novel Current Injection–Based Online Parameter Estimation Method for PMSMs Considering Magnetic Saturation," *IEEE Transactions on Magnetics*, vol. 52, no. 7, pp. 1–4, July 2016.

[8] V. Ostovic, *Computer–aided Analysis Electric Machines: A Mathematica Approach*, New York, Prentuce Hall International Limited, 1994.

[9] V. Ostovic, *Dynamics of Saturated Electric Machines*, New York, Springer–Verlag, 1989.

[10] T. A. Lipo, *Introduction to AC Machine Design*, 3rd ed. Madison, WI, USA: Univ. Wisconsin–Madison, pp. 65, 70,79–80, 2009.

[11] M Rosu, et. al., *Multiphysics Simulation by Design for Electrical Machines, Power Electronics and Drives*, Wiley–IEEE Press, 2018.

[12] M. Fasil, C. Antaloae, N. Mijatovic, B. B. Jensen and J. Holboll, "Improved *dq*–Axes Model of PMSM Considering Airgap Flux Harmonics and Saturation," *IEEE Transactions on Applied Superconductivity*, vol. 26, no. 4, pp. 1–5, June 2016.
[13] P. C. Krause, O. Wasynczuk, and S. Sudhoff, *Analysis of Electric Machinery and Drive Systems*, Wiley–IEEE Press, 2002.
[14] M. Rottach, C. Gerada, T. Hamiti and P. W. Wheeler, "A Computationally Efficient Design Procedure for Actuator Motors Using Magnetic Reluctance–and Thermal Resistance Network Models," in proc. of *XXth International Conference on Electrical Machines*, Marseille, pp. 2526–2532, 2012.
[15] A. Hemeida and P. Sergeant, "Analytical Modeling of Surface PMSM Using a Combined Solution of Maxwell–s Equations and Magnetic Equivalent Circuit," *IEEE Transactions on Magnetics*, vol. 50, no. 12, pp. 1–13, Dec. 2014.
[16] L. Dang, N. Bernard, N. Bracikowski and G. Berthiau, "Analytical model and reluctance network for high–speed PMSM design optimization application to electric vehicles," in proc. of *XXII International Conference on Electrical Machines (ICEM)*, Lausanne, 2016, pp. 1359–1365.
[17] B. Nedjar, L. Vido, S. Hlioui, Y. Amara and M. Gabsi, "Hybrid coupling: Magnetic equivalent circuit coupled to finite element analysis for PMSM electromagnetic modeling," in proc. of *IEEE International Symposium on Industrial Electronics*, Hangzhou, 2012, pp. 858–862.
[18] A. Fatemi, N. A. O. Demerdash, D. M. Ionel, and T. W. Nehl, "Large–scale electromagnetic design optimization of PM machines over a target operating cycle," in proc. of *IEEE Energy Conversion Congress and Exposition (ECCE)*, Montreal, QC, 2015, pp. 4383–4390.
[19] S. J. Galioto, P. B. Reddy, A. M. EL–Refaie and J. P. Alexander, "Effect of Magnet Types on Performance of High–Speed Spoke Interior–Permanent–Magnet Machines Designed for Traction Applications," *IEEE Transactions on Industry Applications*, vol. 51, no. 3, pp. 2148–2160, May–June 2015.
[20] A. Athavale, K. Sasaki, B. S. Gagas, T. Kato and R. D. Lorenz, "Variable Flux Permanent Magnet Synchronous Machine (VF–PMSM) Design Methodologies to Meet Electric Vehicle Traction Requirements with Reduced Losses," *IEEE Transactions on Industry Applications*, vol. 53, no. 5, pp. 4318–4326, Sept.–Oct. 2017.
[21] Y. Zhang, W. Cao, S. McLoone and J. Morrow, "Design and Flux–Weakening Control of an Interior Permanent Magnet Synchronous Motor for Electric Vehicles," *IEEE Transactions on Applied Superconductivity*, vol. 26, no. 7, pp. 1–6, Oct. 2016.

Chapter 6

Pareto ACO Based Optimal Design of Hybrid IPM Rotor for Improved Torque Density and Extended Speed Range

6.1. Introduction

Based on the analysis performed in Chapter 4, it can be observed that star–delta windings are widely implemented towards reduction of space harmonics in fractional–slot wound permanent magnet synchronous machines (PMSMs). However, existing literature is limited to topologies with near sinusoidal rotor magneto motive force (MMF) distribution such as induction machines and surface mounted PMSMs, thereby limiting the machine's torque capability and maximum operating speed making them unsuitable for high–speed application [1] – [3]. While analysis of multi–phase fractional–slot interior PMSMs (IPMSMs) have been conducted [4], [5], according to the authors knowledge, no studies have been performed on the IPMSM rotor design for star–delta winding configuration. Unlike surface PMSMs, IPMSM rotors have non–sinusoidal magneto motive force (MMF) distribution and hence result in some additional harmonics in the air–gap. Thus, accurate modeling of the rotor structure is imperative such that the MMF harmonic orders from the rotor aid the stator winding harmonics towards useful torque production. Therefore, in an effort to maximize the torque density and extend the operating speed range, this chapter presents a coupled winding function and magnetic circuit based modeling of IPMSM for star–delta winding configuration. The stator configuration is modeled using winding function considering stator slotting effects for minimum spatial harmonic contents. The magnetic equivalent circuit model elaborated in Chapter 5, considering all machine non–linearities is implemented to obtain the baseline salient rotor topology which exploits the stator space harmonics for high torque density. However, to obtain maximum saliency and extended operating range, the *d*– and *q*–axis flux paths including the magnet area and flux barrier area must be optimized. Consequently, a Pareto Ant Colony optimization (ACO) is implemented to obtain the optimal rotor structure for the star–delta winding configuration. Comprehensive performance analysis in terms of torque and power–speed characteristics over entire operating range, machine losses, saliency and overall spatial harmonic contents of the optimized machine will be presented.

6.2. Winding Function Based Modeling of Star–Delta Windings for Reduced Space Harmonics

For a series connected star–delta winding topology as seen in Fig. 6.1(a) with fractional–slot windings, having S stator slots and p poles, the slot per pole per phase, Q can be represented as a simple fraction. The denominator, d and the numerator, M are the number of poles and stator slots per phase respectively in one unit the machine can be symmetrically divided into, referred to as the base unit. Thus, for an m–phase machine, the total number of slots in the base unit contributing towards 180° of an electrical cycle will be mM [6].

$$Q = S/mp = M/d \tag{6.1}$$

Further, to obtain equally balanced m–phase voltages, the windings must be symmetrically distributed in each unit across the entire machine. This condition is satisfied only if for any integral value of C, D is a positive integer given by

$$D = \frac{1 + mMC}{d};\ C \in 1,2,\ldots\infty \tag{6.2}$$

From Fig. 6.1(b), it is seen that the configuration is similar to a 6–phase configuration with the winding sets displaced by 30°. Therefore, existing literature restricts the slot numbers of star–delta windings to multiples of 6. However, the overall machine is still operated as a 3–phase machine and hence, this chapter presents a generalized approach to implement unconventional odd slot numbers which are multiples of 3 resulting in further reduced MMF harmonics and torque ripple.

The total number of coils per phase in a unit, $q = M$, must be distributed as q_Y and q_Δ for the star and delta winding sets, respectively. The corresponding n^{th} harmonic winding factors including the stator slotting effect can be obtained as follows:

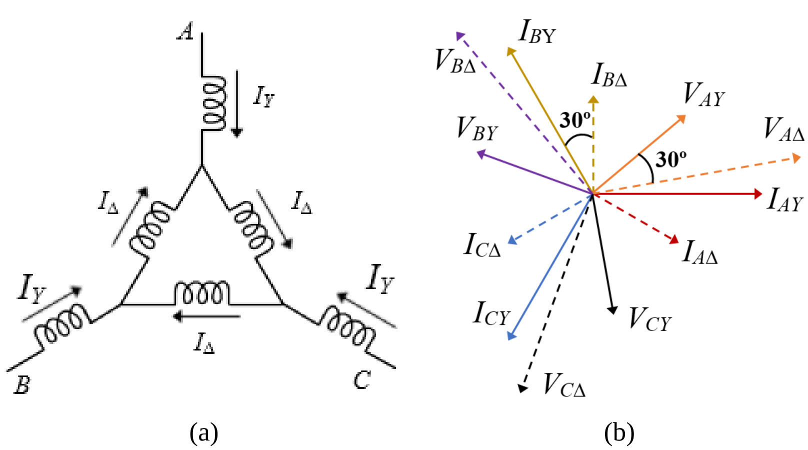

Fig. 6.1. Combined star–delta winding configuration. (a) Star–delta winding sets. (b) Phasor diagram emulating a multiphase topology.

$$k_{wn} = k_{dn} k_{pn} k_{\chi n} \tag{6.3}$$

$$k_{wnY} = \frac{\dfrac{T_{cY}}{a_Y} \sin\left(\dfrac{n\pi q_Y}{2mM}\right)}{\dfrac{q_Y T_{cY}}{a_Y} \sin\left(\dfrac{n\pi}{2mM}\right)} \cos\left(\frac{n\pi N_Y}{mM}\right) \frac{\sin(n\chi_Y/2)}{n\chi_Y/2} \tag{6.4}$$

$$k_{dn\Delta} = \frac{\dfrac{T_{c\Delta}}{a_\Delta} \sin\left(\dfrac{n\pi q_\Delta}{2mM}\right)}{\dfrac{q_\Delta T_{c\Delta}}{a_\Delta} \sin\left(\dfrac{n\pi}{2mM}\right)} \cos\left(\frac{n\pi N_\Delta}{mM}\right) \frac{\sin(n\chi_\Delta/2)}{n\chi_\Delta/2} \tag{6.5}$$

where T_c is the turns per coil, a is the number of parallel paths, k_{dn} is the distribution factor, k_{pn} is the pitch factor, N is the number of slots by which the windings are chorded, k_χ is the slot opening factor and χ is the slot opening angle and the subscripts Y and Δ indicate the star and delta winding sets, respectively. The harmonic orders of the winding factors are always odd orders where the fundamental torque producing component is $n = p/2$ and slot harmonic orders (n_s) as in (6.6) have the same magnitude of k_w as the fundamental order [7].

$$n_s = (2j\,S/p) \pm 1, \quad j = 1,2.3\cdots \tag{6.6}$$

It can be observed from (6.3)–(6.5) that, the star and delta winding sets have 5 degrees of freedom namely, T_c, q, a, N and χ which can be modified individually to reduce one specific harmonic order and obtain a balanced 3–phase system. Thus, the effective winding factor can be written as in (6.7).

$$k_{wnY\Delta} = k_{dnY} k_{pnY} k_{\chi nY} + k_{dn\Delta} k_{pn\Delta} k_{\chi n\Delta} \tag{6.7}$$

The primary objective is to obtain maximum fundamental winding factor and minimize all higher order harmonic winding factors for better induced voltage waveform quality.

The exact coil distribution between winding sets is obtained from the MMF distribution modeled using the winding function. Winding function is a graphical representation of conductor distribution of a phase winding spread across the air gap circumference, θ_r for a base unit [8]

$$T_c(\theta_r) = t_c(\theta_r) - \{t_c(\theta_r)\} \tag{6.8}$$

where $t_c(\theta_r)$ is the turn's function which defines the turns enclosed by a flux path within a coil span and $\{t_c(\theta_r)\}$ is the average value of the turns function. Using Fourier series expansion of the winding function, for any slot–pole combination, the per phase stator MMF distribution can be obtained. Thus, for a balanced m–phase system, the current excitations with k time harmonic orders are given by

$$I(t)=\sum_{i=1}^{m}\sum_{k=1}^{\infty} I_k \sin k\left(\omega t-(i-1)\frac{2\pi}{m}\right) \tag{6.9}$$

where, I_k is the peak phase supply current, ω is the electrical supply angular frequency and t is the time period. Thus, from the winding function and the input current excitation, the per phase MMF distribution along the stator circumference with n^{th} spatial harmonic order for a 3–phase configuration is given by

$$\Im(\theta,t)=\sum_{i=1}^{m}\sum_{k=1}^{\infty}\sum_{n=1}^{\infty}\left[\begin{array}{l}\Im_{k,n} \sin k\left(\omega t-(i-1)\frac{2\pi}{m}\right)\\ \sin n\left(\frac{d}{2}\theta-(i-1)\frac{2\pi}{m}\right)\end{array}\right] \tag{6.10}$$

$$\Im_{k,n}=\frac{4}{\pi}\frac{qT_c I_k}{nd} k_{wn} \sin\left(\frac{n\pi}{M}\right) \tag{6.11}$$

It is known that the ratio of magnitudes of currents in the delta and the star winding set is √3. Thus, to get a balanced system, the coil distribution can be modeled as (6.12) to obtain equal MMF in both the star and delta winding sets. Thereafter, (6.10) and (6.11) can be modified to obtain the effective per phase MMF of the star–delta connected windings as

$$\frac{q_Y T_{cY}}{a_Y}=\frac{q_\Delta T_{c\Delta}}{\sqrt{3}a_\Delta} \tag{6.12}$$

$$\Im_Y(\theta,t)=\sum_{i=1}^{m}\sum_{k=1}^{\infty}\sum_{n=1}^{\infty}\left[\begin{array}{l}\Im_{k,n,Y} \sin k\left(\omega t-(i-1)\frac{2\pi}{m}\right)\\ \sin n\left(\frac{d}{2}\theta-(i-1)\frac{2\pi}{m}\right)\end{array}\right] \tag{6.13}$$

$$\Im_\Delta(\theta,t)=\sum_{i=1}^{m}\sum_{k=1}^{\infty}\sum_{n=1}^{\infty}\left[\begin{array}{l}\Im_{k,n,\Delta} \sin k\left(\omega t-(i-1)\frac{2\pi}{m}-\phi_\Delta\right)\\ \sin n\left(\frac{d}{2}\theta-(i-1)\frac{2\pi}{m}\right)\end{array}\right] \tag{6.14}$$

$$\left.\begin{array}{l}\Im_{k,n,Y}=\frac{4}{\pi}\frac{q_Y T_{cY} I_k}{nd} k_{wnY} \sin\left(\frac{n\pi}{M}\right)\\ \Im_{k,n,\Delta}=\frac{4}{\pi}\frac{q_\Delta T_{c\Delta} I_k}{\sqrt{3}nd} k_{wn\Delta} \sin\left(\frac{n\pi}{M}\right)\end{array}\right\} \tag{6.15}$$

$$\Im_{Y\Delta}(\theta,t)=\Im_Y(\theta,t)+\Im_\Delta(\theta,t) \tag{6.16}$$

The positive and negative sequence components of the MMF for the i^{th} phase, k^{th} and n^{th} time and spatial harmonic orders respectively can be obtained by rearranging (6.10) as

$$\left.\begin{aligned}\Im_{i,k,n}(\theta,t) &= \frac{\Im_{k,n}}{2}\cos\left\{k\left(\omega t-(i-1)\frac{2\pi}{m}\right)-n\left(\frac{d}{2}\theta-(i-1)\frac{2\pi}{m}\right)\right\}\\ &\quad -\frac{\Im_{k,n}}{2}\cos\left\{k\left(\omega t-(i-1)\frac{2\pi}{m}\right)+n\left(\frac{d}{2}\theta-(i-1)\frac{2\pi}{m}\right)\right\}\\ &= \frac{\Im_{k,n}}{2}\cos\left\{k\omega t-n\frac{d}{2}\theta-(i-1)\frac{k-n}{m}2\pi\right\}\\ &\quad -\frac{\Im_{k,n}}{2}\cos\left\{k\omega t+n\frac{d}{2}\theta-(i-1)\frac{k+n}{m}2\pi\right\}\end{aligned}\right\} \tag{6.17}$$

where the first term in (6.17) indicates the positive sequence component and the second term is the negative sequence component of the stator MMF. For a balanced system, the net stator MMF must be zero and hence, the positive and negative sequence components within each phase must be 180º out of phase. This occurs only when

$$\frac{k\pm n}{m}\in Z \tag{6.18}$$

For a fundamental time harmonic component and a 3–phase system, the above condition is satisfied only when $n = 6j \pm 1$, $j = 0, 1, 2, ..\infty$. Using trigonometric identities, it can be proven that, similarly, for a star–delta winding with a fundamental current harmonic order, the spatial harmonic order satisfies the same condition provided $\phi_\Delta = \pi/6$. The generalized expression is

$$n=\begin{cases}\dfrac{j\pi}{\phi_\Delta}\mp 1, & j=1,3,5\cdots\infty\\[2ex] \dfrac{2j\pi}{\phi_\Delta}\mp 1, & j=1,2,3\cdots\infty\end{cases} \tag{6.19}$$

Thus, in order to eliminate the n^{th} order spatial harmonic component, the above condition must be satisfied. Correspondingly, the harmonic winding factor in (6.7) reduces and the fundamental component increases resulting in improved waveform quality denoted by total harmonic distortion (THD) in (6.20). Further, since the parasitic harmonics are minimized, the unit current required to produce rated torque also reduces, thereby reducing the effective machine copper losses.

$$THD=\frac{\sqrt{\sum_{h=1,3,..}^{\infty}k_{wh}^{2}/h}}{k_{w1}} \tag{6.20}$$

TABLE 6.1
PROPOSED MACHINE STRUCTURAL AND PERFORMANCE DETAILS

Target Torque	70 Nm	Coils/phase	13
Target Base Speed	3,000 rpm	Stator Diameter	195 mm
Slots (S)	39	Stack Length	75 mm
Poles (p)	16	Rotor Diameter	133 mm
DC Bus Voltage	400 V DC	Rated Current	78 A
q_Y	7	q_Δ	6
T_{cY}	4	$T_{c\Delta}$	8
$k_{wY\Delta}$	0.9888	THD	1.28

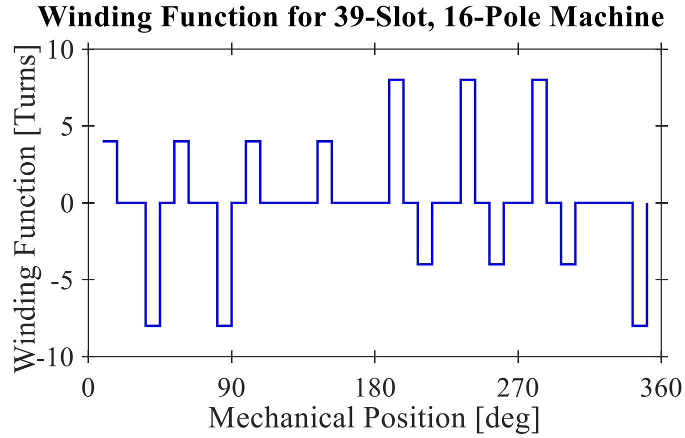

Fig. 6.2. Winding function obtained for the proposed 39–slot, 16–pole machine with star–delta winding configuration.

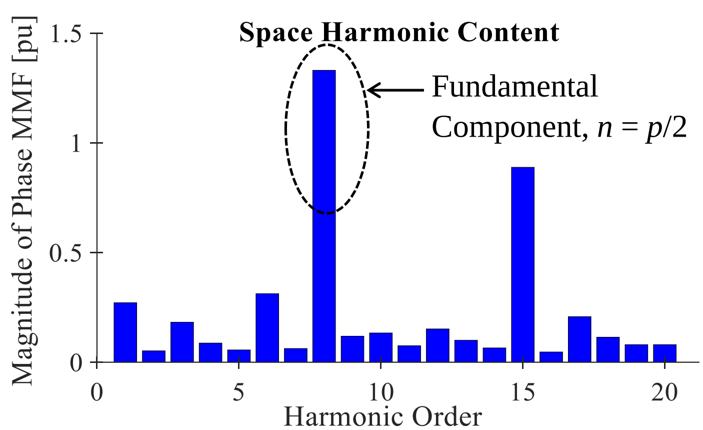

Fig. 6.3. MMF spectrum analysis obtained for the proposed 39–slot, 16–pole machine with star–delta winding configuration.

Using the proposed approach, a novel 39–slot, 16–pole traction PMSM is designed for a laboratory–scale specifications indicated in Table 6.1. The coil distribution and winding details are also highlighted in the table. The winding function obtained for the 39–slot, 16–pole star–delta wound machine is indicated in Fig. 6.2 and the corresponding winding MMF harmonics is illustrated in Fig. 6.3. Since the machine has an even pole pair, certain even order MMF harmonic orders can be observed. However, due to the odd slot number, the magnitudes of all the harmonic orders are significantly reduced. Using (6.19), it can be seen that the 5th and 7th order harmonics are significantly low, aiding to torque ripple minimization. Thus, the design of a salient rotor is taken up to utilize the stator winding harmonics and further maximize the torque production.

6.3. Magnetic Equivalent Circuit Model Based Design of Salient Rotor Considering Machine Non–linarites

The machine parameters contributing to torque production depend on both the winding function and rotor flux distribution. Conventional machine modeling techniques assume the rotor flux density to be either a sinusoidal or trapezoidal function [9], [10] resulting in inaccurate torque computation. However, this chapter implements a comprehensive magnetic equivalent circuit model considering all machine non–linearities such as magnetic saturation, flux leakage and slotting effects to design the salient rotor structure and compute the torque capability accurately. Thus, for the structural details indicated in Table 6.1, the model was developed as shown in Fig. 6.4 for the base unit of the machine. The machine structure is assigned 5 nodes as seen in the figure, namely, the stator yoke, stator tooth, air gap, permanent magnets (PMs), and rotor yoke for analysis. Further, using the node potential method, for known machine permeances, *G*, input winding MMF and flux sources, the magnetic potential, *u* at each node and hence the effective torque–producing flux component can be calculated as

$$[G][u] = [\varphi] \tag{6.21}$$

The stator tooth flux, φ_{st} is obtained from the tooth MMF, F_{st} which is dictated by the winding function, modeled in the previous section and the phase currents. Thus, a MMF transform matrix, w'', correlating the phase currents with the magnetic equivalent circuit model is developed as

$$\left.\begin{aligned} F_{st} &= w''i \\ w'' &= M_{tmmf}^{-1} I'_{k,k} M_{sat} M_{tc} M_{cc} \end{aligned}\right\} \tag{6.22}$$

where *i* is a column matrix of the order *m* and has the details of the phase currents in the machine. To convert the phase currents to individual coil currents in each phase relating to the winding function, the coil current matrix M_{cc} of the order mMxm is obtained. Furthermore, the turn details of each coil in each phase for both the star and delta winding sets as indicated in Fig. 6.2 is represented in matrix form through M_{tc}. Subsequently, using the coil currents and the obtained turns per coil, the individual tooth MMF, M_{tmmf} is estimated using the slot ampere–turns matrix, M_{sat}. Therefore, the winding transform matrix, w'' provides all the details of a given winding

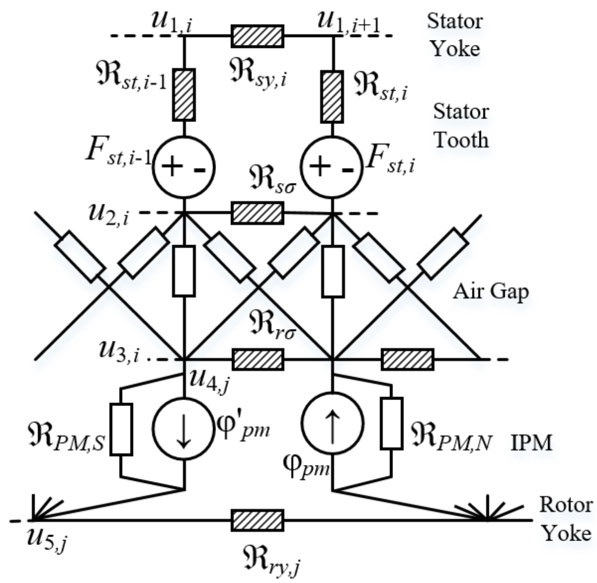

Fig. 6.4. Developed magnetic equivalent circuit model for design of salient rotor considering all machine non–linearities.

structure by relating the phase currents with the stator tooth MMF.

Similarly, the flux transform matrix, w', is developed to give a direct connection between the stator phase fluxes, φ_s and tooth fluxes, φ_{st} as shown in (6.23)

$$\left.\begin{aligned} \varphi_s &= w'\varphi_t \\ w' &= M_{tp}^{-1} M_{pf} M_{cf} \end{aligned}\right\} \tag{6.23}$$

where, the coil flux matrix, M_{cf} relates the individual tooth fluxes with the coil fluxes. The phase flux matrix, M_{pf} provides information from the winding function as to which coils form a particular phase and the winding topology using the turns per phase matrix, M_{tp}. Thus, both (6.22) and (6.23) are used to solve the system of equations obtained from the magnetic equivalent circuit and hence calculate the resultant torque producing air gap flux waveform and its harmonic components.

In this thesis, v–shaped IPM rotor topology is considered as the baseline due to its high saliency and torque capability [11]. Thus, each embedded PM pole is partitioned into j number of segments to accurately obtain the air gap flux waveform. From the material properties (μ_r) and inherent remnant flux density, B_r, the PM flux, $\varphi_{pm,r}$ for a particular magnet volume can be estimated. Hence, from the rotor side, j constant flux sources will contribute towards the air gap flux density. Depending on the magnet volume, the PM reluctance, $\Re_{PM}$ varies and directly affects the air gap flux waveform. The incorporation of machine non–linearities in the model has been previously reported by the author in [12]. Hence, after modeling the physical structure, for known winding MMF and PM fluxes, the effective air gap flux is estimated from (6.21).

$$\left.\begin{aligned}\varphi_{pm,j} &= \frac{2p}{j}\varphi_{pm,r} \\ \varphi_{pm,r} &= \frac{B_r l_{mag}}{\mu_r \Re_{PM}}\end{aligned}\right\} \tag{6.24}$$

Thus, the effect of the non–sinusoidal MMF distribution from the fractional–slot windings are taken into account by w''. Furthermore, the variable reluctance function obtained from the magnetic circuit model attributes for the non–sinusoidal PM flux density from the salient rotor. Thus, the effective torque equation for the IPM salient rotor is written as [13]

$$T_e(\theta_r) = \frac{3p}{4}\left[\lambda_{pm}(\theta_r)i_q + \left(L_d(\theta_r) - L_q(\theta_r)\right)i_d i_q\right] \tag{6.25}$$

Where the flux linkage waveform is estimated as a result of both the winding function, T_c and the PM flux density, B_{pm} as [14]

$$\lambda_{pm}(\theta_r) = \frac{D_g L_{st} k_{wY\Delta}}{2}\int_0^{2\pi} T_c(\theta_r) B_{pm}(\theta_r) d\theta_r \tag{6.26}$$

where D_g is the effective diameter along the air gap and L_{st} is the machine's active length. Further, using Park's transformation matrix, k [15], the dq–axis inductances, L_d and L_q can be obtained from the self–inductance, L_{ph} and mutual inductances, M_{ph}, as

$$L_{ph} = \frac{3\mu_0 \pi D_g L_{st}}{4 l_g}\int_0^{2\pi} T_{c,a}^2(\theta_r)\Re(\theta_r) d\theta_r \tag{6.27}$$

$$M_{ph} = \frac{3\mu_0 \pi D_g L_{st}}{4 l_g}\int_0^{2\pi} T_{c,a}(\theta_r) T_{c,b}(\theta_r)\Re(\theta_r) d\theta_r \tag{6.28}$$

$$\begin{bmatrix} L_d \\ L_q \end{bmatrix} = k\begin{bmatrix} L_{ph} & M_{ph} & M_{ph} \\ M_{ph} & L_{ph} & M_{ph} \\ M_{ph} & M_{ph} & L_{ph}\end{bmatrix}k^T \tag{6.29}$$

Where $T_{c,a}$ and $T_{c.b}$ are the winding functions of phases a and b, respectively, μ_0 is the absolute permeability, l_g is the effective air gap length and $\Re$ is the effective reluctance function of the flux path with respect to rotor position obtained from the developed magnetic circuit model which includes reluctances from all the nodes indicated in Fig. 6.4. Further, from Fourier transformation of the B_{pm} waveform, the rotor spatial harmonic contents can be obtained. Additionally, the characteristic current, I_{ch}, obtained from λ_{pm}/L_d, defines the constant power region of a PMSM [16]. Thus, by modifying the machine structure, magnet volume and orientation, the corresponding rotor space harmonics, machine parameters and hence the torque production and operating range can be modeled as seen from (6.25)–(6.29).

Thus, using the above model and the proposed star–delta winding configuration, the electromagnetic model of a baseline machine as shown in Fig. 6.5 was developed. The rotor flux density waveform obtained from the model and the corresponding rotor space harmonics obtained are illustrated in Figs. 6.6(a) and (b), respectively. Fig. 6.6(a) shows that the flux density values obtained from the analytical magnetic circuit model and finite element analysis (FEA) are in close agreement. The L_{ph} waveform for phase *a* and the M_{ph} waveform between phases *a* and *b* are shown in Fig. 6.7(a) and hence, the torque waveform obtained is shown in Fig. 6.7(b). The corresponding L_d, L_q and average torque values obtained from the machine along with structural and material details implemented are summarized in Table 6.2.

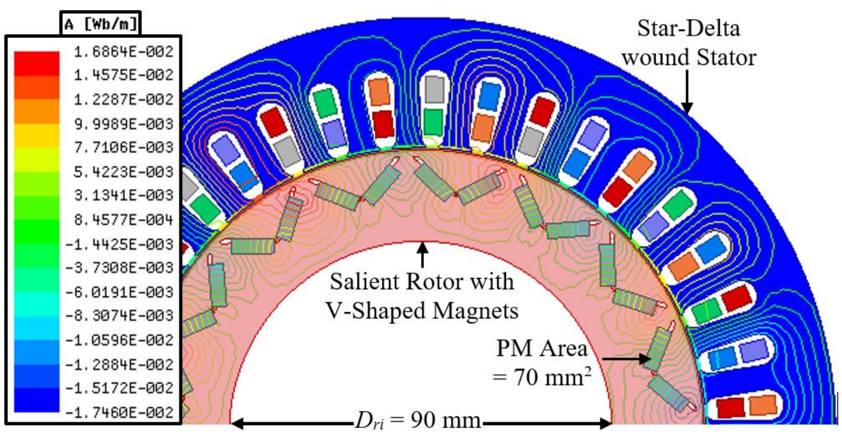

Fig. 6.5. Electromagnetic model of the developed baseline machine with IPM rotor and star–delta winding at rated condition of 78 Arms/phase and 3,000 rpm.

TABLE 6.2
BASELINE MACHINE STRUCTURAL AND PERFORMANCE DETAILS

Electric Steel	M19 29G	PM	NdFeB
Magnet Width	20 mm	Magnet Height	3.5 mm
Shaft Diameter	75 mm	Air Gap Length	1 mm
Average Torque	70.2 Nm	Torque Ripple	9.4 %
L_d	459 µH	L_q	634 µH
λ_{pm}	44 mWb.Turns	Active Weight	12.64 kg

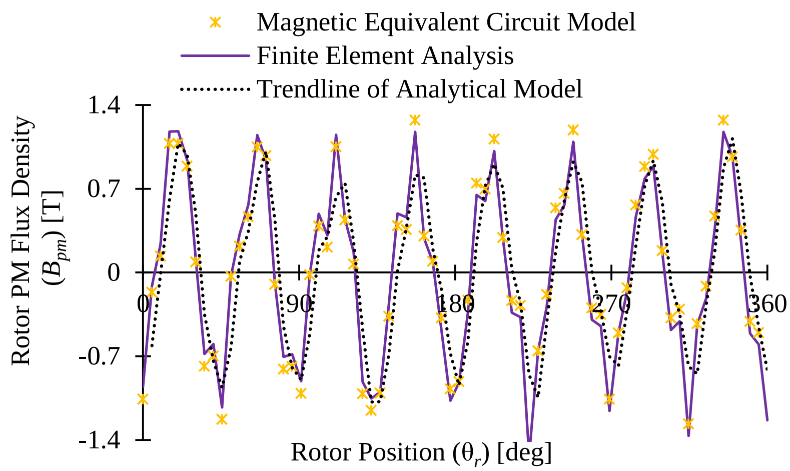

(a)

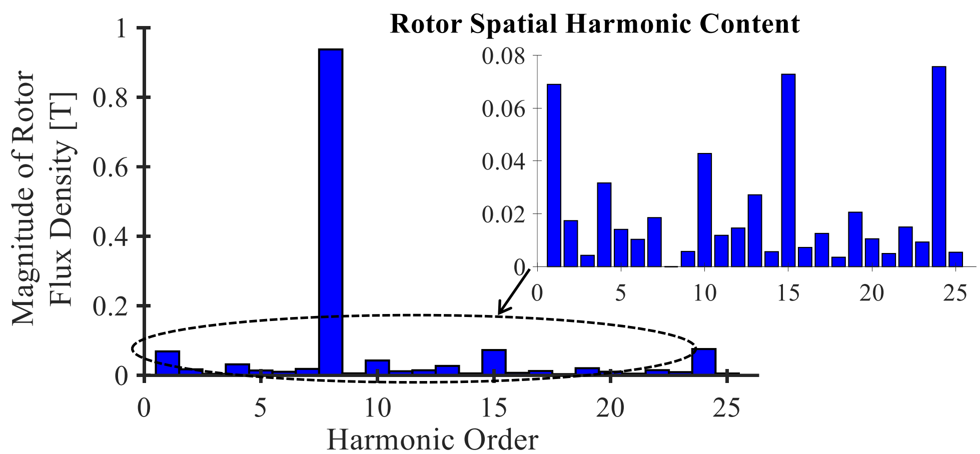

(b)

Fig. 6.6. Rotor flux density obtained from the proposed magnetic equivalent circuit model and FEA at rated condition of 78 Arms/phase and 3,000 rpm. (a) B_{pm} with respect to rotor position. (b) Rotor spatial harmonic contents.

On comparison of Figs. 6.3 and .6.6(b), it can be observed that almost all harmonic orders of both the stator MMF and rotor flux density space harmonics are along the same direction contributing towards effective torque production. However, from Table 6.2, it can be seen that although the machine is capable of achieving the set targets, the saliency ratio (L_q/L_d) is only 1.38 with a high torque ripple of 9.4%. Further, the torque density of the machine is limited to 5.55 Nm/kg which can be improved by reducing the unutilized rotor steel weight as seen from the flux path in Fig. 6.5. Further, the machine's operating range is also restricted as I_{ch} obtained is lower than the rated current. Therefore, this calls for an optimization technique to design the effective *d*– and *q*–axis flux paths in the salient rotor for improved torque density, minimum torque ripple and thereby, also result in improved operating range of the machine.

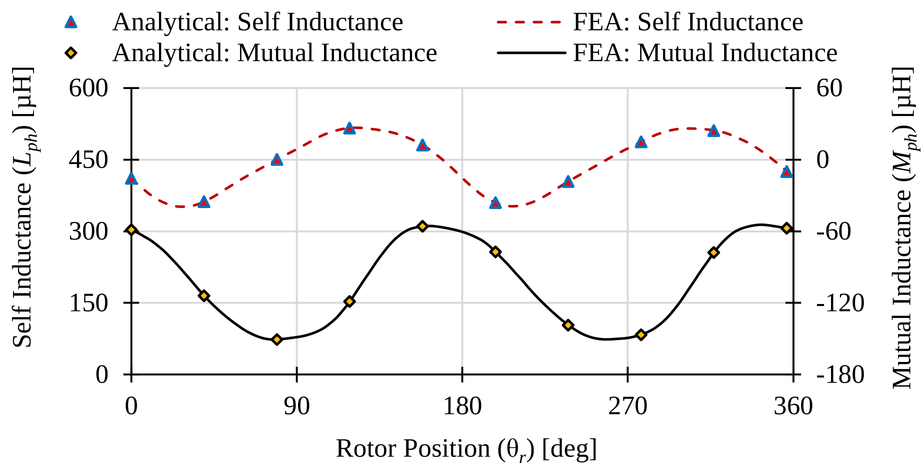

(a)

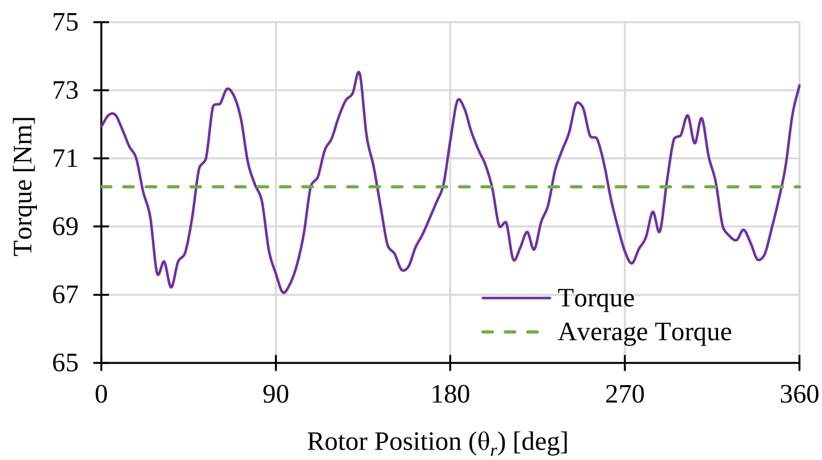

(b)

Fig. 6.7. Performance characteristics of the baseline machine at rated conditions of 78 Arms/phase and 3,000 rpm obtained from the magnetic circuit model. (a) Self and mutual inductance waveforms. (b) Instantaneous torque waveform.

6.4. Pareto ACO Based Optimal Design of Salient IPM Rotor with Star–Delta Windings

A. Criteria for Rotor Design Optimization

The baseline machine in the previous section has undesirable characteristics such as high torque ripple, relatively low torque density and low I_{ch}, restricting the operating range. Therefore, flux barriers along the d–axis flux path are introduced to reduce L_d and hence improve saliency and torque density. However, this may result in either introduction or minimization of rotor spatial harmonic orders which may not aid the stator spatial harmonic orders for torque production. In that case, to compensate for torque reduction, if the magnet volume is increased, L_d and L_q increase, leading to reduction of machine saliency. Further, while introduction of flux barriers results in reduction of torque ripple, modification of the machine parameters could affect the machine's

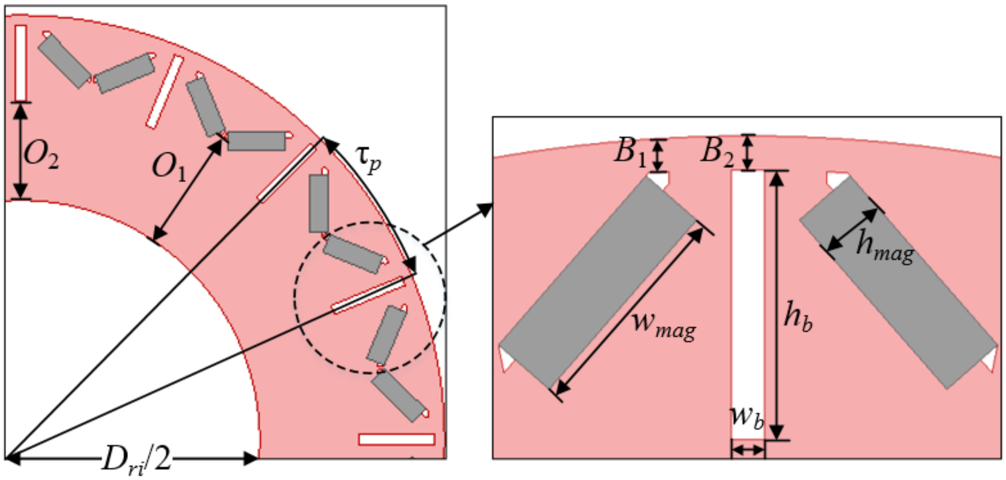

Fig. 6.8. Design variables used for optimizing the IPMSM rotor structure.

operating range. Thus, to satisfy all the design targets, the best solution would be to optimize the reluctance function, $\Re(\theta_r)$, and individually design the d– and q–axis flux paths including the flux barriers. In order to obtain accurate results and reduce the complexity, only the rotor reluctances in $\Re(\theta_r)$ will be considered for optimization. Thus, considering all the design challenges highlighted, the multi–objective optimization can be summarized as: i) maximize torque density (f_1); ii) maximize machine saliency (f_2); and iii) minimize torque ripple (f_3).

For the baseline machine in Fig. 6.5, the winding topology, stator structure and rotor outer diameter are kept constant. A spoke shaped flux barrier is used to reduce torque ripple in the machine [17]. Thus, including the shaft diameter, magnet dimensions, placement and flux barrier area, a total of 10 rotor structural parameters influencing each of the objectives are taken as the design variables as indicated in Fig. 6.8. The major constraints include obtaining the required rotor spatial harmonic orders, maintaining the I_{ch} close to the rated current to maximize the operating range, and avoiding magnetic saturation of the rotor core material. Thus, subject to these constraints, the overall objective function can be obtained as

$$\left.\begin{aligned} f_1 &= \frac{\max\{T_e(\theta_r)\}}{\min\{g(A)\}} \\ &= \frac{\max\left\{\frac{3p}{4}\left[\lambda_{pm}(\theta_r)i_q + \left(L_d(\theta_r) - L_q(\theta_r)\right)i_d i_q\right]\right\}}{\min\left\{\vartheta_{mag}A_{mag} + \vartheta_{rotor}A_{rotor} + \vartheta_b A_b\right\}} \end{aligned}\right\} \tag{6.30}$$

$$f_2 = \max\{L_q - L_d\} \tag{6.31}$$

$$f_3 = \min\left\{\frac{T_{e,average}(\theta_r)}{T_{e,\max}(\theta_r) - T_{e,\min}(\theta_r)}\right\} \tag{6.32}$$

$$f = \sum_{n=1}^{N} p_n f_n(\upsilon) \tag{6.33}$$

$$\upsilon = \Re(\theta_r) = g\left(D_{ri}, \tau_p, w_{mag}, h_{mag}, w_b, h_b, O_1, O_2, B_1, B_2\right) \tag{6.34}$$

where all the objective functions, f, are a function of the design variable vector, υ, p is the prior weight of each objective function, A_{mag}, A_{rotor} and A_b are the areas of the magnet, rotor steel and flux barrier, respectively and similarly, ϑ is a material dependent constant for each area.

B. Pareto Ant Colony based Multiple Objective Optimization

Pareto ant colony optimization is a population–based metaheuristic technique suitable for multi–objective optimization [18], [19]. This technique is preferred over other metaheuristic methods such as genetic algorithm and simulated annealing methods due to the following merits [20], [21]: i) ease of implementation and better performance; ii) capable of handling multiple objectives with constraints; and iii) applicable to dynamic problems where additional heuristic information is included. Thus, for the range of design variables in Table 6.3, pareto ACO is implemented to select the optimal design solution while the magnetic equivalent circuit is used to evaluate each objective function for the design candidates.

The overall optimization procedure is illustrated in Fig. 6.9. First, the star–delta winding distribution is modeled using (6.3)–(6.20). Using the design variable range in Table 6.3, an initial design population, S_1 is created within the feasible solution space. For each design candidate, x, each of the individual objectives is estimated using the magnetic circuit model and the overall objective function as in (6.33) is calculated. Contrary to other metaheuristic algorithms, pareto ACO constructs the design population using a probabilistic technique based on the pheromone factor, η and a heuristic attractiveness factor, κ. Thus, the probability of a design candidate x_j to be included in the population after x_i, can be represented as

$$P(x_j) = \frac{\kappa_j^{\alpha} \eta_j^{\beta}}{\sum_{i \in S} \kappa_i^{\alpha} \eta_i^{\beta}} \tag{6.35}$$

where α and β are parameters to control the influence of κ_i and η_i, respectively. The probability is based on obtaining the maximum aggregate value of pheromone and heuristic attractiveness

TABLE 6.3
OPTIMIZATION DESIGN VARIABLE RANGE

D_{ri} [mm]	80 – 100	h_b [mm]	1 – 3
τ_p [mm]	20 – 26	O_1 [mm]	3 – 15
w_{mag} [mm]	15 – 23	O_2 [mm]	1 – 15
h_{mag} [mm]	2 – 5	B_1 [mm]	0.5 – 2
w_b [mm]	10 – 20	B_2 [mm]	0.5 – 2

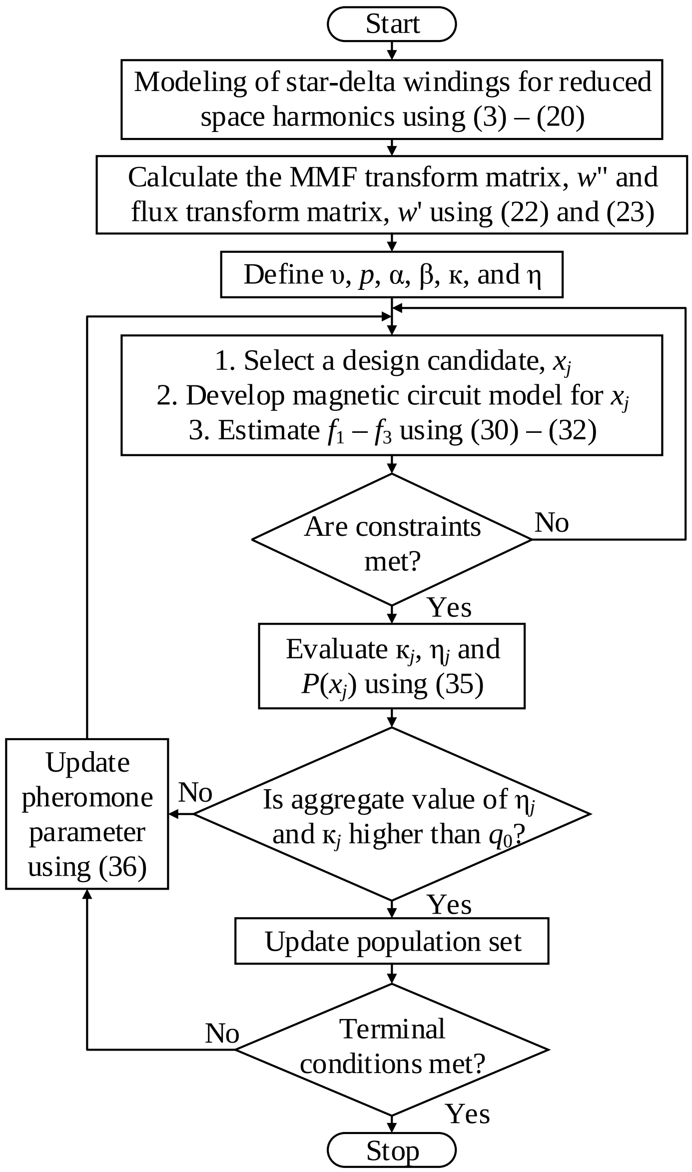

Fig. 6.9. Pareto ACO design procedure to obtain the optimal IPMSM for improved torque density and reduced space harmonics.

compared to a preset value q_0. After the design population is constructed, the feasibility and efficiency of the overall population is determined. Based on the best and second best candidates, the population is updated. When a design candidate, x_i is selected in the updated population, the associated pheromone information, κ is rationalized as

$$\kappa_i = (1-\rho)\kappa_i + \Delta\kappa_{i,j} \tag{6.36}$$

where ρ is the pheromone evaporation rate, $\Delta\kappa_{i,j}$ is the aggregate value of pheromone deposited between the design candidates *i* and *j*. Thus, on successive iteration, pareto ACO results in optimal design candidate selection. The terminal conditions set for the individual objectives are up to 6.5 Nm/kg for f_1, maximum of 200 μH for f_2 and less than 5% for f_3. An iteration limit of 1,500 is set in case of no feasible design candidate.

C. Performance Analysis of Optimally Designed IPMSM

The *d*– and *q*–axis of the optimized IPMSM rotor structure obtained from the proposed procedure is shown in Fig. 6.10. The figure also indicates that the machine is well within the saturation limits at rated conditions. The structural parameters of the optimized machine are presented in Table 6.4. It was observed that the rotor harmonic orders were all along the same direction as that of the stator MMF harmonic orders since it is set as one of the major constraints of the optimization procedure. The torque–speed and power–speed characteristics over the entire speed range for both the baseline and optimal machines are illustrated in Fig. 6.11. While the torque producing capability of the machine increased by 1.6 Nm, the rotor inner diameter, D_{ri}, increased from 90 mm to 100 mm, significantly reducing the rotor yoke steel and hence, the active weight of the machine by 1.07 kg compared to the baseline machine.

On the other hand, because of the introduction of flux barriers in the *d*–axis, the machine saliency increased from 175 to 198 μH through f_2. Due to increase in saliency and reduction of

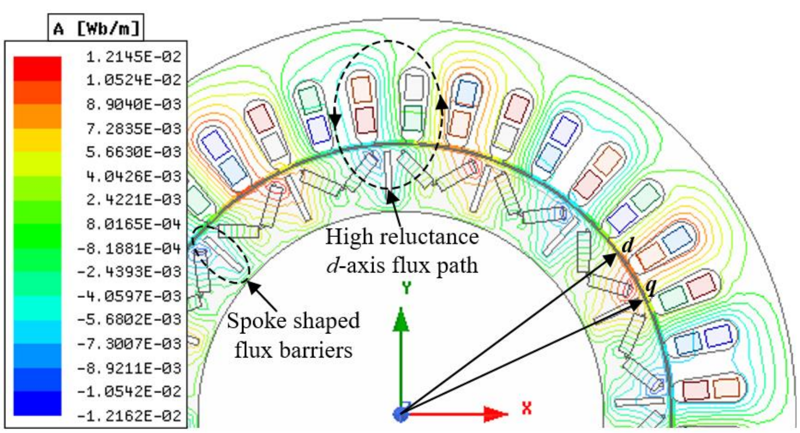

Fig. 6.10. Flux map of the optimized IPMSM with star–delta windings for improved torque density and reduced space harmonics at rated conditions.

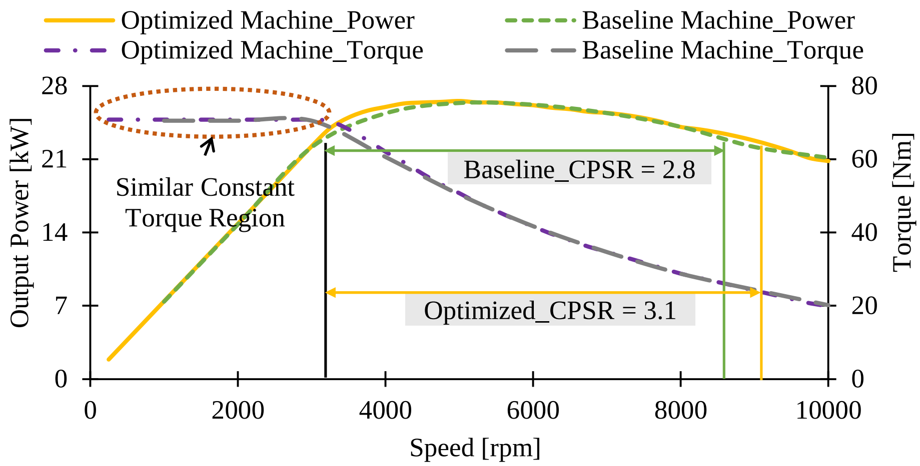

Fig. 6.11. Comparative analysis of the torque–speed and power–speed characteristics of the baseline and optimized machine over entire speed range.

active weight, the torque density increased from 5.5 Nm/kg to 6.1 Nm/kg through f_1. Further, the magnet volume required to produce the rated torque reduced by 14.3%, reducing the PM flux linkage minimally by 0.3 mWb.turns. Thus, from Fig. 6.11, it is seen that for almost the same PM flux linkage and reduced L_d, I_{ch} increased from 67.8 A to 72 A, thereby improving the constant power speed range (CPSR) and hence the overall operating range. Table 6.5 summarizes the machine performance details at the rated operating conditions. The torque ripple of the machine has significantly reduced from 9.4% to 2.4% highlighting the effectiveness of the flux barrier. Moreover, the rated efficiency of the machine is 96.3% as seen in Fig. 6.12 making it ideal for traction application. The rated efficiency of the optimized machine is 0.3% higher than that of the baseline machine since the core losses decreased by 60.9 W due to reduction of effective rotor steel. Therefore, it can be concluded that through optimal design of salient rotor utilizing the

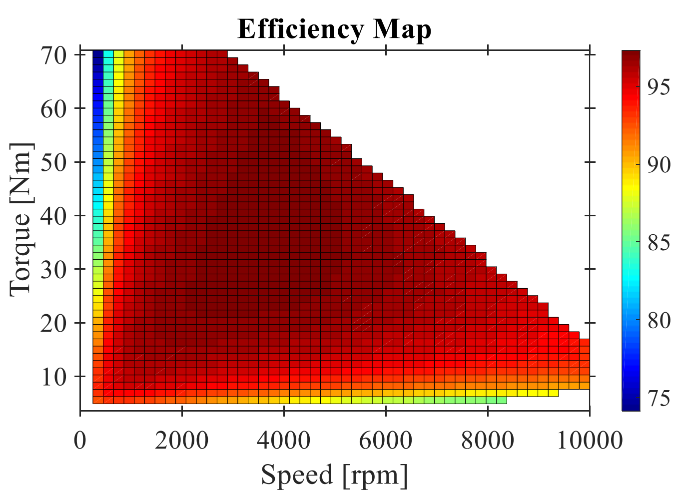

Fig. 6.12. Efficiency map of the optimized machine over entire operating range.

TABLE 6.4
STRUCTURAL DETAILS OF THE OPTIMIZED IPMSM

Parameter	Baseline	Optimized	Parameter	Baseline	Optimized
D_{ri} [mm]	90	100	w_{mag} [mm]	20	20
τ_p [mm]	23.37	25.8	h_{mag} [mm]	3.5	3
B_1 [mm]	1	1.5	O_1 [mm]	11	7
w_b [mm]	0	12	h_b [mm]	0	1.5
O_2 [mm]	0	3	B_2 [mm]	0	1.5

TABLE 6.5
PERFORMANCE DETAILS OF THE OPTIMIZED IPMSM

Torque	71.1 Nm	Voltage	200 V
Torque Ripple	2.4%	Current	78 A
L_d	434 μH	L_q	632 μH
Total Losses	0.85 kW	Magnet Loss	8.6 W
Core Loss	0.19 kW	Copper Loss	0.64 kW
Rated Efficiency	96.3%	CPSR	3.25

harmonics of the star–delta windings, improved torque density over an extended operating range can be achieved.

6.5. Conclusions

This chapter proposes a pareto ACO based design procedure to develop an optimal salient rotor structure for star–delta winding configuration for improved torque density, reduced space harmonics and extended operating range. Winding function is used to model the stator configuration and a magnetic equivalent circuit model is used to design the rotor capable of utilizing the stator space harmonics towards useful torque. It was seen that while the design obtained results in the required torque production, the machine has limited operating range, low torque density and high torque ripple. Thus, spoke type flux barriers were introduced to improve the machine saliency and hence, the operating range. Further, pareto ACO was used to obtain the optimal rotor structure. It was found that the reluctance torque increased and the rotor steel and magnet requirement reduced, resulting in cost savings and improved torque density. Further, introduction of flux barriers led to minimized torque ripple and extended operating range. Thus, using the proposed design procedure, an IPMSM with star–delta windings can be developed for traction application.

6.6. References

[1] Y. Lei *et. al*., "Design and Analysis of Star–Delta Hybrid Windings for High–Voltage Induction Motors," *IEEE Transactions on Industrial Electronics*, vol. 58, no. 9, pp. 3758–3767, Sept. 2011.

[2] X. Chen and J. Wang, "Magneto motive Force Harmonic Reduction Techniques for Fractional–Slot Non–Overlapping Winding Configurations in Permanent–Magnet Synchronous Machines," *Chinese Journal of Elec. Eng.*, vol. 3, no. 2, pp. 102–113, 2017.

[3] O. Misir, S. M. Raziee, N. Hammouche, C. Klaus, R. Kluge, and B. Ponick, "Prediction of Losses and Efficiency for Three–Phase Induction Machines Equipped with Combined Star–Delta Windings," *IEEE Trans. on Industry Applications*, vol. 53, pp. 3579–3587, Aug. 2017.

[4] A. S. Abdel–Khalik, S. Ahmed, and A. Massoud, "Application of Stator Shifting to Five–Phase Fractional–Slot Concentrated Winding Interior Permanent Magnet Synchronous Machine," *IET Electric Power Applications*, vol. 10, no. 7, pp. 681–690, Aug. 2016.

[5] C. Jedryczka *et. al*., "Multiphase Permanent Magnet Synchronous Motors with Fractional Slot Windings: The Future of Low Speed Drives?," *Int. Journal of Computation and Mathematics in Electrical and Electronic Engineering*, vol. 35, no. 6, pp. 1937 – 1948, 2016.

[6] S. Bandyopadhyay *et. al*., "Design Optimization of High Performance Fractional–Slot Distributed Winding PM Synchronous Machines for In–Wheel Application in Electric Vehicles," in proc. of *8th IET International Conference on Power Electronics, Machines and Drives*, Glasgow, 2016.

[7] V. Ostovic, *Dynamics of Saturated Electric Machines*, New York, Springer–Verlag, 1989.

[8] H. Dhulipati, K. L. V. Iyer, S. Mukundan, K. Mukherjee, J. Tjong, and N. C. Kar, "Investigation of 6–Phase Surface PM Machines with Concentrated Windings for Reduction in Space Harmonics, Leakage Inductance and Magnet Loss in Direct–Drive EV," in proc. of *XXIIth Int. Conf. on Elec. Machines*, pp. 811–817, 2016.

[9] R. Krishnan, *Permanent Magnet Synchronous and Brushless DC Motor Drives*, CRC Press, pp. 3–34, 2010.

[10] M. Farshadnia *et. al*., "Detailed Analytical Modeling of Fractional–Slot Concentrated–Wound Interior Permanent Magnet Machines for Prediction of Torque Ripple," *IEEE Transactions on Industry Applications*, vol. 53, no. 6, pp. 5272–5283, Nov.–Dec. 2017.

[11] C. Zhou *et. al*., "Comparison of PMSMs with Different Rotor Structures for EV Application," in proc. of *XIIIth Int. Conf. on Elec. Machines*, pp. 609–614, 2018.

[12] S. Mukundan, H. Dhulipati, J. Tjong and N. C. Kar, "Parameter Determination of PMSM Using Coupled Electromagnetic and Thermal Model Incorporating Current Harmonics," *IEEE Trans. on Magnetics*, vol. 54, no. 11, pp. 1–5, Nov. 2018.

[13] J. R. Hendershot Jr. and T. J. E. Miller, *Design of Brushless Permanent Magnet Motors*, Magna Physics Publishing and Clarendon Press, Oxford, pp. 3.12–3.15, 1994.

[14] T. A. Lipo, *Introduction to AC Machine Design*, 3rd ed. Madison, WI, USA: Univ. Wisconsin–Madison, pp. 65, 70,79–80, 2009.

[15] P. C. Krause, O. Wasynczuk, and S. Sudhoff, *Analysis of Electric Machinery and Drive Systems*, Wiley–IEEE Press, 2002.

[16] S. Mukundan, K. L. V. Iyer, H. Dhulipati, K. Mukherjee, J. Tjong and N. C. Kar, "Response Surface Methodology Based Optimization of Surface PM Machine Incorporating Stator Slotting and PM Sizing Effects to Extend the Operating Limits for Direct–Drive EV Application," in proc. of *XXIIth International Conference on Electrical Machines (ICEM)*, Lausanne, 2016, pp. 2045–2051.

[17] K. Y. Hwang *et. al.*, "A Study on Optimal Pole Design of Spoke–Type IPMSM with Concentrated Winding for Reducing the Torque Ripple by Experiment Design Method," *IEEE Trans. on Magnetics*, vol. 45, no. 10, pp. 4712–4715, Oct. 2009.
[18] M. Dorigo and T. Stutzle, *Ant Colony Optimization*, Cambridge, MA, MIT Press, 2004.
[19] D. Angus and C. Woodward, "Multiple Objective Ant Colony Optimization," *Swarm Intelligence*, vol. 3, no. 1, pp. 69 – 85, 2009.
[20] S. Chebli *et. al*., "Ant Colony Optimization Based on Pareto Optimality: Application to a Congested Router Controlled by PID Regulation," *Sys. Science and Control Eng.*, vol. 6, no. 1, pp. 360 – 369, Aug. 2018.
[21] K. Doerner *et. al.*, "Pareto Ant Colony Optimization: A Metaheuristic Approach to Multiobjective Portfolio Selection " *Annals of Operations Research*, vol. 131, no. 1 – 4, pp. 79 – 99, Oct. 2004.

Chapter 7

Design and Optimization of Traction IPMSM for Integrated Charging Capability

7.1. Introduction

The 3–phase windings of interior permanent magnet synchronous machines (IPMSMs) used in electric vehicles (EVs) for traction can also be utilized for charging the battery. This integrated charging technology eliminates the on–board charger, leading to significant reduction in overall weight and cost of the EV and hence increases the driving range per charge of the vehicle. Integrated charging technology can be implemented by using the stator winding inductances of a conventional 3–phase traction IPMSM as line inductors while the machine is in stand–still condition as shown in Fig. 7.1 [1]. Due to non–uniform air–gap nature of an IPMSM, the reluctance paths as seen from the stator side are unequal. Hence, the magnetic fields induced across the stator windings will be unequal along all 3 phases during integrated charging operation, resulting in asymmetrical currents/voltages. Such asymmetrical currents/voltages in an existing vehicle drivetrain, can lead to even harmonic currents, especially 2nd order harmonic currents, to be induced in the DC bus of the system at the battery side affecting battery life and performance. As seen in Fig. 7.1, the system DC bus includes the DC link bulk capacitor, battery and a DC–DC converter that may or may not exist in the traction powertrain. While the DC–DC converter can minimize harmonics, the capacitors need to be designed for higher ripple current ratings, which results in added size and cost of the capacitors and hence the overall system. Therefore, in an existing vehicle drivetrain, it is of paramount significance to eliminate the asymmetry in 3–phase AC line voltages/currents and hence the harmonic current oscillations induced in the DC bus during integrated charging. Further, the asynchronous machine operation during integrated charging causes high magnitudes of oscillating torque resulting in harmful mechanical vibrations, acoustic noises and deterioration of permanent magnets (PMs) [2].

While single–phase chargers are an easier solution, due to limited power levels, it is difficult to accomplish fast charging capacity [3]. Various solutions to avoid torque production and unbalanced voltages during integrated charging have been discussed in terms of galvanic isolation between charger and the grid [4], multi–phase machine topology [5] – [7], split–winding design [8] and multi–level converter topologies [9]. However, all these methods require complicated

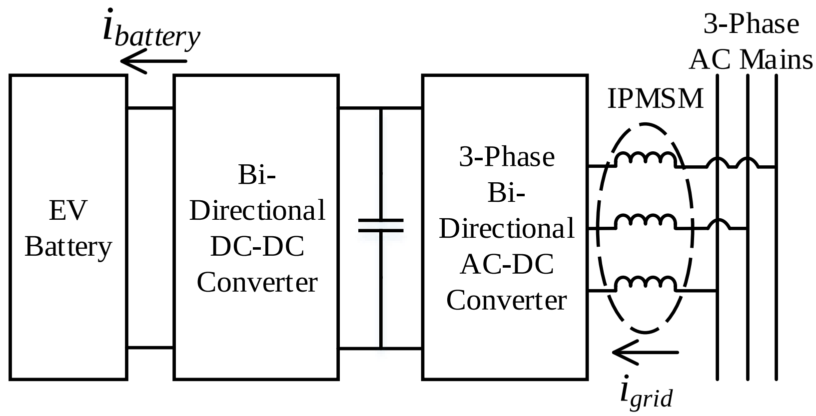

Fig. 7.1. Overall integrated charging system using existing 3–phase traction motor drive components.

hardware reconfiguration, advanced control methodologies and complex power electronic systems which might affect the traction operation or lead to significant increase in overall system losses, weight and cost of the vehicle. Thus, in this chapter, two simple design solutions to overcome the challenges of utilizing a 3–phase traction IPMSM for integrated charging are proposed and investigated.

First, employing novel asymmetrical damper bars in the rotor of the IPMSM to obtain balanced voltages across the machine windings during integrated charging is studied. Conventional *dq*–axis model of IPMSM with damper bars is implemented to design the dampers and analyze the machine inductances during charging operation. However, during traction operation, the damper bars act as rotor flux barriers affecting useful flux linking the stator towards torque production. Similarly, while saliency effects should be minimum during charging, the non–uniform air–gap structure contributes towards desired torque production during traction operation. Thus, a computationally efficient magnetic equivalent circuit model based differential evolutionary algorithm is implemented to optimally design and analyze a traction IPMSM with charging capability. The major objectives of optimization are to obtain minimum torque during charging and high electromagnetic torque per unit machine losses during traction condition thereby ensuring maximized operating efficiency.

Based on the analysis and understanding the practical challenges associated with using asymmetrical dampers in the machine, a simplistic approach of using combined star–delta wound PMSMs for integrated charging application is proposed. As indicated in the previous chapters, such star–delta wound topologies provide additional advantages during traction application and hence can be easily applied for charging as well. While additional contactors might be required for realizing the system, the challenges associated with unbalanced voltages/currents and high oscillating torques are completely eliminated by accurate modeling of balanced magneto motive forces between the star and delta connected winding sets. Thus, a comprehensive analysis of the proposed star–delta wound PMSM topology from the previous chapters, for integrated charging application is presented in this chapter.

7.2. Performance Investigation of Conventional Traction IPMSM for Integrated Charging

To understand the challenges associated with integrated charging operation using a conventional IPMSM, an existing laboratory traction machine with 27–slots, 6–poles and V–shaped magnet configuration is employed for experimental investigation. The structural and traction performance details of the machine are shown in Table 7.1. In order to investigate the unbalanced impedance issue, experiments were conducted to obtain the phase voltages and current waveforms under an emulated integrated charging scenario. During integrated charging, one end of the 3–phase machine terminals will be connected to the utility grid and the other end will be connected to the AC/DC converter. Thus, the voltages measured between the two terminals of the same phase will be the equivalent voltage drop across the machine winding inductances between the voltages from the grid supply and the AC/DC converter. Hence, to emulate the situation of integrated charging without implementing any controls, the stator terminals are connected to the utility grid through a 3–phase variac as shown in Fig. 7.2(a) and the currents and voltage drop across each phase impedance is measured as shown in Fig. 7.2(b). Therefore, the magnitudes of voltages are observed to be low.

However, the unbalances in 3–phase current waveforms due to machine's saliency can be clearly observed in Fig. 7.2(b). According to the overall system configuration during integrated charging shown in Fig. 7.1, the machine windings are used as inductive filters to ensure a low THD in the AC currents drawn from the utility grid. When these currents through the windings are unbalanced, it could lead to introduction of 2nd harmonic oscillations across the DC link capacitor. Thus, in order for the proposed integrated charger to function as a regular balanced 3–phase AC charger, mitigation of this voltage unbalances are of significance. An overall system study including the control strategy and grid side voltage distortion is required to determine the THD level in the line currents during charging. However, this thesis only focuses on resolving the unbalanced magnetic fields induced across the stator winding inductances so that a traction IPMSM can be used to facilitate battery charging capability.

TABLE 7.1

DETAILS OF THE LABORATORY 3–PHASE IPMSM

Rated Torque	100 Nm	Rated Speed	4,000 rpm
Rated Efficiency	90 %	Maximum Speed	10,000 rpm
DC bus Voltage	400 $V_{(max)}$	Current/phase	120 A rms
Stator ID	135 mm	Stack Length	136 mm
Current Density	7 A/mm^2	Slots/Pole	27/6

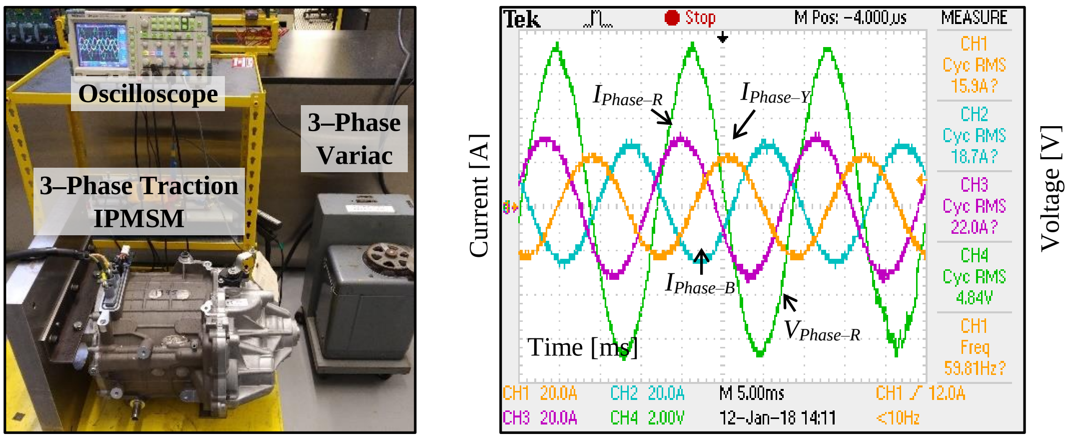

(a) (b)

Fig. 7.2. (a) Experimental test setup of emulated integrated charging operation using a laboratory traction IPMSM with standard 60 Hz utility grid supply. (b) Measured voltage and current waveforms across the machine terminals.

Further, due to stand–still operation, the PMs are subjected to the continuous unbalanced operation of the stator. Thus, it is understood that repetitive and prolonged charging could cause irreversible demagnetization and saturation of the rotor iron core compromising the machine's traction performance. During experimentation, severe noise and vibrations were observed which can be attributed to the high magnitudes of oscillating torque. Thus, to utilize a traction motor for integrated charging operation, it is imperative to mitigate the saliency effects in IPMSM without compensating the rated torque and power–speed characteristic traction performance.

7.3. Design and Implementation of Damper Bars in IPMSM for Integrated Charging

A. Design Challenges Associated with Traction IPMSM for Integrated Charging Capability

The operating conditions, magnetic field distribution, and performance characteristics of an IPMSM under traction and integrated charging operations are drastically different. Any additional structural components or design modifications incorporated in the traction IPMSM to overcome the challenges associated with integrated charging, should be modeled without altering the traction performance. Therefore, the following design challenges arise: 1) the *dq*–axis flux paths should be designed such that the difference in machine *dq*–inductances should be low during integrated charging while it is high during traction operation; 2) during integrated charging, the machine should not rotate and have near zero average torque while in traction performance, the machine should be capable of giving high average torque over a wide speed range; 3) the machine should not be saturated or demagnetized or cause phenomenal increase in machine temperature while operating in both traction and charging conditions; 4) any additional structural components added to the rotor to obtain symmetrical voltages during charging, should not induce harmonic components causing non–sinusoidal mmf distribution and increased rotor losses during traction operation; and 5) the modified IPMSM should satisfy the target performance of both traction and charging conditions with maximized efficiency.

Thus, in this chapter, addition of damper bars in the rotor is taken up for analysis to equip the traction IPMSM with integrated charging capability. Since the machine is connected to the grid during charging, implementing dampers in the rotor emulates an induction assisted PMSM configuration and is expected to yield satisfactory charging performance. Authors in [10] have investigated the traction performance of an IPMSM drive incorporating damper bars for EV application and concluded that proper design and placement of the dampers could result in: 1) more sinusoidal induced emf distribution aiding to the magnet torque production; 2) improved transient performance in high speed region; 3) better fault tolerant capability through faster isolation; and 4) reduced risk of PM demagnetization and torque ripple content. In [11], authors have analyzed the integrated charging and discharging operation of IPMSM with damper bars for EV application. However, the design procedure to develop specialized dampers to achieve optimal charging and traction performance was not established and there was still scope for improvement in terms of unbalanced voltages and oscillating torque. Hence, this thesis focuses on the design aspect of developing a traction IPMSM with dampers for integrated charging capability.

B. Proposed Damper Bar Design and Modeling

The operating conditions of an IPMSM during charging emulates an induction machine when the speed slip is close to unity. During charging, voltage across the magnetizing inductances at the supply grid frequency (ω_s) will induce currents in the dampers. Thus, the dampers provide additional inductances along the *dq*–axis flux paths to compensate machine saliency and result in symmetrical voltage/current waveforms. Alternatively, during traction, since there is no slip frequency, the damper bars simply act as rotor flux barriers. The *d*– and *q*–axis equivalent circuits of an IPMSM with dampers in the rotor reference frame rotating at a speed of ω_r are shown in Figs. 7.3(a) and (b) respectively and the voltage equations can be obtained as in (7.1) – (7.4) [12] where v_{ds} and v_{qs} are the machine's *d*– and *q*–axis voltages respectively, i_{ds} and i_{qs} are the corresponding currents, r_s is the winding phase resistance, L_{ls} is the phase leakage inductance, L_{ds} and L_{qs} are the effective stator *d*– and *q*–axis inductances, L_{md} and L_{mq} are the corresponding magnetizing inductances, r'_{kd} and r'_{kq} are the *dq*–axis damper bar resistances referred to the stator side, L'_{kd} and L'_{kq} are the corresponding damper bar leakage inductances and i'_{kd} and i'_{kq} are the damper bar currents respectively, λ'_o is the no–load phase flux linkage and p is the differential operator.

$$v_{ds} = (r_s + L_{ds}p)i_{ds} - \omega_r\left(L_{qs}i_{qs} \pm L_{mq}i'_{kq}\right) - L_{md}\,pi'_{kd} \tag{7.1}$$

$$v_{qs} = (r_s + L_{ds}p)i_{qs} + \omega_r\left(\lambda'_o + L_{ds}i_{ds} \pm L_{md}i'_{kd}\right) - L_{mq}\,pi'_{kq} \tag{7.2}$$

$$\left(r'_{kd} + L'_{kd}\,p\right)i'_{kd} - L_{md}\,pi_{ds} = 0 \tag{7.3}$$

$$\left(r'_{kq} + L'_{kq}\,p\right)i'_{kq} - L_{mq}\,pi_{qs} = 0 \tag{7.4}$$

During integrated charging, since the rotor is in stand–still condition, $\omega_r = 0$ and the short–circuited damper windings can be approximated to be composed of two windings, one along *d*–axis and the other along *q*–axis in which the bars are connected in series. To compensate the machine's salient nature ($L_{mq}>L_{md}$), the damper bar resistance (r'_k) and inductance (L'_k) referred to the stator side along the parallel branch must be designed in such a way that the effective impedance along the *d*– and *q*–axis magnetizing branches are equal.

The effective damper bar impedance can be related to the structural aspects of the damper and the machine under consideration. The *dq*–axis damper bar resistance can be estimated as in (7.5) – (7.8) [1] where P is the number of poles, L_b is the length of the damper bar, k_b and k_r are the

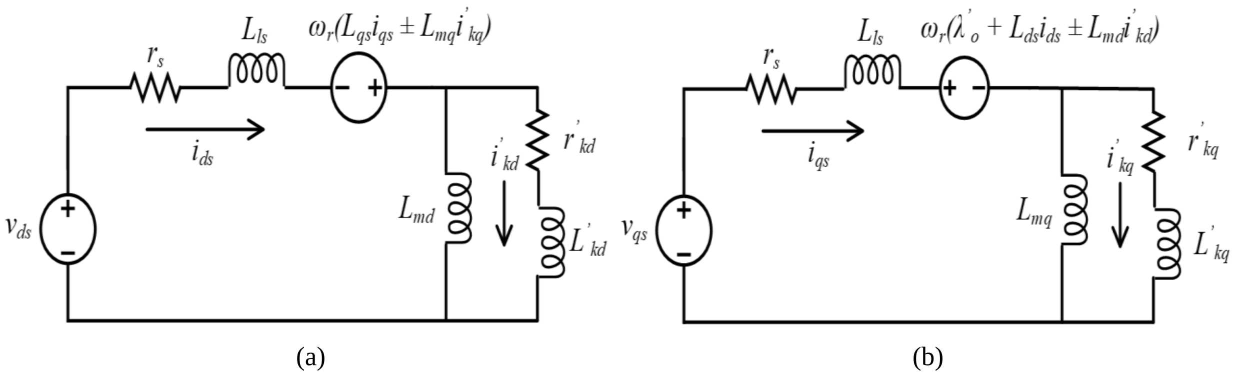

(a) (b)

Fig. 7.3. Equivalent circuit of IPMSM with damper bars. (a) *d*–axis. (b) *q*–axis.

conductivities of the damper bar and damper end ring materials respectively, Z_d is the number of damper bars per pole, A_b and A_r are the cross–sectional areas of the bars and end ring respectively in mm^2, τ_p is the pole–pitch and τ_{sd} is the slot–pitch of the dampers.

$$r_{kd/q} = r_{kd/q(bars)} + r_{kd/q(endring)} \tag{7.5}$$

$$r_{kd(bars)} = r_{kq(bars)} = \frac{PL_b Z_d}{k_b A_b} \tag{7.6}$$

$$r_{kd(endring)} = \frac{2P}{k_r A_r} \sum_{n=0}^{(Z_d-2)/2} (2n+1)\tau_{sd} \tag{7.7}$$

$$r_{kq(endring)} = \frac{2P}{k_r A_r} \sum_{n=0}^{(Z_d-2)/2} \left[\tau_p - (2n+1)\tau_{sd}\right] \tag{7.8}$$

Similarly, for a known magnetizing reactance ($L_{md/q}$) at 60 Hz supply frequency, the damper bar leakage reactances can be obtained from (7.9) and (7.10) [1] where f is the grid frequency, b_r is the breadth of the end ring, $h_{od/q}$, $h_{sd/q}$, $b_{od/q}$ and $b_{sd/q}$ are the heights and breadths of the damper slot opening and slot body respectively along d– and q–axis. These damper parameters (r_{kd}, r_{kq}, X_{kd}, X_{kq}) can be referred to the stator side as seen in the dq–axis equivalent circuit shown in Fig. 7.3 using (7.11) – (7.14), [13] where m is the number of machine phases, T_{ph} is the stator winding turns per phase and k_w is the stator winding factor.

$$X_{kd/q} = 0.79 f Z_d P(L_b - b_r)\lambda_{sd/q} \times 10^{-7}\,\Omega \tag{7.9}$$

$$\lambda_{sd/q} = 0.66 + \frac{h_{od/q}}{b_{od/q}} + \frac{h_{sd/q}}{3b_{sd/q}} \tag{7.10}$$

$$X'_{kd/q} = \frac{m(T_{ph}k_w)^2}{2(N_{Dd/q}k_{Dd/q})^2} X_{kd/q} \tag{7.11}$$

$$r'_{kd/q} = \frac{m(T_{ph}k_w)^2}{2(N_{Dd/q}k_{Dd/q})^2} r_{kd/q} \tag{7.12}$$

$$N_{Dd}k_{Dd} = P\frac{\sin^2(\pi Z_d \tau_{sd}/4\tau_p)}{\sin(\pi\tau_{sd}/2\tau_p)} \tag{7.13}$$

$$N_{Dq}k_{Dq} = P/2\,\frac{\sin\left(\pi Z_d \tau_{sd}/2\tau_p\right)}{\sin\left(\pi\tau_{sd}/2\tau_p\right)} \tag{7.14}$$

Thus, for the machine dq–axis magnetizing reactances ($X_{md/q}$) at 60 Hz frequency estimated using (7.15) – (7.18) [14], the damper bar structure can be designed to determine the damper parameters using (7.5) – (7.14). Where D and L are the machine dimensions, k_c is the carter's coefficient, g_0 is the air–gap length, g_m is the PM thickness, k_{sd} and k_{sq} are the d– and q–axis saturation coefficients respectively.

$$L_{ph} = \frac{4m\mu_0 (k_w T_{ph})^2 DL}{\pi P^2 k_c g_0} \tag{7.15}$$

$$X_{md} = \frac{2\pi f L_{ph} k_{ad}}{k_{sd}}; \quad X_{mq} = \frac{2\pi f L_{ph}}{k_{sq}} \tag{7.16}$$

$$k_{ad} = \frac{k_c g_0}{k_c g_0 + \dfrac{g_m}{2\mu_r}} \tag{7.17}$$

$$X_{md} = 2\pi f L_{md}; \quad X_{mq} = 2\pi f L_{mq} \tag{7.18}$$

Using the calculated damper parameters, the voltages across the windings can be estimated using (7.1) and (7.2). The machine's damper bar impedances are significantly low compared to the magnetizing inductances. Hence, the overall machine impedance, which is a function of magnetizing component, damper bar impedance and armature leakage component will still be nominal for assisting in charging operation.

C. Comparative Performance Analysis of IPMSM with Symmetrical and Asymmetrical Dampers during Integrated Charging Operation

To compensate for the machine saliency, the damper impedances along d– and q–axis can either be equal or unequal resulting in symmetrical or asymmetrical dampers respectively. In case of symmetrical configuration, dampers with same structural details along both d– and q–axis are introduced equidistantly along the entire rotor circumference under each pole. However, in asymmetrical configuration, since L_{mq} is greater than L_{md}, the damper bar along q–axis will have lower impedance than that of d–axis. This can be achieved by using a damper with higher h_s or lower b_s along q–axis than d–axis from (7.9) and (7.10), resulting in reduced effective L_q. An electromagnetic model of the baseline machine with performance details indicated in Table 7.1 was developed. Both symmetrical dampers and asymmetrical dampers were designed using the proposed approach and a comparative performance analysis is presented. For machines with

TABLE 7.2
STRUCTURAL AND PARAMETRIC DETAILS OF THE DEVELOPED DAMPER BARS

Parameter	Symmetrical Dampers		Asymmetrical Dampers	
	d–axis	*q*–axis	*d*–axis	*q*–axis
r_k (Ω)	0.0015	0.0015	0.0030	0.0053
X_k (mΩ)	0.8122	0.8122	0.913	0.412
L_{dq} (μH)	13.78	14.98	14.8	14.8

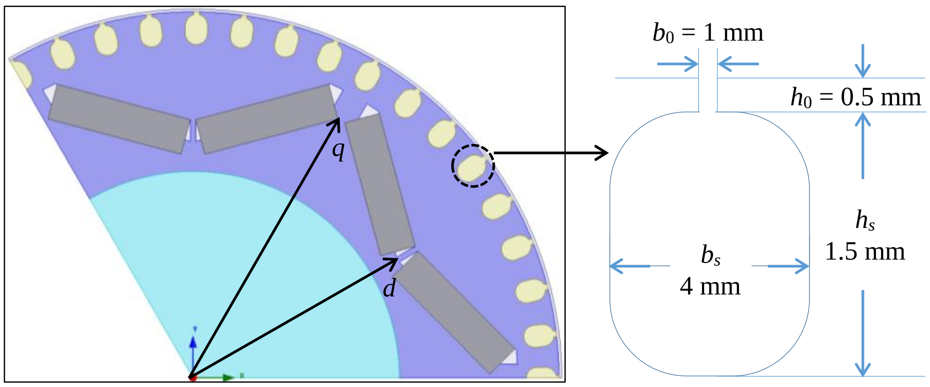

(a)

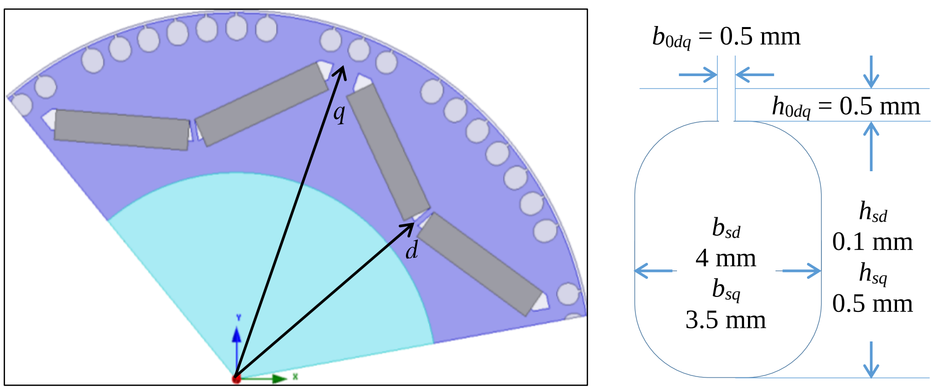

(b)

Fig. 7.4. IPMSM with dampers for traction and charging operation. (a) Electromagnetic model of Machine A with symmetrical dampers. (b) Electromagnetic model of Machine B with asymmetrical dampers.

integral slot winding configuration, the number of damper bars per pole, Z_d, can be close to the stator slot per pole number. However, in case of fractional slot configuration, Z_d can be greater than or close to the pole number itself. The electromagnetic models of the designed IPMSM with symmetrical (Machine A) and asymmetrical (Machine B) damper bars along with the dimensional details are depicted in Figs. 7.4(a) and (b) respectively. The calculated parameters along *dq*–axis for both the machines are indicated in Table 7.2. It can be observed that the effective inductances are almost equal with a difference of about only 1.2 μH in case of symmetrical dampers. On the other hand, in case of asymmetrical dampers, the effective *d*– and *q*–axis inductances are almost equal. To verify the charging operation, the 3–phase voltage waveforms obtained using FEA, when a 120 A rms current at 60 Hz frequency is applied across the two machines windings are illustrated in Figs. 7.5(a) and (b). It is important to note that these voltages represent the effective voltage drop across the machine phase impedances during integrated charging.

The voltage unbalances in case of Machine A can be clearly observed in Fig. 7.5(a) in spite of the minimal difference in *dq*– axis inductances. This is due to the unbalanced flux linkages at the stator side. For instance, when phase–*a* is aligned along *d*–axis, the flux linking the stator phase–*a* conductors are relatively lower than the other phases during stand–still condition. Thus, with the help of asymmetrical dampers the voltage unbalances can be reduced phenomenally as shown in Fig. 7.5(b). Further structural optimization is required to completely eliminate the voltage unbalances. The oscillating torque waveforms of both machines during charging are shown in Fig. 7.5(c). It can be seen that the average torques are 2.7 Nm and 5 Nm respectively for Machines A and B, but the oscillating torques are high. However, it was observed from FEA that the operating flux densities were all within the saturation limits. Further, conventional traction motors with relatively low noise and vibrations and will remain at stand–still condition. From [2] and [3], it was found that for both single and 3–phase charging, the minimal torque oscillation was obtained when the rotor position was such that '*a*' phase was aligned to '*d*' axis of the machine. However, adding a mechanical brake could also be a plausible solution to dampen the noise and vibration and facilitate safe operation.

The designed machines with dampers were analyzed under synchronous speed operation to understand the machine's torque capability. Fig. 7.5(d) illustrates the torque at rated speed of 4,000

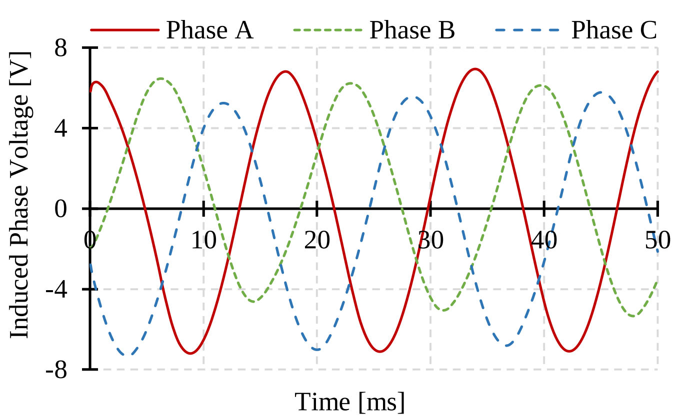

(a)

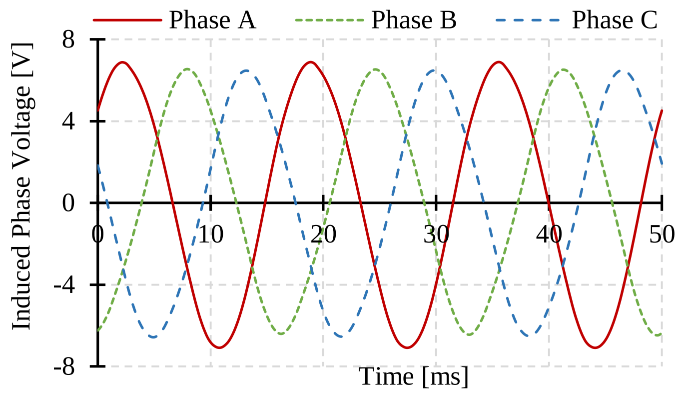

(b)

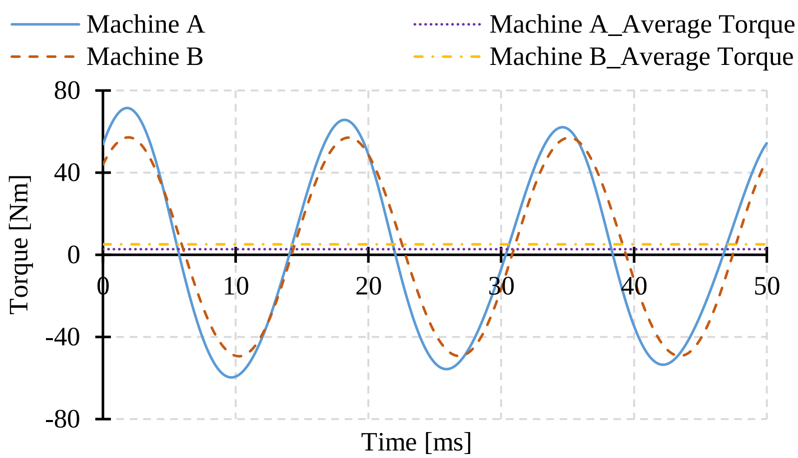

(c)

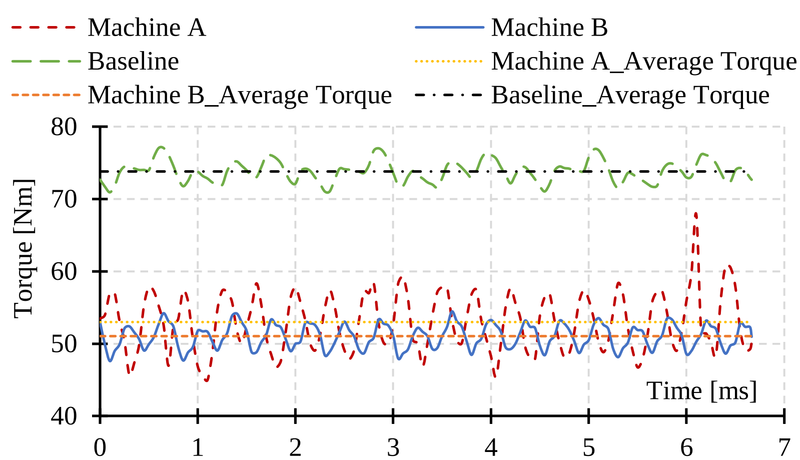

(d)

Fig. 7.5. Performance analysis of developed Machines A and B under traction and charging operations. (a) Induced voltages for an input current of 120 A rms at 60 Hz in machine A. (b) Induced voltages for an input current of 120 A rms at 60 Hz in machine B. (c) Comparison of oscillating torque during charging operation. (d) Comparison of rated electromagnetic torque during traction operation at rated speed of 4,000 rpm and rated current of 120 A rms/phase.

rpm for the baseline IPMSM, Machine A and B. It can be observed that with dampers, the torque production reduced by about 28% in both Machines A and B. Thus, PM volume or stator turns per phase has to be increased to increase torque. However, such design modifications increase the magnetizing reactances as well and hence the dampers have to be redesigned to obtain symmetrical voltage waveforms during charging. Thus, this calls for an optimization problem to design the IPMSM rotor structure with asymmetrical dampers for desired traction and charging performance.

7.4. Optimal Design of Traction IPMSM with Damper Bars for Integrated Charging

A. Design Optimization Problem Statement

Considering the design challenges highlighted in Section 7.3–*A* to achieve a traction IPMSM equipped with integrated charging capability, the optimization objectives can be summarized as: i) minimize average torque (T_s) produced during charging; ii) reduced voltage unbalances during constant current based charging by obtaining near–zero machine saliency; and iii) maximize the average electromagnetic torque per unit machine losses resulting in maximized operating efficiency (T_e/P_{loss}) during rated traction operation. Since all the functions are dependent on the *dq*–axis inductances, the rotor structure is taken up for optimization. For the baseline traction IPMSM shown in Fig. 7.2(a), the stator structure including the winding distribution, PM, damper bar and steel core materials used are all kept constant. A total of 9 rotor structural parameters influencing the machine inductances are taken as design variables as indicated in Fig. 7.6 and the parameter vector, v is represented as

$$v = \left[h_s, b_s, g_m, w_m, \tau_p, \tau_{sd}, g_o, O_1, w_{rib}\right] \tag{7.19}$$

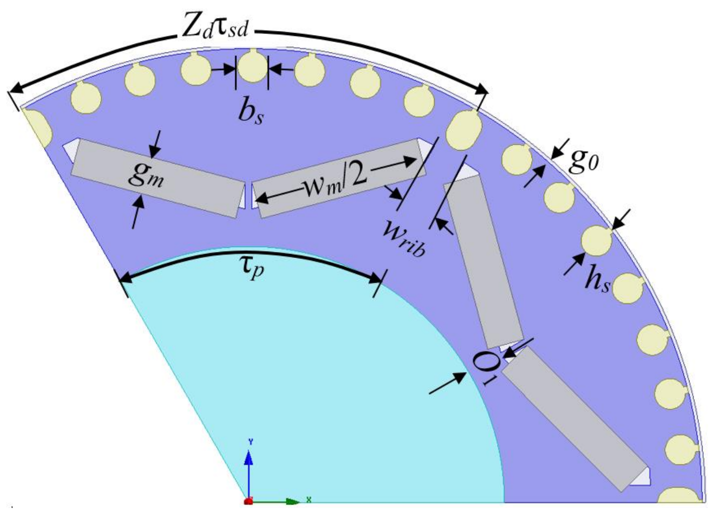

Fig. 7.6. Illustration of design variables implemented for optimizing rotor structure of IPMSM with dampers.

It is vital to avoid magnetic saturation of the rotor core material and PM demagnetization during both charging and traction operation with minimum overall machine losses. It is also important to maintain the machine's operating temperature within permissible limits throughout performance. The magnet and damper bars must be designed in such a way that they can be accommodated within the permissible rotor volume. Thus, subject to the aforementioned constraints, the overall objective function can be obtained as

$$f_1 = T_s = \frac{P}{2\pi f}\frac{V^2\left(L_d - L_q\right)^2 r_s}{2\left(L_d L_q + r_s{}^2\right)^2} \tag{7.20}$$

$$f_2 = {T_e}/{\eta} = \frac{\frac{3P}{4}\left[\lambda_m i_{qs} + i_{ds} i_{qs}\left(L_d - L_q\right)\right]}{\min\left(P_{cu} + P_{fe} + P_{eddy} + P_{damper}\right)} \tag{7.21}$$

$$f = \sum_{n=1}^{N} w_n f_n(v) \tag{7.22}$$

$$f = w_1 \min\left[f_1(v)\right] + w_2 \max\left[f_2(v)\right] \tag{7.23}$$

where V is the amplitude of the supply voltage, i_{ds} and i_{qs} are the dq–axis currents and λ_m is the magnet flux linkage, w_1 and w_2 are the weights of each of the objective functions, P_{cu}, P_{fe}, P_{eddy}, $P_{dampers}$ are copper, core, magnet eddy current and damper bar losses respectively.

B. Overview of the Proposed Optimization Approach

The conventional dq–axis based damper design provide the maximum limits for the structural dimensions of the damper bars up to which saliency effect can be mitigated during integrated charging. Further, based on the structural limitations after including the dampers, the minimum and maximum limits of the magnet dimensions and effective air–gap length can be estimated. Thus, for the range of design variables chosen, differential evolutionary algorithm is implemented to select the best design candidate while magnetic equivalent circuit is implemented for electromagnetic analysis of the design candidates. While differential evolutionary algorithm facilitates improved design population towards the optimal design candidate, magnetic equivalent circuit is a computationally less extensive and accurate approach to extract the objective function for each design candidate. A comprehensive magnetic equivalent circuit model including stator and rotor slotting effects, magnetic saturation and slot leakage effects as shown in Fig. 7.7 for IPMSM with damper bars was developed where symbols have their usual meanings [15]. During the optimization process, it is implemented for estimating machine fluxes to check for saturation and useful flux linkage calculation using (7.24) at various operating conditions including traction and charging operation where u is the node magnetic potential matrix, $\Re$ is the effective reluctance matrix and Φ is the estimated flux matrix. Based on the calculated fluxes, machine inductances and induced voltages for the design solution are calculated and the rotor geometry is updated accordingly using differential evolutionary algorithm.

$$[u]\cdot[\Re]^{-1}=[\Phi] \tag{7.24}$$

Thus, within the design population (N_p), for each parameter vector candidate (v_i), initially, the damper bar impedances are estimated under charging conditions. If the objective function f_1, for integrated charging are satisfied, the same vector candidate is analyzed for traction operation for f_2. Otherwise, the population is updated and the differential evolutionary algorithm generates a new parameter vector candidate (v_{i+1}) for analysis. If the overall objective function f is satisfied, an optimal design solution for IPMSM with asymmetrical dampers is obtained. This overview of the approach is shown using a flowchart shown in Fig. 7.8.

For satisfying f_1, the initial damper bar design obtained from (7.5) – (7.14) are used to determine if the torque produced during charging is at least within 2% of the rated electromagnetic torque rating of the machine. Further, for the damper bar dimensions obtained, at rated current conditions, keeping the material properties, baseline rotor and magnet dimensions fixed, the rated

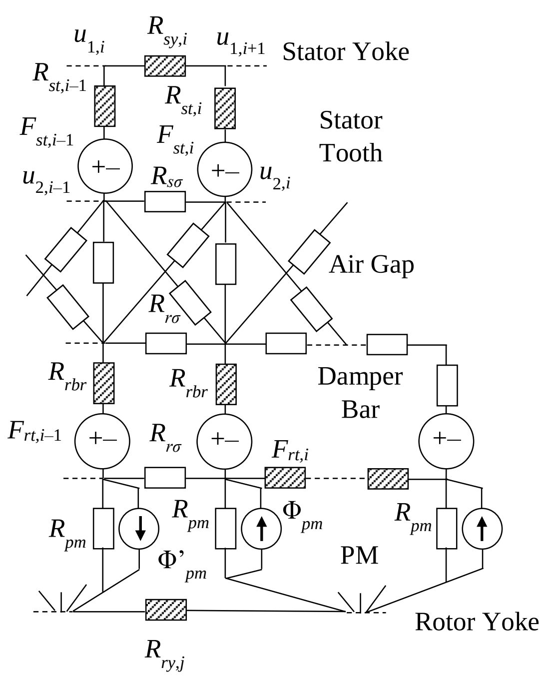

Fig. 7.7. Comprehensive magnetic equivalent circuit model developed to analyze IPMSM with dampers under traction and integrated charging conditions.

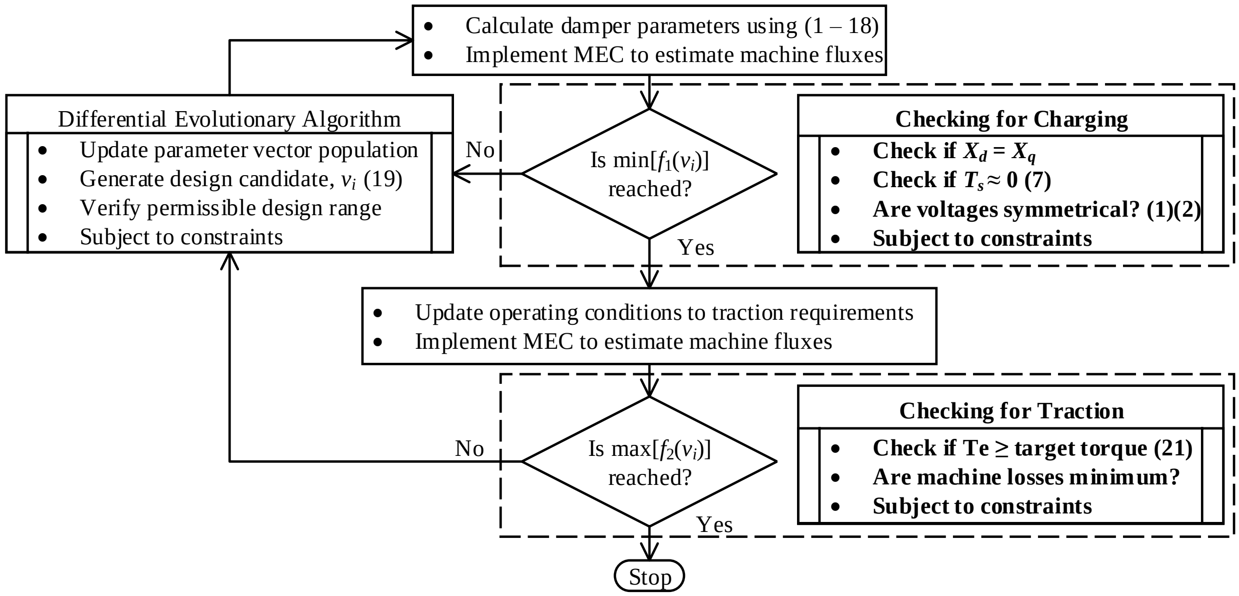

Fig. 7.8. Optimization design procedure to obtain an optimal rotor structure of IPMSM with asymmetrical dampers for traction and integrated charging operations.

torque per unit efficiency, f_2, produced is estimated. Usually, due to damper bars, it is lesser than the target value and hence the magnet volume has to be increased subject to saturation constraints. Thus, for the updated magnet dimensions, f_1 is again calculated and the optimization procedure can be expressed in terms of the inductance values obtained for the overall objective function, f. While indicating the optimization algorithm for each design variable might be complicated, it is evident from (7.20) and (7.21) that the objective function depends directly on L_d and L_q estimated using the design variables from the magnetic circuit. Thus, the variation of f_1 and f_2 with L_d and L_q are illustrated in Figs. 7.9(a) and (b). A terminal condition for f_1 is set for up to 2% of rated torque; f_2 is set up to rated efficiency greater than 90% and for no possible design solution, an iteration limit of 1,500 is set.

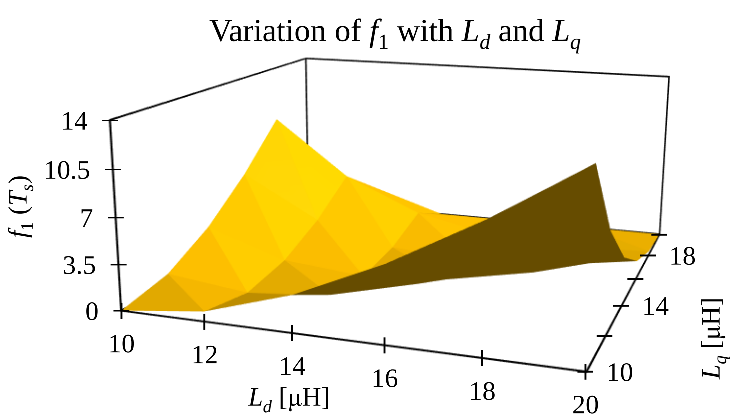

(a)

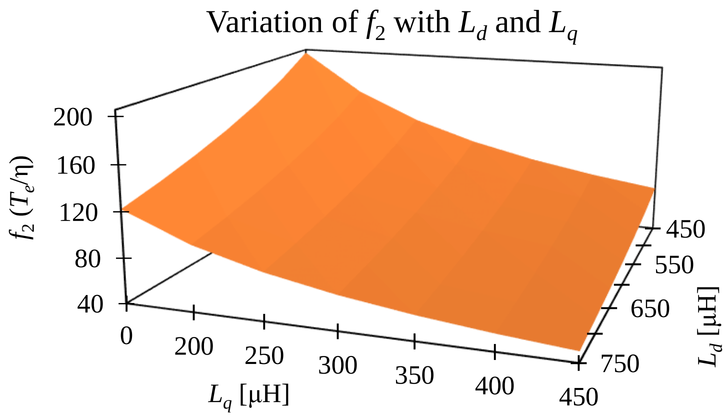

(b)

Fig. 7.9. Variation of applied optimization algorithm objective function with L_d and L_q. (a) f_1. (b) f_2.

C. Performance Analysis of Optimized IPMSM with Dampers

The performance details given in Table 7.1 for the laboratory traction IPMSM are kept as design targets for traction performance. Using (7.1) – (7.18) and the geometrical details of the baseline machine, the maximum and minimum limits of the design variables are obtained as indicated in Table 7.3. All the minimum and maximum limits of the design variables are estimated depending upon the available rotor volume and to avoid magnetic saturation of the steel core. For instance, the maximum limits of τ_p and τ_{sd} are fixed based on the stator and rotor outer diameters and the number of damper bars. Depending upon τ_p and the minimum gap between magnets to avoid steel saturation, the maximum limits for w_m are calculated while τ_{sd} decides the width of the damper bars. Similarly, for a specific rotor yoke thickness, the limits on O_1 and hence the height of both magnet and damper bars can be estimated. The optimized IPMSM rotor structure obtained with dampers for traction and charging operations is shown in Fig. 7.10(a) and the structural parameters are included in Table 7.4.

The machine was analyzed under two main operating conditions. First, during charging, when a rated 3–phase current of 120 A rms, 60 Hz supply was applied across the machine windings. Considering a practical scenario of charging a commercially available EV, for instance, Mitsubishi i–MiEV, having a 47 kW PMSM is equipped to charge its 16 kWh battery pack with level 3 charging capability. The level 3 fast charging capability is rated until a maximum of 44 kW at 480 V DC bus voltage. This results in a DC current of around 91.6 A. With the grid–side AC–DC converter of the traction powertrain controlled at unity power factor, the corresponding peak AC current that will be flowing through the armature will be around 170 A and the rms current/phase

TABLE 7.3
DESIGN RANGE OF PARAMETER VECTOR

Design Variable	Minimum Limit [mm]	Maximum Limit [mm]
$h_{sd/sq}$	0.5	6
$h_{0d/0q}$	0	1
$b_{sd/sq}$	0.5	6.964
$b_{0d/0q}$	0	1
g_m	4	7.2
w_m	30.89	34.295
g_0	0.5	1.5
τ_p	48.75	69.639
τ_{sd}	4.875	6.964
O_1	1	15
w_{rib}	1	5

will be 120 A. Hence, in this thesis, the IPMSM with damper is investigated at 120 A rms/phase. Fig. 7.10(b) shows 3–phase voltages across the machine windings during charging operation, which indicate the equivalent voltage drop across the machine winding inductances between the grid supply and the AC/DC converter. It can be observed that the voltages unbalances are almost eliminated when compared to Fig. 7.5(b) due to the optimized damper bars. The minimized average torque production during charging was found to be close to 3 Nm resulting in noise and vibrations at rotor stand–still condition. The saliency effects during charging is almost negligible as seen from the calculated parameters of optimized machine highlighted in Table 7.4. From the flux map observed in Fig. 7.10(a), it can be seen that the charging operation does not result in saturation of the machine.

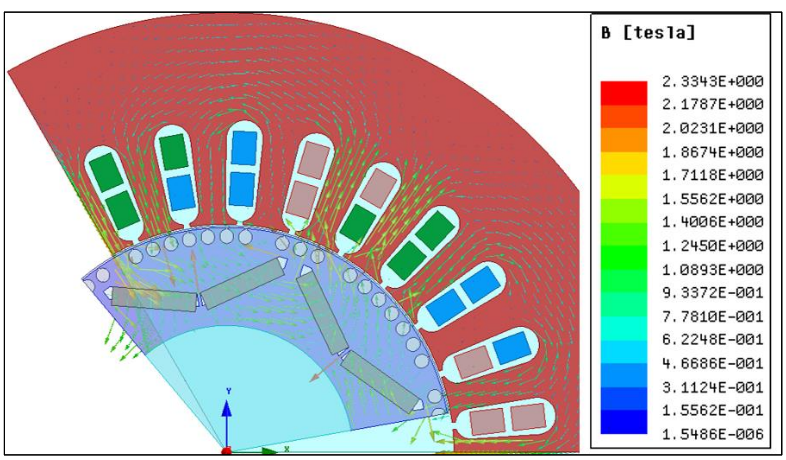

(a)

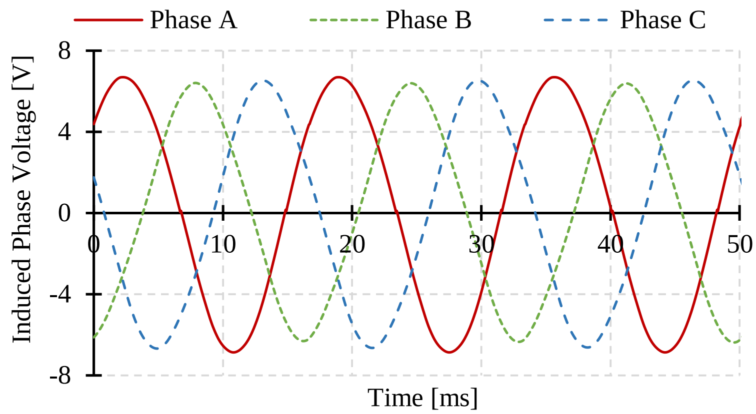

(b)

Fig. 7.10. (a) Flux map of optimized traction IPMSM with asymmetrical damper bars during charging with 120 A rms/phase, 60 Hz supply. (b) 3–Phase induced voltages during charging when 120 A rms/phase, 60 Hz grid supply is applied across windings of the optimized machine.

Further, Fig. 7.11(a) compares the torque and output power characteristics of the baseline machine shown in Fig. 7.2(a), machine B shown in Fig. 7.4(b) and the optimized machine as shown in Fig. 7.10(a) under traction operation. It can be seen that the optimized machine produces a rated torque of about 102 Nm which is close to the target baseline machine with 103 Nm. However, in

TABLE 7.4

ASYMMETRICAL DAMPER BAR STRUCTURAL DETAILS AND PARAMETERS USED FOR OPTIMIZED IPMSM

r_s	0.0325 Ω	X_{ls}	9.99 m Ω
r_{kq}	0.0027 Ω	r_{kd}	0.0016 Ω
X_{kd}	0.48 mΩ	X_{kq}	0.39 mΩ
L_d	12.2 µH	L_q	12.2 µH
h_{0d}	0.5 mm	h_{0q}	0.5 mm
h_{sd}	0.45 mm	h_{sq}	0.3 mm
b_{0d}	0.5 mm	b_{0q}	0.5 mm
b_{sd}	4 mm	b_{sq}	3.5 mm

TABLE 7.5

ANALYSIS ON MACHINE LOSSES AND PM OPERATING POINT DURING TRACTION AND INTEGRATED CHARGING

Parameter	Traction	Integrated charging
B_m	0.94 T	0.92 T
H_m	1032 AT	676.82 AT
Rotor Losses	149.5 W	460.28 W
Core Losses	2971 W	1984 W

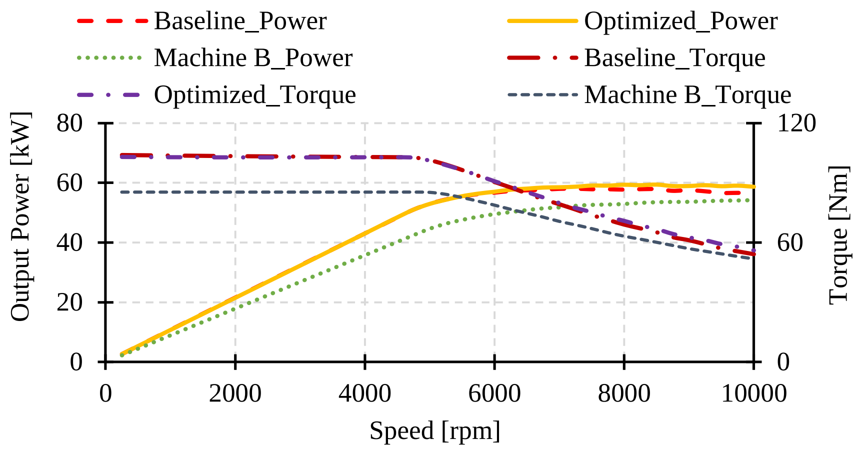

(a)

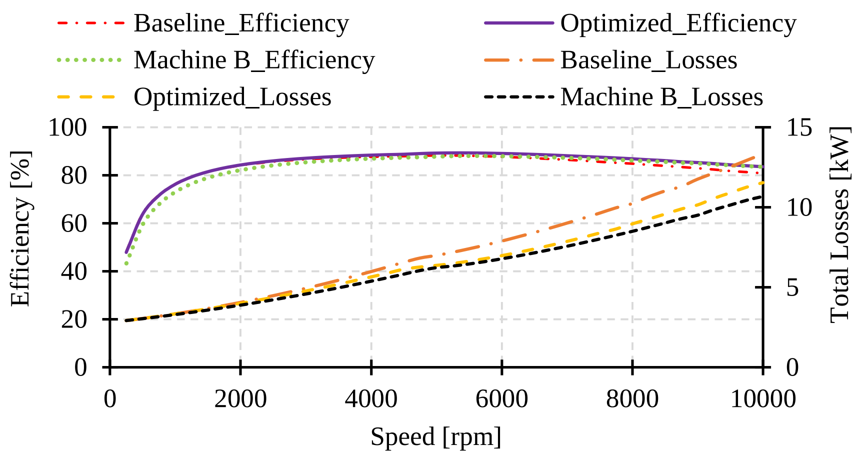

(b)

Fig. 7.11. Comparative performance analysis of baseline machine, Machine B and optimized machine during traction operation. (a) Torque and output power characteristics. (b) Efficiency and total loss characteristics.

order to meet the target torque, the PM volume was increased from 325 mm^2 to 382.5 mm^2 and the damper volume was reduced by 15%. Although this might lead to additional magnet losses, the machine efficiency is maintained within targets and the magnets can be accommodated in the rotor without any saturation resulting in effective traction and charging operations. Fig. 7.11(b) presents the efficiency and total loss characteristics for the 3 machines and it can be seen that the rated efficiency of the optimized machine is close to 89%. An analysis on the machine losses during traction and charging operations were performed and presented in Table 7.5. The rotor losses during charging is almost 3 times greater than that during traction operation due to the copper losses across the dampers. Alternatively, core losses during charging is almost 1.5 times lower than that during traction since most of the eddy current effects are across the dampers and not the rotor core. It can be observed from Table 7.5 that during traction, the dampers act as a flux barrier and hence the magnet operating point is relatively higher. Conversely, during charging, the high eddy currents across the damper affects the magnet operating point. It can be seen that. with the use of strong magnets, the operating points during traction and charging operations are within the nominal PM operating range.

7.5. Star–Delta Windings for Integrated Charging Operation

While damper bars assist in mitigating the problems associated with integrated charging operation and also improve the transient and fault tolerant capabilities of the machine during traction operation, including such dense copper or aluminum bars in the rotor significantly increases the motor's active weight thereby limiting the motor's specific power and torque densities. For instance, for the baseline machine shown in Fig. 7.2(a), adding the asymmetrical dampers increases the motor weight by almost 2 kg. Thus, the torque density of the motor reduces by 5.4% with introduction of the dampers. Furthermore, as seen from Fig. 7.5(c), the dampers cannot totally eliminate the oscillating torque during charging operation. Thus, the integrated charging operation is obtained at the cost of increased manufacturing cost and reduced torque density of the motor. While this still supersedes the conventional on–board charger based system, if a simplistic machine design solution satisfying both traction and charging operation without affecting the motor performance can be obtained, it would result in phenomenal improvement to the overall system.

As discussed previously, multiphase machines have been commonly used for integrated charging operation to avoid the issues of unbalanced voltages and oscillating torques. However, such systems require additional switching devices in the inverter or two inverter systems for machine operation resulting in increased cost and system losses. On the other hand, the combined star–delta winding topology as discussed in the previous chapters, emulates a multiphase winding configuration without the requirement of additional switching devices and hence can be easily incorporate for integrated charging operation as well. Furthermore, as seen in Chapter 4, star–delta winding configuration result in reduced spatial harmonics, improved torque production and improved efficiency during traction operation. Thus, the star–delta winding topology is studied for integrated charging operation.

In order to use the combined star–delta wound machine for integrated charging, the motor must have an open wound configuration so that the terminals of each phase winding can be accessed and connected accordingly. Typically, the star connected winding set is used as line inductors during charging while the delta connected winding set is used to cancel the induced MMF in the machine so that the rotor is at stand still. Thus, the resultant MMF in the star connected winding set ($\Im_Y$) during charging and the MMF induced in the delta connected winding set ($\Im_\Delta$) must be equal in magnitude but in phase opposition as indicated in (7.25) resulting in a net zero MMF ($\Im_{Y\Delta}$) and hence near zero torque in the machine.

$$\begin{aligned} &\Im_\Delta(\theta,t) = -\Im_Y(\theta,t) \\ &\Im_{Y\Delta}(\theta,t) = \Im_Y(\theta,t) + \Im_\Delta(\theta,t) = 0 \end{aligned} \tag{7.25}$$

Thus, for an input grid voltage of 208 V_{L-L}, the currents induced in the delta winding set, I_Δ, can be computed depending upon the winding distribution, as shown in (7.26) – (7.28).

$$\frac{q_Y T_{cY}}{a_Y} I_{kY} \sin(k\omega t) = \frac{q_\Delta T_{c\Delta}}{a_\Delta} I_{k\Delta} \sin(k\omega t - \phi_\Delta) \tag{7.26}$$

$$\phi_\Delta = \sin^{-1}\left(\frac{\sqrt{3} q_Y T_{cY} a_\Delta}{q_\Delta T_{c\Delta} a_Y}\right) \cong \frac{\pi}{6} \tag{7.27}$$

$$I_\Delta = -\frac{q_Y T_{cY} I_Y}{q_\Delta T_{c\Delta}} \tag{7.28}$$

However, in order to realize such a system, additional contactors must be incorporated to switch the connections between traction and charging operation. While this might result in some losses in the system, the overall advantages obtained from the machine compensates for it. Thus, for a balanced set of 3–phase inductances of the star connected winding set, the induced voltages during charging will be balanced since the effect of the salient rotor is completely eliminated by the delta connected winding set. Therefore, it is expected that the machine will have near zero torque and balanced voltages during charging operation.

In order to validate the proposed design, the electromagnetic model of the 39–slot, 16–pole machine designed in the Chapter 6 was implemented. The major constraints are to avoid rotor core saturation and magnet demagnetization with the objectives of balanced voltages and reduced oscillating torque during charging. The machine was analyzed for an input current of 120 A at 60 Hz frequency emulating a grid supply. Using (7.28), the induced currents in the delta winding set was calculated to be 70 A. Fig. 7.12(a) illustrates the balanced induced voltages in both the winding sets and Fig 7.12(b) shows the oscillating torque waveform observed in the machine. The average oscillating torque was found to be 0.1 Nm while the peak–to–peak oscillating torque was 3.67

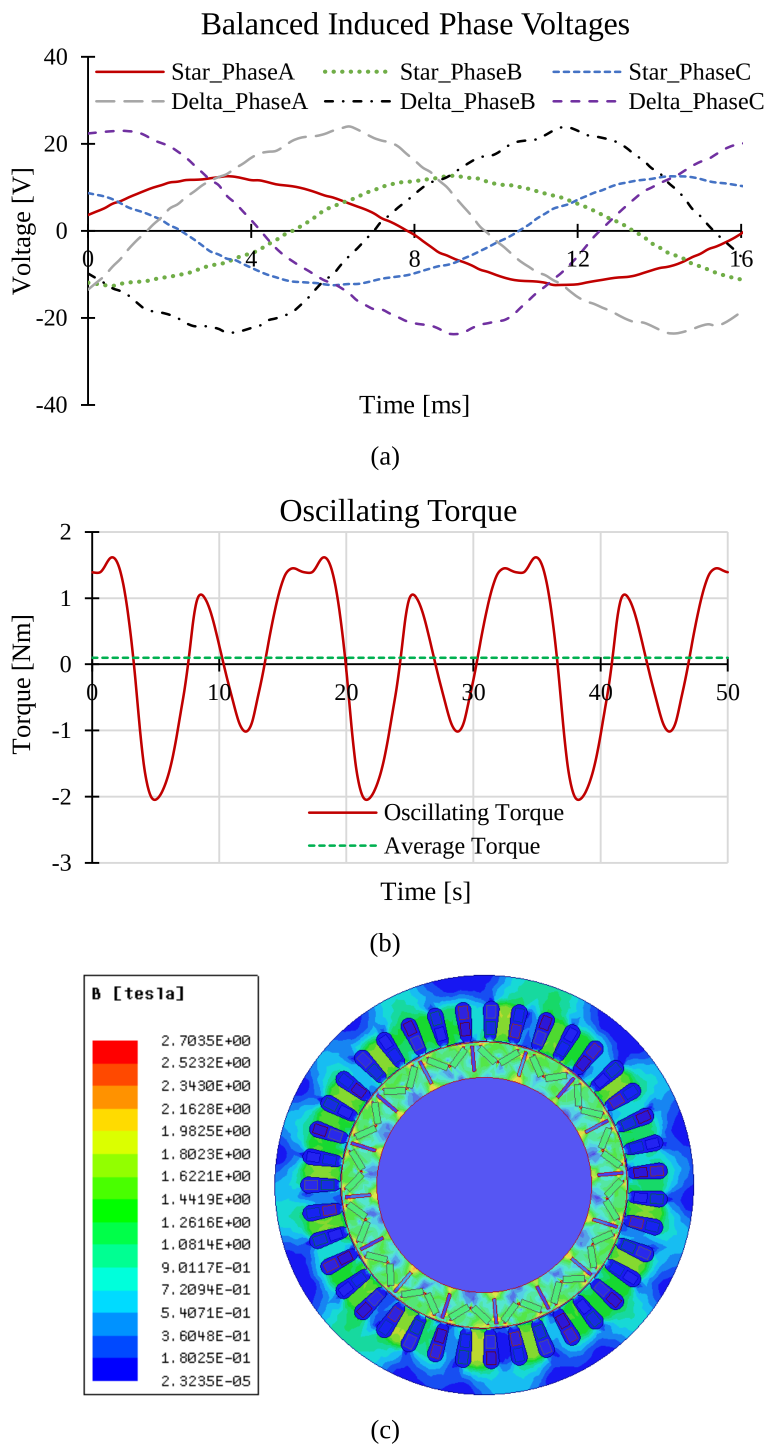

Fig. 7.12. Performance analysis of 39–slot, 16–pole star–delta wound machine during charging operation. (a) Induced voltages. (b) Oscillating torque. (c) Saturation map.

Nm which can be easily accommodated by the inertia of the machine. Thus, compared to the machine with asymmetrical damper bars, the peak–to–peak oscillating torque is significantly reduced. The saturation map of the motor during charging conditions is indicated in Fig. 7.12(c) and it can be seen that rotor core and magnet are all well within the saturation limits. The average rotor losses during charging operation was found to be 2.75 W which is significantly lower than that of the machine with damper bars. The machine's traction operation performance characteristics have already been analyzed in the previous chapters and it was seen that the machine is capable of satisfying all the desired targets. Thus, based on the analysis, it can be concluded that the star–delta wound PMSM is ideal and well–suited for both traction and integrating charging operation.

7.6. Conclusions

In this chapter, damper bars are introduced in the IPMSM rotor to overcome the effects of unbalanced voltages during integrated charging. While symmetrical dampers compensate for the machine saliency, voltage unbalances still exist due to unequal stator phase flux linkages. Conversely, asymmetrical dampers result in relatively more balanced voltages during charging but lead to reduction of useful electromagnetic torque production during traction condition. Therefore, using a magnetic equivalent circuit based differential evolutionary algorithm, an optimized rotor structure for both traction and integrated charging operation was modeled and analyzed. It was observed that although higher PM volume is required to compensate for torque production, effective reduction in weight and cost of the vehicle by eliminating an on–board charger proves to be highly advantageous. Further investigations on the effects of torque oscillations on the motor lifetime, noise and vibrations including design and optimization solutions for minimizing the large torque oscillations produced during integrated charging is set as future work.

Based on the analysis conducted on damper bars for integrated charging application and understanding the challenges and drawbacks of such a configuration, a combined star–delta wound PMSM was studied for charging operation. It was observed that the machine results in near zero oscillating torque, balanced voltages and significantly low rotor core losses during charging operation. Further, considering the advantages obtained during traction operation, it can be concluded that the star–delta wound PMSM is well–suited for both charging and traction operation. A system–level analysis incorporating the machine for integrated charging to maintain unity power factor, low THD levels with proper system modulation and control and control is set as future work.

7.7. References

[1] S. Mukundan, H. Dhulipati, K. L. V. Iyer, C. Lai, K. Mukherjee, and N. C. Kar, "Comparative performance analysis of 3–phase IPMSM rotor configurations with dampers for integrated charging application in EVs," in proc. of *43rd Annual Conference of the IEEE Industrial Electronics Society*, Beijing, China, 2017, pp. 1856–1861.

[2] C. Lai, K. L. V. Iyer, K. Mukherjee, and N. C. Kar, "Analysis of electromagnetic torque and effective winding inductance in a surface mounted PMSM during integrated battery charging operation," *IEEE Transactions on Magnetics*, vol. 51, no. 11, 2015.

[3] E. Subotic, N. Bodo, and E. Levi, "Single–phase on–board integrated battery chargers for EVs based on multiphase machines," *IEEE Transactions on Power Electronics*, vol. 31, no. 9, pp. 6511–6523, 2016.

[4] S. Haghbin, S. Lundmark, M. Alakula, and O. Carlson, "An isolated high–power integrated charger in electrified–vehicle applications," *IEEE Transactions on Vehicular Tech.*, vol. 60, no. 9, pp.4115–4126, 2011.

[5] L. De Sousa, B. Silvestre, and B. Bouchez, "A combined multiphase electric drive and fast battery charger for electric vehicles," in proc. of *IEEE Vehicle Power and Propulsion Conference*, Lille, 2010, pp. 1–6.

[6] A. Bruyère *et. al.*, "A multiphase traction/fast–battery–charger drive for electric or plug–in hybrid vehicles: Solutions for control in traction mode," in proc. of *IEEE Vehicle Power and Propulsion Conference*, Lille, 2010, pp. 1–7.

[7] E. Levi, R. Bojoi, F. Profumo, H. A. Toliyat, and S. Williamson, "Multiphase induction motor drives – A technology status review," in proc. of *IET Electric Power Applications*, vol. 1, no. 4, pp. 489–516, 2007.

[8] S. Haghbin, K. Khan, S. Zhao, M. Alakula, S. Lundmark, and O. Carlson, "An integrated 20–kW motor drive and isolated battery charger for plug–in vehicles," *IEEE Transactions on Power Electronics*, vol. 28, no. 8, pp. 4013–4029, Aug. 2013.

[9] N. Bodo *et al*., "An integrated on–board battery charger with a nine–phase PM machine," in proc. of the *42nd Annual Conference of the IEEE Industrial Electronics Society*, Florence, 2016, pp. 1767–1772.

[10] X. Lu, K. L. V. Iyer, K. Mukherjee, K. Ramkumar, and N. C. Kar, "Investigation of permanent magnet motor drives incorporating damper bars for electrified vehicles," *IEEE Transactions on Industrial Electronics*, vol. 62, pp. 3234–3244, 2015.

[11] X. Lu, K. L. V. Iyer, K. Mukherjee, and N. C. Kar, "Investigation of integrated charging and discharging incorporating interior permanent magnet machine with damper bars for electric vehicles," *IEEE Transactions on Energy Conversion*, vol. 31, pp. 260–269, March 2016.

[12] P. C. Krause, O. Wasynczuk, and S. Sudhoff, *Analysis of Electric Machinery and Drive Systems*, Wiley–IEEE Press, 2002.

[13] G. C. Jain, *Design, Operation and Testing of Synchronous Machines*, Asia Publishing House, 1966.

[14] S. Mukundan, K. L. V. Iyer, H. Dhulipati, K. Mukherjee, J. Tjong, and N. C. Kar, "Response surface methodology based optimization of surface PM machine incorporating stator slotting and PM sizing effects to extend the operating limits for direct–drive EV application," in proc. of *IEEE International Conference on Electrical Machines (ICEM)*, Lausanne, 2016, pp. 2045–2051.

[15] V. Ostovic, *Dynamics of Saturated Electric Machines*, New York, Springer–Verlag, 1989.

[16] W. Zheng, X. Wang, and Y. Pi, "Study of the fractional order proportional integral controller for PMSM based on differential evolution algorithm," in proc. of *IEEE Advanced Information Tech., Electronic and Automation Control Conference (IAEAC)*, Chongqing, 2015, pp. 201–205.
[17] A. Fatemi, N. A. O. Demerdash, D. M. Ionel, and T. W. Nehl, "Large–scale electromagnetic design optimization of PM machines over a target operating cycle," in proc. of *IEEE Energy Conversion Congress and Exposition (ECCE)*, Montreal, QC, 2015, pp. 4383–4390.
[18] R. Krishnan, *Permanent Magnet Synchronous and Brushless DC Motor Drives*, CRC Press, 2010, pp. 3–34.
[19] S. Haghbin *et. al.*, "Grid–connected integrated battery chargers in vehicle applications: review and new solution," *IEEE Transactions on Industrial Electronics*, vol. 60, no. 2, pp. 459–473, 2013.
[20] K. L. V. Iyer, S. Mukundan, H. Dhulipati, K. Mukherjee, B. Minaker, and N. C. Kar, "Design considerations for permanent magnet machine drives for direct–drive electric vehicles," in proc. of *IEEE International Electric Machines & Drives Conference (IEMDC)*, Idaho, 2015, pp. 1170–1176.
[21] C. Lai, G. Feng, K. Mukherjee, and N. C. Kar, "Investigations of the influence of PMSM parameter variations in optimal stator current design for torque ripple minimization," *IEEE Transactions on Energy Conversion*, vol. 32, no. 3, pp. 1052–1062, 2017.

Chapter 8

Performance Validation of Proposed Fractional–Slot Star–Delta Wound Interior PMSM

8.1. Introduction

In this chapter, in order to assess the proposed machine's traction capability, a drive–cycle based analysis is conducted for common drive cycles including urban, highway and worldwide lightweight test cycle (WLTC) for a commercially available Ford Focus vehicle. Motor performance characteristics in terms of torque–speed characteristics and maximum energy density efficiency over the selected drive cycles will be presented. Further, considering the comprehensive performance analysis conducted in the previous chapters, a prototype of the scaled–down 3–phase fractional–slot star–delta wound interior permanent magnet motor will be developed and validated experimentally. This chapter presents the details of the developed prototype and results obtained from experimental verification at various operating conditions. Subsequently, understanding the capabilities and challenges in the developed scaled–down prototype, a full–scale design with traction level ratings highlighted in Chapter 2, will be developed and analyzed using finite element analysis. Further recommendations for design improvement, future work and analysis will also be summarized towards the end of the chapter.

8.2. Drive Cycle Performance Analysis of Proposed Scaled–down PMSM

Drive cycle based performance analysis is an important aspect to evaluate traction machines. In this section, drive cycle analysis of the proposed scaled–down PMSM will be presented for a commercially existing Ford Focus electric vehicle. Drive cycles are a data series of speed variations as a function of time which are used as input to a particular vehicle dynamic model and translated to the required motor torque and speed points [1]. The desired wheel torque is initially calculated from the tractive forces acting on the vehicle which include the aerodynamic drag, rolling resistance, friction and force due to gravity [2]. Further, using the gear ratio of the vehicle under consideration, the desired motor torque is calculated from the wheel torque [3]. The relevant equations are highlighted in Chapter 2. While the full–scale machine ratings were fixed based on the drive cycle analysis for a Ford Focus electric vehicle, it is important to verify if the scaled–down motor is also capable of satisfying all the drive cycle requirements. The vehicle dynamics model parameters implemented for analysis are summarized in Table 8.1 [4]. Since the machine

TABLE 8.1
FORD FOCUS VEHICLE PARAMETERS [4]

Parameter	Value	Parameter	Value
Vehicle Mass	1700	Density of Air	1.202
Wheel Radius	0.3284 m	Drag Coefficient	0.33
Gear Ratio	7.8	Gravitational Acceleration	9.81
Frontal Vehicle Surface Area	2.77 m^2	Rolling Resistance Coefficient	0.013
Transmission Efficiency	98%	Road Grade	$0^o – 3^o$
Vehicle Speed [m/s]	Varying	Wind Speed [m/s]	0

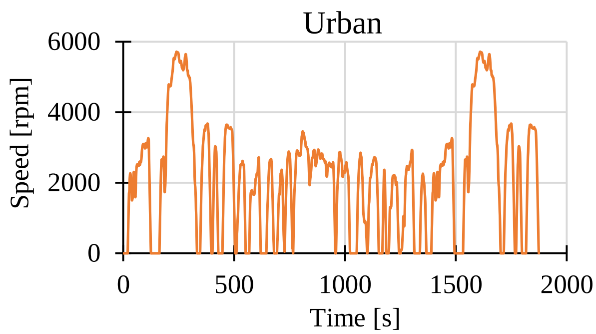

(a)

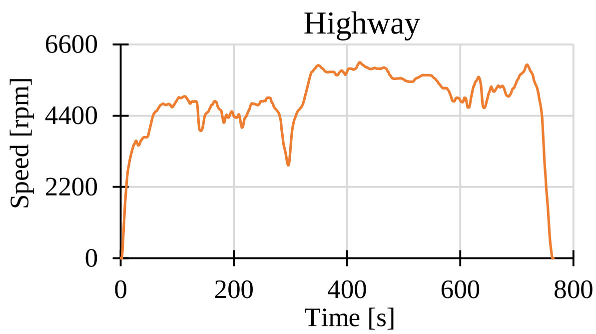

(b)

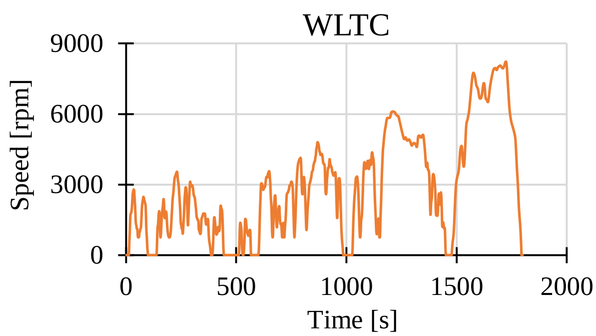

(c)

Fig. 8.1. Drive cycle characteristics used for analysis. (a) Urban. (b) Highway. (c) WLTC.

TABLE 8.2
DRIVE CYCLE CHARACTERISTICS

Parameter	Urban	Highway	WLTC
Total Duration [s]	1,874	765	1,800
Peak Motor Speed [rpm]	5716	6,038	8,224
Peak Motor Torque [Nm]	119.7	114.2	137.5
Peak Motor Power [kW]	38.8	31.9	50.3

under consideration is a high–speed motor, the urban, highway and worldwide lightweight test cycle (WLTC) drive cycles emulating real–life driving conditions are considered for analysis as shown in Fig. 8.1 and the characteristics are summarized in Table 8.2. For the calculated drive cycle torque speed points over the entire operating range, performance in terms of torque–speed characteristics and maximum energy density efficiency are analyzed for the developed machine.

From Table 8.2, it can be seen that to satisfy the maximum torque and power values of the drive cycles, the motors peak characteristics have to be considered. Thus, the torque–speed characteristics are obtained for a peak current of 196.6 A. In order to estimate the maximum drive cycle energy efficiency, each of the drive cycle torque–speed points were overlaid on the efficiency maps over the entire torque–speed range of the proposed PMSM. Figs. 8.2(a), (b) and (c) illustrate the overlaid torque–speed points on the corresponding efficiency maps for the urban, highway and WLTC drive cycles respectively. The maximum drive cycle energy efficiency thus obtained for all the 3 drive cycles considered was found to be about 97%. Although the maximum energy efficiency of the machine is well above 95%, the machine cannot be operated at peak characteristics for a prolonged period of time due to thermal and demagnetization issues.

Thus, to distinguish the percentage of the drive cycle which require the motor's peak operation, the drive cycle torque speed points were overlaid on the motor's peak and continuous torque–speed envelopes as illustrated in Figs. 8.3(a), (b) and (c). It can be seen that almost all the torque–speed points are satisfied by the motor's continuous operation for the highway drive cycle. However, in case of the urban drive cycle, almost 50% of the drive cycle torque points within the base speed lie under the peak operation envelope. Similarly, in the WLTC cycle, 50% of the torque points over the entire operating speed range can only be provided under the motor's peak operating conditions. While the direct impact on the motor and the amount of battery savings can be calculated from the amount of time the drive cycle operates under the motor's peak operation, it can be concluded that even the scaled down motor is capable of satisfying the conventional drive cycle operation.

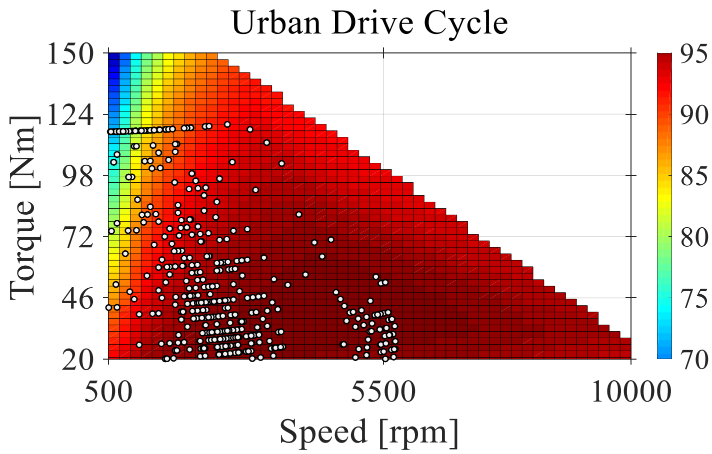

(a)

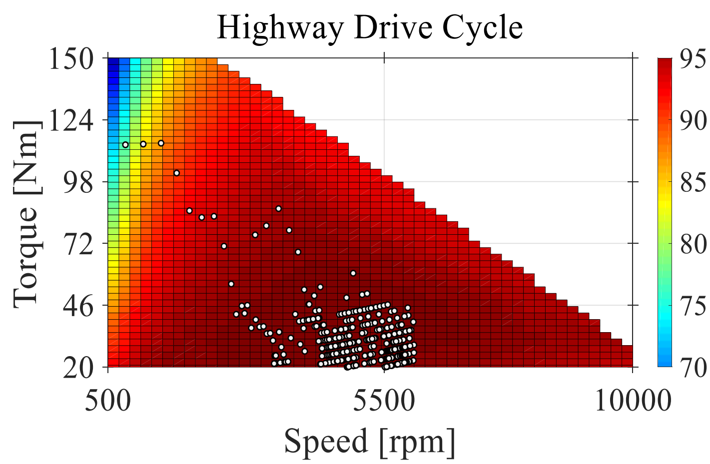

(b)

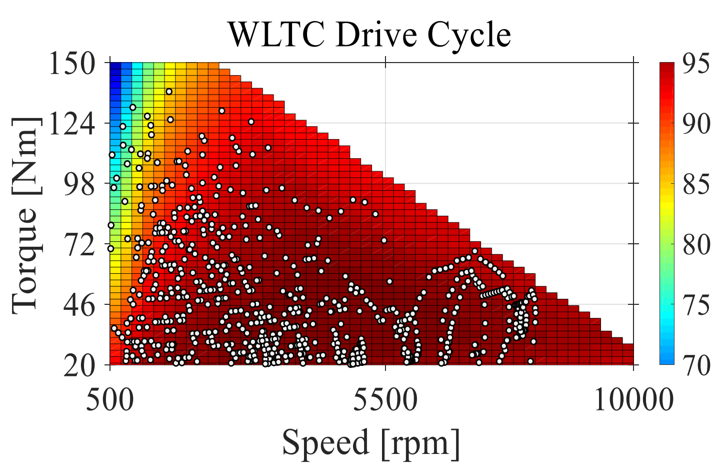

(c)

Fig. 8.2. Drive cycle torque speed points overlaid on the motor's peak efficiency characteristics to calculate the maximum drive cycle energy efficiency. (a) Urban. (b) Highway. (c) WLTC.

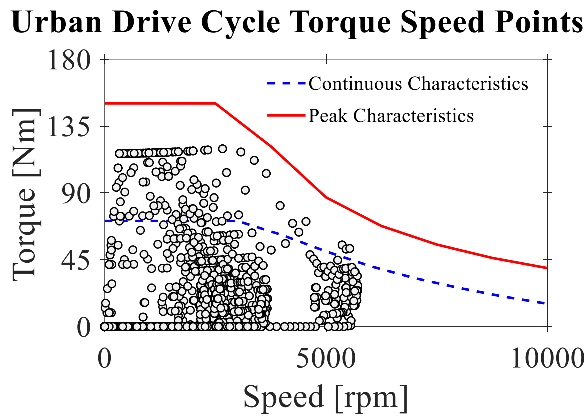

(a)

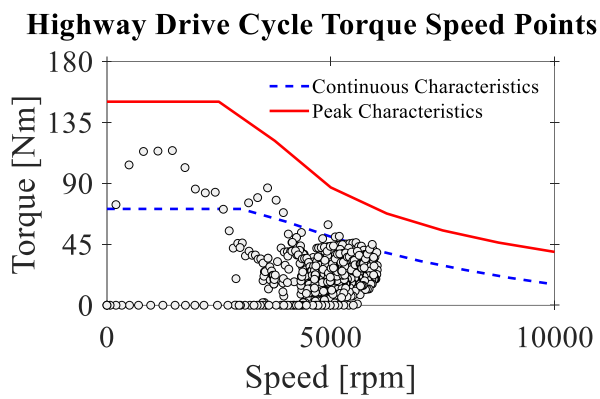

(b)

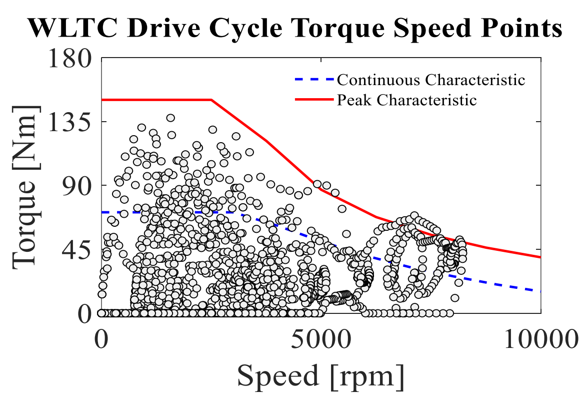

(c)

Fig. 8.3. Drive cycle torque speed points overlaid on the motor’s peak and continuous torque–speed envelope. (a) Urban. (b) Highway. (c) WLTC.

8.3. Prototype Development of the Proposed Scaled–down PMSM

Thus, based on the performance analysis conducted in the previous chapters, the proposed scaled–down 22 kW fractional–slot, star–delta wound, interior PMSM was prototyped. The stator and rotor core laminations were cut using a waterjet and stacked together to form the 39–slot stator and 16–pole rotor cores as shown in Figs. 8.4(a) and (b) respectively. A conventional M19 29G electrical steel material was used for the cores. On the completed stator core, copper conductors were wound to form the proposed fractional–slot star–delta winding configuration. During initial design and finite element analysis, 8.5 AWG and 11.5 AWG solid conductors were chosen for the star and delta winding conductors respectively. However, during prototyping, to ease the mechanical bending process around the slots, the conductors were made using 1.06 mm wire strands. Using stranded conductors also provides added advantages of reducing the AC skin effects during high–frequency operation which is ideal for high–speed traction application [5]. The inherent advantage of end–winding length reduction expected from the proposed winding configuration with coil pitch of 2 which was highlighted in Chapter 3, can be clearly seen from Figs. 8.5(a) and (b) respectively. The completed stator core with the proposed winding

(a) (b)

Fig. 8.4. Developed stator and rotor cores using M19 29G electrical steel material. (a) 39–Slot stator. (b) 16–Pole Rotor.

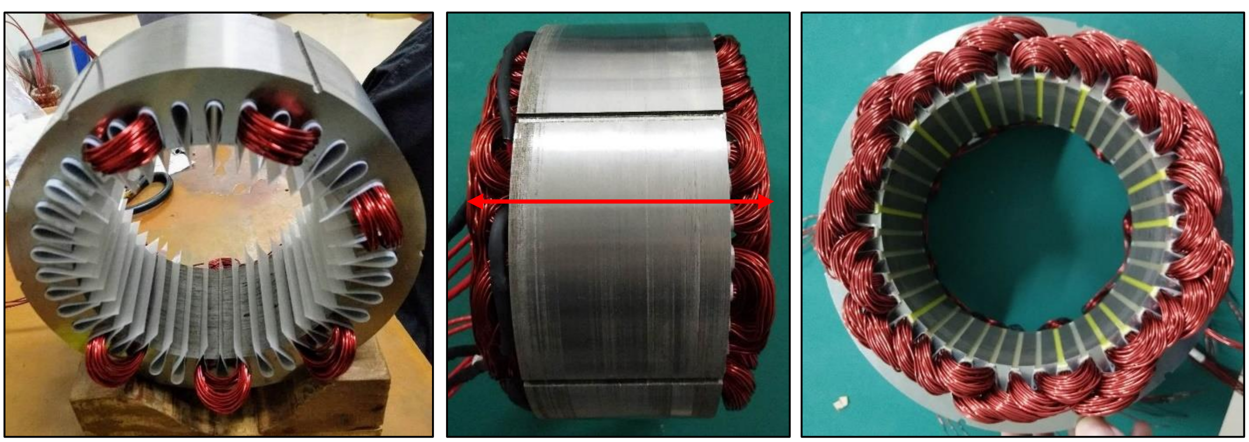

(a) (b) (c)

Fig. 8.5. Proposed fractional–slot star–delta winding with copper conductors. (a) Initial phase winding with coil pitch of 2. (b) Side view of the completed stator core with windings highlighting the short end–winding length. (c) Completed stator core with proposed windings.

configuration is shown in Fig. 8.5(c).

A rectangular block of NdFeB magnet as shown in Fig. 8.6(a) is fitted in the rotor slot to form

(a) (b)

Fig. 8.6. Rare–earth material based NdFeB magnets. (a) 1 rectangular piece of magnet to be fit into rotor slots. (b) Total block of magnet pieces with north and south magnet orientations which will form the 16 rotor poles.

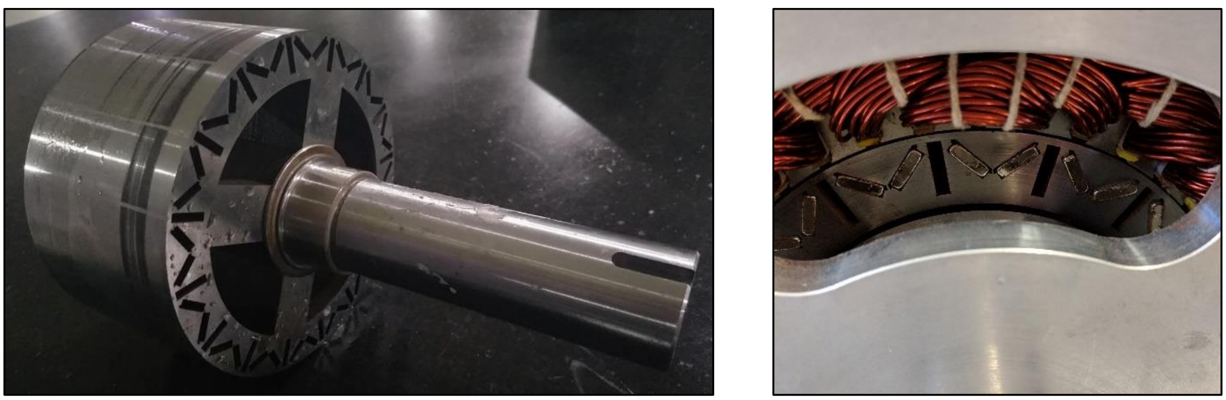

(a) (b)

Fig. 8.7. Proposed rotor topology with flux barriers. (a) Rotor with shaft. (b) Rotor with PMs inserted.

(a) (b)

Fig. 8.8. Aluminum based cooling sleeve and motor housing developed. (a) Cooling sleeve with helical cooling channels. (b) Motor casing.

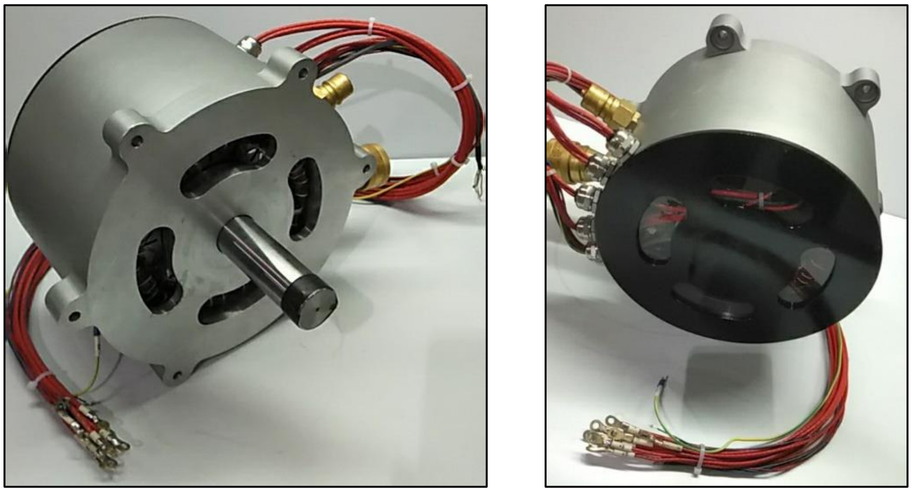

(a) (b)

Fig. 8.9. Proposed scaled–down 22 kW fractional–slot, star–delta wound, interior PMSM prototype.

the v–shaped magnet configuration. To form 16–pole in the rotor, 16 pieces each were magnetized in the North and South directions respectively. Subsequently, the rotor shaft was cold compressed in the rotor core. An aluminum based cooling sleeve with helical cooling channels as shown in Fig. 8.8 was also cold compressed onto the stator core surface. Finally, a cylindrical aluminum motor housing was fitted over the cooling sleeve encompassing the entire motor structure. The completed prototype is shown in Fig. 8.9. The nameplate details of the motor describing the continuous power, rated voltage and current, operating speed range, material and coolant details were etched on the motor casing using laser.

8.4. Experimental Validation of the Developed Scaled–down PMSM Prototype

A. Preliminary Verifications Under Stationary Conditions

In this section, preliminary analysis of the motor conducted under stationary conditions will be presented including measurement of the motor weight, DC resistance test and DC inductance test. From finite element simulations, using the electromagnetic model of the developed prototype, the active weight of the motor, without the rotor shaft, cooling channel and housing was found to be 11.6 kg. The segregation of the individual weights is summarized in Table 8.3. The weight of the physical rotor and shaft, without the magnets was measured to be 10 pounds or 4.5 kg equivalent as shown in Fig. 8.10(a) which is close to the rotor net weight obtained from simulation. Thus, the rotor shaft weight can be calculated to be about 1.67 kg. However, when the physical prototype with the casing and cooling sleeve was measured using a weighing scale as shown in Fig. 8.10(b), the total weight was found to be about 55 pounds which is equal to 25 kg roughly.

TABLE 8.3
SEGREGATION OF WEIGHTS OF MOTOR PARTS OBTAINED FROM FEA

Motor Part	**Weight [kg]**
Rotor Core	2.83
Magnet	0.53
Stator Core	6.1
Stator Copper	2.14

(a) (b)

Fig. 8.10. Weight measurement of the developed physical structure using a weighing scale. (a) Rotor with shaft and no magnets. (b) Full motor.

Thus, the casing and cooling sleeve alone contribute to 47% of the motor's total weight reducing the torque density from 13 to 6 Nm/kg. While the effective motor weight can be reduced by implementing innovative light–weight materials for the motor casing such as carbon based materials [6], the scope of the thesis is limited to conventionally used aluminum motor casing. It is to be noted that even with the total motor weight, the torque density obtained for the scaled down prototype is a nominal value for typical commercially available traction motors.

The phase resistance of the machine was measured using a Keithley 3330 LCZ meter. Since we had access to all the phase windings from both the star and delta sets, first, the individual star and delta winding resistances were measured. Later, the windings were connected to form the 3–phase star–delta configuration and the terminal resistances were measured and verified using both finite element simulation and the measured individual winding resistances. Figs. 8.11(a) and (b) show the measured phase A resistance of the star and delta windings respectively and Fig. 8.11(c) shows the measured AB terminal resistance of the star–delta wound machine. Resistance across all the phases and lines were measured and verified to be equal. Thus, using basic Kirchoff's laws as in (8.1), the measured star and delta phase resistances of 35 mΩ and 92 mΩ result in a terminal

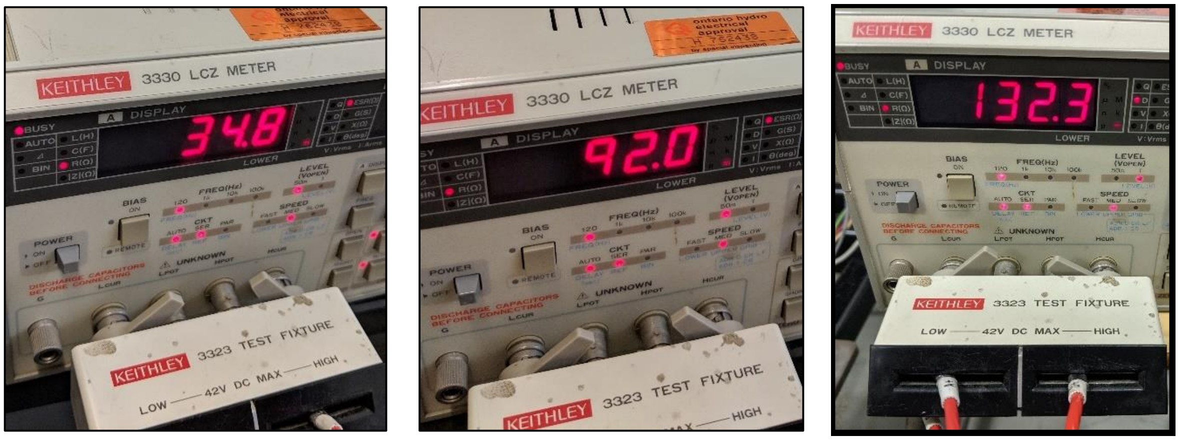

(a) (b) (c)

Fig. 8.11. DC Resistance measurement using LCZ meter. (a) Phase resistance of star winding. (b) Phase resistance of delta winding. (c) Terminal resistance of combined star–delta winding.

resistance of 131.33 mΩ when connected as a combined star–delta, which is very close to the measured terminal resistance of 132.3 mΩ. From FEA, a terminal resistance of 125 mΩ was obtained resulting in a 5.5% error from experimental value which can be attributed to mismatch of material properties.

$$R_{AB} = R_{Y_A} + \frac{R_{\Delta_A}}{3} \tag{8.1}$$

Similar to the DC resistance test, a DC inductance test was performed using the same LCZ meter which gives the phase inductance of the windings at a fixed frequency. The rated frequency of the motor is 400 Hz. Therefore, the LCZ meter was set to provide a frequency of 120 Hz which is relatively close to the rated frequency. The same procedure as that of resistance test was applied with the inductance measurement as well. The star and delta winding phase A inductances were measured to be 125.6 µH and 509 µH respectively as shown in Figs. 8.12(a) and (b). Thus, the calculated terminal AB inductance of the combined star–delta winding is 590.53 µH. However, the measured terminal AB inductance of the star–delta connected machine was found to be 644.5 µH as shown in Fig. 8.12(c). This can be attributed to the fact that, in case of combined star–delta connection, when a current/voltage is applied across a line, circulating currents are induced in the delta winding set, which results in a mutual inductance effect across the measured lines. However, using Kirchoff's law, this mutual effect cannot be considered and hence a discrepancy of 8.4% is observed. On the other hand, using FEA, the terminal inductance of the star–delta wound machine at 120 Hz was found to be 688.7 µH which is slightly higher than the measured value. Similar to the resistance test, this error could be because of the material properties considered in simulation.

(a) (b) (c)

Fig. 8.12. DC Inductance measurement using LCZ meter. (a) Phase inductance of star winding. (b) Phase inductance of delta winding. (c) Terminal inductance of combined star–delta winding.

Therefore, it can be seen that for all the stationary tests conducted, the experimental values are very close to the results obtained from FEA.

B. No–Load Operating Conditions

In this section, a no–load analysis of the motor conducted up to base speed is presented. The prototyped motor is coupled to a dynamometer and allowed to spin freely without any electrical load as shown in Fig. 8.13(a). The speed of the dynamometer is controlled and varied in steps and the induced no–load voltages at the terminals are measured. For a PMSM, from this no–load or back EMF test, the PM flux linkage parameter, λ_{pm} can be calculated using (8.2) where E_{ph} is the peak no–load induced phase voltage, ω_r is the electrical speed in rad/s corresponding to the rotor's mechanical speed in rpm. Also, based on the waveform quality of the induced voltages and the corresponding harmonic spectrum, the dominant space harmonic orders in the machine can be determined. The variation of induced voltages with increase in speed is shown in Fig. 8.13(b) and the variation of the PM flux linkage with increase in speed is illustrated in Fig. 8.13(c) up to the motor's base speed of 3,000 rpm. The observed trends are in line with conventional PMSM operating characteristics and λ_{pm} was calculated as 0.045 Wb.turns. Fig. 8.13(d) compares the calculated PM flux linkages from the induced voltages obtained experimentally and from FEA for a sample speed range. It can be seen that the results are in close agreement and the average percentage error in PM flux linkage was found to be 2.09% which is within the acceptable range.

Further, Fig. 8.13(e) shows the measured induced voltages at a sample speed of 1,500 rpm. As expected from Chapter 4, the waveform is almost perfectly sinusoidal with very low space harmonic contents. The harmonic spectrum of the corresponding voltages is shown in Fig. 8.13(f).

It can be seen that the peak value of fundamental voltage is 93.77 V which corresponds to the rms voltage of 66.3 V. Also, the space harmonic content in the machine is significantly low and the maximum harmonic magnitude is about 0.5% of the fundamental voltage magnitude indicating superior waveform quality. The total harmonic distortion (THD) up to 20th harmonic order was

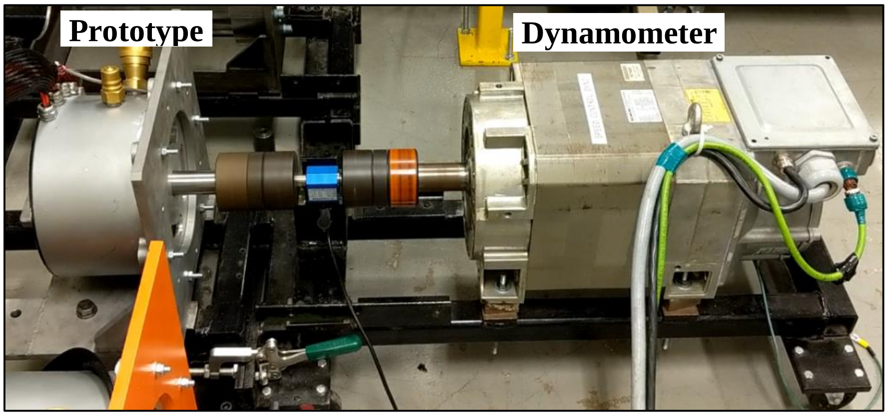

(a)

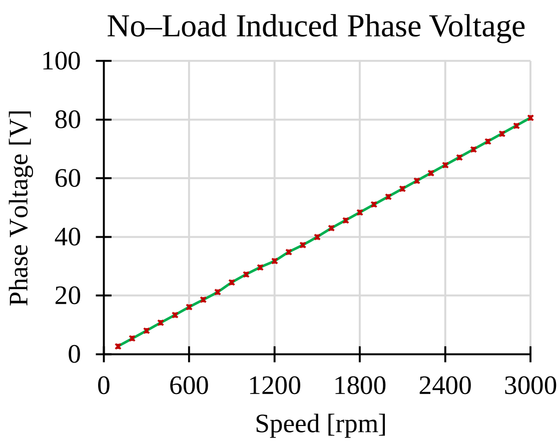

(b)

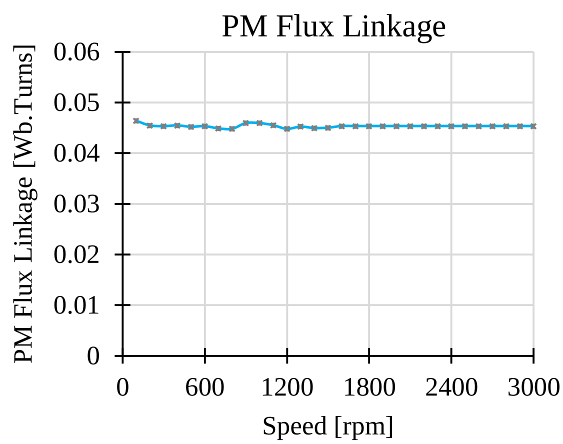

(c)

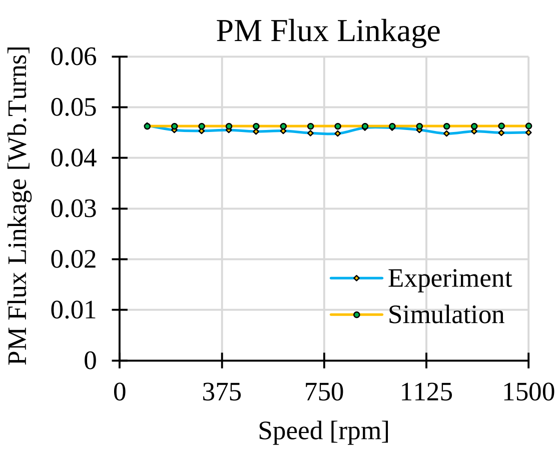

(d)

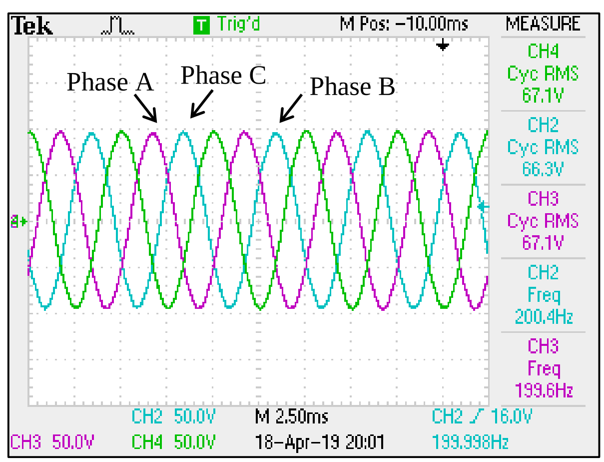

(e)

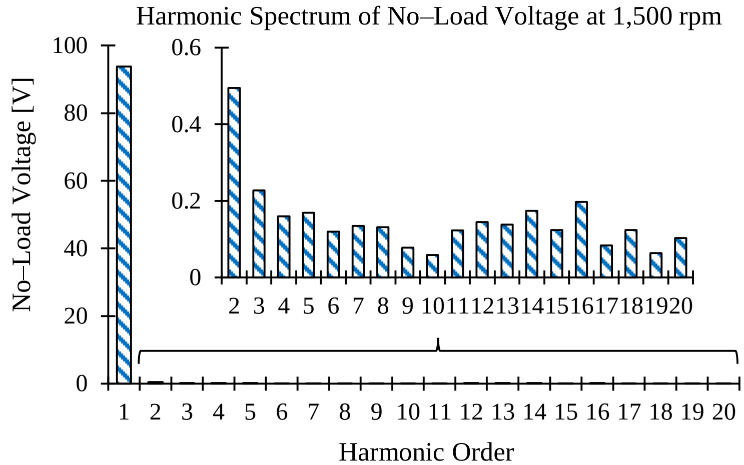

(f)

Fig. 8.13. Experimental validation of the scaled–down PMSM prototype under no–load conditions. (a) Prototype coupled to the dynamometer. (b) Variation of no–load induced voltage with speed up to base speed of 3,000 rpm. (c) Variation of PM flux linkage with speed up to base speed of 3,000 rpm. (d) Comparison of experimentally obtained PM flux linkage with simulation results. (e) Sample harmonic spectrum of no–load voltage at 1,500 rpm highlighting the low space harmonic content.

0.816 highlighting the low spatial harmonic content in the proposed star–delta winding configuration.

C. Performance Analysis Under Load Conditions

In this section performance analysis of the machine conducted under loaded conditions will be presented. The machine was operated under both generating and motoring modes with respective electrical and mechanical loads to determine the *dq*–axis inductances, motor voltages and currents, torque and power speed characteristics, efficiency and loss maps at various speeds. First, the machine was coupled to the dynamometer and operated as a generator with an inductive load as shown in Fig. 8.14 connected to the 3–phase machine's terminals. The inductance can be varied between 161 µH and 5.64 mH. The objective of this load test is to determine the *d*– and *q*–axis inductance parameters at different operating conditions considering the influence of armature reaction. The estimated *dq*–axis inductances will be used to calculate the field–oriented controller parameters when the prototype is operated as a motor. This method requires accurate measurement of the machine load angle (δ) and hence the machine is initially operated as a generator at no–load condition and the position sensor signal is aligned along the zero–crossing point of the Phase A emf waveform (E_{ph}) which is taken as the reference point as shown in Fig. 8.15(c). For the same speed operation, the electrical load to the machine is varied in steps. Based on the phase

(a) (b)

Fig. 8.14. Inductance load bank used in load test for parameter determination.

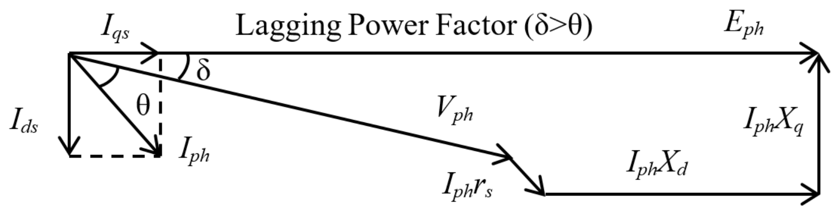

(a)

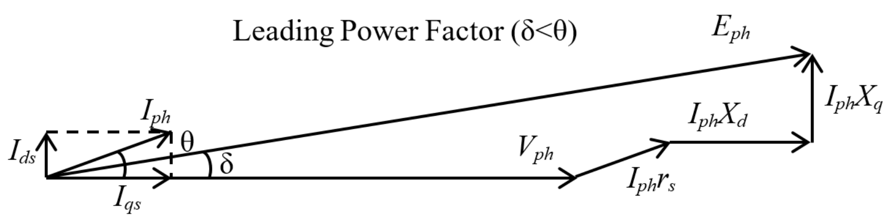

(b)

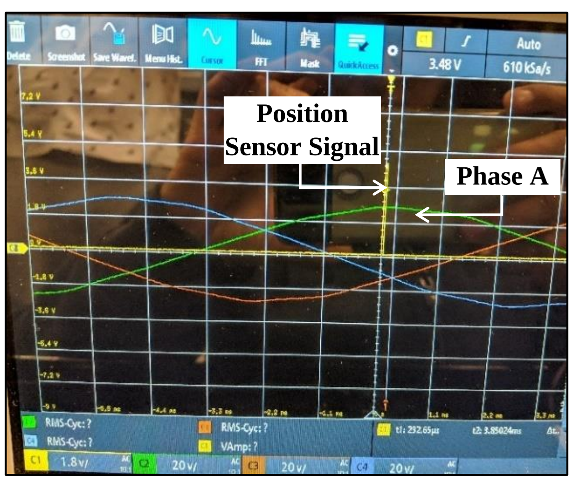

(c)

Fig. 8.15. Estimation of load angle and power factor angle. (a) Phasor diagram for lagging power factor. (b) Phasor diagram for leading power factor. (c) Aligning the zero–crossing of Phase A back emf waveform with reference position sensor signal.

displacement of the phase voltage (V_{ph}) waveforms from the reference position sensor signal, δ is determined and the power factor angle (θ) is determined by the displacement between the voltage and phase current (I_{ph}) waveforms. According to the phasor diagrams indicated in Figs. 8.15(a) and (b), depending on leading or lagging power factor, the L_d and L_q can be estimated using (8.2).

$$\left.\begin{aligned} X_d &= \frac{E_{ph} - V_{ph}\cos\delta - I_{ph} r_a \cos(\delta \pm \theta)}{I_{ph}\sin(\delta \pm \theta)} \\ X_q &= \frac{V_{ph}\sin\delta + I_{ph} r_a \sin(\delta \pm \theta)}{I_{ph}\cos(\delta \pm \theta)} \\ L_d &= X_d/(2\pi f) \\ L_q &= X_q/(2\pi f) \end{aligned}\right\} \tag{8.2}$$

The dynamometer was varied in steps of 100 rpm from 0 to 1,500 rpm for each load condition. A maximum current of 37 A was induced across the machine windings. Figs. 8.16(a) and (b) illustrate the current and voltages signals along with the position sensor signal obtained at a sample loading and operating condition. The current and voltage waveforms quality also indicates low harmonic content and hence reduced ripple content. Using (8.2), L_d and L_q were calculated at different operating conditions and compared with that obtained from simulation as seen in Figs. 8.16(c) and (d). It can be seen that the average error between experiment and simulation obtained for L_q was about 9.27% while that for L_d was 17.65%. This can be attributed to the fact that the *d*–axis flux path includes the PM magnet flux and the variation of material properties incorporated in simulation are not as accurate as the experimental data. Further, using the experimentally obtained data and simple interpolation, the *d*– and *q*–axis inductance maps over the entire operating range at varying *d*– and *q*–axis currents was estimated as seen in Figs. 8.17(a) and (b).

Subsequently, using the rated L_d and L_q of 312.67 μH and 693.92 μH respectively from the load test, the PMSM prototype was operated as a motor to determine the rated torque capability and machine efficiency. The scaled–down PMSM prototype was driven using a field–oriented control scheme under current control mode. RT–lab controller and a 9–leg IGBT inverter as seen in Figs. 8.18(b) and (d) were used to drive the motor and with the help of current and voltage sensors shown in Fig. 8.18(c), measurements were taken. A torque transducer was employed to measure the output torque of the machine. Fig. 8.18(a). shows the complete experimental test setup. The speed was varied in steps of 100 rpm and for each speed, the input current was varied in steps of 10% up to the maximum current and the corresponding voltages, currents and torque were measured to estimate the motor rated efficiency.

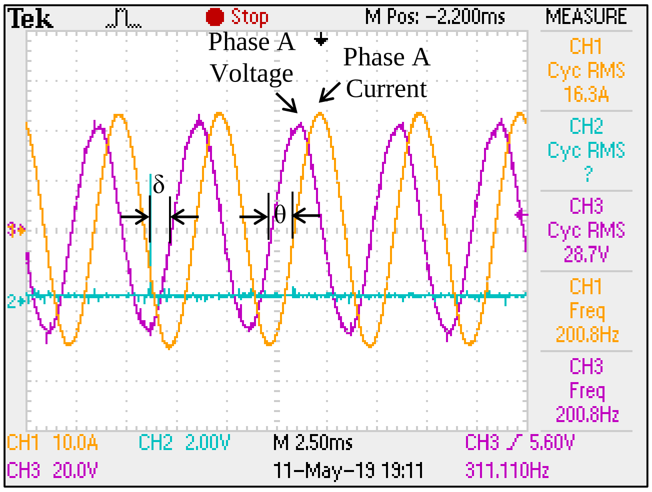

(a)

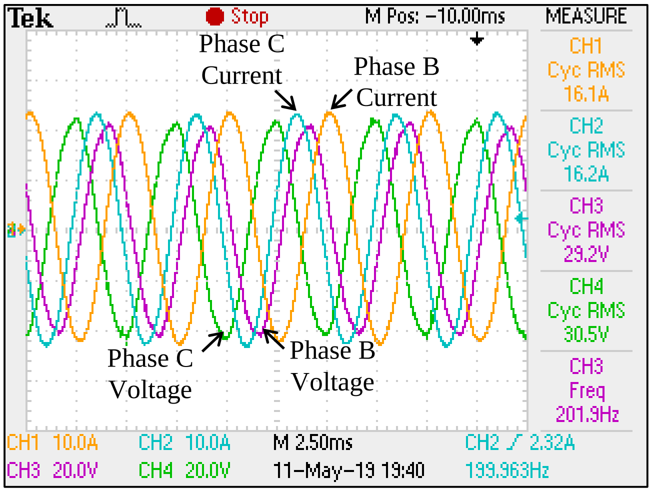

(b)

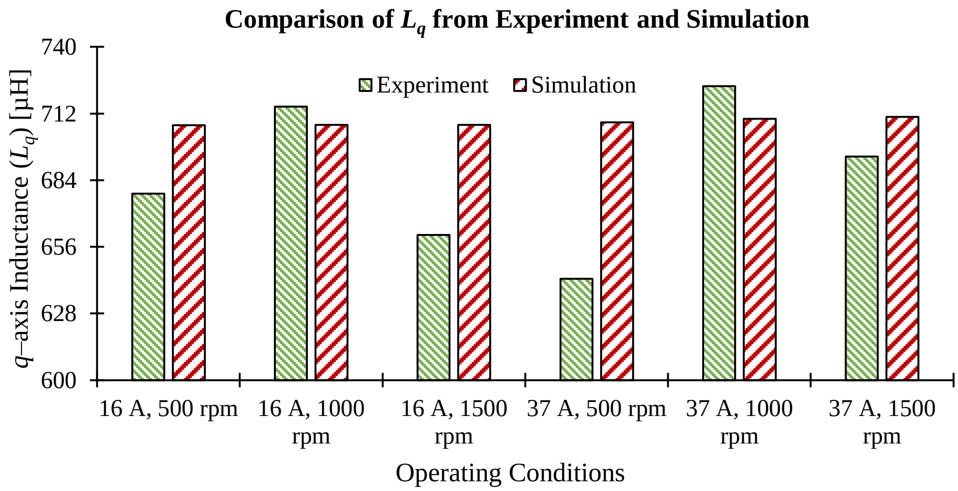

(c)

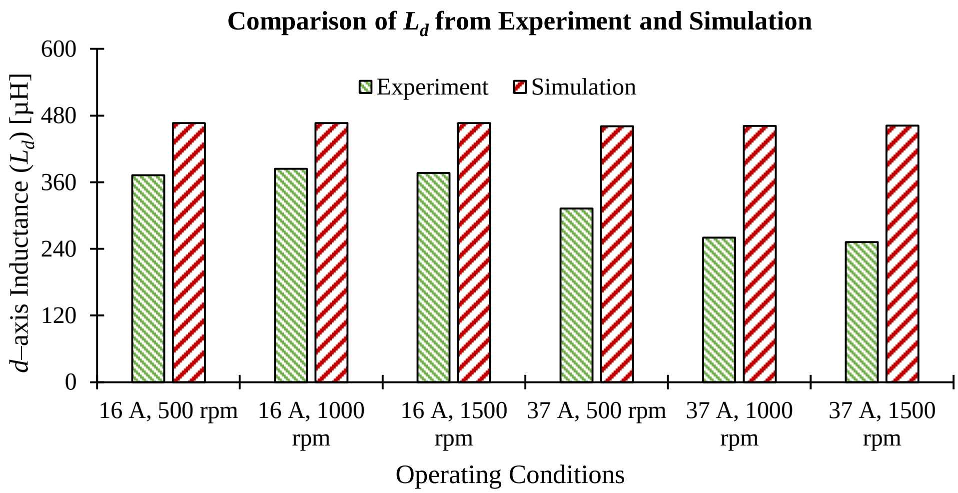

(d)

Fig. 8.16. Experimentally obtained *dq*–axis inductance parameters. (a) Sample Phase A current and voltage waveforms with the position sensor signal at 1,500 rpm. (b) Sample Phases B and C current and voltage waveforms at 1,500 rpm. (c) Comparison of L_q obtained from experiment and simulation. (d) Comparison of L_d obtained from experiment and simulation.

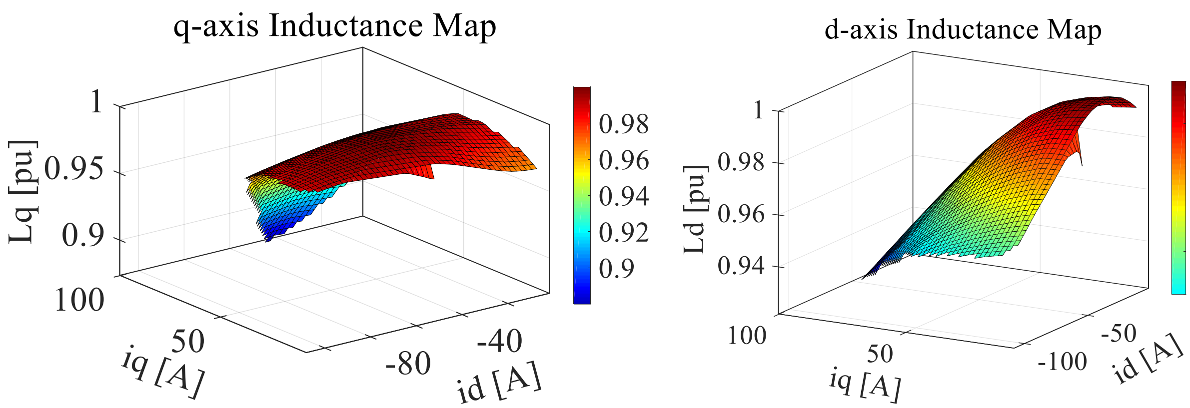

(a) (b)

Fig. 8.17. Variation of *dq*–axis inductances with currents. (a) *q*–axis inductance map. (b) *d*–axis inductance map.

Furthermore, to obtain the maximum torque per ampere, the current angle, γ, was varied from 0º to 90º for each operating current as seen in Fig. 8.19. The corresponding torque obtained at each operating condition up to a sample speed of 700 rpm is shown in Fig. 8.20 and compared with that obtained from simulation. It can be seen that the trend of constant torque operation up to the base speed is as expected from both simulation and experiment. The maximum error between the measured and simulated torque was found to be 14.45% which is well within the nominal range. Further, to verify the machine's torque ripple, the torque waveforms at two sample conditions namely low speed, low current and high current, high speed conditions were compared as seen in Figs. 8.21 and 8.22. From Fig. 8.21(a), it can be seen that the torque waveform quality at low

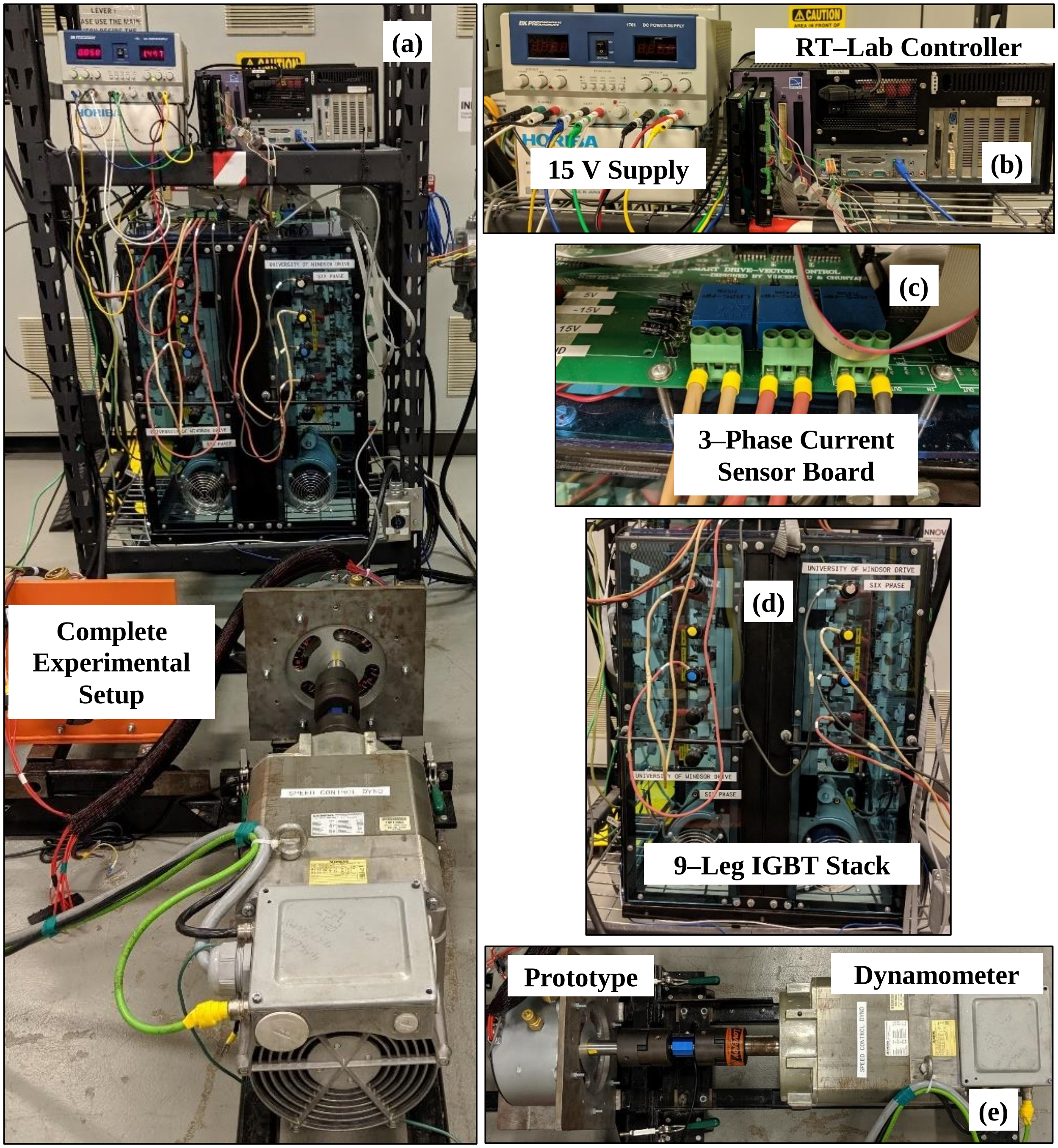

Fig. 8.18. Experimental validation of the scaled–down PMSM prototype under load conditions. (a) Complete experimental setup of the scaled–down PMSM prototype under field–oriented control scheme. (b) RT–lab controller with the 15 V DC supply. (c) 3–phase current sensor circuit board. (d) 9–leg IGBT stack inverter. (e) Scaled–down PMSM prototype coupled to the dynamometer.

speed, low current operation of 700 rpm and 10 A is not very good as expected. Further, from Fig. 8.21(b), it can be seen that the measured torque ripple is almost higher than two times the torque ripple obtained from simulation. The high torque ripple from experiment can be attributed to the fact that the motor is coupled to an induction machine dynamometer which contributes to majority of the torque ripple at low speed operation.

Furthermore, the torque ripple obtained from simulation does not include the effects of the inverter induced time harmonics resulting in a better waveform quality. Similarly, from Fig. 8.22, the torque ripple obtained from simulation and experiment are compared at high speed operation and the error was computed to be about 2.7%. It further highlights that the proposed PMSM

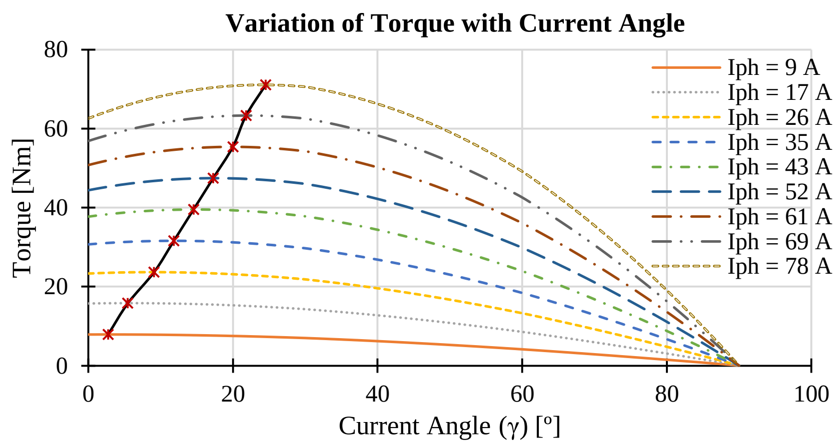

Fig. 8.19. Variation of electromagnetic torque with current angle at different operating current conditions.

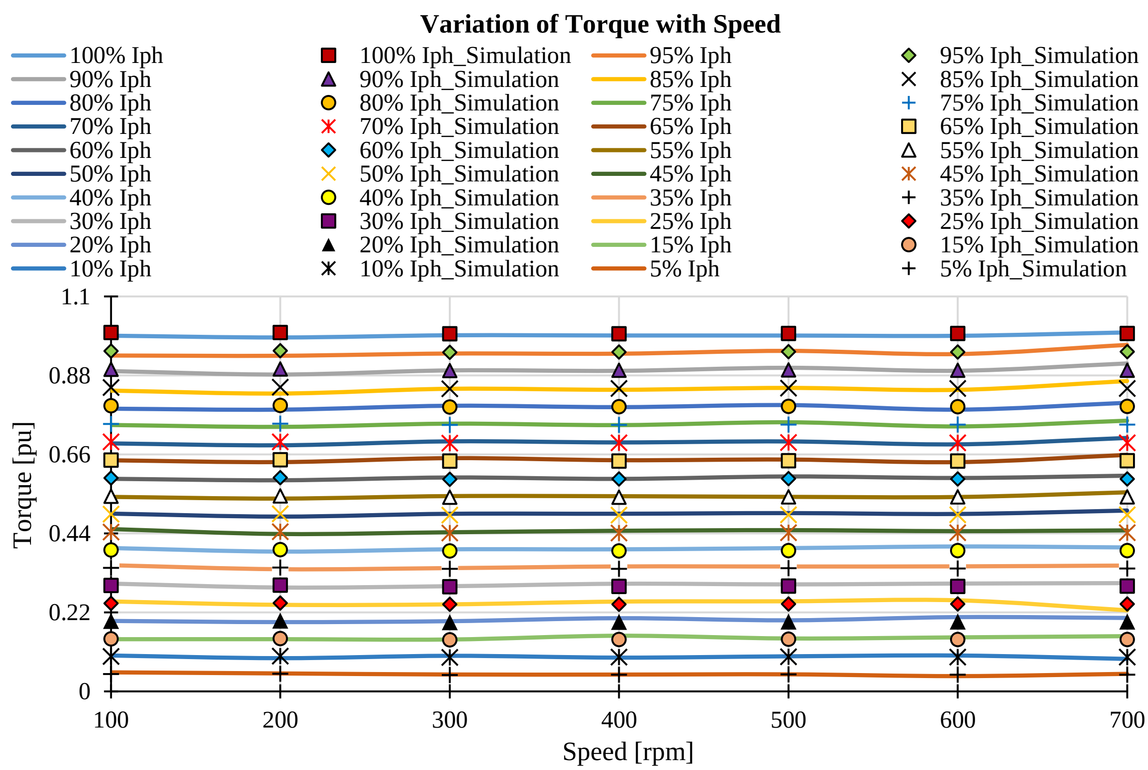

Fig. 8.20. Comparison of electromagnetic torque obtained from experiment and simulation at different speeds and currents.

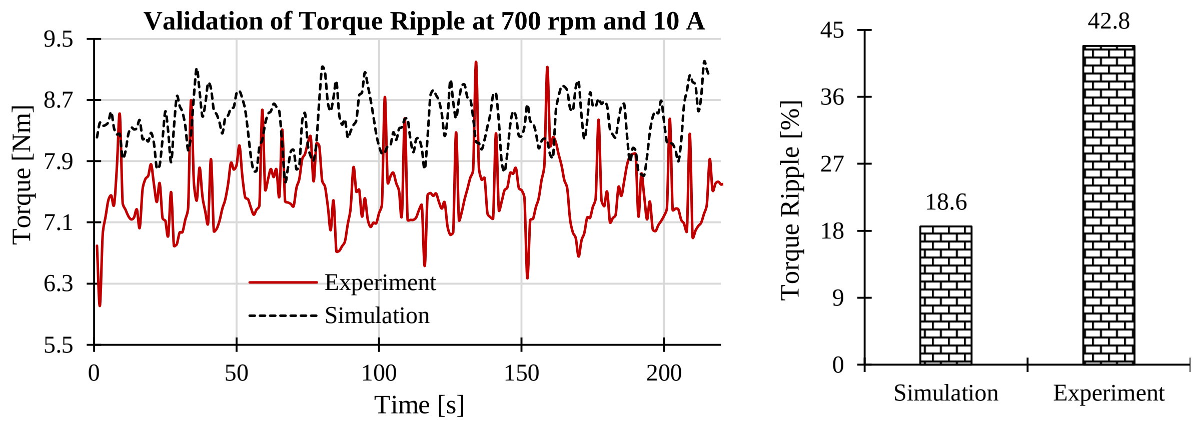

(a) (b)

Fig. 8.21. Comparison of motor torque ripple at low speed, low current operation of 700 rpm and 10 A. (a) Torque waveforms. (b) Torque ripple.

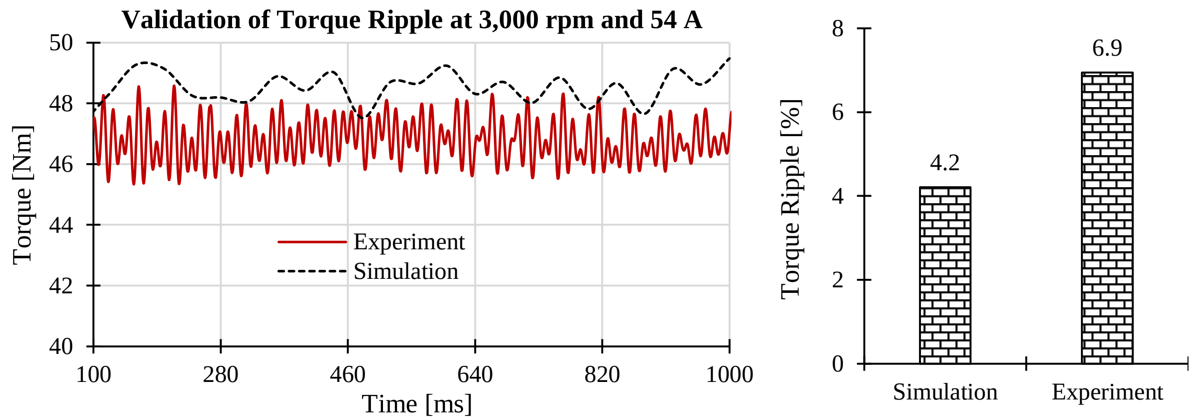

(a) (b)

Fig. 8.22. Comparison of motor torque ripple at high speed, high current operation of 3,000 rpm and 54 A. (a) Torque waveforms. (b) Torque ripple.

prototype has reduced torque ripple content thereby meeting the research objective.

Similarly, under each operating condition, the input currents and voltages were measured along with the output torque and speed to estimate the respective input and output powers and hence the motor rated efficiency. The copper losses are calculated using the measured phase currents and the corresponding phase resistances measured previously in the DC resistance test. The summation of other losses is obtained by subtracting the estimated copper losses from the difference between the measured input and output powers. Figs. 8.23(a) and (b) illustrate a sample of the measured efficiencies obtained from both experiment and simulation at 100 rpm and 700 rpm respectively. The maximum errors in measured efficiencies from simulation and experiment at 100 rpm and 700 rpm was calculated to be 5.93 and 12.47% respectively. Further,

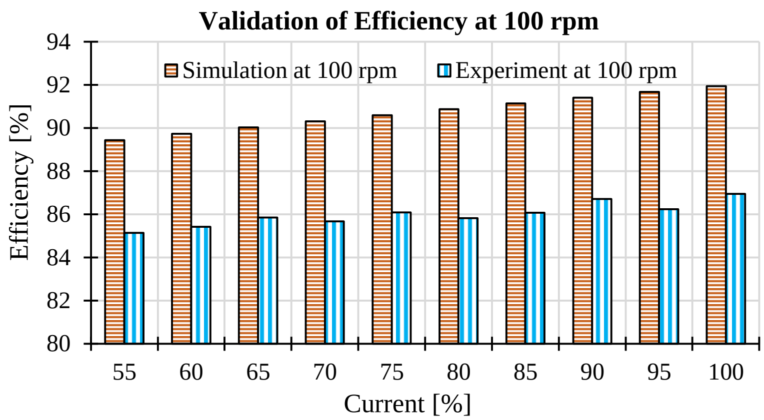

(a)

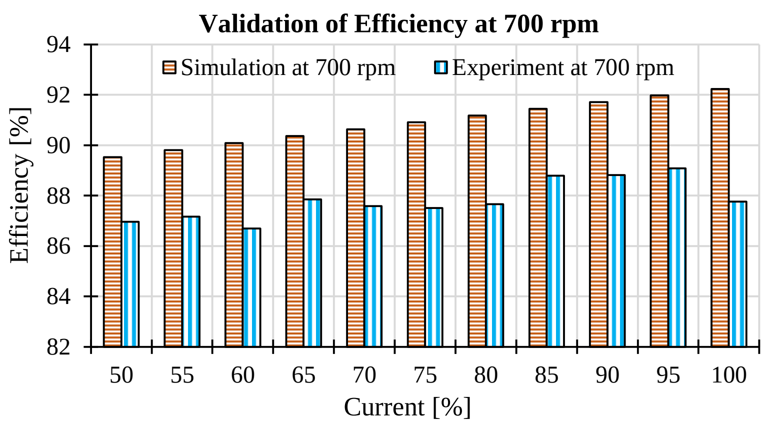

(b)

Fig. 8.23. Comparison of estimated motor efficiency obtained from experiment and simulation. (a) At 100 rpm. (b) At 700 rpm.

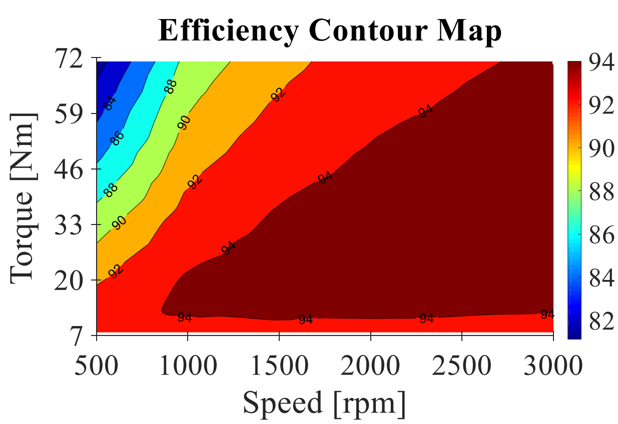

Fig. 8.24. Motor efficiency contour map up to base speed of 3,000 rpm.

using the experimentally measured efficiencies and interpolation, the efficiency contour map of the motor up to 3,000 rpm was obtained as shown in Fig. 8.24. Similarly, the motor copper losses and other losses contour maps up to 3,000 rpm were obtained as seen in Figs. 8.25(a) and (b). The

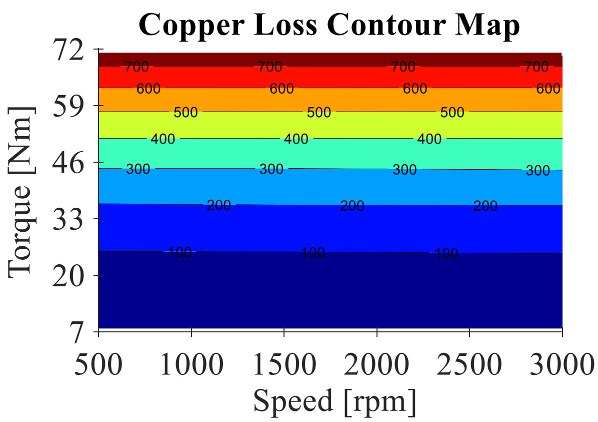

(a)

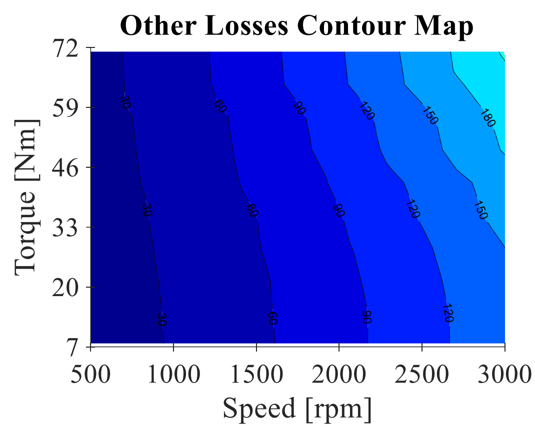

(b)

Fig. 8.25. Calculated motor loss contour maps up to base speed of 3,000 rpm. (a) Copper losses. (b) Other losses.

rated motor efficiency obtained from experiments was found to be about 95.55% which is 1.65% lesser than that obtained from simulation. Thus, it can be concluded that the developed scaled–down PMSM prototype is capable of delivering the rated torque of 71.12 Nm at 3,000 rpm with a rated efficiency of 95.55% and a rated torque ripple of about 8.76% thereby meeting all the specified research objectives summarized in Chapter 1.

8.5. Full–Scale Motor Development and Analysis

Considering the performance analysis of the developed scaled down PMSM prototype discussed above, this section proposes a full–scale motor design capable of meeting traction level requirements summarized in Chapter 1. While the developed scaled down PMSM prototype is rated for a continuous and peak power of 22 kW and 45 kW respectively, the full–scale machine must be developed for a 45 kW continuous power rating and a peak power of 100 kW. Instead of redesigning the entire motor from scratch, a few structural dimensions of the scaled down prototype can be altered as summarized in Table 8.4 and verified for the full–scale motor performance targets. To increase the current rating of the motor, the conductor diameter of the star windings was changed from 8.5 AWG to 6.5 AWG and that of the delta winding was changed from 11.5 AWG to 9.5 AWG. However, from simulation it was observed that the machine was

TABLE 8.4
STRUCTURAL TARGETS OF THE FULL–SCALE MACHINE

Parameter	Target	Value
Active Weight [kg]	< 37	28.2
Torque Density	> 6.6 Nm/kg	8.7 Nm/kg

TABLE 8.5
STRUCTURAL MODIFICATIONS OF BASELINE PMSM TOWARDS FULL–SCALE MACHINE

Parameter	Baseline	Full–Scale
Length	75 mm	120 mm
Wire Gauge	8.5 AWG	6.5 AWG
Peak Current	196.6 Arms	400 Arms

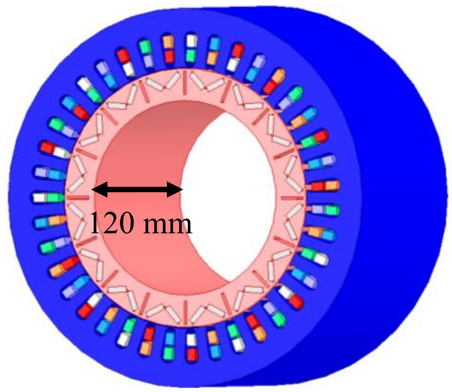

Fig. 8.26. Developed electromagnetic model of the proposed full–scale 39–slot, 16–pole interior PMSM.

still not able to meet the peak torque target of 245 Nm. To meet the torque requirements, either the PM thickness or the machine's active length can be increased. To obtain a cost effective solution, the machine's active length was increased from 75 mm to 120 mm and it was observed that the machine was capable of producing 245 Nm with a peak current of 400 A rms only. Thus, with a slight increase in the machine's active weight, the machine was capable of meeting the full–scale performance targets as seen in Table 8.5. The developed electromagnetic model of the proposed full–scale machine is shown in Fig. 8.26. The continuous and peak torque and power speed envelopes obtained from FEA for the full–scale machine is shown in Fig. 8.27(a) and the corresponding efficiency maps are illustrated in Figs. 8.27(b) and (c). In conclusion, considering the research objectives and performance targets, it can be seen that the proposed 39–slot, 16–pole PMSM can be directly scaled to satisfy the full–scale ratings and can be applied as a suitable traction motor for commercial EVs like Ford Focus Electric.

8.6. Uniqueness and Future Improvement Suggestions of Developed Prototype

The proposed scaled down PMSM is equipped with fractional–slot distributed windings with a coil pitch of 2 resulting in reduced end winding length. It also has a combined star–delta winding configuration with an odd number of 39 slots for minimum torque ripple. The interior PM rotor is equipped with v–shaped magnets with spoke type barriers for improved torque density and

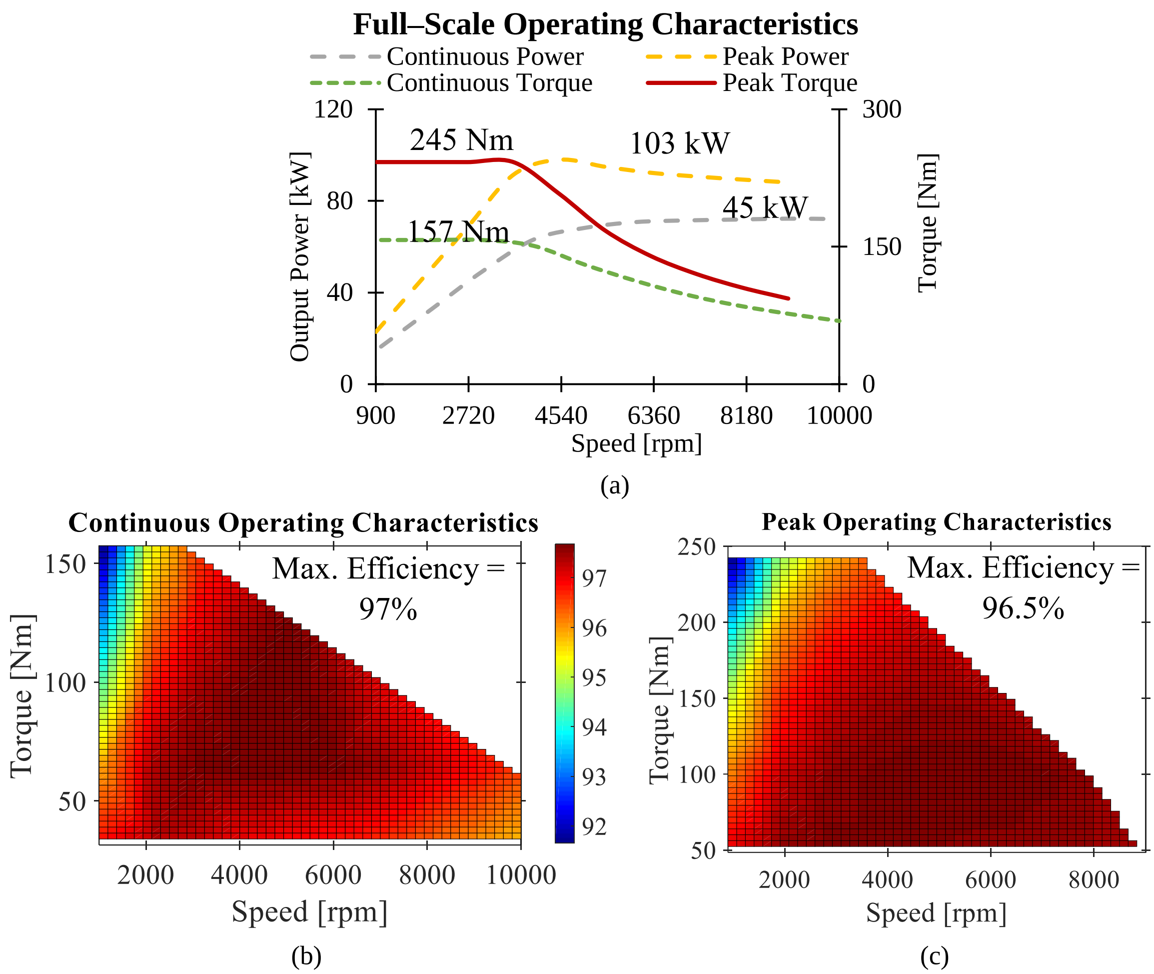

Fig. 8.27. Performance characteristics of the proposed full–scale machine obtained from FEA. (a) Continuous and peak torque and power speed characteristics. (b) Efficiency map under continuous operating conditions. (c) Efficiency map under peak operating conditions.

extended operating range. The machine has a reduced active weight of 11.6 kg and reduced PM cost of $42.4 capable of producing 150 Nm torque. Table 8.6 compares the proposed machine topology with commercially existing traction motors to highlight its potential.

While the proposed machine topology has significant advantages including scalability, there is still room for improvement to obtain increased motor performance. One of the major challenges associated with combined star–delta winding topologies is the circulating currents in the delta winding set. Hence, it is of utmost importance to take care of short–circuit conditions during operation or experimentation. Further, if the circulating currents can be reduced, the winding losses associated can be reduced and hence the machine efficiency can be subsequently improved. With respect to charging operation, while the problems associated with voltage imbalances and high oscillating torques on the motor's side are eliminated, additional switching circuitry is required

TABLE 8.6
FEATURES OF PROPOSED MACHINE TOPOLOGY COMPARED TO COMMERCIAL TRACTION MOTORS

Parameter	**Commercial Traction Motors**		**Proposed Machine Topology**
Winding topology	Distributed windings with coil pitch > 3	Fractional slot concentrated windings	Fractional–slot distributed winding with coil pitch = 2
Winding Configuration	Star or Delta		Combined star and delta
Torque Density [Nm/kg]	5 to 8		13 (without casing) 6 (with casing)
PM volume per unit torque [m^3/Nm]	~ 1.496 x 10^{-6} m^3/Nm		4.8 x 10^{-7} m^3/Nm

from the inverter side to adjust the input currents to the delta winding set. Therefore, future improvements need to be incorporated to address these shortcomings. Furthermore, considering the traction motor targets of 2040, the operating speed has to be increased to up to 20,000 rpm with almost 80% reduction in machine volume. Thus, the proposed machine topology has to be updated for such futuristic EV targets.

8.7. Conclusions

In this chapter, in order to assess the proposed machine's traction capability, a drive–cycle based analysis was conducted for common drive cycles including urban, highway and worldwide lightweight test cycle (WLTC) for a commercially available Ford Focus vehicle. It was observed from the motor performance characteristics that the proposed PMSM is capable of satisfying all the desired torque–speed points of the urban and highway drive cycles and most of the torque–speed points of the WLTC drive cycle. Further, the maximum drive cycle energy density efficiency of the motor was found to be 97%. The prototype development process of the scaled–down 3–phase fractional–slot star–delta wound interior permanent magnet motor was presented. Experimental validation under stationary conditions, no–load and loaded conditions was performed and it was observed that the developed prototype is capable of delivering the rated torque of 71.12 Nm at 3,000 rpm with a rated efficiency of 95.55% and a rated torque ripple of about 8.76% thereby meeting all the specified research objectives. Further, based on the performance analysis, a full–scale traction machine meeting the actual EV targets was developed and analyzed using FEA highlighting the scalability and potential application of the proposed machine topology. In conclusion, understanding the merits and demerits of the proposed machine topology, recommendations for design improvement and future work were also presented.

8.8. References

[1] P. Korta, L. V. Iyer, C. Lai, K. Mukherjee, J. Tjong and N. C. Kar, "A novel hybrid approach towards drive–cycle based design and optimization of a fractional slot concentrated winding SPMSM for BEVs," in proc. of *IEEE Energy Conversion Congress and Exposition (ECCE)*, Cincinnati, OH, 2017, pp. 2086–2092.

[2] J. M. Miller, Propulsion Systems for Hybrid Vehicles. Stevenage: IET, 2010.

[3] M. Ehsani, Y. Gao, and A. Emadi, Modern Electric, Hybrid Electric, and Fuel Cell Vehicles, CRC Press, USA, 2010, pp. 30–51, 105–108.

[4] ASM Handbook, Available: http://sme.vimaru.edu.vn/sites/sme.vimaru.edu.vn/files/volume_2 properties_and_selection_nonf.pdf

[5] S. Jurkovic, J. C. Morgante, K. M. Rahman and P. J. Savagian, "Electric machine design and selection for General Motors e–Assist Light Electrification Technology," in proc. of *IEEE Energy Conversion Congress and Exposition (ECCE)*, Raleigh, NC, 2012, pp. 906–913.

[6] N. Schweizer, A. Giessl, O. Schwarzhaupt and A. Buter, "Development of a Composite Wheel with Integrated Hub Motor," in proc. of 15th European Conference on Composite Materials (ECCM), Venice, Italy, 2012.

[7] 2018 Ford Focus Electric Specifications, [Online], Available: https://www.ford.ca/cars/focus/models/focus–electric

Chapter 9

Conclusions and Suggest Future Work

9.1. Conclusions

Towards the objectives listed in Chapter 1, the following research contributions were made:

1. To develop a novel analytical model for accurate performance evaluation of a PMSM for traction and charging applications
   - ✓ A universally applicable novel coupled magnetic circuit model considering all machine non–linearities
2. Using the proposed analytical model, develop and experimentally validate a futuristic high–speed traction PMSM with
   - ✓ A novel 39–slot, 16–pole IPMSM with star–delta windings with:
     1. Maximized torque density: 13 Nm/kg (without casing); 6 Nm/kg (with casing)
     2. Improved efficiency: 96.3%
     3. Reduced torque ripple: 2.4%

Although the proposed machine satisfies all of the research objectives, further analysis of the proposed star–delta windings in terms of circulating currents, unbalanced magnetic pull and winding loss minimization is required, which will be conducted in the future.

This chapter presents an overall summary of the research work and contributions presented over chapters 1–8 in this dissertation towards developing a novel high–speed PMSM with maximized torque density, improved efficiency, reduced torque ripple and extended operating range suitable for both traction and integrated charging applications.

Chapter 1 presented the opportunities and challenges of the current EV market and a comprehensive survey of the state–of–the–art traction motors, charging schemes and infrastructures available for BEVs. Understanding the technical limitations of high–speed traction motors and EVs to be addressed, the research objectives of this dissertation was established.

In *Chapter 2*, the traction motor's output performance target definitions for a typical compact electric vehicle (EV) were calculated using vehicle dynamics based analytical equations, details of a commercially available Ford Focus EV, existing traction motors, drives and transmission systems and comprehensive literature study. Further, based on the existing charging power levels, the motor's charging targets were determined. Other performance targets such as active motor weight, torque density, torque ripple and rated efficiency were fixed based on commercially available traction motors and FreedomCar 2020 EV targets. The preliminary structural dimensions and certain structural restrictions were calculated using conventional D^2L formulation approach, practical limitations, previous design experiences and motor design conventions. Thereafter, based on the target performances and traction motor requirements, along with the understanding of the merits and demerits of existing machine configurations, a baseline machine topology was selected for further analysis and improvement. In this thesis, a fractional–slot distributed wound interior permanent magnet motor was taken up for analysis.

Chapter 3 presented a non–dominated sorting genetic algorithm (NSGA) based optimal slot–pole selection for slot–shifted fractional slot wound PMSMs with coil pitch of 2 for reduced space harmonics, high torque and reduced torque ripple. Unlike conventional stator slot shifting approach of simply using twice the stator slot numbers of the baseline machine, this chapter aims to expand the design solution for slot shifted fractional–slot wound machines by analyzing all feasible slot–pole combinations. Based on the study, a 39–slot and 16–pole combination was selected for the traction motor.

For the selected slot–pole combination in the previous chapter for a 3–phase machine, *Chapter 4* explored the possibility of implementing novel odd slot numbers with star–delta winding configuration towards reduced spatial harmonic content, torque ripple minimization and improved torque density. Using winding function theory, appropriate coil and turns distribution among the two winding sets of star–delta winding topology was analyzed. A 39–slot, 16–pole interior PMSM with the proposed star–delta winding distribution was developed and its superior performance characteristics were validated using FEA. It was observed that compared to conventional star–delta wound machines, with suitable coil distribution, the proposed star–delta windings for odd slot numbers produce higher torque density, reduced torque ripple and reduced winding losses. Thus, this chapter provides a guideline for selection of suitable slot–pole combinations and coil distribution for star–delta winding topologies for various performance targets.

Chapter 5 demonstrated a novel magnetic equivalent circuit (MEC) model incorporating effects of machine nonlinearities such as magnetic saturation, temperature rise, and introduction of spatial and time harmonic contents for parameter determination of PMSMs. With advent in permanent magnet synchronous machine (PMSM) structure and inverter topologies, accurate parameter determination is of significance for high–performance control, analysis and making critical decisions on inter–dependent design parameter variations for machine optimization. The proposed coupled electromagnetic and thermal model was validated for various operating conditions of a fractional–slot distributed wound (FSDW) laboratory PMSM with finite element analysis (FEA) and experimental investigations. Based on the analysis, the proposed analytical model is implemented in the subsequent chapter to develop an optimal rotor structure for the selected stator winding configuration for reduced magnet volume, improved efficiency and extended operating range.

In *Chapter 6*, a Pareto Ant Colony optimization (ACO) was implemented with the proposed analytical model to obtain the optimal rotor structure for the recommended star–delta winding configuration. While existing literature is limited to topologies with near sinusoidal rotor magneto motive force (MMF) distribution for star–delta winding configuration, in this chapter, an IPMSM rotor design with non–sinusoidal rotor MMF was developed. It was observed that while the 39–slot, 16–pole PMSM with simple v–shaped magnets in the rotor, was capable of producing the required torque production, the machine has limited operating range, low torque density and high torque ripple. Thus, using the optimization algorithm, spoke barriers were introduced in the rotor which resulted in increased reluctance torque, reduced rotor steel and magnet requirements, resulting in cost savings and improved torque density. Further, introduction of flux barriers led to minimized torque ripple and extended operating range.

Chapter 7 presented a computationally efficient magnetic equivalent circuit model based differential evolutionary algorithm to optimally design and analyze a traction IPMSM with novel asymmetrical damper bars for integrated charging capability. The major objectives of optimization were set to obtain minimum torque during charging and high electromagnetic torque per unit machine losses during traction condition thereby ensuring maximized operating efficiency. It was observed that although higher PM volume is required to compensate for traction torque production, asymmetrical dampers result in relatively more balanced voltages during charging and hence reduced oscillating torques. Based on the analysis and understanding the practical challenges associated with using asymmetrical dampers in the machine, a simplistic approach of using the proposed 39–slot, 16–pole star–delta wound PMSM for integrated charging application was proposed and a comprehensive performance analysis was conducted. It was observed that the machine results in near zero oscillating torque, balanced voltages and significantly low rotor core losses during charging operation. Further, considering the advantages obtained during traction operation, it can be concluded that the star–delta wound PMSM is well–suited for both charging and traction operation.

In *Chapter 8*, in order to assess the proposed machine's traction capability, a drive–cycle based analysis was conducted for common drive cycles including urban, highway and worldwide lightweight test cycle (WLTC) for a commercially available Ford Focus vehicle. It was observed from the motor performance characteristics that the proposed PMSM is capable of satisfying all the desired torque–speed points of the urban and highway drive cycles and most of the torque–speed points of the WLTC drive cycle. Further, the maximum drive cycle energy density efficiency of the motor was found to be 97%. Further, considering the comprehensive performance analysis conducted in the previous chapters, a prototype of the scaled–down 3–phase fractional–slot star–delta wound interior permanent magnet motor was developed and validated experimentally. it was observed that the developed prototype is capable of delivering the rated torque of 71.12 Nm at 3,000 rpm with a rated efficiency of 95.55% and a rated torque ripple of about 8.76% thereby meeting all the specified research objectives. Subsequently, understanding the capabilities and challenges in the developed scaled–down prototype, a full–scale design with traction level ratings highlighted in Chapter 2, was developed and analyzed using FEA. With slight increase in the machine's active weight, the machine was capable of meeting the full–scale performance targets highlighting the scalability and potential application of the proposed machine topology.

Hence, it can be concluded that the proposed 39–slot, 16–pole fractional–slot star–delta wound interior PMSM: a) Satisfies the set research targets and is suitable for both traction and charging application; b) Is worth analyzing for further improvements and can be used for commercialization in the future; c) the practical implementation of integrated charging can be challenging and required further investigation to design the entire system and analyze the performance.

9.2. Suggested Future Work

1. <u>Comprehensive two–axis based analytical modeling of star–delta windings</u>: In order to capture the detrimental effects of the circulating currents in the delta winding set and accurately determine the motor parameters, further investigation of two–axis modeling of

star–delta windings is required. Also, very limited literature exists on modeling of such winding topologies.

2. Unbalanced magnetic pull and short–circuit analysis of proposed machine configuration: While the proposed topology has significant advantages, further investigations on short–circuit analysis and unbalanced forces are required to identify its shortcomings.
3. System level analysis of integrated charging operation using proposed motor: Challenges associated with practical implementation of the star–delta winding for integrated charging needs to be addressed and system level analysis is required to identify meaningful merits and demerits.
4. Analysis of aluminum windings for further light–weighting of the motor: Due to low turns required by high–speed motors, aluminum windings are a potential candidate for such traction motors. However, to improve the aluminum wound motor efficiency, analysis of bar conductors or form windings is required.
5. Structural and thermal analysis of the proposed full–scale motor design: While the full–scale motor design satisfies the electromagnetic requirements, for commercialization, comprehensive structural and thermal analysis is required to understand the integrity and feasibility of the proposed motor structure.
6. Futuristic, light–weight materials for motor casing: As seen from Chapter 8, although the active weight of the motor is significantly reduced to meet the torque and power density targets, the motor casing contributes to almost 47% of the motor weight reducing the torque density from 13 to 6 Nm/kg. Thus, further investigations on optimal motor housing design and new, light–weight material analysis is required to decrease the machine weight further.
7. Optimal cooling design: In this thesis, a simple helical cooling system was implemented for ease of manufacture. However, with high–speed machines, a good thermal management system is of significance.
8. Comprehensive cost savings analysis of proposed motor compared to commercially available traction motors. Extension of design targets to meet DOE 2025 EV motor targets.

APPENDIX A
LIST OF PUBLICATIONS

A.1. Published peer–reviewed and submitted Journal Papers:

1. **S. Mukundan**, E. Ghosh, H. Dhulipati, J. Tjong, and N.C. Kar, “Pareto ACO Algorithm Based Optimal Design of IPM Rotor Utilizing Star–Delta Winding Harmonics towards Maximum Torque Density and Extended Operating Range,” submitted to *IEEE Transactions on Energy Conversion*, 2019.
2. **S. Mukundan**, H. Dhulipati, J. Tjong, and N. C. Kar, “Parameter Determination of PMSM using Coupled Electromagnetic and Thermal Model Incorporating Current Harmonics,” *IEEE Transactions on Magnetics*, vol. 54, no. 11, pp. 1–5, Nov. 2018.
3. **S. Mukundan**, H. Dhulipati, C. Lai, K. Mukherjee, J. Tjong and N. C. Kar, “Design and Optimization of Traction IPMSM with Asymmetrical Damper Bars for Integrated Charging Capability using Evolutionary Algorithm”, *IEEE Transactions on Energy Conversion*, vol. 33, no. 4, pp. 2060–2069, Dec. 2018.
4. H. Dhulipati, E. Ghosh, P. Korta, **S. Mukundan**, J. Tjong, and N.C. Kar, “Advanced Design Optimization Technique for Torque Profile Improvement in Six–Phase PMSM Using Supervised Machine Learning for Direct–Drive EV,” *IEEE Transactions on Energy Conversion*, 2019 [Early Access].
5. Y. He, M. Mehdi, E. J. Hilinski, A. Edrisy, A. Mollaeian, **S. Mukundan**, and N. C. Kar, “Evaluation of Local Anisotropy of Magnetic Response from Non–Oriented Electrical Steel by Magnetic Barkhausen Noise,” *IEEE Transactions on Magnetics*, vol. 54, no. 11, pp. 1–5, Nov. 2018.
6. H. Dhulipati, **S. Mukundan**, C. Lai, K. Mukherjee, J. Tjong and N. C. Kar, “Multiple Reference Frame–based Extended Concentrated Wound PMSM Model considering PM Flux Linkage and Inductance Harmonics,” *IEEE Transactions on Energy Conversion*, vol. 34, no. 2, pp. 731 – 740, June 2019.
7. K.L.V. Iyer, C. Lai, **S. Mukundan**, H. Dhulipati, K. Mukherjee, and N.C. Kar, “Investigation of a Six–phase Interior Permanent Magnet Synchronous Machine for Integrated Charging and Propulsion in EVs,” *SAE International Journal of Alternative Powertrains*, 2018.

8. K. L. V. Iyer, C. Lai, **S. Mukundan**, H. Dhulipati, K. Mukherjee and N. C. Kar, “Investigation of Challenges in Interior and Surface Permanent Magnet Synchronous Machines during Integrated Charging Operation in Electric Vehicles,” *International Journal of Powertrains*, vol. 7, no. 4, 2018.
9. K. L. V. Iyer, C. Lai, H. Dhulipati, **S. Mukundan**, K. Mukherjee, Jimi Tjong and N. C. Kar, “A Novel MTPA theory based Bottom–up Approach towards Parametric and Structural Design of Interior PMSM for Direct–Drive Electric Vehicles”, *IEEE Transactions on Electrical Energy Systems*, vol. 28, no. 2, 2018.
10. K. L. V. Iyer, C. Lai, **S. Mukundan**, H. Dhulipati, K. Mukherjee and N. C. Kar, "Investigation of Interior Permanent Magnet Motor With Dampers for Electric Vehicle Propulsion and Mitigation of Saliency Effect During Integrated Charging Operation," *IEEE Transactions on Vehicular Technology*, vol. 68, no. 2, pp. 1254–1265, Feb. 2019.

A.2. Published peer–reviewed Conference papers:

1. **S. Mukundan**, M. Mehdi, H. Dhulipati, L. Chauvin, A. Edrisy, Y. He, J. Tjong, and N.C. Kar, “Performance Analysis of Non–Oriented Electrical Steel with Optimum Texture for High–Speed Traction Motors,” Presented at the *International Conference on Materials and Intelligent Manufacturing* (ICMIM), Incheon, S. Korea, August 2019.
2. **S. Mukundan**, H. Dhulipati, E. Ghosh, G Feng, and N. C. Kar, “Non–Dominated Sorting Genetic Algorithm Based Investigation of Optimal Odd Slot Numbers for Stator Shifted Fractional–Slot Wound PMSMs,” Presented at *IEEE Energy Conversion. Congress and Exposition* (ECCE), Baltimore, USA, September 2019.
3. **S. Mukundan**, H. Dhulipati, L. Chauvin, A. Edrisy, J. Tjong, and N. C. Kar, “Comparative Performance Analysis of Copper and Aluminum Wound Fractional–Slot PMSMs for High–Speed Traction Application,” Presented at the *IEEE 22nd International Conference on Electrical Machines and Systems* (ICEMS), China, August 2019.
4. **S. Mukundan**, H. Dhulipati, G. Feng, J. Tjong and N. C. Kar, "Modeling and Analysis of Novel Star-Delta Winding Configuration with Odd Slot Numbers for Reduced Space Harmonics Using Winding Function," in proc. of *IEEE International Electric Machines & Drives Conference* (IEMDC), San Diego, CA, USA, 2019, pp. 1910–1916.
5. **S. Mukundan**, H. Dhulipati, J. Tjong, and N. C. Kar, “Parameter Determination of PMSM using Coupled Electromagnetic and Thermal Model Incorporating Current Harmonics”, in

proc. of *IEEE International Magnetic Conference* (Intermag), 2018.

6. **S. Mukundan**, H. Dhulipati, K. L. V. Iyer, C. Lai, K. Mukherjee and N. C. Kar, "Comparative Performance Analysis of 3–Phase IPMSM Rotor Configurations with Dampers for Integrated Charging Application in EVs," in proc. of *IEEE 43rd Annual Conf. of the Ind. Electronics Society* (IECON), Beijing, China, 2017, pp. 1856–1861.
7. **S. Mukundan**, H. Dhulipati, K. L. V. Iyer, N. C. Kar and K. Mukherjee, "Comparison of inductance determination methods of PMSMs for EV application," in proc. of *IEEE 30th Canadian Conference on Electrical and Computer Engineering* (CCECE), Windsor, ON, 2017, pp. 1–4.
8. **S. Mukundan**, K. L. V. Iyer, H. Dhulipati, K. Mukherjee, Jimi Tjong and N. C. Kar, "Response Surface Methodology based Optimization of Surface PM Machine Incorporating Stator Slotting and PM Sizing Effects to Extend the Operating Limits for Direct–Drive EV Application," in proc. of *IEEE International Conference on Electric Machines* (ICEM), Switzerland, 2016, pp. 2045–2051.
9. P. Roy, M. Towhidi, F. Ahmed, **S. Mukundan**, H. Dhulipati, and N. C. Kar, "A Novel Hybrid Technique for Thermal Analysis of Permanent Magnet Synchronous Motor Used in Electric Vehicle Application," Submitted to *SAE World Congress Experience*, 2019.
10. M. Towhidi, F. Ahmed, P. Roy, **S. Mukundan**, and N. C. Kar, "Lumped Parameter Thermal Network Modeling for Online Temperature Prediction of Permanent Magnet Synchronous Motor for Different Drive Cycles in Electric Vehicle Applications," Submitted to *SAE World Congress Experience*, 2019.
11. M. Towhidi, P. Roy, **S. Mukundan**, F. Ahmed, and N. C. Kar, "Cooling Design Optimization and Cooling Performance Investigation of Newly Designed Traction Motor," Submitted to *SAE World Congress Experience*, 2019.
12. P. Roy, A. Bourgault, F. Ahmed, M. Towhidi, **S. Mukundan**, H. Dhulipati, E. Ghosh, and N. C. Kar, "Thermal Representation of Interior and Surface Mounted PMSMs for Electric Vehicle Application," Accepted for presentation at the *IEEE 45th Annual Conference of the Industrial Electronics Society* (IECON), Lisbon, Portugal, October 2019.
13. H. Dhulipati, **S. Mukundan**, L. Chauvin, C. Riczu, A. Edrisy, M. Kozdras, J. Bauman, S. Habibi, J. Tjong, and N.C. Kar, "Investigation of Aluminium and Copper Wound PMSM for Direct–drive Electric Vehicle Application," Presented at the *International Conference*

on Materials and Intelligent Manufacturing (ICMIM), Incheon, S. Korea, August 2019.

14. H. Dhulipati, **S. Mukundan**, E. Ghosh, J. Tjong, and N. C. Kar, "Slot–pole Combination Selection for Concentrated Wound Consequent Pole PMSM with Reduced EMF and Inductance Harmonics," Presented at the *IEEE 22nd International Conference on Electrical Machines and Systems* (ICEMS), China, August 2019.
15. P. Roy, M. Towhidi, F. Ahmed, **S. Mukundan**, A. Balamurali, and N. C. Kar, "A Comprehensive Review of Thermal Design and Analysis of Traction Motors," Presented at the *IEEE 28th International Symposium on Industrial Electronics* (ISIE), Vancouver, June 2019, pp. 203–208.
16. F. Ahmed, E. Ghosh, **S. Mukundan**, H. Dhulipati, and N. C. Kar, "LPTN and FEA Modeling for Thermal Characterization of an Interior Permanent Magnet Synchronous Motor (IPMSM) for Electric Vehicle Application," in proc. of *Energy and Sustainability Conference*, June 2018.
17. H. Dhulipati, **S. Mukundan**, W. Li, and N. C. Kar, "Investigation of Phase Angle Displacements in Six–phase PMSM with Non–Overlapping Windings for Reduced MMF Harmonics," in proc. of *IEEE International Conference on Electrical Machines and Systems* (ICEMS), South Korea, 2018, pp. 308–313.
18. D. Banerjee, Z. Li, **S. Mukundan**, A. Balamurali, C. Lai, and N. C. Kar, "Online Parameter Estimation and Self Commissioning of Interior Permanent Magnet Motor Drive," in proc. of *IEEE International Conference on Electrical Machines and Systems* (ICEMS), South Korea, 2018, pp. 1401–1406.
19. Y. He, M. Mehdi, E. J. Hilinski, A. Edrisy, A. Mollaeian, **S. Mukundan**, and N. C. Kar, "Evaluation of Local Anisotropy of Magnetic Response from Non–Oriented Electrical Steel by Magnetic Barkhausen Noise," in proc. of *IEEE International Magnetics Conference* (Intermag), 2018.
20. M. Zhu, W. Hu, **S. Mukundan**, M. Kelly, and N. C. Kar, "Multi–Sensor Fusion Based Permanent Magnet Demagnetization Detection in Permanent Magnet Synchronous Machines", in proc. of *IEEE International Magnetics Conference* (Intermag), 2018.
21. H. Dhulipati, E. Ghosh, **S. Mukundan**, J. Tjong, and N. C. Kar, "Adagrad Algorithm based Optimal Slot–Pole Selection for Reduced Inductance Harmonics in Concentrated Wound Multiphase PMSM," in proc. of *IEEE Int. Magnetics Conference* (Intermag), 2018.

22. H. Dhulipati, **S. Mukundan**, K. L. V. Iyer and N. C. Kar, "Skewing of stator windings for reduction of spatial harmonics in concentrated wound PMSM," in proc. of *IEEE 30th Canadian Conference on Electrical and Computer Engineering* (CCECE), Windsor, ON, 2017, pp. 1–4.
23. K. L. V. Iyer, H. Dhulipati, **S. Mukundan**, K. Mukherjee, Jimi Tjong and N. C. Kar, "Design Approach Incorporating MTPA and Winding Function Theories for On–board Direct–Drive Surface PM Machines with Concentrated Windings in EVs," in proc. of *IEEE International Conference on Elec. Machines* (ICEM), Switzerland, 2016, pp. 1499–1505.
24. H. Dhulipati, K. L. V. Iyer, **S. Mukundan**, K. Mukherjee, Jimi Tjong and N. C. Kar, "Investigation of 6–Phase Surface PM Machines with Concentrated Windings for Reduction in Space Harmonics, Leakage Inductance and Magnet Loss in Direct–Drive EV," in proc. of *IEEE International Conference on Electric Machines* (ICEM), Switzerland, 2016, pp. 811–817.
25. K. L. V. Iyer, **S. Mukundan**, H. Dhulipati, K. Mukherjee, B. Minaker, and N. C. Kar, "Design Considerations for Permanent Magnet Machine Drives for Direct–Drive Electric Vehicles," in proc. of *IEEE International Electric Machines Drives Conference* (IEMDC), USA, pp. 1170–1176, 2015.

APPENDIX B
INDUSTRIAL PROJECT CONTRIBUTIONS AND SCHOLARSHIPS

B.1. Industrial R&D contributions at the University of Windsor towards:

- NSERC CRD Project on “Powertrain Components and Systems for Next Generation Electric Vehicles” – *Ford Motor Company, Canada and D&V Electronics, Canada (In progress)*

- NSERC ORF Project on “Electric Extended Range Clean Affordable Ontario Mobility (EECOMOBILITY)” – *Ford Motor Company, Canada and D&V Electronics, Canada (In progress)*

- NSERC CRD Project on “Traction E–Motor Drive System Testing and Analysis” – *Magna International Inc., (In progress)*

- NSERC CRD Project on “Development of Enhanced Powertrain Component Tester with Electric and Hybrid Electric Vehicle Emulation Capabilities” – *D&V Electronics, Canada (In Progress)*

- NSERC CREATE Project on “Hybrid Electric Vehicle Powertrain Design and Development” – *Ford Motor Company, Canada and McMaster University, Canada (In Progress)*

- Ontario Centres of Excellence (OCE) TalentEdge Intern with *Magna International Inc.*, on ‘Testing and Evaluation of Conventional and GaN based Traction Motor Drives’ from January to April 2019

B.2. Scholarships Received:

- Ontario Centres of Excellence (OCE) TalentEdge Scholarship, 2019

- University of Windsor Graduate Teaching Assistance Scholarships, 2014 – 2019

- Research Scholarship from the Canada Research Chair Program in Electrified Transportation Systems at the Centre for Hybrid Automotive Research and Green Energy, 2014 – 2019

APPENDIX C
PERMISSION FOR USING IEEE PUBLICATIONS

8/16/2019 Rightslink® by Copyright Clearance Center

Copyright Clearance Center RightsLink® Home Account Info Help LIVE CHAT

IEEE Requesting permission to reuse content from an IEEE publication

Title: Design and Optimization of Traction IPMSM With Asymmetrical Damper Bars for Integrated Charging Capability Using Evolutionary Algorithm

Author: Shruthi Mukundan

Publication: Energy Conversion, IEEE Transactions on

Publisher: IEEE

Date: Dec. 2018

Copyright © 2018, IEEE

Logged in as:
Shruthi Mukundan
University of Windsor
LOGOUT

Thesis / Dissertation Reuse

The IEEE does not require individuals working on a thesis to obtain a formal reuse license, however, you may print out this statement to be used as a permission grant:

Requirements to be followed when using any portion (e.g., figure, graph, table, or textual material) of an IEEE copyrighted paper in a thesis:

1) In the case of textual material (e.g., using short quotes or referring to the work within these papers) users must give full credit to the original source (author, paper, publication) followed by the IEEE copyright line © 2011 IEEE.
2) In the case of illustrations or tabular material, we require that the copyright line © [Year of original publication] IEEE appear prominently with each reprinted figure and/or table.
3) If a substantial portion of the original paper is to be used, and if you are not the senior author, also obtain the senior author's approval.

Requirements to be followed when using an entire IEEE copyrighted paper in a thesis:

1) The following IEEE copyright/ credit notice should be placed prominently in the references: © [year of original publication] IEEE. Reprinted, with permission, from [author names, paper title, IEEE publication title, and month/year of publication]
2) Only the accepted version of an IEEE copyrighted paper can be used when posting the paper or your thesis on-line.
3) In placing the thesis on the author's university website, please display the following message in a prominent place on the website: In reference to IEEE copyrighted material which is used with permission in this thesis, the IEEE does not endorse any of [university/educational entity's name goes here]'s products or services. Internal or personal use of this material is permitted. If interested in reprinting/republishing IEEE copyrighted material for advertising or promotional purposes or for creating new collective works for resale or redistribution, please go to http://www.ieee.org/publications_standards/publications/rights/rights_link.html to learn how to obtain a License from RightsLink.

If applicable, University Microfilms and/or ProQuest Library, or the Archives of Canada may supply single copies of the dissertation.

BACK CLOSE WINDOW

Copyright © 2019 Copyright Clearance Center, Inc. All Rights Reserved. Privacy statement. Terms and Conditions.
Comments? We would like to hear from you. E-mail us at customercare@copyright.com

https://s100.copyright.com/AppDispatchServlet#formTop 1/1

Copyright Clearance Center RightsLink® Home Account Info Help LIVE CHAT

IEEE Requesting permission to reuse content from an IEEE publication

Title: Parameter Determination of PMSM Using Coupled Electromagnetic and Thermal Model Incorporating Current Harmonics

Author: Shruthi Mukundan

Publication: Magnetics, IEEE Transactions on

Publisher: IEEE

Date: Nov. 2018

Copyright © 2018, IEEE

Logged in as:
Shruthi Mukundan
University of Windsor
LOGOUT

Thesis / Dissertation Reuse

The IEEE does not require individuals working on a thesis to obtain a formal reuse license, however, you may print out this statement to be used as a permission grant:

Requirements to be followed when using any portion (e.g., figure, graph, table, or textual material) of an IEEE copyrighted paper in a thesis:

1) In the case of textual material (e.g., using short quotes or referring to the work within these papers) users must give full credit to the original source (author, paper, publication) followed by the IEEE copyright line © 2011 IEEE.
2) In the case of illustrations or tabular material, we require that the copyright line © [Year of original publication] IEEE appear prominently with each reprinted figure and/or table.
3) If a substantial portion of the original paper is to be used, and if you are not the senior author, also obtain the senior author's approval.

Requirements to be followed when using an entire IEEE copyrighted paper in a thesis:

1) The following IEEE copyright/ credit notice should be placed prominently in the references: © [year of original publication] IEEE. Reprinted, with permission, from [author names, paper title, IEEE publication title, and month/year of publication]
2) Only the accepted version of an IEEE copyrighted paper can be used when posting the paper or your thesis on-line.
3) In placing the thesis on the author's university website, please display the following message in a prominent place on the website: In reference to IEEE copyrighted material which is used with permission in this thesis, the IEEE does not endorse any of [university/educational entity's name goes here]'s products or services. Internal or personal use of this material is permitted. If interested in reprinting/republishing IEEE copyrighted material for advertising or promotional purposes or for creating new collective works for resale or redistribution, please go to http://www.ieee.org/publications_standards/publications/rights/rights_link.html to learn how to obtain a License from RightsLink.

If applicable, University Microfilms and/or ProQuest Library, or the Archives of Canada may supply single copies of the dissertation.

BACK CLOSE WINDOW

Copyright © 2019 Copyright Clearance Center, Inc. All Rights Reserved. Privacy statement. Terms and Conditions.
Comments? We would like to hear from you. E-mail us at customercare@copyright.com

Copyright Clearance Center RightsLink®

Home | Account Info | Help

IEEE
Requesting permission to reuse content from an IEEE publication

Title:	Modeling and Analysis of Novel Star-Delta Winding Configuration with Odd Slot Numbers for Reduced Space Harmonics Using Winding Function
Conference Proceedings:	2019 IEEE International Electric Machines & Drives Conference (IEMDC)
Author:	Shruthi Mukundan
Publisher:	IEEE
Date:	May 2019

Copyright © 2019, IEEE

Logged in as:
Shruthi Mukundan
University of Windsor

LOGOUT

Thesis / Dissertation Reuse

The IEEE does not require individuals working on a thesis to obtain a formal reuse license, however, you may print out this statement to be used as a permission grant:

Requirements to be followed when using any portion (e.g., figure, graph, table, or textual material) of an IEEE copyrighted paper in a thesis:

1) In the case of textual material (e.g., using short quotes or referring to the work within these papers) users must give full credit to the original source (author, paper, publication) followed by the IEEE copyright line © 2011 IEEE.
2) In the case of illustrations or tabular material, we require that the copyright line © [Year of original publication] IEEE appear prominently with each reprinted figure and/or table.
3) If a substantial portion of the original paper is to be used, and if you are not the senior author, also obtain the senior author's approval.

Requirements to be followed when using an entire IEEE copyrighted paper in a thesis:

1) The following IEEE copyright/ credit notice should be placed prominently in the references: © [year of original publication] IEEE. Reprinted, with permission, from [author names, paper title, IEEE publication title, and month/year of publication]
2) Only the accepted version of an IEEE copyrighted paper can be used when posting the paper or your thesis on-line.
3) In placing the thesis on the author's university website, please display the following message in a prominent place on the website: In reference to IEEE copyrighted material which is used with permission in this thesis, the IEEE does not endorse any of [university/educational entity's name goes here]'s products or services. Internal or personal use of this material is permitted. If interested in reprinting/republishing IEEE copyrighted material for advertising or promotional purposes or for creating new collective works for resale or redistribution, please go to http://www.ieee.org/publications_standards/publications/rights/rights_link.html to learn how to obtain a License from RightsLink.

If applicable, University Microfilms and/or ProQuest Library, or the Archives of Canada may supply single copies of the dissertation.

BACK | CLOSE WINDOW

Copyright © 2019 Copyright Clearance Center, Inc. All Rights Reserved. Privacy statement. Terms and Conditions.
Comments? We would like to hear from you. E-mail us at customercare@copyright.com

Copyright Clearance Center RightsLink® Home Account Info Help LIVE CHAT

IEEE Requesting permission to reuse content from an IEEE publication

Title:	Comparative performance analysis of 3-phase IPMSM rotor configurations with dampers for integrated charging application in EVs
Conference Proceedings:	IECON 2017 - 43rd Annual Conference of the IEEE Industrial Electronics Society
Author:	Shruthi Mukundan
Publisher:	IEEE
Date:	Oct. 2017

Copyright © 2017, IEEE

Logged in as:
Shruthi Mukundan
University of Windsor
LOGOUT

Thesis / Dissertation Reuse

The IEEE does not require individuals working on a thesis to obtain a formal reuse license, however, you may print out this statement to be used as a permission grant:

Requirements to be followed when using any portion (e.g., figure, graph, table, or textual material) of an IEEE copyrighted paper in a thesis:

1) In the case of textual material (e.g., using short quotes or referring to the work within these papers) users must give full credit to the original source (author, paper, publication) followed by the IEEE copyright line © 2011 IEEE.
2) In the case of illustrations or tabular material, we require that the copyright line © [Year of original publication] IEEE appear prominently with each reprinted figure and/or table.
3) If a substantial portion of the original paper is to be used, and if you are not the senior author, also obtain the senior author's approval.

Requirements to be followed when using an entire IEEE copyrighted paper in a thesis:

1) The following IEEE copyright/ credit notice should be placed prominently in the references: © [year of original publication] IEEE. Reprinted, with permission, from [author names, paper title, IEEE publication title, and month/year of publication]
2) Only the accepted version of an IEEE copyrighted paper can be used when posting the paper or your thesis on-line.
3) In placing the thesis on the author's university website, please display the following message in a prominent place on the website: In reference to IEEE copyrighted material which is used with permission in this thesis, the IEEE does not endorse any of [university/educational entity's name goes here]'s products or services. Internal or personal use of this material is permitted. If interested in reprinting/republishing IEEE copyrighted material for advertising or promotional purposes or for creating new collective works for resale or redistribution, please go to http://www.ieee.org/publications_standards/publications/rights/rights_link.html to learn how to obtain a License from RightsLink.

If applicable, University Microfilms and/or ProQuest Library, or the Archives of Canada may supply single copies of the dissertation.

BACK CLOSE WINDOW

Copyright © 2019 Copyright Clearance Center, Inc. All Rights Reserved. Privacy statement. Terms and Conditions.
Comments? We would like to hear from you. E-mail us at customercare@copyright.com

Copyright Clearance Center RightsLink®

Home | Account Info | Help | LIVE CHAT

IEEE Requesting permission to reuse content from an IEEE publication

Title: Response surface methodology based optimization of surface PM machine incorporating stator slotting and PM sizing effects to extend the operating limits for direct-drive EV application

Conference Proceedings: 2016 XXII International Conference on Electrical Machines (ICEM)

Author: Shruthi Mukundan

Publisher: IEEE

Date: Sept. 2016

Copyright © 2016, IEEE

Logged in as:
Shruthi Mukundan
University of Windsor
LOGOUT

Thesis / Dissertation Reuse

The IEEE does not require individuals working on a thesis to obtain a formal reuse license, however, you may print out this statement to be used as a permission grant:

Requirements to be followed when using any portion (e.g., figure, graph, table, or textual material) of an IEEE copyrighted paper in a thesis:

1) In the case of textual material (e.g., using short quotes or referring to the work within these papers) users must give full credit to the original source (author, paper, publication) followed by the IEEE copyright line © 2011 IEEE.
2) In the case of illustrations or tabular material, we require that the copyright line © [Year of original publication] IEEE appear prominently with each reprinted figure and/or table.
3) If a substantial portion of the original paper is to be used, and if you are not the senior author, also obtain the senior author's approval.

Requirements to be followed when using an entire IEEE copyrighted paper in a thesis:

1) The following IEEE copyright/ credit notice should be placed prominently in the references: © [year of original publication] IEEE. Reprinted, with permission, from [author names, paper title, IEEE publication title, and month/year of publication]
2) Only the accepted version of an IEEE copyrighted paper can be used when posting the paper or your thesis on-line.
3) In placing the thesis on the author's university website, please display the following message in a prominent place on the website: In reference to IEEE copyrighted material which is used with permission in this thesis, the IEEE does not endorse any of [university/educational entity's name goes here]'s products or services. Internal or personal use of this material is permitted. If interested in reprinting/republishing IEEE copyrighted material for advertising or promotional purposes or for creating new collective works for resale or redistribution, please go to http://www.ieee.org/publications_standards/publications/rights/rights_link.html to learn how to obtain a License from RightsLink.

If applicable, University Microfilms and/or ProQuest Library, or the Archives of Canada may supply single copies of the dissertation.

BACK | CLOSE WINDOW

Copyright © 2019 Copyright Clearance Center, Inc. All Rights Reserved. Privacy statement. Terms and Conditions.
Comments? We would like to hear from you. E-mail us at customercare@copyright.com

Copyright Clearance Center RightsLink® Home Account Info Help LIVE CHAT

IEEE Requesting permission to reuse content from an IEEE publication

Title: Comparison of inductance determination methods of PMSMs for EV application

Conference Proceedings: 2017 IEEE 30th Canadian Conference on Electrical and Computer Engineering (CCECE)

Author: Shruthi Mukundan

Publisher: IEEE

Date: April 2017

Copyright © 2017, IEEE

Logged in as:
Shruthi Mukundan
University of Windsor
LOGOUT

Thesis / Dissertation Reuse

The IEEE does not require individuals working on a thesis to obtain a formal reuse license, however, you may print out this statement to be used as a permission grant:

Requirements to be followed when using any portion (e.g., figure, graph, table, or textual material) of an IEEE copyrighted paper in a thesis:

1) In the case of textual material (e.g., using short quotes or referring to the work within these papers) users must give full credit to the original source (author, paper, publication) followed by the IEEE copyright line © 2011 IEEE.
2) In the case of illustrations or tabular material, we require that the copyright line © [Year of original publication] IEEE appear prominently with each reprinted figure and/or table.
3) If a substantial portion of the original paper is to be used, and if you are not the senior author, also obtain the senior author's approval.

Requirements to be followed when using an entire IEEE copyrighted paper in a thesis:

1) The following IEEE copyright/ credit notice should be placed prominently in the references: © [year of original publication] IEEE. Reprinted, with permission, from [author names, paper title, IEEE publication title, and month/year of publication]
2) Only the accepted version of an IEEE copyrighted paper can be used when posting the paper or your thesis on-line.
3) In placing the thesis on the author's university website, please display the following message in a prominent place on the website: In reference to IEEE copyrighted material which is used with permission in this thesis, the IEEE does not endorse any of [university/educational entity's name goes here]'s products or services. Internal or personal use of this material is permitted. If interested in reprinting/republishing IEEE copyrighted material for advertising or promotional purposes or for creating new collective works for resale or redistribution, please go to http://www.ieee.org/publications_standards/publications/rights/rights_link.html to learn how to obtain a License from RightsLink.

If applicable, University Microfilms and/or ProQuest Library, or the Archives of Canada may supply single copies of the dissertation.

BACK CLOSE WINDOW

Copyright © 2019 Copyright Clearance Center, Inc. All Rights Reserved. Privacy statement. Terms and Conditions.
Comments? We would like to hear from you. E-mail us at customercare@copyright.com

VITA AUCTORIS

NAME:	Shruthi Mukundan
PLACE OF BIRTH:	Chennai, India
YEAR OF BIRTH:	1993
EDUCATION:	SASTRA University, India B.Tech Electrical and Electronics Engineering, 2010 – 2014
	Modern Senior Secondary School, India